



2D droplet microfluidics driven by confinement gradients

Rémi Dangla

► To cite this version:

Rémi Dangla. 2D droplet microfluidics driven by confinement gradients. Mechanics of the fluids [physics.class-ph]. Ecole Polytechnique X, 2012. English. <tel-00835536>

HAL Id: tel-00835536

<https://tel.archives-ouvertes.fr/tel-00835536>

Submitted on 18 Jun 2013

HAL is a multi-disciplinary open access archive for the deposit and dissemination of scientific research documents, whether they are published or not. The documents may come from teaching and research institutions in France or abroad, or from public or private research centers.

L'archive ouverte pluridisciplinaire **HAL**, est destinée au dépôt et à la diffusion de documents scientifiques de niveau recherche, publiés ou non, émanant des établissements d'enseignement et de recherche français ou étrangers, des laboratoires publics ou privés.



École Polytechnique
Laboratoire d'Hydrodynamique

Thèse présentée pour obtenir le grade de
DOCTEUR DE L'ÉCOLE POLYTECHNIQUE

Spécialité : Mécanique

par

Rémi DANGLA

2D droplet microfluidics driven by confinement gradients

Soutenance prévue le 8 octobre 2012 devant le jury composé de

José Bico	rapporteur	ESPCI
Philippe Marmottant	rapporteur	LIPhy
Isabelle Cantat	examineur	IP Rennes
François Gallaire	examineur	EPFL
Philippe Renaud	examineur	EPFL
Charles N. Baroud	directeur de thèse	Ecole Polytechnique



ABSTRACT

Over the last decade, the field of droplet microfluidics has built upon the concept of droplet microreactors, i.e. the idea that a drop can be used to collect, carry and characterize chemicals, biological systems or genetic material. Although droplet microfluidics promises to miniaturize and automate standard microtiter plates on-a-chip, the field has remained dominated by a serial mindset which contrast with the inherent 2D format of the microtiter plate. This manuscript provides a novel strategy for droplet management that allows droplet microfluidics to be implemented easily inside 2D chambers. To do so, it relies on confinement gradients to apply forces on the droplets.

This manuscript is divided into two complementary parts. The first is dedicated to the theoretical modelling of droplet motion in a 2D chamber with confinement gradients. The theory relies on a minimum principle that applies to viscous two phase flows. We apply this minimum principle to the simple case of a drop moving in a flat chamber and provide new physical insights on phenomena initially predicted by Taylor and Saffman. We then build onto the minimum principle to predict the trajectory of a droplet in a chamber with confinement gradients. We compare our model with trajectories measured experimentally in deformed microchannels and find satisfying agreement.

The second presents and analyzes experimental implementations of droplet actuation by confinement gradients within microfluidic devices. First, we show how rails and anchors, which are small grooves and holes etched in one of the channel walls respectively, are able to guide and trap droplets against a mean outer flow in a 2D chamber. Then, we address the issue of droplet production and transport using confinement gradients. We show that when fluid is injected from an inlet channel into a non-parallel reservoir, it breaks up into monodisperse droplets. Combined with rails and anchors, this techniques opens perspectives for a new generation of droplet 2D microfluidic devices that are simpler to operate than flow powered serial droplet microfluidics and less expensive than electrode based digital microfluidics.

RÉSUMÉ

L'usage de goutte comme microreacteurs motive le développement rapide de la microfluidique de gouttes. En effet, une goutte peut être utilisée pour collecter, transporter et analyser du matériel chimique, biologique ou génétique. Ainsi, la microfluidique de goutte porte la promesse d'une miniaturisation et d'une automatisation sur puce des process actuellement mis en œuvre sur microplaques. Toutefois, l'architecture des dispositifs reste essentiellement sérielle et en opposition avec le format intrinsèquement 2D des microplaques. Ce travail de thèse fournit une nouvelle stratégie de gestion de gouttes sur puce qui permet d'implémenter des procédés de microfluidique de goutte au sein de chambres bidimensionnelles. Les méthodes mises au point emploient des gradients de confinement pour agir sur les gouttes.

Le manuscrit comporte deux parties complémentaires. La première fournit un cadre théorique pour l'étude de la dynamique de gouttes dans des chambres avec gradients de confinement. La théorie s'appuie sur un principe minimum pour écoulements visqueux bi-phasiques. Nous appliquons ce principe minimum au cas élémentaires d'une goutte en mouvement dans une chambre mince et obtenons ainsi une réinterprétation physique des phénomènes initialement prédits par Taylor et Saffman. Ensuite, nous ajoutons des gradients de confinements dans le modèle et décrivons la trajectoire d'une goutte dans ce cas. Les trajectoires prédites sont en accord avec les observations expérimentales obtenues.

La seconde partie présente et analyse l'implémentation expérimentale de la gestion de goutte par gradient de confinement au sein de puces microfluidiques. Tout d'abord, nous montrons comment rails et ancrs, qui sont de petites rainures et puits gravés à la surface du canal, sont capables de guider et piéger des gouttes respectivement. Ensuite, nous adressons la production et le transport de goutte par gradient de confinement. Nous montrons que lorsqu'un fluide arrive à l'extrémité d'un injecteur se jetant dans un réservoir en forme de biseau, celui-ci se scinde spontanément en gouttes monodisperses. Combinée avec les rails et ancrs, cette méthode de production de goutte nous permet d'imaginer une nouvelle génération de dispositifs microfluidiques à base de goutte dont l'architecture bidimensionnelle se rapproche de la microplaque, tout en restant simple à utiliser et peu cher à fabriquer.

REMERCIEMENTS

Je remercie tous celles ou ceux qui ont une part de responsabilité dans l'aboutissement de cette thèse de doctorat. La liste est longue, sans doute incomplète, et difficile à ordonnée...

... à commencer bien sûr par Charles Baroud avec qui il est un réel plaisir de travailler ; qui m'a offert un sujet vaste et passionnant dans lequel j'ai pu pleinement exprimé ma créativité ; qui a su me forcer à garder un fil conducteur pendant trois années de recherches foisonnantes ; et évidemment sans qui cette thèse n'aurait pas lieu d'être.

... Lucy, ma fiancée, qui m'a toujours soutenu et encouragé dans mes choix, et avec qui j'ai l'immense bonheur de partager ma vie.

... ma famille, mes parents, mon frère, ma belle-famille également, pour leur soutien et leur confiance ; qui ont eu la patience d'attendre ma soutenance pour que je leur explique en 3 slides et 5 minutes à quoi pourrait éventuellement servir mon travail.

... Caroline Frot qui a participé à tous mes nombreux projets de microfabrication, même les plus fous, et qui a joué un rôle crucial dans toutes les études expérimentales de ma thèse.

... François Gallaire, que je remercie pour son amitié, son enthousiasme et son hospitalité avant tout ; sur qui j'ai toujours pu compter pour discuter abstrait, mathématiques et philosophie, mais également champignons, ski et montagne.

... Cédric Poulain, qui m'a transmis sa passion pour la recherche et la science ; et illustre au quotidien le dicton « Il n'y a pas de problème, il n'y a que des solutions ».

... mes rapporteurs José Bico et Philippe Marmottant qui ont pris le temps de lire et commenter mon manuscrit avec soin ; mes examinateurs Philippe Renaud et Isabelle Cantat pour leur évaluation sincère de mon travail de thèse.

... tous ceux avec qui j'ai réfléchi, travaillé, bricolé et collaboré au sein du nouvellement nommé IBEM : Maria-Luisa, Mickael, Yu, Sungyon, Sherif, Nadia, Yonatan, Tanmay, Nicolas, Gabriel, Anette, et évidemment Etienne qui a hérité des sujets trop compliqués pour que je prenne le temps de m'y atteler.

... l'ensemble du LadHyx, qui fut pour moi bien plus qu'un lieu de travail : un lieu de rencontre, un lieu cosmopolite, un lieu rempli de créativité et un lieu où sport et divertissement ont leur légitime place ; à ses membres, permanents, temporaires ou éphémères, entre autres Patrick Huerre, Jean-Marc Chomaz, Christophe Clanet, Paul Manneville, Tonio, Dany, Thérèse, Delphine, etc....

... tous ceux qui m'ont fait passé deux mois monstres biens à Lausanne : Mathias, Edouard, Marc-Antoine, Isa, Davy, Cristobal, Vlado, et Viviane ; j'en garde une montagne de bons souvenirs.

... Anna Kehres-Diaz, Philippe Guédon, Matthieu Sommekh et la DRIP en général, pour avoir vu en mon travail de thèse une innovation avec un potentiel industriel ; pour m'avoir motivé et soutenu dans l'élaboration du projet de valorisation.

... ceux qui, tout comme moi, ont choisi la gravité comme ennemi, Fontainebleau comme camp d'entraînement et les montagnes de France et d'ailleurs comme champ de bataille ; à François Lésin donc, à Rémi Wolf, PT Brown, Romain Mérandenthal, Jon, Wietze, Guillaume, Romain Monnier, et au reste de la tribu aux mains blanches.

... mes amis, Rikhâl notamment qui a eu le courage de rejoindre le monde de la recherche après trois années passées à gérer les porte-monnaie du monde

... ceux que j'oublie et qui je l'espère, me le pardonneront.

Contents

Introduction	1
0.1 Motivations for 2D droplet microfluidics	2
0.1.1 A very brief history of droplet microfluidics	2
0.1.2 A serial mindset in droplet microfluidics	3
0.1.3 Inherent weaknesses of serial architectures	4
0.1.4 The microplate: a 2D lab standard	5
0.1.5 Towards 2D droplet microfluidics	6
0.2 Outline	9
 First Part - An energy model for droplet manipulation with confinement gradients	 13
Nomenclature for Part 1	13
 1 Interfacial tension and droplets in confinement gradients: a rich inter- twined history	 19
1.1 Interfacial tension	20
1.2 The Young-Laplace equation	21
1.3 Drops on solid surfaces: wetting properties, contact angle and shapes . . .	22
1.4 Drops in confinement gradients: a force model	24
1.5 Examples of droplet propulsion in confinement gradients	27
1.6 Surface energy	29
1.7 Drops in confinement gradients: energy considerations	30
1.7.1 Application to the case of a pancake drop over a trench	31
1.8 The free and constrained interface of confined non-wetting drop at equilibrium	32
 2 A minimum principle for the flow of a droplet in a Hele-Shaw cell	 37
2.1 A minimum principle for viscous two phase flows	38
2.1.1 Generalities	38
2.1.2 Note on stationary states	40
2.1.3 Equivalence between the minimum dissipation and the Stokes equa- tions for two phase flows	42

2.2	The motion of a drop in a Hele-Shaw cell	46
2.2.1	The Taylor-Saffman analysis	47
2.2.2	Applying the minimum principle	49
2.2.3	Comparison with the Taylor-Saffman results	57
2.2.4	The shape selection mechanism	58
2.3	Summary and discussion of Chapter 2	61
3	Droplet trajectories in a Hele-Shaw cell with confinement gradients	63
3.1	An energy production-dissipation balance	63
3.2	Geometry, velocity fields and assumptions	65
3.2.1	Flow domains	65
3.2.2	Control volume and simplifications	69
3.3	Equation of motion	69
3.3.1	Power injected into the control volume	70
3.3.2	Energy dissipation in the far-field flows	70
3.3.3	Other sources of viscous dissipation	71
3.3.4	Rate of change of surface energy	71
3.3.5	Equation of motion	72
3.4	Trajectory equation of the droplet	73
3.5	Experiments in swollen microchannels	74
3.6	Comparing observed and predicted trajectories	76
3.7	Summary and discussion of Chapter 3	78
3.7.1	Physical insight on the Taylor-Saffman result	79
3.7.2	An interpretation of the energy production-dissipation balance in terms of forces	79
3.7.3	The viscous drag and velocity of a non-wetting droplet in a Hele-Shaw cell	81
 Second Part - Experimental study of droplet actuation with confinement gradients		87
4	Guiding and trapping drops with rails and anchors	87
4.1	Guiding and trapping in <i>serial</i> microfluidics	87
4.1.1	Guides	87
4.1.2	Traps	89
4.2	Droplet manipulation by confinement gradients in the context of microfluidics	92
4.3	Rails and anchors: proof of concept and applications	93
4.3.1	Proof of concept	93
4.3.2	Controlling the chemical environment of an anchored drop	96
4.3.3	Application to the study of the sickle cell disease	96
4.4	A model and measure of the trapping force	97
4.4.1	The force balance on an anchored drop	97

4.4.2	A model and measure of the drag force F_d	98
4.4.3	The theoretical estimate of the trapping force F_γ	100
4.4.4	Comparison with the measured trapping force	101
4.5	Towards addressable 2D droplet arrays	102
4.5.1	Combining rails and anchors with laser actuation	103
4.6	Summary and discussion of Chapter 4	103
	Paper: <i>Rails and anchors: guiding and trapping droplet microreactors in two dimensions</i>	106
	Paper: <i>Trapping microfluidic drops in wells of surface energy</i>	115
	Paper: <i>Combining rails and anchors with laser forcing for selective manipulation within 2D droplet arrays</i>	121
5	Producing and transporting drops with wedges	129
5.1	Device microfabrication	130
5.2	Experimental observations	132
5.2.1	A control experiment	132
5.2.2	A generic scenario for droplet production	133
5.2.3	Influence of α , fluid properties and the injection flow rate on R_d . .	133
5.2.4	Recap of the experimental observations	135
5.3	A novel mechanism for droplet formation	135
5.3.1	The minimum curvature of a confined non-wetting thread at equilibrium	136
5.3.2	Equilibrium of the thread attached to the tongue in the reservoir .	137
5.3.3	Beyond R^* , a system out of equilibrium	141
5.3.4	A scenario for droplet formation	142
5.4	Confronting the model to the experimental observations	143
5.5	Comparison with a classical force argument	146
5.5.1	The non-wetting pendant drop	147
5.6	Nozzle parallelization for emulsion production	149
5.6.1	Emulsions with chemical gradients	149
5.6.2	High throughput emulsification	151
5.6.3	High throughput emulsification with a micropipette	153
5.7	Discussion and summary of Chapter 5	154
	Perspectives	157
	Appendix	159
A	Potential flow generated by a deforming elliptical cylinder	159
A.1	The kinematic boundary condition	159
A.2	The velocity potential	161

B	The shape of a non-wetting pancake droplet	163
B.1	Delaunay surfaces	163
B.2	Non-wetting pancake droplets	165
B.3	The curvature of a pancake droplet	167
B.4	The asymptotic curvature of a pancake droplet	168
C	Published paper: <i>Microchannel deformations due to solvent-induced PDMS swelling</i>, LOC 2010	173
	Bibliography	188

Introduction

Let's start with a riddle: what played an important role both in the historical measurements of q the unit charge of the electron at the turn of the 20th century and in the current advent of sequencing in biological research? Or, as illustrated below,

WHAT DO THESE MACHINES HAVE IN COMMON?



Hint 1: on the left is the apparatus used by Robert Andrews Millikan and Harvey Fletcher to perform their famous oil drop experiment between 1908 and 1917.

Hint 2: on the right is the IonTorrent OneTouch instrument which prepares a genetic sample for sequencing by performing an emulsion PCR.

Answer: The use of droplets as carriers of rare quantified amounts of information.

The fact that droplets played a crucial role in the discovery of the electron is little known in the microfluidic community. Yet, in my opinion, Millikan's oil drop experiment marks the dawn of droplet microfluidics.

Soon after the experimental discovery of the electron by Sir Thompson in 1897, Millikan designed a clever experiment to measure the unit charge of the electron [1]. He built a closed container at the top which could be introduced a single oil droplet several microns in radius. An X-ray source then ionized the gas in the chamber in order to charge the droplet with a relatively small number of electrons (up to a few hundred) and an electric field was applied to induce an electromagnetic force opposite to gravity on the drop. He then measured the terminal velocity of the drops with and without the electric field and noticed that the change in velocity was always quantified and a multiple of some constant

number. Last, he related this constant to the unit charge of electrons and found the remarkable measure $e = 1.5924(17) \cdot 10^{-19}$ C, less than a percent off the actual value $e = 1.602176487(40) \cdot 10^{-19}$ C. Millikan was rewarded with the Nobel prize in 1923 for *his work on the elementary charge of electricity and on the photoelectric effect* [2].

In Millikan’s experiment, the droplet is used to collect, carry and characterize a number of electrons. In modern droplet microfluidics, a droplet is used to collect, carry and characterize chemicals [], biological systems [] or genetic material as in the case of the IonTorrent OneTouch instrument. And remarkably, Millikan’s justification for the use of droplets is still relevant today: it is far more practical to produce nano- to femto-liter droplet containers than equivalent solid spheres, capsules or gels.

0.1 Motivations for 2D droplet microfluidics

0.1.1 A very brief history of droplet microfluidics

Lederberg in 1954 [3] and Rotman in 1961 [4] published two seminal papers concerning the use of droplets to address biological and chemical questions. They introduced the idea that a droplet could be considered as a tiny version of the chemist’s flask, a nanoliter compartment in which cell cultures and chemical reactions could be performed. Indeed, a droplet presents a number of advantages:

- It is a natural microreactor: the interface of the drop provides a natural chemical boundary for molecules, cells or biological systems if they are not soluble in the medium surrounding the drop (air, oil, etc...). As a result, the contents of a drop are isolated from the contents of a neighboring drop.
- It covers a wide range of small volumes: droplets range in size from the millimetric capillary length down under a micron depending on the method of production, which translates to a volume range from the micro- to the atto-liter. In all cases, these volumes are small compared to the milliliter volume of a chemist flask.
- It allows straightforward multiplexing: droplets are usually produced in numbers and since each droplet is an individual microreactor, multiplexing of an experiment is easily achieved.

Despite these promising assets, the field of droplet microfluidics stayed dormant for almost 50 years. This is largely due to the fact that methods to produce, manipulate and monitor droplets then lacked in throughput, efficiency and/or reproducibility [5] when compared with competing bulk approaches.

In the early 2000’s, microfluidics underwent a boom in activity with the development of soft lithography techniques that enabled the rapid and cost effective prototyping of microfluidic device in polymer [6, 7]. The field of droplet microfluidics wasn’t left behind with the emergence of new methods for droplet production and transport, namely the T-junction [8] and the flow focusing [9] microchannel geometries shown on Fig. 1.

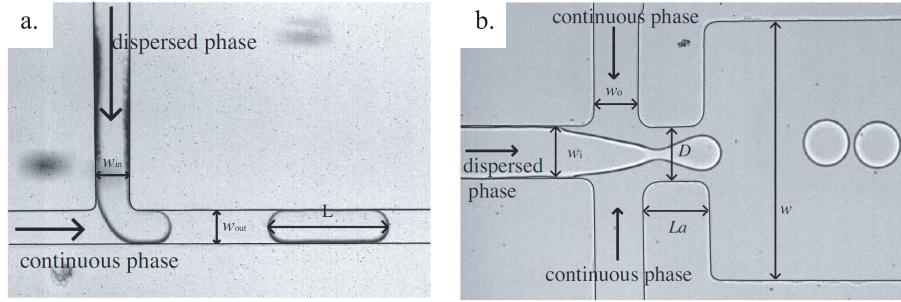


Figure 1: Image of **a)** T-junction and **b)** flow focusing microchannels producing water droplets in oil.

These methods differed from techniques like ink-jet printing [10], membrane emulsification [11], the historical vaporisation [1, 4] and the everyday mixing of the vinaigrette mainly because the droplets were produced on-chip, inside the closed and controlled environment of the microdevice. Furthermore, since in both cases a strong flow of continuous phase is required to shear the dispersed phase and produce the droplets, advection from the outer flow was readily available to transport the droplets inside the device [12].

0.1.2 A serial mindset in droplet microfluidics

Ultimately, these new methods of droplet production drove the field of droplet microfluidics towards a serial mindset. Because droplets are produced and arrayed in a train which flows inside linear microchannels, operations on individual droplets can only occur in series, one droplet after the other.

The conceptual workflow of chemical or biological assays [13, 14, 15, 16, 17] in droplet microfluidics is shown below on Fig. 2. First, a train of droplets containing various reagents is produced, forming a chemical library. Then, a drop of the sample to be analyzed is merged with each individual reagent droplet. Last, the merged droplets are analyzed one by one, by fluorescence for example, to obtain a readout of the assay.

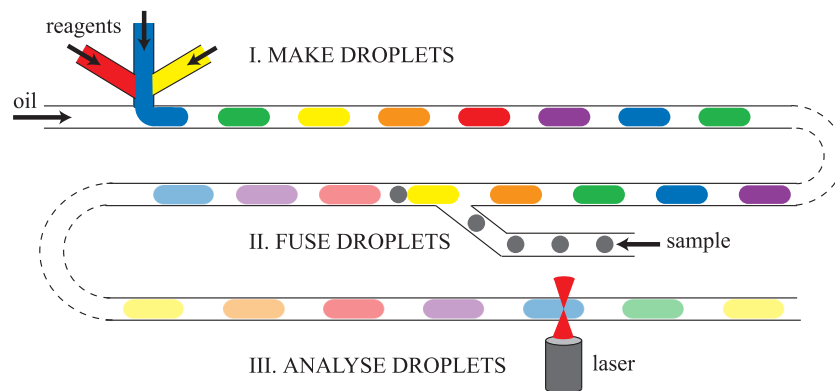


Figure 2: Illustration of the conceptual architecture and workflow of a droplet microfluidic device for chemical or biological assays.

Tremendous efforts have been dedicated to the implementation in series of the key operations that are necessary to perform chemistry or biology in droplets. This includes merging, splitting, dilution (the combination of merging and splitting), sorting, readout, etc... A number of reviews [14, 18, 12, 5] give inventories of the techniques available.

The issues of throughput and reproducibility that initially rendered droplet microfluidics impractical [3, 4] are today solved. As a matter of fact, the first commercial products based on such a serial approach have hit the market and triggered a wave of excitement in the biotechnology community.

0.1.3 Inherent weaknesses of serial architectures

However, serial droplet microfluidics, like all serial architectures, have one unavoidable weakness: long range interactions. Imagine that for one reason or another (dirt, wetting, crystallization, etc...) a droplet suddenly stops in the microchannel. The entire train of following droplets eventually abuts onto the one blocking the channel and the device completely breaks down. This examples illustrates the overall sensitivity of the train of droplets to any localized perturbation. What affects one drop affects all drops.

Building analogies with electronics is often useful in microfluidics [19] and in this case, Christmas fairy lights are ideal. If the tinsel is designed in series, when one light bulb breaks, the entire tinsel turns off. Not only is the tree in the dark but it is also a nightmare to identify which light bulb is broken. What affects one light bulb affects the entire tinsel.

A related yet distinct problem is the issue of traffic jams which are a signature phenomenon of transport in serial architectures, as illustrated on Fig. 3. Traffic jams can occur spontaneously even when the device is perfectly functional [20], or more frequently when the droplets are heterogeneous in size or content. Indeed, a change in the geometry, surface tension or viscosity of the droplet affects its transport velocity [12]. Eventually, the fast drops catch up with slower ones and a packed group of droplets develops inside the device, jeopardizing the performance of the microfluidic device. This is none other than the delivery-truck-in-a-one-lane-street (DTOLS) issue to which can be attributed a large proportion of the honking concerts in the streets of Paris.



Figure 3: Limitations to a serial mindset reach the top of Everest as a traffic jam forms in the *death zone* while hundreds of climbers try to summit on May 23 2012.

Because of long range interactions, the vertical integration on a single chip of a chain of operations lacks robustness and turns out to be impractical for chemical or biological applications. As a result, protocols are cut down to individual steps which are then implemented individually on separate microfluidic devices [15, 16, 17]. The effective schematic of a serial droplet microfluidic protocol is shown on Fig 4.

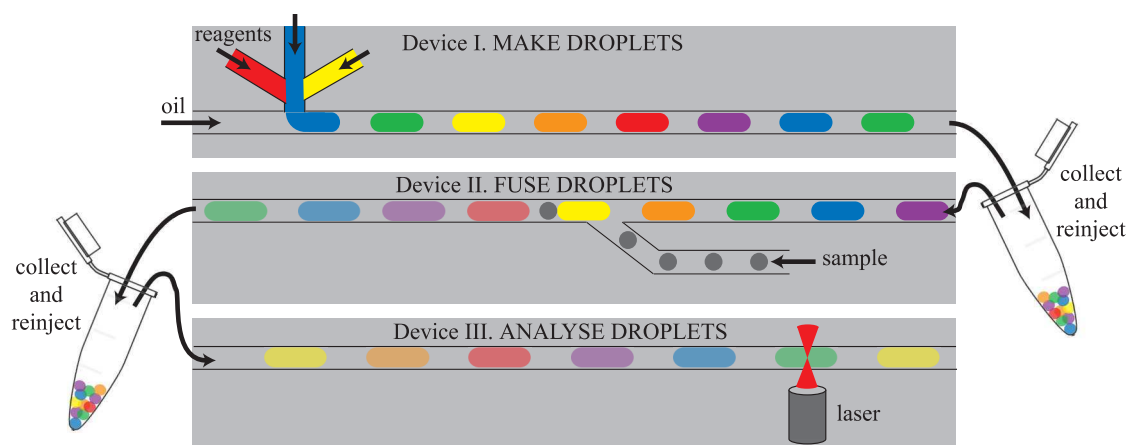


Figure 4: In order to limit long range interactions, assay protocols are cut down to individual steps and performed separately of distinct chips. For example, a first device produces a library of droplets which is collected in an Eperdorf tube. The emulsion is reinjected in a second chip to be merged with a sample. A third chip is used to analyze the result.

This representation of serial droplet microfluidics is to some extent an exaggeration since there are reports in the literature of devices integrating multiple steps [21]. Nonetheless, all commercial products which by definition require irreproachable robustness, like the Raindance RainDropTM or the BioRad QX100TM, are one-operation-per-chip solutions.

0.1.4 The microplate: a 2D lab standard

A few years before the first demonstration by Lederberg [3] of the use of droplets for biology and chemistry, the hungarian doctor Gyula Takátsy invented another alternative to the chemist's flask. In order to improve the screening throughput of influenza during a violent epidemic, he created a plate into which was machined an 8 by 12 array of small sample wells. In 1951, the 96 wells microtitration or microtiter plate was born [22].

Microtiter plates do not differ significantly from the original droplet microfluidic format of Rotman [4] since essentially, each well contains a droplet of sample or reagent. In fact, microtiter plates and droplets share a number of advantages:

- Isolated microreactors: each wells is separated from the others by solid walls.
- Small volumes: the microliter volume of a well is significantly smaller than the milliliter volume of a flask.
- Multiplexing: the array format of the wells is ideal for parallel experiments.

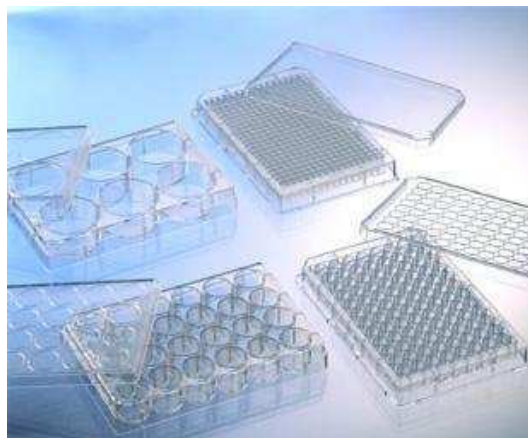


Figure 5: Photograph of a collection of microtiter plates with various number of wells. [23]

Yet, whereas droplet microfluidics stayed dormant for half a century, microtiter plates quickly became a standard in labs around the world. The combination of the arrayed format of the plate with the accessibility of the wells by pipetting is in great part responsible for this success since it enabled the parallelization of the labor intensive pipetting and its automation [22].

To compare with serial droplet microfluidics, the workflow for an assay in a microtiter plate is straightforward: load each well with a specific reagent, pipette simultaneously the sample into the wells, incubate if necessary and read the results directly on the plate by absorbance, fluorescence, spectroscopy, etc... Here, owing to the parallel 2D format of the plate, what happens in a well does not affect neighboring wells. Interactions between samples are minimal. Furthermore, wells can be accessed individually or collectively and at any time during the experimental procedure and vertical integration is natural. In particular, the results of successful experiments can be easily recovered for further use with a standard pipette.

If droplet microfluidics have a chance at competing with microtiter plate technologies, it is because pipetting accuracy is largely compromised at volumes below $1\ \mu\text{L}$. Droplet dispensing is not the limiting operation. Microarray technologies for example use inkjet printing or derivatives to array thousands of nanoliter drops on microscope slides. However, owing to surface tension, small droplet strongly resist detachment from solid surfaces [24] such that reverse pipetting is compromised. A significant proportion of the droplet always remains on the surface after aspiration. Overall, the miniaturization of the microtiter plate below microliter volumes is possible but at the cost of losing accessibility to the contents of the wells.

0.1.5 Towards 2D droplet microfluidics

The combined observations that *i)* serial droplet microfluidics cannot be used to design vertically integrated microfluidic devices and that *ii)* the downscaling of the microtiter

plate has reached its limits motivates the field of microfluidics to elaborate alternative approaches for liquid handling at the nanoliter scale. Innovations in microplumbury like the elastomeric Quake valve [25, 26] have enabled the design of small volume fluidic circuits for example. Droplet manipulation on surfaces with surface acoustic waves (SAW) is another approach [27]. Amongst these technologies, 2D droplet microfluidics is emerging as a promising solution.

In a 2D droplet microfluidic device, the linear microchannels are replaced by a single large, wide but thin chamber in which droplets are free to move in a plane. Such a chamber, with a high width-to-thickness aspect ratio, is often referred to as a Hele-Shaw cell in the fluid mechanics literature [28] and we adopt this vocabulary here on.

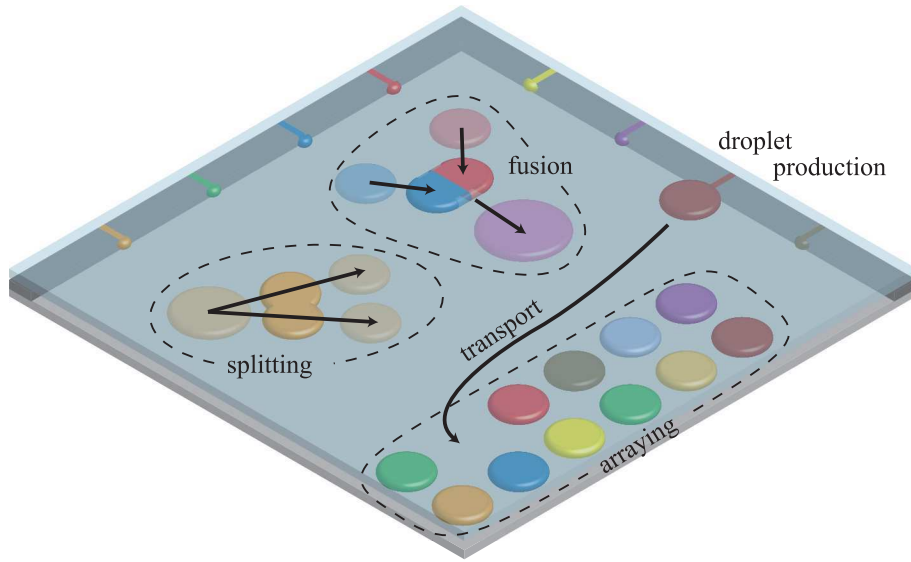


Figure 6: Sketch of an ideal 2D droplet microfluidic device. Droplet production, transport, arraying, merging and splitting can all occur simultaneously within the Hele-Shaw cell.

Ideally, all the key droplet operations necessary to carry out an assay take place in the chamber as illustrated on Fig. 6. Some drops are produced and transported to be stacked in an array. Others are merged to initiate a chemical reaction while a third is split into two daughter droplets. Owing to the 2D format of the chamber, droplet to droplet interactions are reduced. Static arrayed drops do not impede the movement of other drops elsewhere in the device for example.

The fundamental difficulty in implementing a 2D droplet microfluidic device lies in the actuation of individual droplets inside the chamber. Unlike the microtiter plate, the closed environment of the Hele-Shaw cell hinders a direct access to the drops.

A first approach was developed over the last 10 years. Digital microfluidics uses electrodes patterned on the chamber walls to locally apply electric fields and manipulate the

droplets. The actuation relies either on electrowetting (EW) [29], electrowetting on dielectrics (EWOD) or on dielectrophoresis [30] to exert a force on a droplet. Digital microfluidic devices have been developed for numerous applications from cell culture to combinatorial chemistry [31]. Furthermore, the recent combination of an EWOD device with a high resolution electrode array usually found in LCD display technologies paves the way for the large scale integration of droplet manipulations with digital microfluidics, as it enables a decrease in the size of the electrodes and an up-scaling in the number of individual addressable droplets [32]. An issue with digital microfluidics remains the cost of chips which are often disposable in biochemical applications.

A second approach consists in using an outer flow like with serial droplet microfluidics. In this case, all droplets are advected in a given direction by the flow and actuation then boils down to either altering the nominal motion or trajectory of the droplets or controlling the outer flow. A simple solution is suggested by Huebner *et. al.* [33]: small structures with solid walls are placed inside the Hele-Shaw cell to trap droplets as shown on Fig. 7. When the flow comes from one direction, it pushes the drops into the pockets. In the other direction, it releases them. In a more elaborate version, two drops with different contents are loaded in each trap and coalescence is triggered with electrodes [34]. Although the vertical integration of a chemical reaction in droplets is achieved on a single chip from production to readout, all drops are here actuated simultaneously and the device is far from the ideal 2D droplet microfluidic layout of Fig. 6.

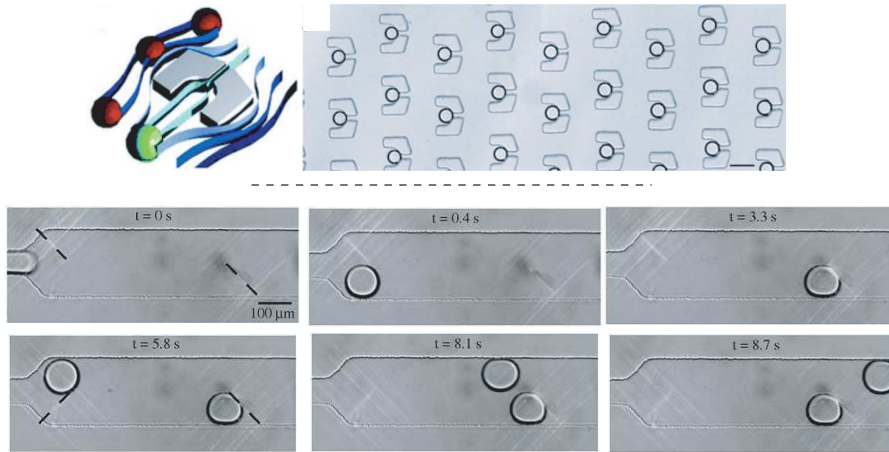


Figure 7: **Top:** figures from Huebner *et. al.* [33] illustrating the use of solid pockets to trap droplets in a Hele-Shaw cell. Numerous drops are flowed from left to right into the device and some of them randomly enter the traps to form an static array. Reversing the flow direction releases the droplets. **Bottom:** Demonstration of droplet actuation with a focused laser spot. In a channel wider than a droplet diameter, a first pattern of light highlighted with the dotted line is used to deviate a droplet onto the side of the channel and trap it further downstream. Then, the pattern is switched to deflect the next drop on the other side of the channel while holding the first drop in place. Eventually, the second drop passes the first. Time stamps indicate chronological order. Adapted from Cordero *et. al.* [35].

Another elegant solution was developed in the lab by M.-C. Cordero and collaborators. When a laser is focused on the interface of a droplet, a repulsive force appears from soluto-Marangoni effects [36]. Consequently, points and lines of light act as invisible pillars or walls that strongly influence the motion of the drops. This property is illustrated in Fig. 7 which shows how drops are deflected and trapped by active light patterns [35]. Laser actuation was also adapted to force rapid mixing of a drop's contents [37] and was shown to trigger coalescence [35]. Unfortunately, the focused laser locally heats the droplet, possibly jeopardizing this technology for biological applications.

Nonetheless, the experiment shown on Fig. 7 also clearly demonstrates that the long range interactions so critical in serial droplet microfluidics vanish as soon as the microchannel is wide enough for one drop to pass another. It validates the idea that 2D droplet microfluidics is a viable solution for vertically integrated devices.

My PhD work, presented below, reveals yet another strategy for droplet management in Hele-Shaw cells which relies on confinement heterogeneities to apply forces on droplets. Confinement heterogeneities are local and small amplitude variations in the thickness of the Hele-Shaw cell: instead of having perfectly flat and parallel walls, the chamber contains wedges, bumps, grooves, etc... This approach is shown to provide a robust, passive and cost effective solution for droplet production, guiding and trapping. When combined with local active actuation, it enables the design of fully operational 2D droplet microfluidic devices.

0.2 Outline

This manuscript is divided into two complementary parts. The first is dedicated to the theoretical modeling of droplet motion in a Hele-Shaw cell with confinement gradients. The second presents and analyzes experimental implementations of droplet actuation by confinement gradients within microfluidic devices.

The first half of Part I is a review and critical analysis of the literature on droplet actuation by confinement gradients and on viscous two phase flows in general. In the second half, we formulate an energy approach to these phenomena that differs from the classical force based models. We apply it the cases of a droplet flowing in parallel and deformed Hele-Shaw cells respectively.

- In Chapter 1, we review the basic concepts behind droplet actuation using confinement gradients and identify the pioneering literature on the subject. Starting from the seminal experiments performed by Hauksbee in 1710 [38], we follow history to introduce interfacial tension, surface energy and related phenomena relevant for our study. Along the way, we define useful vocabulary specific to droplet microfluidics in confined geometries.
- The first half of Chapter 2 is a reminder of the minimum principle that applies to viscous two phases flows, which we show to be equivalent to the classical Stokes

equations combined with the dynamic Young-Laplace equation. Given the frequent misuses of this principle in the literature, we give a critical analysis of its implications. In the second half of Chapter 2, we apply this minimum principle to the case of a drop moving in a Hele-Shaw cell and compare our results with the Taylor-Saffman prediction [39] obtained from a kinematic analysis of the flow. Our analysis provides new physical insights on the phenomena at play in this system.

- We then build onto the minimum principle to formally derive a new formulation for the energy production-dissipation balance of viscous two phase flows that accounts for variations of surface energy. In the rest of Chapter 3, we make use of this equation to predict the trajectory of a droplet advected by an outer flow in a Hele-Shaw cell with confinement gradients. We compare our model with trajectories measured experimentally in deformed microchannels and find satisfying agreement.

In Part 2 of the manuscript, we demonstrate experimentally droplet actuation by confinement gradients within 2D microfluidic devices. This includes droplet production, transport, guiding and trapping.

- Chapter 4 is a summary of three articles that we published over the last three years. First, we show how rails and anchors, which are small grooves and holes etched in one of the channel walls respectively, are able to guide and trap droplets against a mean outer flow in a Hele-Shaw cell. After presenting proof of concept experiments and some early applications to chemistry and biology in droplets, we rely on the energy approach developed in Part 1 to give a quantitative analysis of the trapping force developed by an anchor. Last, we add controllable laser actuation to microfluidic devices with rails and anchors to create addressable 2d droplet arrays. The articles are included at the end of the chapter.
- To finish, we address the issue of droplet production and transport using confinement gradients in Chapter 5. We show that when fluid is injected from an inlet channel into a non-parallel Hele-Shaw cell, it breaks up into monodisperse droplets. We study experimentally the performance of this new method for droplet production and reveal its peculiar properties. To explain our observations, we identify a novel droplet formation mechanism that originates from an equilibrium condition of the fluid thread upstream of the injection nozzle rather than from an instability of the droplet forming in the Hele-Shaw cell. Last, we demonstrate that massive parallelization of the injection nozzles is straightforward and enables the production of complex emulsions and high-throughput droplet production.

We conclude with the presentation of a new generation of 2D droplet microfluidics that does not require a flow of the outer phase.

Part I

An energy model for droplet manipulation with confinement gradients

Nomenclature

g Gravity

INTERFACIAL TENSION

γ Interfacial tension

γ_{SL} Surface energy density of a Solid-Liquid interface

γ_{SV} Surface energy density of a Solid-Vapor or Solid-Outer Fluid interface

θ_γ Contact angle

FLUID PROPERTIES

ρ Fluid density

μ Fluid viscosity

μ_1 Viscosity of the drop

μ_2 Viscosity of the outer fluid

GENERAL GEOMETRY

\vec{n} Normal vector of an interface, oriented from the drop to the outer fluid

\mathcal{C} Mean curvature of an interface

Ω Entire fluid domain of the system

Ω_1 Fluid domain inside the drop

Ω_2 Fluid domain outside the drop

\mathcal{S} Domain of the fluid interface

\mathcal{B}_∞ Outer boundaries of the system

CHANNEL OR HELE-SHAW GEOMETRY

h	Gap width of a Hele-Shaw cell
h_0	Nominal gap width of a Hele-Shaw cell
Δh	Spatial variations in the gap width of a Hele-Shaw cell
W	Width of a Hele-Shaw cell

DROPLET GEOMETRY

O	Center of mass of a droplet
(x_d, y_d)	Position of O
R	Radius of a droplet
V	Volume of a droplet
S	Surface area of a droplet
k	Aspect ratio $k = \sqrt{12S}/h$ of the droplet
a	Semi-major axis of an elliptic droplet
b	Semi-minor axis of an elliptic droplet
c	Focal distance $c = \sqrt{a^2 - b^2}$ of an elliptic droplet
e	Eccentricity $e = c/a$ of an elliptic droplet
λ	Aspect ratio $\lambda = a/b$ of an elliptic droplet
P	Perimeter of an elliptic droplet

VELOCITY FIELDS, VELOCITY POTENTIALS, STREAM FUNCTIONS

\vec{u}	General notation for a velocity field
\vec{u}_∞	Imposed velocity at the outer boundaries of the system
$\vec{\nabla}u$	Gradient operator of the velocity field
$\Delta\vec{u}$	Laplacian operator of the velocity field
\vec{U}	Height averaged velocity field in the Hele-Shaw cell
Q	Flow rate of the outer fluid in the Hele-Shaw cell
\vec{U}_f	Uniform height averaged velocity field imposed at the boundaries of the Hele-Shaw cell

\vec{U}_d	Velocity of the center of mass of the droplet
U	Velocity ratio $U = U_d/U_f$
\dot{a}	Relaxation velocity $\dot{a} = da/dt$ of an elliptic droplet
$\dot{\lambda}$	Rate of change $\dot{\lambda} = d\lambda/dt$ of the aspect ratio
$\dot{\Lambda}$	Normalized $\dot{\Lambda} = \dot{\Lambda} = \sqrt{S/\pi}\dot{\lambda}/U_f$
\dot{S}	Rate of change dS/dt of the surface area of the droplet interface
\vec{U}_1	Inner height averaged velocity field
\vec{U}_2	Outer height averaged velocity field
U_x	Component in x of the height averaged velocity field
U_y	Component in y of the height averaged velocity field
$U_{r,1}$	Inner radial component of \vec{U}
$U_{\theta,1}$	Inner angular component of \vec{U}
$U_{r,2}$	Outer radial component of \vec{U}
$U_{\theta,2}$	Outer angular component of \vec{U}
Φ	Potential of the height averaged velocity field \vec{U}
Φ_1	Inner potential
Φ_2	Outer potential
Ψ	Stream function of the height averaged velocity field \vec{U}
Ψ_1	Inner stream function
Ψ_2	Outer stream function
w	Complex velocity potential $w = \Phi + i\Psi$
w_1	Inner complex velocity potential
w_2	Outer complex velocity potential
v	Complex velocity $v = U_x + iU_y$ of the height averaged velocity field \vec{U}
\mathcal{T}	Material trajectory of the droplet

FORCES

- \vec{G} Weight of the drop
- \vec{F}_γ Force due to the confinement gradients
- \vec{F}_{U_f} Propulsion force from the outer fluid flow of mean velocity U_f
- \vec{F}_μ Viscous drag of a droplet moving in a Hele-Shaw cell
- \vec{F}_H Viscous drag due to far-field flows in the Hele-Shaw cell
- \vec{F}_{lf} Viscous drag due to the lubrication films around the drop

CAPILLARY NUMBERS

- Ca_f Capillary number $\text{Ca}_f = \mu_2 C a_f / \gamma$ based on the outer flow velocity
- Ca_d Capillary number $\text{Ca}_d = \mu_2 C a_d / \gamma$ based on the droplet velocity

COORDINATE SYSTEMS

- (x, y, z) Cartesian coordinates
- ξ *Radial* coordinate in an elliptic coordinate system
- η *Angular* coordinate in an elliptic coordinate system
- ξ_0 *Radial* coordinate $\xi_0 = 1/2 \log(a+b)/(a-b)$ of an ellipse (a, b)
- ξ_1 *Radial* coordinate of the elliptic control volume in Chapter 2
- ζ Complex coordinate $\zeta = \xi + i\eta$ in an elliptic coordinate system
- g_ξ, g_η Metrics of an elliptic coordinate system
- (r, θ) Polar coordinates
- ρ Radius of the control volume in Chapter 3

ENERGIES, LAGRANGIANS

- \mathcal{E} Total free energy of a system
- \mathcal{E}_γ Surface energy of a fluid interface
- $\mathcal{E}_{\gamma_{SL}}$ Surface energy of a Solid-Liquid interface
- $\mathcal{E}_{\gamma_{SV}}$ Surface energy of a Solid-Vapor interface

\mathcal{E}_p	Potential energy of a system, other than the surface energy \mathcal{E}_γ
$\dot{\mathcal{E}}_\gamma$	Rate of change of the surface energy of a fluid interface
$\dot{\mathcal{E}}_p$	Rate of change of the potential energy
\mathcal{L}	Lagrangian of the system
L	Normalized Lagrangian
\mathcal{D}	Dissipation function
\mathcal{B}_f	Contribution of the far field boundary conditions \vec{U}_∞ to the Lagrangian \mathcal{L}
\mathcal{W}	Power injected in the control volume
\mathcal{P}	Energy dissipation from viscosity
\mathcal{P}_1	Inner energy dissipation from viscosity
\mathcal{P}_{ff1}	Inner energy dissipation from the far-field flows
\mathcal{P}_{ni1}	Inner energy dissipation from the near-interface flows
\mathcal{P}_{lf}	Inner energy dissipation from the lubrication films
\mathcal{P}_2	Outer energy dissipation from viscosity
\mathcal{P}_{ff2}	Outer energy dissipation from the far-field flows
\mathcal{P}_{ni2}	Outer energy dissipation from the near-interface flows

MISCALLENEOUS

p_i	Pressure field inside the drop
p_o	Pressure field outside the drop
$\Pi(e)$	Disjoining pressure in thin lubrication films
σ_i	Fluid stress tensor inside the drop
σ_o	Fluid stress tensor outside the drop
Su	Subsidence number

Chapter 1

Interfacial tension and droplets in confinement gradients: a rich intertwined history

“Un des phénomènes capillaires les plus intéressants et les plus propres à vérifier la théorie est celui de la suspension d’une goutte de fluide entre deux plans formant entre eux un très-petit angle”.

Laplace, *Supplément au Livre X de la Mécanique Céleste*, p. 55.

My PhD work addresses the use of confinement gradients to drive droplet microfluidics, a topical subject given the current explosion of interest for Lab-on-a-Chip technologies. Yet, it finds its origins more than 300 years ago, long before anyone saw in droplets a solution to the miniaturization of chemical and biological reactors.

In 1710, Francis Hauksbee the elder, one of Sir Isaac Newton’s lab assistants, observes that a drop of oil placed between two non-parallel glass plates is immediately set in motion and travels towards the thinnest side of the apparatus [38]. Three centuries before the first applications, he thereby demonstrates how confinement gradients are able to propel drops and bubbles.

At the time, the understanding of capillary phenomena is in its infancy. Hauksbee and Newton invoke *the power of attraction* of surfaces which, from their accounts, increases in strength as the distance between the plates becomes smaller [38, 40]. In the sections that follow, we navigate through the long history [41] of this experiment to introduce the basic concepts around interfacial tension upon which this dissertation is built.

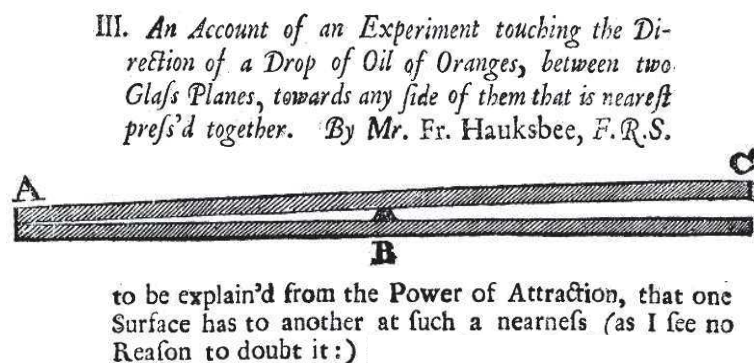


Figure 1.1: Title, main figure and analysis in the original work by Francis Hawksby [38]. Is it also the first subtle use of emoticons?

1.1 Interfacial tension

It took nearly one hundred years before two scientists, namely Thomas Young and Pierre-Simon de Laplace, explained Hauksbee's account as a consequence of the interfacial tension of the drop itself and not as the result of some force exerted by the plates on the liquid.

In the meantime, the concept of a tension at the interface between immiscible fluids slowly emerged. In 1787, Gaspard Monge finishes his essay [42] on the attraction or repulsion of bodies floating at the surface of liquids by suggesting a molecular origin for interfacial tension. His explanation is essentially the one found in textbooks today [43]. He says

En supposant ainsi que l'adhérence des molécules d'un liquide n'ait d'effet sensible qu'à la surface même, et dans le sens de la surface, il feroit facile de déterminer la courbure des surfaces des liquides dans le voisinage des parois qui les contiennent; ces surfaces feroient des linteaires dont la tension, constante dans tous les sens, feroit par-tout égale à l'adhérence de deux molécules; et les phénomènes des tubes capillaires n'auroient plus rien qui ne pût être déterminé par l'analyse.

Excerpt from *Mémoire sur quelques effets d'attraction ou de répulsion apparente entre les molécules de matière* by Gaspard Monge [42].

The interfacial tension, here on written γ , is a molecular force per unit length which pulls the interface equally in every direction. The famous experiment of the loop of string placed in a soap film shown on Fig. 1.2 illustrates perfectly this force-like nature of interfacial tension. Initially, the loop hangs under gravity as it would outside the film. Once the inner soap film is punctured, interfacial tension from the outer film starts to pull strongly on the string. In the end, the loop is stretched out in all direction and has a circular shape.

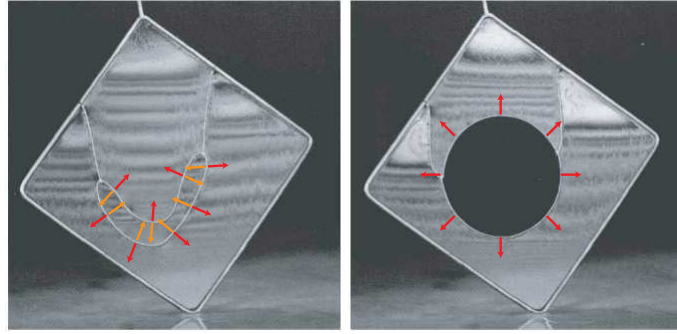


Figure 1.2: Photographs by Walter Wick [44] of a loop of string immersed in a planar soap film before (left) and after (right) perforation of the inner film. Initially, interfacial tension from the outer film represented with the red arrows is exactly balanced by its counterpart from the inner film (orange arrows). Once the inner film is punctured, the outer film interfacial tension pulls the string radially until it is balanced by tension from the string itself. The loop is stretched into a circle.

1.2 The Young-Laplace equation

The conclusion of Monge's essay foresees the mathematical formulation of capillarity given by Laplace in his famous *Supplément au X^e Livre du Traité de Mécanique Céleste* [45] of 1806. In this work, Laplace rigorously establishes the equation suggested by Monge which dictates the curvature of a fluid interface.

Assuming an interface has an inherent and isotropic tension, an equilibrium condition is easily derived from the force equilibrium of a small segment of curved interface, as sketched in Fig. 1.3. The interfacial tension γ on the left does not exactly balance its counterpart on the right and a normal force component remains. The only other forces that apply on the segment are the inner and outer pressures, p_i and p_o , which must then differ in order to compensate for interfacial tension. It yields that the mean curvature \mathcal{C} of the interface verifies

$$\gamma \cdot \mathcal{C} = p_i - p_o, \quad (1.1)$$

an equation known today as the Young-Laplace equation. The pressure difference $\Delta p = p_i - p_o$ is known as the Laplace pressure jump. If there are no other forces that act on the fluids besides the interfacial tension, then the pressure fields p_i and p_o are constant at equilibrium. It immediately follows from the Young-Laplace equation that the mean curvature \mathcal{C} is then also constant everywhere on the interface, explaining the typical spherical shape of bubbles and drops.

In the presence of gradients of γ along the interface and of flows in either fluid phase, the system is out of equilibrium. Yet, because the interface can be treated as a mechanical system with no mass, acceleration disappears from Newton's second law of motion and the sum of forces acting on the segment of interface must still be zero. Balancing normal and tangential stresses yields the dynamic boundary condition at a fluid interface, also known

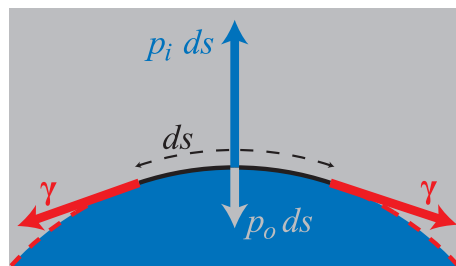


Figure 1.3: Illustration of the force balance on the small segment of interface in black. The tension from the rest of the interface pulls on both side of the segment tangentially to the interface (red vectors). The inner pressure in blue pushes the interface outwards while the outer pressure in gray does the contrary. The segment is at equilibrium only if the sum of these forces is zero.

as the generalized Young-Laplace equation [46]:

$$\gamma \mathcal{C} \cdot \vec{n} = -(\sigma_i - \sigma_o) \cdot \vec{n} - \frac{\partial \gamma}{\partial \vec{n}} \cdot \vec{n} \quad (1.2)$$

in which σ_i and σ_o are the inner and outer stress tensors at the interface, $\partial \gamma / \partial \vec{n}$ denotes the gradient operator of γ along the interface and \vec{n} is the normal vector oriented from the inner to the outer fluid.

1.3 Drops on solid surfaces: wetting properties, contact angle and shapes

A remarkable manifestation of capillarity is the variety of shapes that droplets can adopt on a solid surface. The shape of a drop actually defines the *wetting properties* of the liquid on the solid:

- Complete wetting: the drop spreads into a thin layer that covers a large surface of the solid. This is typically cooking oil in a pan.
- Non-wetting: the drop forms a very mobile liquid marble that is not in direct contact with the solid, like mercury on most surfaces.
- Partial wetting: the drop adopts the shape of a spherical cap which intersects the solid surface at an angle θ_γ called the contact angle. A rain drop on a windshield is an example.

These three states are illustrated on Fig. 1.4.

Within partial wetting, hydrophilic surfaces on which the contact angle of a water drop is below 90° as pictured on Fig. 1.4 are usually distinguished from hydrophobic surfaces for which the contact angle exceeds 90° . This is the modern definition of the solids *that are or are not wet by the liquid* often encountered in the historic literature [42, 47, 45]. The more a surface is hydrophobic, the larger is the contact angle. Above 150° , the term

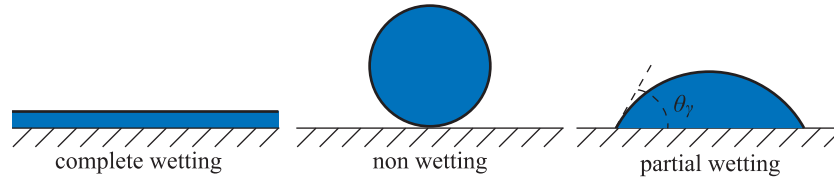


Figure 1.4: Illustration of the three wetting configurations of a drop on a solid surface and definition of the contact angle θ_γ .

superhydrophobicity is often used [48] and non-wetting can be considered as an extreme case of partial wetting with $\theta_\gamma = 180^\circ$. If the droplet is oily rather than aqueous, then the terms oleophylic and oleophobic are preferred. In the Hawksbee's experiments for example, the glass plates are partially wet by the oil of oranges: $0 < \theta_\gamma < \pi/2$.

Thomas Young is accredited with the first theoretical model for the contact angle θ_γ . In his famous essay of 1805 [47], he writes

We may therefore inquire into the conditions of equilibrium of the three forces acting on the angular particles, one in the direction of the surface of the fluid only, a second in that of the common surface of the solid and fluid and a third in that of the exposed surface of the solid.

Excerpt from *An Essay on the Cohesion of Fluids* by Thomas Young [47].

The first force is the interfacial tension γ of the fluid interface. The other two are similar in nature but capture the attractive molecular interactions at the wet and dry solid interfaces respectively. We name these tensions γ_{SL} and γ_{SV} for the Solid-Liquid and Solid-Vapor interfaces, as sketched on Fig. 1.5. Balancing the forces at the contact line yields a condition on the contact angle θ_γ known as the Young equation:

$$\gamma \cos \theta_\gamma = \gamma_{SV} - \gamma_{SL} \quad (1.3)$$

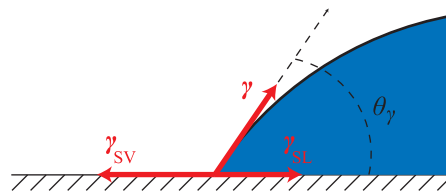


Figure 1.5: Representation of the three tensions γ , γ_{SL} and γ_{SV} that apply at the contact line.

Obviously, the wetting properties strongly affect the shape that the droplet adopts in contact with the solid surface. This is especially true in the confined geometries of microfluidic devices. The contemporary vocabulary used to differentiate between the different configurations encountered in microfluidics is illustrated in Fig. 1.6. In a hydrophobic square

capillary, a drop has an elongated *sausage* shape whereas in the case of hydrophilic channels, the drop is referred to as a *plug*. In a Hele-Shaw cell, a drop bridging two hydrophilic plates resembles a *pulley*. However, a non-wetting drop has the shape of a *pancake*. The case of complete wetting is not mentioned here because it has to be avoided at all costs in droplet microfluidics. Indeed, if the drop transforms into a layer of fluid when in contact with the solid surface, it no longer forms a closed container.

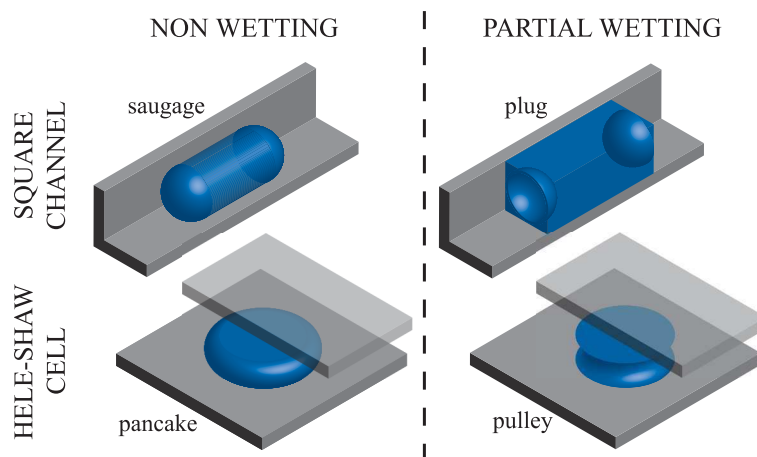


Figure 1.6: 3D schematics of the different droplet shapes when channel geometries and wetting properties are varied.

1.4 Drops in confinement gradients: a force model

Having both worked out the relation between the curvature of interfaces and capillary effects, Young and Laplace suggest explanations for Hauksbee's account amongst other things.

It is regrettable that Young was refractory to calculus: his essay does not contain a single equation or formula, and surprisingly not a single illustration. For a reader today, his analysis of the drop squeezed between two non-parallel plates appears as qualitative and confusing. He invokes the suction force of a concave meniscus and quantifies it with the height of the water column it would raise in a capillary. According to Jurin's law [49], the height of rise of a liquid in a tube is inversely proportional to the radius of the tube and thereby, he concludes

The theory is sufficient to explain the law of the force by which a drop is attracted towards the junction of two plates inclined at each other [...] If both plates were parallel, the capillary action would be equal on both sides of the drop: but when they are inclined, the curvature of the surface at the thinnest part requires a force proportionate to the appropriate height to counteract it; and this force is greater than that which acts on the opposite side.

Excerpt from *An Essay on the Cohesion of Fluids* by Thomas Young [47], p. 80.

At first, this analysis seems flawed since it uses a height to measure a force. The weight of the water column should have instead been used. However, the weight of the column of liquid that rises in the capillary tube is proportional to the radius of the capillary, which would mean that the *capillary action* on the thinnest side is less than that on the opposite side and the liquid should move towards the thickest side, in contradiction with experiments.

A second interpretation is that by *force*, Young means pressure which is indeed directly proportionate to the height of a liquid column. Then, according to the Young-Laplace law (1.1), the pressure jump across the thinnest meniscus is greater than the one on the opposite side. The pressure in the droplet is lowest near the thinnest meniscus and the drop sucked towards the touching end of the plates.

Surprisingly, the first qualitative explanation in terms of forces contradicts the second in terms of pressures.

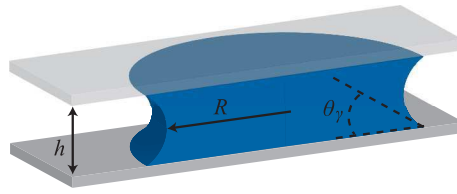


Figure 1.7: Geometric parameters of a liquid bridge between parallel plates.

In his analysis, Laplace is instead methodical and relies intensively on calculus to obtain his results. In his theory, curvature plays a central role. In question 9 of his book, he starts by computing the mean curvature of a droplet of radius R squeezed between two horizontal plates of gap width h for any contact angle θ_γ of the liquid on the plates, as sketched on Fig. 1.7. For large droplet ($R \gg h$), he obtains the general asymptotic expression

$$\mathcal{C} = -\frac{2 \cos \theta_\gamma}{h} + \left(\frac{\pi/2 - \theta_\gamma}{2 \cos \theta_\gamma} + \frac{1}{2} \sin \theta_\gamma \right) \frac{1}{R}, \quad (1.4)$$

which gives the curvature of bridges ($\theta_\gamma < \pi/2$) and pancakes ($\theta_\gamma > \pi/2$). In the case of a non-wetting pancake drop, it simplifies to

$$\mathcal{C} = \frac{2}{h} + \frac{\pi}{4} \frac{1}{R} \quad (1.5)$$

whereas for a completely wetting pulley droplet, it becomes

$$\mathcal{C} = -\frac{2}{h} + \frac{\pi}{4} \frac{1}{R}. \quad (1.6)$$

It is noteworthy that both of these equations are often forgotten in the literature [50] and re-derived on occasions [51]. In Appendix B, we identify the shape of a droplet squeezed

between two plates as a portion of a Delaunay surface [52] and give an alternative derivation of the expressions above, along with a discussion of the $\pi/4$ prefactor.

In the case of non-parallel plates, equation (1.4) shows that the curvature of the interface is greater on the thinnest side of the drop. The Young-Laplace equation (1.1) can then be applied to estimate the pressures in the liquid as illustrated on Fig. 1.8:

- for $\theta_\gamma < \pi/2$, the pressure on the thinnest side is less than on the opposite side. The liquid flows towards the touching end of the plates.
- for $\theta_\gamma > \pi/2$, the pressure on the thickest side is less than on the opposite side. The liquid flows towards the diverging end of the plates.

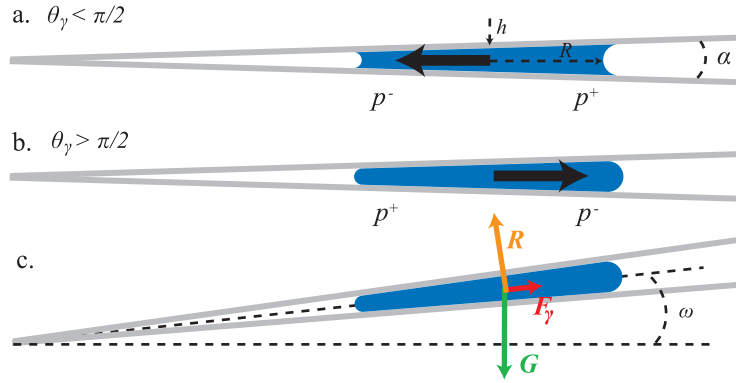


Figure 1.8: Asymmetric pressures inside **a)** a pulley and **b)** a pancake squeezed between plates inclined at an angle α force the drop to flow in the direction of the arrows. **b)** Drop equilibrium is possible by tilting both plates at an angle ω with respect to gravity. In that case, the weight G of the drop is balanced the capillary force from the confinement gradient F_γ and the reaction R from the bottom plate.

Laplace and later contributors [53, 54] never directly compute the capillary force F_γ that applies on the drop due to the wedged geometry and in fact, never express it as such. Instead, they consider an apparatus tilted at an angle ω with respect to gravity (see Fig. 1.8) for which the hydrostatic pressure across the drop Δp_g exactly balances the capillary pressure difference from the wedged geometry Δp_γ . In this particular configuration, the drop is at equilibrium and the tilting angle ω measured experimentally can be used to confront the theory [38, 40, 47, 45, 53].

Yet, if the drop is at equilibrium, then the weight $G = \pi R^2 h \rho g$ of the drop projected in the direction of the plates provides an indirect measure for the capillary force: $F_\gamma = G \sin \omega$. Calling α the angle of the wedge, balancing Δp_g with Δp_γ yields $\rho g 2R \tan \omega \approx 4\gamma \tan \alpha R / h^2$. It is then found that

$$F_\gamma = \gamma \cos \theta_\gamma \frac{2 \tan \alpha \cdot \pi R^2}{h}. \quad (1.7)$$

1.5 Examples of droplet propulsion in confinement gradients

In the 300 years that followed Hauksbee's initial observation of spontaneous droplet movement between non-parallel plates, only a small number of other asymmetric geometries were studied in that spirit. There is essentially the case of a drop in a conical or tapered tube. It is the direct the analogue of the inclined plates but has the advantage of rotational symmetry which eases geometrical considerations [45, 54, 55]. A less evident manifestation of droplet propulsion from confinement gradients is the spontaneous motion of a wetting drop towards the diverging end of a conical wire [56].



Figure 1.9: Left panel: **a.** A Red Necked Phalarope feeding by confinement gradient. **b.** A drop of silicon oil spontaneously moves towards the closing end of an artificial beak [57]. Right panel: **a-b.** The web of the cribellate spider *Uloborus walckenaerius* is capable of capturing large droplets from moist air. **c-d** This is due to the succession of spindle knots and joints along the threads of silk which act as two-sided conical wires. Water drops are attracted to the spindle knots by the combined action of confinement gradients and asymmetric contact angle between the joints and knots [58].

Nonetheless, it was recently found that there are actually animals which use either one of these geometries to collect water droplets [57, 58]. In the case of the conical tube, these animals are certain species of shorebirds that are part of the Phalarope family, like the red necked phalarope (*Phalaropus lobatus*) shown on the left panel of Fig. 1.9. These birds have beaks too long for suction feeding. Instead, they bring food to their mouth by collecting their prey in water drops at the tip of their beak (see left Fig. 1.9.a), drops

which are then propelled upwards by confinement gradients [59]. Using artificial beaks, it was shown that capillarity alone is sufficient to drive only completely wetting liquids like silicone oil (Fig. 1.9.b). For partially wetting water drops, the bird has to tweeze its beak to enhance droplet motion. [57].

Associated to the conical wires is the cribellate spider *Uloborus walckenaerius* shown on the right panel of Fig. 1.9. This spider produces a silk which has the remarkable ability to collect air moisture in large droplets. This phenomenon is due to the architecture of the silk thread which is a succession of spindle knots and joints. To small droplets, the thread appears as a conical wire and propels the liquid towards the knots (see Fig. 1.9.c-d, right). The effect of the confinement gradient is enhanced by variations of the contact angle between the joints and knots [58].

In all the cases listed above, the behavior of the droplet is well captured by the force approach of Laplace which essentially compares the curvatures and consequent pressures at two extremities of the drop in order to predict motion. For more complex confinement geometries as the one depicted in Fig. 1.10, this type of analysis may prove delicate. In this example, a pancake drop is placed between two parallel plates, one of which features a rectangular trench. Let's consider that the center of the droplet is off-center with the trench. As drawn on 1.10, the curvature of the droplet appears to be constant everywhere along the interface and a force approach would conclude that no force is applied on the droplet by the trench. Yet intuition tells that at equilibrium, the drop should be centered with the trench.

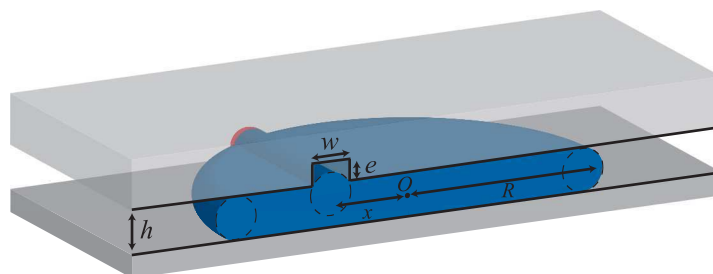


Figure 1.10: Sketch of pancake droplet of radius R squeezed between two horizontal plates of gap width h , one of which features a trench of width w and depth e . The droplet is off-centered by a distance x with the trench. The curvature of the linear flange that enters the trench can be set equal to the curvature at the rim, as illustrated by the dotted circles. Only where the flange meets the outer rims (red region) is the geometry complex and the curvature *a priori* unknown.

Here, the force approach fails because the pressure variations are localized at the intersection of the trench and the outer rim of the droplet where geometric details and exact curvature variations are unknown. A thorough analysis of this situation is given in Chapter 4.

1.6 Surface energy

In the wake of Young and Laplace, the next significant contribution to the modelling of interfacial tension was brought by Karl Friedrich Gauss in 1830 with the *Principia generalia Theoriae Figurae Fluidorum in statu Aequilibrui* [60, 41]. Rather than looking at the conditions of equilibrium of one element of fluid (or *molecule* in the text) at the interface, he applies the principle of virtual velocities to all the fluid particles and thereby derives an expression for the potential energy (or *force-function*) of the system. He finds that, regardless to the nature of the cohesive forces between the fluid molecules, an interface (fluid-fluid or fluid-solid) has an energetic cost proportional to its surface. Schematically, a molecule of fluid at the interface is missing half the cohesive interactions it would have if it were in the bulk of the fluid and as a result, is in a higher state of energy [43]. Last, he finds that at equilibrium, the potential energy is a minimum and goes on to recover not only the Young-Laplace equation (1.1) but also the Young equation for the contact angle (1.3) from a variational minimization.

Ad stabiliendam aequationem aequilibrui systematis punctorum physicorum quocunque, quorum motus conditionibus qualibuscunque adstringuntur, maxime idoneum est principium motuum virtualium, quod sic enunciamus.

Aequatio ista constituit theorema fundamentale primum in theoria aequilibrui fluidorum, quo iam ab ill. Laplace erutum est, sed per methodum a nostra plane diuersam.

Hoc est theorema fundamental secundum, quod etiam inuestigationibus ill. Laplace intertextum, sed e principio virium molecularium haud demonstratum videmus.

Three excerpts ¹from *Principia generalia Theoriae Figurae Fluidorum in statu Aequilibrui* by Karl Friedrich Gauss [60].

Finally, a comparison of the equation of Gauss with the Young-Laplace equation yields that the energetic cost per surface area is equal to the interfacial tension γ . It adds up over the entire interface and defines the surface energy \mathcal{E}_γ of the droplet

$$\mathcal{E}_\gamma = \int_S \gamma dS. \quad (1.8)$$

¹Personal English translation with help from the German edition [61] **First:** *An equilibrium equation for a system of any number of mass points, whose movements are subject to any conditions, is best established with the principle of virtual work.* **Second:** *This equation is the first fundamental theorem for the equilibrium theory of liquids, the same that Laplace had already found by in a very different way.* **Third:** *This is the second fundamental theorem, which was also established in the investigations of Laplace. However, it was not derived from a principle of molecular forces.*

When the interfacial tension γ is homogeneous over the interface of the drop, the surface energy is simply proportional to the surface area S of the drop: $\mathcal{E}_\gamma = \gamma \cdot S$. For a drop in an unbounded domain and in the absence of an external force, minimizing surface energy is then equivalent to minimizing surface area. This yields the trivial result that the drop is spherical in equilibrium.

Similarly, when a drop touches a surface, the energetic costs per surface area of the Liquid-Solid interface and the Solid-Vapor interface are γ_{SL} and γ_{SV} respectively. The overall surface energy \mathcal{E} of the system is then the sum of the three surface energies

$$\mathcal{E} = \mathcal{E}_\gamma + \mathcal{E}_{\gamma_{SV}} + \mathcal{E}_{\gamma_{SL}} \quad (1.9)$$

and it is a minimum at equilibrium.

Clearly, there is a strong force-energy duality in surface tension. The force proposition *at equilibrium, the interface and its contact angle verify the Young-Laplace and the Young equations* is equivalent to the energy proposition *at equilibrium, the interface minimizes the surface energy \mathcal{E} of the system*.

However, concerning the out-of-equilibrium analysis of the dynamic of a droplet, surface energy provides a simple and rigorous approach. The qualitative force proposition *the droplet flows from high to low pressures* is replaced by the established theorem *the system evolves in a direction that reduces its potential energy* [60].

1.7 Drops in confinement gradients: energy considerations

Amongst all systems, completely wetting and non-wetting droplets are particularly well suited for an analysis in terms of energy.

Because a non-wetting droplet is never in direct contact with solid walls (it may flatten against a surface but a lubrication layer of outer fluid must remain between the droplet and the solid), it does not modify the surface energy of the solid. In the overall surface energy \mathcal{E} of the system, the term $\mathcal{E}_{\gamma_{SL}}$ is zero and the term $\mathcal{E}_{\gamma_{SV}}$ is a constant. Hence, the effective surface energy of an unbounded or confined non-wetting droplet is the same:

$$\mathcal{E} = \mathcal{E}_\gamma = \int_S \gamma dS . \quad (1.10)$$

The same considerations apply for a completely wetting droplet, although in this case $\mathcal{E}_{\gamma_{SV}} = 0$ and $\mathcal{E}_{\gamma_{SL}}$ is constant.

We may then conclude that in confined geometries, a completely wetting or a non-wetting droplet of homogeneous interfacial tension

- is at equilibrium where the surface area of its fluid interface is minimum
- and otherwise moves in a direction that reduces the surface area of its fluid interface.

The equilibrium shape of a droplet in a confined geometry may differ from the spherical shape that minimizes energy in the unbounded case because the solid walls add constraints to the minimization. For example, the circular pancake drop is the shape of minimum surface area under the constraint that the thickness of the pancake cannot exceed the thickness h of the Hele-Shaw cell.

Such considerations allow to easily predict the motion of drops in confinement gradients, as suggested by Henri Bouasse in his textbook *Capillarité - phénomènes superficiels* of 1924 [54]. He considers a drop in a conical tube. In the case of complete wetting, the drop minimizes its fluid interfaces by minimizing the size of its meniscus and therefore moves towards the tip of the cone. In the opposite case of non-wetting, the flat section of the interface that is pressed against the walls of the tube dominates the surface area of the drop. Its area and thereby the surface energy decrease as the drop moves away from the tip.

These examples illustrate the following rules of thumb which will prove useful through the rest of the manuscript:

- in the case of complete wetting, drops are attracted to regions of maximum confinement.
- in the case of non-wetting, drops are attracted to regions of minimum confinement.

1.7.1 Application to the case of a pancake drop over a trench

These rules are simple to implement in simple confinement gradients like cones, wedges, etc... and also in more complex geometries like the trench from Fig. 1.10. The trench is a region of weaker confinement and the more a non-wetting drop expands into the trench, the smaller its surface energy. The minimum position is when the drop is centered on the trench.

This result can be verified by calculus. To simplify the geometry, we consider a trench of geometry $w = h$ and $e = h/2$. In this case, the cross-section of the flange in the trench is a half-circle of diameter h . For very large pancakes ($R \gg h$), the volume of the droplet is well approximated by $V = \pi R^2 \cdot h$ and the surface area S of the droplet is dominated by the top and bottom flattened interfaces. Hence, we model the drop by combining a vertical circular cylinder of radius R and height h with an horizontal half-cylinder of diameter h and length L , as shown on Fig.1.11.

The volume of the drop when over the trench is the sum of the volume of the pancake $\pi R^2 h$ and the volume of the flange $\pi L \cdot h^2/8$. Hence, we have

$$V = \pi R^2 \cdot h + \frac{\pi}{8} h^2 \cdot L , \quad (1.11)$$

which must be the same as when the drop is away from the trench, provided the fluid is incompressible. The surface area is the sum of the surface area of the bottom interface πR^2 and that of the top interface. The latter is approximately a disk minus the rectangular

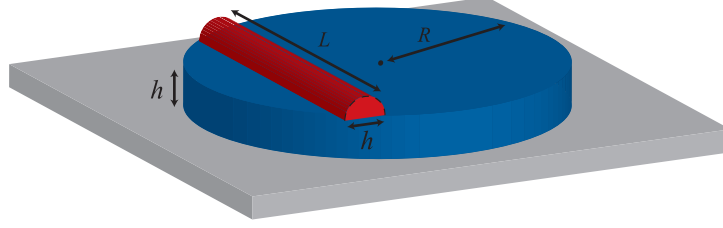


Figure 1.11: Simplified model of a pancake drop over a trench. It is the combination of a vertical cylinder of radius R and height h (in blue) with an horizontal half-cylinder of diameter h and length L spanning the width of the drop (in red).

band of the trench which is replaced by the surface of a half-cylinder of diameter h and length L . Overall,

$$S = 2\pi R^2 \cdot h - h \cdot L + \frac{\pi}{2} h \cdot L . \quad (1.12)$$

In the end, we can express S from the volume V to obtain

$$S = 2\frac{V}{h} - \left(1 - \frac{\pi}{4}\right) h \cdot L . \quad (1.13)$$

Clearly, the surface area of the droplet decreases as L increases and the extremum position is when the droplet is centered with the trench, for which $L = 2R$.

1.8 The free and constrained interface of confined non-wetting drop at equilibrium

Given that we will mostly study confined non-wetting drops in the rest of this thesis, we finish this brief review of the literature concerning droplets in confinement gradients with the description of two distinct regions of the interface: the *free interface* and the *constrained interface*. The effect of confinement on the geometry of a non-wetting interface at equilibrium is illustrated on Fig. 1.12 with the example of a drop in a square box of size h .

When the drop is much smaller than the box, it is as if the drop were in an unbounded medium. For this configuration sketched in Fig. 1.12.a, the Young-Laplace equation (1.1) implies a homogeneous curvature of the interface and therefore a spherical geometry for the drop. However, as soon as the volume V of the drop exceeds the volume $\pi/6h^2$ of the largest inscribed sphere in the box, it cannot retain its spherical shape since it no longer fits into the box. Furthermore, the drop cannot have the shape of a truncated sphere as sketched in Fig. 1.12.b since the interface would then intersect the walls of the box at a finite angle, violating the non-wetting property of the fluid in the drop. The only solution is for part of the interface to flatten against the walls of the box while the rest bends in the corners to smoothly connect the flattened segments as illustrated on Fig. 1.12.c.

Clearly, this geometry of the interface does not have a constant mean curvature. The flattened sections have zero curvature while the bent segments in the corner have a strong

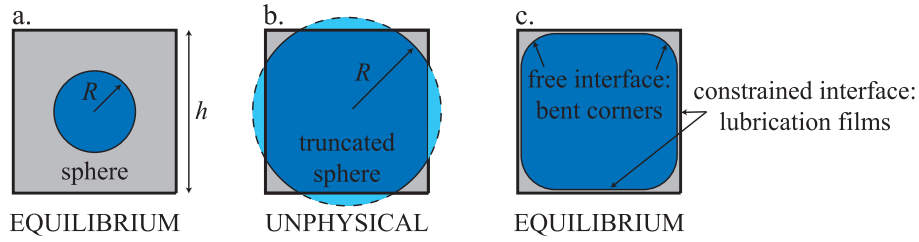


Figure 1.12: Sketches of a non-wetting drop confined in a square box of size h . **a.** A small drop is unconfined and has the shape of a sphere of radius $R < h/2$ at equilibrium. **b.** A spherical drop of radius R greater than $h/2$ does not fit in the box. At equilibrium, the shape of the interface in the box cannot be a truncated sphere as it would then intersect the walls at a finite angle, violating the non-wetting condition at the wall. **c.** Instead, the drop flattens against the walls, forming thin flat lubrication films of outer fluid while bending in the corners to connect the flat segments.

positive curvature. Hence, this shape *a priori* contradicts the equilibrium condition set above. In particular, if we assume that the pressure p_i in the drop is constant, the pressure of the outer phase in the thin lubrication films exceeds the pressure in the corners which leads to a flow of the outer phase from the films to the corners and a thinning of the films.

However, when the fluid in the drop is non-wetting, the films cannot vanish completely: the energy cost of having a drop/solid interface is so high compared to the cost of an outer-fluid/solid interface that a layer of outer fluid necessarily screens the drop from the surface. In terms of molecular forces, this means that there is an attractive force that keeps molecules of the outer fluid near the wall. Forty years ago, Derjaguin *et. al.* [62] suggested to represent these forces at the macroscopic level by adding a negative disjoining pressure $\Pi(e)$ to the hydrostatic outer pressure field p_o of the outer phase. The magnitude of the disjoining pressure decreases as the thickness of the films e increases and vanishes above a cutoff length e_{dp} , a few tenths of nanometers classically [63].

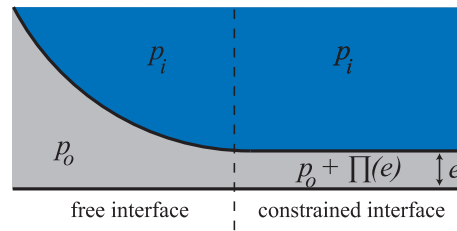


Figure 1.13: Illustration of the two types of regions on the interface of the drop. On the left, the interface is far from the wall, verifies the classic Young-Laplace equation. This is a *free interface* region. On the right, the pressure in the outer phase is modified by the disjoining pressure $\Pi(e)$ which represent the microscopic molecular forces that maintain a finite thickness e of the lubrication films. This is a *constrained interface* region.

As a result, we can distinguish two types of regions on the interface of the drop, as

sketched on Fig. 1.13:

- regions of *free interface* that are farther than e_{dp} from any solid wall and for which the classical Young-Laplace equation applies:

$$\gamma\mathcal{C} = p_i - p_o \quad (1.14)$$

- regions of *constrained interface* influenced by the disjoining pressure for which the augmented Young-Laplace equation for the curvature \mathcal{C}_{lf} of the lubrication films applies [64]:

$$\gamma\mathcal{C}_{lf} = p_i - p_o + \Pi(e) \quad (1.15)$$

At equilibrium, there are no flows in both phases and the pressure fields p_i and p_o are constant. Hence, the mean curvature of the free interface is homogeneous as in the unbounded case and implies an overpressure $p_i > p_o$ inside the drop. This overpressure in the drop presses the constrained interface against the walls and drains outer fluid out of the lubrication films. The films thin until their thickness reaches a value e for which the disjoining pressure $\Pi(e)$ exactly balances the Laplace pressure jump $p_i - p_o$ imposed by the regions of free interface elsewhere on the drop. In this configuration, the entire interface is at equilibrium.

In the microfluidic systems that we consider, the nanometric thickness of the equilibrium lubrication films is much smaller than all other micrometric length scales (dimension of the channel, size of the drop, etc). Hence we model the lubrication films as layers of outer fluid of zero thickness, which results in the condition that the free interface connects directly to the walls and with a contact angle $\theta_\gamma = 180^\circ$. The shape of the non-wetting drop is then fully described by the shape of the free interface and the apparent contact line where it *touches* the walls and meets the constrained interface. The exact thickness of the equilibrium lubrication films is effectively irrelevant to the model.

Consequently, we will improperly refer to the free interface as *the* interface of the non-wetting drop and assume lubrication films on the walls where needed. These assumptions simplify the discussion: for example, we can then say that the shape of the drop confined in the square box shown in Fig. 1.12 has a constant mean curvature of its interface. By interface we mean free interface since obviously, the flat constrained interface has a different curvature that is imposed by the walls.

Summary of Chapter 1

In this first chapter, we recalled Hauksbee's account of spontaneous droplet motion between non-parallel plates and traced its historical implication in the development of the basic concepts explaining droplet manipulation in confinement gradients, namely interfacial tension and surface wetting. We then summarized the existing work on the most commonly studied geometries (wedges and cones) and listed examples of droplet manipulation by confinement gradient in nature.

We continued our course in history with the introduction by Gauss of the concept of surface energy. Last, we showed that an energy approach to interfacial tension is often more practical than a force approach when it comes to modeling droplet manipulation in confinement gradients. Indeed, the minimum principle of potential energy gives simple and general criteria to qualitatively predict droplet motion and identify equilibrium states.

However, this minimum principle does not provide any information on the actual dynamics of the droplet when out-of-equilibrium and there are no models for the motion of the droplet in the literature. Therefore, over the next two chapter, we derive an energy-based model for the flow of a droplet in confinement gradients.

Chapter 2

A minimum principle for the flow of a droplet in a Hele-Shaw cell

“Such principles are fascinating, and it is always worth while to try to see how general they are. But also from a more practical point of view, I want to know.”
Feynam, lecture II.19

We begin this chapter by recalling a little known minimum principle for viscous two phase flows. Minimum principles are usually derived for conservative systems but viscous flows are the opposite: they are systems dominated by energy dissipation. In that sense, this minimum principle is peculiar and include a discussion of its origin useful to its understanding. In addition, we give a critical analysis of its implications in order to avoid misuses.

We then apply the minimum principle to the simplest possible system related to 2D droplet microfluidics: the flow of a droplet in a perfectly flat Hele-Shaw cell. Our approach recovers classic results first obtained by G.I. Taylor and P.G. Saffman from a kinematic analysis of the problem but also clearly identifies the key role played by interfacial tension in the mechanism that selects the shape of the flowing droplet, a question in debate in the literature.

Only in the Chapter 3 are confinement gradients added to the model.

2.1 A minimum principle for viscous two phase flows

2.1.1 Generalities

Minimum principles, or extremum principles in the more general sense, arise naturally in mechanics and electrodynamics, from Fermat's principle of least time for the trajectory of a light ray to Hamilton's canonical formulation of classical and later on of quantum mechanics [65, 66, 67]. They provide global expressions for the laws of physics and often offer a clearer and broader understanding of the fundamental physics at play than their local equivalent.

Mechanical systems at equilibrium verify the principle of minimum free energy [65] and an interface between two immiscible fluids makes no exception as we have seen in the previous chapter. Gauss showed that an interface has an energy \mathcal{E}_γ of surface density equal to the interfacial tension γ . Including all other contributions to the free energy of the system in the potential energy \mathcal{E}_p , the principle of minimum free energy then states that

the shape of an interface at equilibrium minimizes

$$\mathcal{E}_\gamma + \mathcal{E}_p = \int_S \gamma dS + \mathcal{E}_p \quad (\text{P1})$$

amongst all possible shapes,

where the potential energy \mathcal{E}_p may be gravitational for example.

The most famous consequence is that, in the absence of potential energy, an interface of homogeneous interfacial tension γ has a shape of minimum surface area. Hence, a freely suspended drop is spherical and the interface of a liquid bridge stretched between two circular plates describes a catenoid. The statement (P1) can also be used to obtain the shape of the pendant drop pulled by gravity from the tip of a syringe, as sketched on Fig. 2.1.

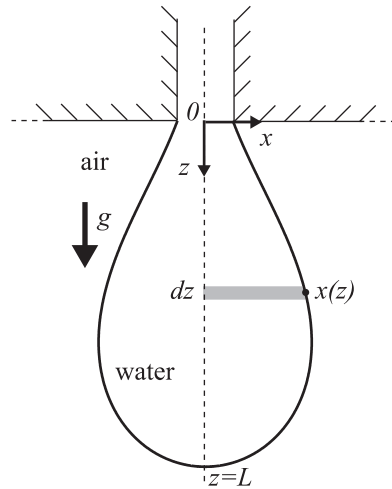


Figure 2.1: Sketch of a pendant drop of water in air.

The case of a 2D pendant drop will serve as an example to illustrate the minimum energy principle. The potential energy is the gravitational potential energy which is equal to $-\rho g x(z) z dz$ for the infinitesimal slice of thickness dz shaded on Fig. 2.1, with ρ the density of the drop fluid and g gravity. The length of the interface on the side of this same slice is given by $ds = \sqrt{dx^2 + dz^2} = \sqrt{1 + (dx/dz)^2} dz$. Therefore, the shape of the drop $x(z)$ minimizes

$$\mathcal{E}_\gamma + \mathcal{E}_p = \int_0^L \left[\gamma \sqrt{1 + \left(\frac{dx}{dz} \right)^2} - \rho g z x(z) \right] dz \quad (2.1)$$

for all possible shapes $x(z)$ that verify the boundary conditions $x(0) = a/2$, $x(L) = 0$ and $dx/dz(L) = -\infty$. Taking the Gateaux derivative of the integral with respect to the function $x(z)$ then yields that the interface verifies the pendant drop equation

$$\gamma \cdot \mathcal{C} - \rho g z = \text{cst} , \quad (2.2)$$

in which \mathcal{C} is the interface curvature. It is noteworthy that this variational approach relies only on the statement (P1) and a general formula for the length of a curve to finally recover a particular case of the Laplace equation (1.1), a local equilibrium condition of the interface.

In addition, although the principle of minimum free energy only applies to free surfaces at equilibrium, it is easily extended to dynamic systems of conservative energy as the principle of least action [65]. This formalism can then describe the free undamped oscillations of a droplet which exchange surface and kinetic energy.

Viscous flows

Viscous flows however do not verify the principle of least action since the laws of physics involved are dominated by energy dissipation rather than energy conservation. Instead, Batchelor [46] states that for single phase viscous flows

the rate of dissipation (of energy) in the flow in a given region with negligible inertia forces is less than that in any other solenoidal velocity distribution (of zero divergence) in the same region with the same values of the velocity at all points of the boundary of the region.

This statement is a detailed expression of the principle of minimum energy dissipation suggested by Helmholtz in 1868 [68]. Using the dissipation function of a viscous flow as defined by Rayleigh [69], its algebraic formulation is the following:

the velocity field \vec{u} minimizes the dissipation function

$$\mathcal{D}(\vec{u}) = \frac{1}{2} \int_{\Omega} \mu (\vec{\nabla} u)^2 d\Omega \quad (\text{P2})$$

amongst all possible divergence free velocity fields \vec{u}

that satisfy the kinematic boundary conditions of the fluid domain Ω .

Viscous two phase flows

An interesting question arises in the case of viscous two phase flows which combine interfaces and viscous flows: “which minimum principle applies?” Arguably, both (P1) and (P2). Indeed, the interface should still work to minimize interfacial energy while the flow should continue to distribute across the domain so as to minimize energy dissipation. However, combining (P1) and (P2) is dimensionally ill stated since the first minimizes energy while the second minimizes energy dissipation, i.e. the rate of change of energy per unit of time.

In fact, viscous flows are one example of systems which follow irreversible processes characterized by energy dissipation or entropy production. Other examples are heat diffusion or electric conduction. For such systems, Onsager [70, 71] extended the principle of least dissipation of energy to include the presence of potential energy and showed that

$$\begin{aligned} &\text{the system's free energy decreases as quickly as possible} \\ &\text{subject to a penalty of energy dissipation.} \end{aligned} \tag{P3}$$

An interpretation in the case of viscous flows is given by Glasner [72]:

Suppose that a system's free energy is a function of the Eulerian configuration (for incompressible fluids, this is just the volume the fluid occupies) but does not depend on the Lagrangian positions of individual molecules. Then there may be many trajectories the system can take which each reduce the free energy by the same amount. In this case, the second half of the minimum dissipation principle can be invoked, requiring the selected trajectory to be the one with the least dissipation.

Mathematically, the principle of minimum dissipation states that

$$\begin{aligned} &\text{for any given configuration of the interface,} \\ &\text{the velocity field } \vec{u} \text{ that captures the evolution of the system minimizes} \\ &\mathcal{D}(\vec{u}) + \dot{\mathcal{E}}_\gamma + \dot{\mathcal{E}}_p = \frac{1}{2} \int_{\Omega} \mu (\vec{\nabla} u)^2 d\Omega + \dot{\mathcal{E}}_\gamma(\vec{u}) + \dot{\mathcal{E}}_p(\vec{u}) \tag{P3-bis} \\ &\text{amongst all possible divergence free velocity fields } \vec{u}. \end{aligned}$$

Here, $\dot{\mathcal{E}}_\gamma$ and $\dot{\mathcal{E}}_p$ are the rate of change of the surface and potential energies as the system is advected by the flow.

2.1.2 Note on stationary states

A frequent misunderstanding concerning the principle of minimum dissipation is that it identifies stationary states of the system. In the case of viscous two phase flows, possible misinterpretations are: *in its stationary state, a viscous two phase flow minimizes viscous dissipation* or *the stationary shape of an interface in a two phase flow is the one that*

minimizes viscous dissipation. Such statements are wrong in most cases. It is possible that this misunderstanding originates from erroneous analogies with the principle of minimum energy for an interface at equilibrium.

As a first comment, the expression *stationary state* too often lacks definition. Does it refer to a state for which the energy of the system is independent of time? Or to a state for which the surface energy of the drop is constant? Imagine a drop of water falling in a bath of oil under gravity. The shape of the drop will reach a stationary state but the potential and total energy of the system will constantly decrease as the drop falls down. When searching for a stationary state, it is always essential to clearly state of which physical quantity.

Second, the principle of minimum dissipation has little to do with the principle of minimum energy. Surely, the system will tend to reduce its free energy but it may not necessarily reach a minimum in its stationary state. Hence, it cannot be said that a drop flowing in a viscous fluid adopts a shape that minimizes the free energy of the system. Moreover, it has *a priori* no meaning to search for the state of minimal free energy since there is no fundamental reason that it be the stationary state of the system. The case studied by Taylor [73] of a droplet placed in a *four roller* apparatus illustrates this consideration (see Fig. 2.2). Neglecting kinetic energy and gravity, the free energy of the system is equal to the surface energy of the drop. It is minimum when the drop is spherical and yet, the drop reaches an elongated stationary state of higher free energy.

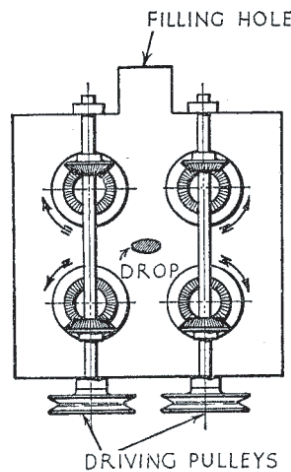


Fig. 1. 'Four roller' apparatus.

Figure 2.2: Sketch of the four-roller apparatus as drawn in the publication by G.I. Taylor illustrating the stationary shape of the drop at the center of the extensional flow

Another valid interpretation of the minimum principle (P3-bis) is that

an interface in a viscous flow relaxes towards its shape of minimum surface energy as long as the associated deformations along the way do not imply a substantial increase in viscous dissipation.

For example, the minimum principle can be used to describe how an elongated drop in a quiescent unbounded viscous fluid restores its spherical shape. At a time t , amongst all the velocity fields that could make the droplet more spherical, the one that effectively applies is the one that verifies (P3-bis): it decreases the surface energy but not too fast so that viscous dissipation stays small. At time $t + dt$, the shape of the drop has partially relaxed and the minimum principle selects the next velocity field, etc...

The statement above also sheds light onto the case of the elongated in the *four roller* apparatus of Fig. 2.2. If the droplet has a stationary elongated shape, it is because all velocity fields that advect the shape of the droplet towards the sphere would causes a cost in viscous dissipation greater than the rate of decrease in surface energy. Similarly, it does not elongate any more although it would reduce viscous dissipation because the rate of increase in surface energy would exceed the reduction in viscous dissipation.

Overall, it is essential to understand the minimum principle (P3-bis) is a minimization with respect to the velocity field only, like the minimum of dissipation for single phase viscous flows. It is not a minimization with respect to the shape of the drop. It is unrelated to any sort of general property, if one exists, of the stationary state of an interface in a viscous flow.

The simplicity to express Onsager's theory underlines a beauty common to all variational principles. However, it also hides the difficult task of translating it to solvable mathematical equations. Below, we start by showing that (P3) is indeed equivalent to the two phase Stokes equations. Then, we apply the principle of minimum dissipation to the elementary case of a droplet flowing in a Hele-Shaw cell. We recover the classic results of Taylor and Saffman [39] and rigorously confirm that they are a consequence of surface tension.

2.1.3 Equivalence between the minimum dissipation and the Stokes equations for two phase flows

Below, we demonstrate the the principle of minimum dissipation (P3-bis) is equivalent to the Stokes equations in both fluids combined with the dynamic Young-Laplace equation at the interface. While this result is not new [72, 74], it is the cornerstone of this study and we therefore include its demonstration.

We consider the inertia-less motion of a droplet of viscosity μ_1 in an outer incompressible liquid of viscosity μ_2 . The two immiscible Newtonian fluids are separated by an interface characterized by an interfacial tension γ . The droplet occupies a volume Ω_1 never in contact with the outer boundaries \mathcal{B}_∞ of the system, whether they are fluid or solid. The rest of the domain Ω_2 is filled with the outer fluid. The interface \mathcal{S} is referenced by the positions $\vec{x}_\mathcal{S}$ of its points. We impose the velocity \vec{u}_∞ at outer fluid boundaries \mathcal{B}_∞ , provided it verifies the incompressibility constraint $\int_{\mathcal{B}_\infty} \vec{u}_\infty \cdot \vec{n} d\mathcal{B}_\infty = 0$. The system is sketched in Figure 1.

For simplicity, we neglect all energy potentials (such as the gravitational potential energy) apart from the surface energy of the drop. The formulation (P3-bis) of the principle

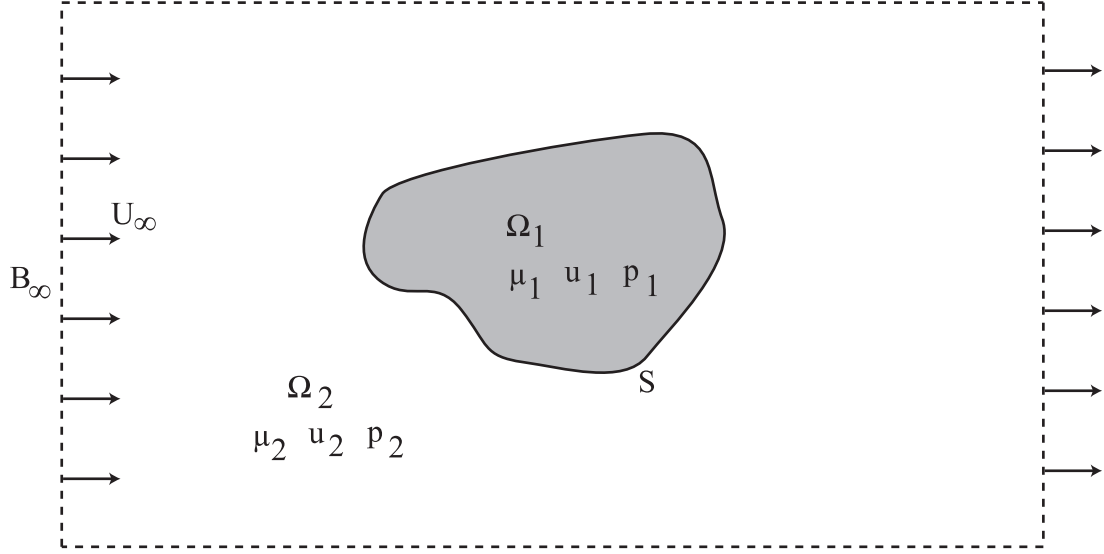


Figure 2.3: Sketch of the two incompressible two phase system

of minimum energy dissipation requires an expression for $\dot{\mathcal{E}}_\gamma$, the rate of change of surface energy as the interface is advected by the flow. Conceptually, $\dot{\mathcal{E}}_\gamma$ is the material derivative $d\mathcal{E}_\gamma/dt$ of surface energy. The general expression for the material derivative of a surface integral is obtained by applying the theorem

$$\text{For a quantity } C_t = \int_{S(t)} f(t) dS \text{ then } \dot{C}_t = \int_{S(t)} \frac{\partial f}{\partial t} dS + \int_{S(t)} \left[\left(\frac{\partial f}{\partial \vec{n}} + f\mathcal{C} \right) \cdot \vec{u} \right] \cdot \vec{n} dS, \quad (2.3)$$

in which \mathcal{C} is the mean curvature of the interface and \vec{u} is the velocity field at the interface. In the above expression, the first component is the partial temporal derivative $\partial/\partial t$ of C_t , while the second term is the change due to advection by the flow \vec{u} . Here, we will assume that surface tension γ does not vary in time. Hence, applying the formula above, we obtain

$$\dot{\mathcal{E}}_\gamma = \int_{S(t)} \gamma \mathcal{C} \vec{u} \cdot \vec{n} dS + \int_{S(t)} \frac{\partial \gamma}{\partial \vec{n}} \vec{n} \cdot \vec{u} dS. \quad (2.4)$$

Inserting this expression for $\dot{\mathcal{E}}_\gamma$ into (P3-bis), we obtain that the velocity field minimizes

$$\frac{1}{2} \int_{\Omega_1} \mu_1 (\nabla \vec{u})^2 d\Omega_1 + \frac{1}{2} \int_{\Omega_2} \mu_2 (\nabla \vec{u})^2 d\Omega_2 + \int_{S(t)} \gamma \mathcal{C} \vec{u} \cdot \vec{n} dS + \int_{S(t)} \frac{\partial \gamma}{\partial \vec{n}} \vec{n} \cdot \vec{u} dS. \quad (2.5)$$

At this point, it is useful to incorporate the incompressibility constraints and the imposed velocity field at the far-field boundaries directly into the minimization problem using La-

grange multipliers p_1 , p_2 and λ . The corresponding Lagrangian is

$$\begin{aligned} \mathcal{L} = & \underbrace{\frac{1}{2} \int_{\Omega_1} \mu_1 (\nabla \vec{u})^2 d\Omega_1 + \frac{1}{2} \int_{\Omega_2} \mu_2 (\nabla \vec{u})^2 d\Omega_2}_{\text{dissipation function}} + \underbrace{\int_{S(t)} \gamma \mathcal{C} \vec{u} \cdot \vec{n} dS + \int_{S(t)} \frac{\partial \gamma}{\partial \vec{n}} \vec{n} \cdot \vec{u} dS}_{\text{rate of change of surface energy}} \\ & - \underbrace{\int_{\Omega_1} p_1 \operatorname{div}(\vec{u}) d\Omega_1 - \int_{\Omega_2} p_2 \operatorname{div}(\vec{u}) d\Omega_2}_{\text{incompressibility constraints}} - \underbrace{\int_{\mathcal{B}_\infty} \lambda (\vec{u} - \vec{u}_\infty) d\mathcal{B}_\infty}_{\text{imposed far-field velocity}} \end{aligned} \quad (2.6)$$

which has to be minimized with respect to the velocity field \vec{u} , the pressures p and the Lagrange multiplier λ .

Taking the variations of \mathcal{L} with respect to the Lagrange multipliers simply gives back to constraints inserted in the Lagrangian. For example, writing that the Gateaux derivative of the Lagrangian with respect to p_1 is zero simply yields the condition $\operatorname{div}(\vec{u}_1) = 0$ that was injected into the Lagrangian via the multiplier p_1 . Hence, we expect to obtain the Stokes equations along with free surface boundary conditions from an evaluation of the variations with respect to the velocity field \vec{u} only. These are obtained by considering an infinitesimal variation $\delta \vec{u}$ in the velocity field \vec{u} to compute the Gateaux derivative of the Lagrangian \mathcal{L} :

$$\begin{aligned} \frac{\partial \mathcal{L}}{\partial \vec{u}} \delta \vec{u} = & \int_{\Omega_1} \mu_1 (\nabla \vec{u}) \cdot (\nabla \vec{\delta u}) d\Omega_1 + \int_{\Omega_2} \mu_2 (\nabla \vec{u}) \cdot (\nabla \vec{\delta u}) d\Omega_2 + \int_{S(t)} \gamma \mathcal{C} \vec{n} \cdot \vec{\delta u} dS + \int_{S(t)} \frac{\partial \gamma}{\partial \vec{n}} \vec{n} \cdot \vec{\delta u} dS \\ & - \int_{\Omega_1} p_1 \operatorname{div}(\vec{\delta u}) d\Omega_1 - \int_{\Omega_2} p_2 \operatorname{div}(\vec{\delta u}) d\Omega_2 - \int_{\mathcal{B}_\infty} \lambda \cdot \vec{\delta u} d\mathcal{B}_\infty \end{aligned} \quad (2.7)$$

However, the Gateaux derivative is not directly expressed as a function of $\vec{\delta u}$ as it involves differential operators $\nabla \vec{\delta u}$ and $\operatorname{div}(\vec{\delta u})$. Each time such an operator appears, an integration by parts is required in order to transform the operator into a *workable* form. For example,

$$\int_{\Omega_1} \mu_1 (\nabla \vec{u}) \cdot (\nabla \vec{\delta u}) d\Omega_1 = \int_{S(t)} (\mu_1 \nabla \vec{u} \vec{n}_{1 \rightarrow 2}) \cdot \vec{\delta u} dS - \int_{\Omega_1} \mu_1 \Delta \vec{u} \cdot \vec{\delta u} d\Omega_1.$$

After these transformations, the Gateaux derivative becomes

$$\begin{aligned} \frac{\partial \mathcal{L}}{\partial \vec{u}} \delta \vec{u} = & \int_{\Omega_1} (\vec{\nabla} p_1 - \mu_1 \Delta \vec{u}) \cdot \vec{\delta u} d\Omega_1 \\ & + \int_{\Omega_2} (\vec{\nabla} p_2 - \mu_2 \Delta \vec{u}) \cdot \vec{\delta u} d\Omega_2 \\ & - \int_{S(t)} [(-p_2 + \mu_2 \nabla \vec{u}) - (-p_1 + \mu_1 \nabla \vec{u})] \cdot \vec{n}_{1 \rightarrow 2} - (\gamma \mathcal{C} \vec{n}_{1 \rightarrow 2} + \frac{\partial \gamma}{\partial \vec{n}} \vec{n}_{1 \rightarrow 2}) \cdot \vec{\delta u} dS \\ & - \int_{\mathcal{B}_\infty} [\lambda - (-p_2 + \mu_2 \nabla \vec{u}) \cdot \vec{n}] \cdot \vec{\delta u} d\mathcal{B}_\infty \end{aligned} \quad (2.8)$$

with $\vec{n}_{1 \rightarrow 2}$ the oriented normal at the interface. The Lagrangian is at an extremum when $(\partial \mathcal{L} / \partial \vec{u}) \delta \vec{u} = 0$ for all possible variations $\delta \vec{u}$. The variations can be located exclusively in Ω_1 or Ω_2 , and on \mathcal{S} or \mathcal{B}_∞ . Therefore, we obtain 4 local equations to be verified everywhere by the fluid:

$$\vec{\nabla} p_1 - \mu_1 \Delta \vec{u} = 0 \quad \text{in } \Omega_1 \quad (2.9a)$$

$$\vec{\nabla} p_2 - \mu_2 \Delta \vec{u} = 0 \quad \text{in } \Omega_2 \quad (2.9b)$$

$$[(-p_2 + \mu_2 \nabla \vec{u}) - (-p_1 + \mu_1 \nabla \vec{u})] \cdot \vec{n}_{1 \rightarrow 2} = \gamma \mathcal{C} \vec{n}_{1 \rightarrow 2} + \frac{\partial \gamma}{\partial \vec{n}} \vec{n}_{1 \rightarrow 2} \quad \text{on } \mathcal{S}(t) \quad (2.9c)$$

$$\lambda = (-p_2 + \mu_2 \nabla \vec{u}) \cdot \vec{n} \quad \text{on } \mathcal{B}_\infty \quad (2.9d)$$

In the boundary condition, $\partial \gamma / \partial \vec{n}$ denotes the gradient operator of γ on the interface. It is a tensor, like $\nabla \vec{u}$.

These equations are precisely the bulk Stokes equations in both fluids along with the dynamic Young-Laplace boundary condition at the interface with Marangoni stresses [46] (see (1.2)). Reciprocally, if the velocity field verifies these equations, each integral in the Gateaux derivative $(\partial \mathcal{L} / \partial \vec{u}) \delta \vec{u}$ is zero and the Lagrangian is at an extremum.

As a result, we have shown that

Minimizing the Lagrangian

$$\begin{aligned} \mathcal{L} = & \frac{1}{2} \int_{\Omega_1} \mu_1 (\nabla \vec{u})^2 d\Omega_1 + \frac{1}{2} \int_{\Omega_2} \mu_2 (\nabla \vec{u})^2 d\Omega_2 + \int_{\mathcal{S}(t)} \gamma \mathcal{C} \vec{u} \cdot \vec{n} dS + \int_{\mathcal{S}(t)} \frac{\partial \gamma}{\partial \vec{n}} \vec{n} \cdot \vec{u} dS \\ & - \int_{\Omega_1} p_1 \operatorname{div}(\vec{u}) d\Omega_1 - \int_{\Omega_2} p_2 \operatorname{div}(\vec{u}) d\Omega_2 - \int_{\mathcal{B}_\infty} \lambda (\vec{u} - \vec{u}_\infty) d\mathcal{B}_\infty \end{aligned}$$

with respect to the variables \vec{u}, p_1, p_2 and λ is equivalent to

$$\vec{\nabla} p_1 - \mu_1 \Delta \vec{u} = 0 \quad \text{in } \Omega_1$$

$$\operatorname{div}(\vec{u}) = 0 \quad \text{in } \Omega_1$$

$$\vec{\nabla} p_2 - \mu_2 \Delta \vec{u} = 0 \quad \text{in } \Omega_2$$

$$\operatorname{div}(\vec{u}) = 0 \quad \text{in } \Omega_2$$

$$[(-p_2 + \mu_2 \nabla \vec{u}) - (-p_1 + \mu_1 \nabla \vec{u})] \cdot \vec{n}_{1 \rightarrow 2} = \gamma \mathcal{C} \vec{n}_{1 \rightarrow 2} + \frac{\partial \gamma}{\partial \vec{n}} \vec{n}_{1 \rightarrow 2} \quad \text{on } \mathcal{S}(t)$$

$$\vec{u} = \vec{u}_\infty \quad \text{on } \mathcal{B}_\infty$$

which is precisely the Stokes equation for incompressible two phase flows with the dynamic Young-Laplace boundary condition at the interface

2.2 The motion of a drop in a Hele-Shaw cell

We now turn to the case of a non-wetting drop flowing in a Hele-Shaw cell since this configuration is closely related to the flow of a droplet in a 2D microchannel.

Let's introduce the Hele-Shaw cell: a Hele-Shaw cell is a generic name for a channel of length L and width W much larger than its height h ($L \gg h$, $W \gg h$). It is named after Henry Selby Hele-Shaw who first suggested in 1898 such an apparatus could be used to visualize the solutions for potential flows past solid objects [28]. Indeed, assuming that the flow has a low Reynolds number and verifies the Stokes equations, then, owing to the scale separation between the in-plane (x, y) and transverse z dimensions, the velocity field $\vec{u}(x, y, z)$ is given by the set of equations

$$\vec{u} = \vec{U}(x, y) \frac{6z(h-z)}{h^2} \quad (2.10a)$$

$$\vec{U} \approx -\frac{h^2}{12\mu} \vec{\nabla} p, \quad \vec{\nabla} \cdot \vec{U} = 0. \quad (2.10b)$$

Hence, the velocity field is fully captured by the in-plane height averaged velocity field $\vec{U}(x, y)$ which derives from the potential $\Phi = -h^2/12\mu \cdot p$ proportional to the height-invariant hydrodynamic pressure p .

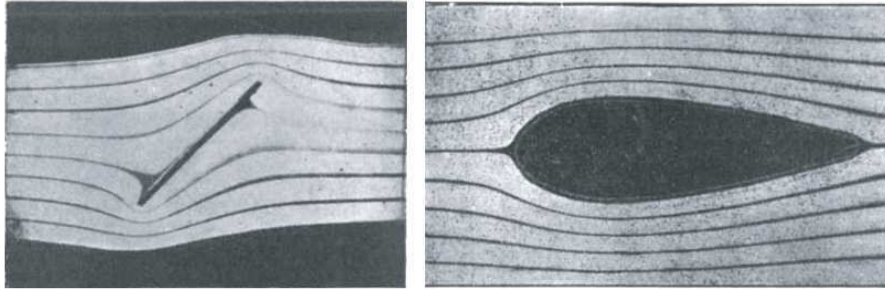


Figure 2.4: Two photographs of colored streamlines past a flat plate and an airfoil from the original publication by H. S. Hele-Shaw [28]

Hele-Shaw cells saw a renewal of academic interest with studies concerning viscous two-phase flows. In 1958, G. I. Taylor and P. G. Saffman (hereon TS) published a seminal paper [75] in which they investigate the penetration of a fluid into a Hele-Shaw cell filled with a second more viscous liquid. Their initial motivation came from oil recovery methods that consist in injecting a fluid into the porous oil reservoir. Taylor noticed the striking similarity between the Darcy law that models flows in such porous media and the equations (2.10). He understood two phase flows in a Hele-Shaw cell could serve as a model experiment and this study lead to the discovery of the now famous Saffman-Taylor instability [76].

While exploring viscous fingering, TS sometimes observed bubbles flowing in the Hele-Shaw cell, leading to the publication of “A note on the motion of bubbles in a Hele-Shaw

cell and porous medium” in 1959 [39]. Here and in the rest of the discussion below, the bubble size is large compared to the height of the Hele-Shaw cell such that the bubble is squeezed between the plates and has a flattened pancake shape, as sketched on Fig. 1.6 and discussed in Appendix B. The authors discuss the in-plane shape and the velocity \vec{U}_d a bubble should take when propelled in a Hele-Shaw cell by a flow of velocity \vec{U}_f of the outer fluid. In the framework of potential flow theory and ignoring interfacial tension, they find a family of possible solutions and select one they suspect in agreement with the principle of minimum dissipation: the bubble is circular and travels at twice the flow velocity $\vec{U}_d = 2\vec{U}_f$.

However, the authors were unable to derive the shape selection mechanism from physical grounds. Many studies tackled this issue and several explanations have been suggested. The most common is the interfacial tension of the bubble interface [77, 78], but others [79] applied *ad hoc* extremum principles to justify the results found by TS.

Here, we apply the minimum principle (P3) to recover the counter-intuitive bubble velocity $\vec{U}_d = 2\vec{U}_f$ and firmly identify interfacial tension as the shape selection mechanism. The tedious calculations lead to another counter-intuitive result: the stationary shape of the droplet does not minimize energy dissipation, it maximizes it.

2.2.1 The Taylor-Saffman analysis

In their analysis, TS model the bubble in the Hele-Shaw cell as a cylinder of arbitrary in-plane shape moving at a velocity \vec{U}_d in a Hele-Shaw cell with a far field velocity of the outer fluid \vec{U}_f as sketched in Fig. 2.5. Hence, they neglect the curved rim of the bubble and the lubrication films between the bubble and the cell walls.

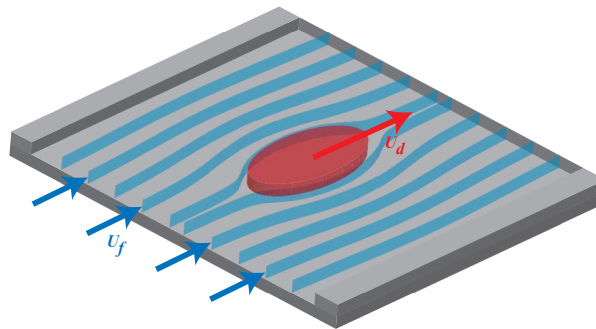


Figure 2.5: 3D sketch of the Taylor-Saffman model of a bubble moving in a Hele-Shaw cell.

Implicitly, they are searching for stationary solutions since they do not consider variations in the velocity of bubble. From the Hele-Shaw equations, they conclude that the velocity field \vec{U} is potential and define the velocity potential $\Phi(x, y)$ and the stream function

$\Psi(x, y)$

$$U_x = \frac{\partial \Phi}{\partial x} = \frac{\partial \Psi}{\partial y} \text{ and } U_y = \frac{\partial \Phi}{\partial y} = -\frac{\partial \Psi}{\partial x} \quad (2.11)$$

which both verify Laplace equations $\Delta \Phi = \Delta \Psi = 0$.

The far-field boundary condition is a uniform flow $\vec{U} = U_f \vec{e}_x$ such that $\Phi \rightarrow U_f x$ and $\Psi \rightarrow U_f y$ as $\sqrt{x^2 + y^2} \rightarrow \infty$. For the boundary conditions at the surface of the bubble, they assume that the pressure inside the bubble is constant and neglect interfacial tension to apply this constant pressure to the outer fluid near the interface. Clearly, this violates the Laplace pressure jump but it could be valid if the pressure jump remains small compared to the viscous pressure drop along the bubble or if it is constant around the bubble. The condition of constant pressure leads to a constant velocity potential, $\Phi = 0$ for example. Also, they impose the normal velocity

$$\frac{\partial \Phi}{\partial n} = \frac{\partial \Psi}{\partial s} = U_d \vec{e}_x \cdot \vec{n} = U_d \frac{\partial y}{\partial s} \quad (2.12)$$

where (n, s) are the local normal and tangential coordinates near the interface. The projection of the bubble velocity $U_d \vec{e}_x \cdot \vec{n}$ is transformed by noting that $\vec{e}_x \cdot \vec{n} = \partial y / \partial s$. It follows an expression for the stream function along the surface of the bubble: $\Psi = U_d y$.

Illustrated on Fig. 2.6, the TS model becomes a 2D potential flow problem:

*What are the bubble shapes and velocities U_d
for which there exists a velocity potential Φ and a stream function Ψ
that verify the boundary conditions*

$\Psi = U_d \cdot y$ at the interface where $\Phi = 0$
and
 $\Psi = U_f y$ at infinity ?

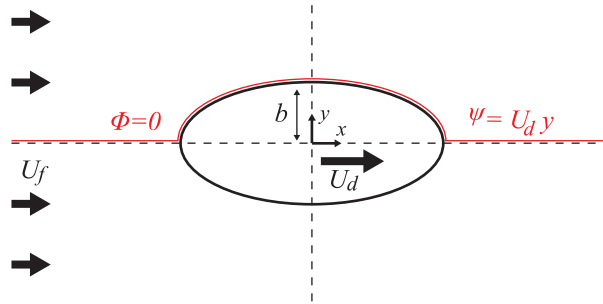


Figure 2.6: Sketch of 2D potential flow problem for the Taylor-Saffman problem and definition of the necessary variables.

TS obtain a family of solutions parametrized by the half-width $0 < b < \infty$ and velocity $U_f < U_d < \infty$ of the bubble. Given values for (b, U_d) , the problem above selects the ellipse

$$\frac{x^2}{b^2(U_d/U_f - 1)^2} + \frac{y^2}{b^2} = 1 \quad (2.13)$$

of axis ratio $a/b = U_d/U_f - 1$ as the shape of the bubble. It is noteworthy that there are only solutions for bubbles traveling faster than the fluid.

Amongst these solutions, one stands out: for $\vec{U}_d = 2\vec{U}_f$, the bubble is circular. The authors select this particular solution because it minimizes the quantity $b \cdot U_d$ but they are unable to find a physical basis to this minimization, while briefly recalling the principle of minimum dissipation:

The product “ $b \cdot U_d$ ” of the velocity of the bubble and half its maximum width does not have a clear physical significance, although it may be identified intuitively with the rate at which fluid is pushed aside by the bubble. We have in fact been unable to place the hypothesis on a sound physical basis (attempts to relate it to a minimum rate of energy dissipation fail).

Excerpt from *A note on the motion of bubbles in a Hele-Shaw cell and porous medium* by G.I. Taylor and P.G Saffman [39].

Another property of the solution $\vec{U}_d = 2\vec{U}_f$ is that the circular bubble has a constant curvature such that the Laplace pressure jump across the interface is also constant, in agreement with the *ad hoc* boundary condition of a constant outer pressure along the interface. As a result, the solution of a circular drop traveling at twice the fluid velocity is the only exact solution still valid when interfacial tension is taken into account. It is also the one that minimizes surface energy.

In the end, the circular bubble appears to be singular both in terms of energy dissipation and surface energy. In the following sections, we show that the minimum principle (P3-bis) provides a way to identify which mechanism truly selects the bubble shape and obtain new insights on the physical mechanisms at play.

2.2.2 Applying the minimum principle

The goal of this work is to apply the minimum principle (P3-bis) in order to identify the stationary state of a drop flowing in a Hele-Shaw cell. The stationary state here refers to a state in which the shape of the drop is unchanged as it travels through the Hele-Shaw cell.

As explained previously, the minimum principle cannot directly identify a stationary state. Consequently, we consider a family of shapes which we believe includes the stationary shape and apply the minimum principle to each configuration. If for one of these configurations, the result of the minimum principle is a flow field which does not deform the droplet, then it is a stationary state. Last, we verify its stability.

The original analysis by TS has selected the family of elliptic drops (or bubbles) as the family of shapes that have a stationary potential flow solution for the motion of the drop. Hence, we consider elliptic droplets (viscosity μ_1), of major axis a and minor axis b , moving at a velocity \vec{U}_d in an outer flow (viscosity μ_2) of far-field velocity $U_f \vec{e}_x$ and ignore the relationships found by TS. In other words, a/b and \vec{U}_d can take any arbitrary

values. In addition, we allow the droplet to deform into another ellipse by elongation or contraction at a rate $\dot{a} = da/dt$.

Last, instead of trying to minimize the Lagrangian (2.6) over all possible velocity fields, we restrain the minimization domain to incompressible potential flows which are known to partially verify the equations motion for viscous two phase flows in Hele-Shaw cells. For each elliptic drop geometry, this procedure reduces the space of unknowns to the droplet velocity U_d and elongation rate \dot{a} . A stationary solution is then one for which $\dot{a} = 0$.

A bit of geometry

The elliptic shape of the drop dictates the use of inconvenient elliptic coordinates. We recall briefly some generalities concerning ellipse and the associated coordinate systems.

An ellipse of major axis a and minor axis b can also be described by its focal distance $c = \sqrt{a^2 - b^2}$, its eccentricity $e = c/a$ or its aspect ratio $\lambda = b/a$. It has a surface area $S = \pi ab$ and a perimeter $P = 4aE(e)$ where $E(x)$ is the complete elliptic integral of the second kind [80]. Elliptic coordinates (ξ, η) are defined from the cartesian coordinates (x, y) as

$$x = c \cosh \xi \cos \eta \quad (2.14a)$$

$$y = c \sinh \xi \sin \eta . \quad (2.14b)$$

A representation is given in Fig. 2.7. The family of curves parametrized by $\xi = \text{cst}$ is the family of ellipse of focal distance c . Amongst those, we select the ellipse of major and minor axis a and b by taking $\xi^0 = 1/2 \cdot (a + b)(a - b)$. Last, the complex plane $z = x + iy$ transforms to the elliptic complex plane $\zeta = \xi + i\eta$ via the equation $z = c \cosh \zeta$.

In this coordinate system, the base vectors \vec{e}_ξ and \vec{e}_η are orthogonal since the lines of iso- ξ and iso- η are orthogonal. However, they are not normal and the metrics for ξ and η are equal:

$$g_\xi = g_\eta = c \sqrt{\sinh^2 \xi + \sin^2 \eta} \quad (2.15)$$

As a result, surface elements are given by

$$dxdy = g_\xi g_\eta d\xi d\eta . \quad (2.16)$$

Potential flow past a moving and deforming elliptic cylinder

The potential flows around a static elliptic cylinder or due to a moving elliptic cylinder can be found in the litterature [81, 82]. However, the flow created by an elliptic drop elongating at a rate \dot{a} has not yet been treated to our knowledge.

To obtain this flow, we consider an elliptic drop of given dimensions (a, b) that it is continuously elongating at a rate \dot{a} while keeping its volume V constant. As discussed in Chapter 1, the volume of a large pancake is well approximated by $V = h \cdot S$, the product between the height of the Hele-Shaw cell and the in-plane surface area S of the drop. Since h is constant, conservation of volume implies conservation of S . Hence, the drop

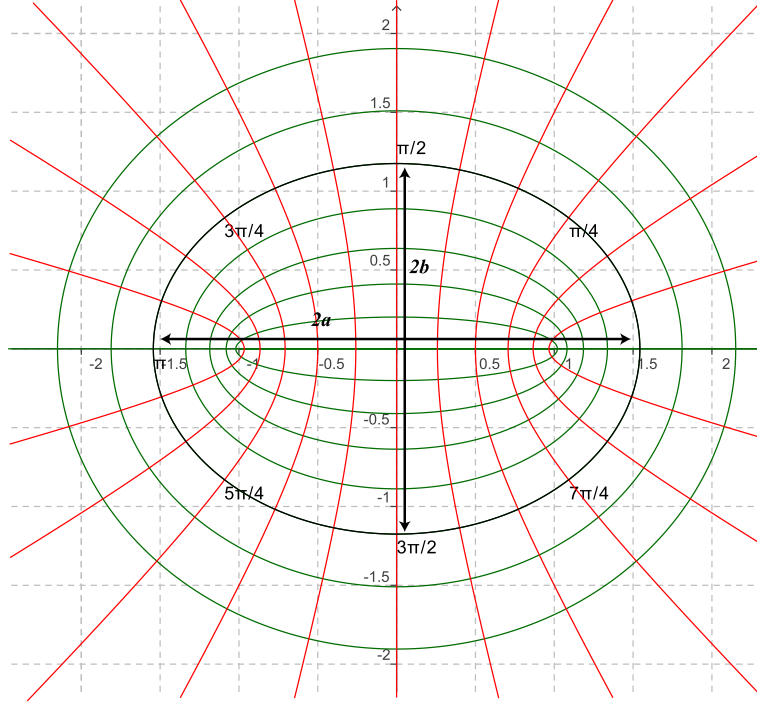


Figure 2.7: Definition of the elliptic coordinates. The green lines are lines of iso- ξ and red lines are iso- η . Lines of iso- ξ are all the centered ellipses of focal distance c . The black one is the ellipse of parameters a and b , which is found by taking $\xi = \xi^0 = 1/2 \log(a+b)/(a-b)$.

is elongating while keeping constant the product ab . This defines a unique path amongst the parameter space (a, b) that the droplet follows as it deforms. It is then possible to identify the necessary flow field around the drop to stay on that particular path of shapes, as detailed in Appendix A.

Using elliptic coordinates, it is possible to express the complex velocity potential w for the flow around a moving and deforming elliptic drop. We distinguish the inner flow of potential w_1 and the outer flow of potential w_2 :

$$w_1(U_f, U_d, \dot{a}) = 0 + U_d c \cosh \zeta + \frac{\dot{a}}{2} b e^{2(\zeta - \xi_0)} \quad (2.17a)$$

$$w_2(U_f, U_d, \dot{a}) = \underbrace{U_f(a+b) \cosh(\zeta - \xi_0)}_{\text{flow past a static cylinder}} - \underbrace{U_d b e^{-(\zeta - \xi_0)}}_{\text{flow due to a moving cylinder}} - \underbrace{\frac{\dot{a}}{2} b e^{-2(\zeta - \xi_0)}}_{\text{flow due to the elongations}}. \quad (2.17b)$$

The flow is simply the linear superposition of the flow past a static cylinder, the flow due to a moving cylinder and the flow due to the elongation of the cylinder. Hence, the potential has three parameters: the outer velocity U_d , the droplet velocity U_f and the elongation rate \dot{a} .

Taking the real and imaginary parts of the complex potential $w = \Phi + i\Psi$, we obtain the corresponding velocity potentials Φ and streamfunction Ψ for the inner and outer flows:

$$\Phi_1(U_f, U_d, \dot{a}) = U_d c \cosh \xi \cos \eta + \frac{\dot{a}}{2} b e^{2(\xi - \xi_0)} \cos 2\eta \quad (2.18a)$$

$$\Phi_2(U_f, U_d, \dot{a}) = U_f c \cosh \xi \cos \eta - (U_d - U_f) b \sqrt{\frac{a+b}{a-b}} e^{-\xi} \cos \eta - \frac{\dot{a}}{2} b e^{-2(\xi - \xi_0)} \cos 2\eta \quad (2.18b)$$

and

$$\Psi_1(U_f, U_d, \dot{a}) = U_d c \sinh \xi \sin \eta - \frac{\dot{a}}{2} b e^{2(\xi - \xi_0)} \sin 2\eta \quad (2.19a)$$

$$\Psi_2(U_f, U_d, \dot{a}) = U_f c \sinh \xi \sin \eta + (U_d - U_f) b \sqrt{\frac{a+b}{a-b}} e^{-\xi} \sin \eta + \frac{\dot{a}}{2} b e^{-2(\xi - \xi_0)} \sin 2\eta \quad (2.19b)$$

Plotting lines of constant streamfunction Ψ yields the streamlines of the flow, as illustrated on Fig. 2.8. We recover the known flow characteristics for the static and moving circular cylinder but in elliptic coordinates. The flow past a moving cylinder is the superposition of a uniform flow and a dipole while the flow due to a moving cylinder is a dipole. In addition, we find that the flow due to the elliptic drop elongating into another ellipse of identical surface area is a quadrupole. For details on this last flow, refer to Appendix A.

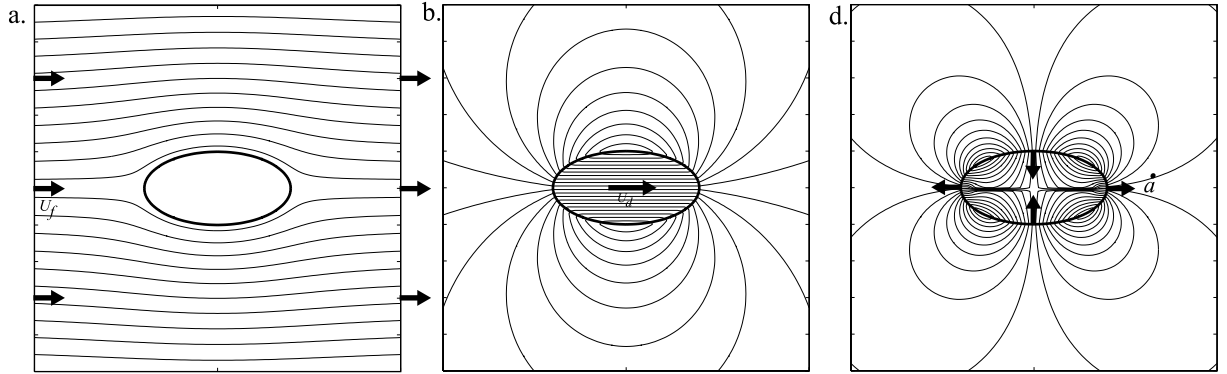


Figure 2.8: Streamlines for a) the flow past a static elliptic drop; b) the flow due to a moving elliptic drop and c) the flow due to an elongating elliptic drop. The drop dimensions are always $a = 2$ and $b = 1$.

The complex velocity in the z -complex plane, $v = U_x + iU_y$, is found by applying the classical formula

$$v = \frac{dw}{dz} = \frac{dw}{d\zeta} \cdot \frac{d\zeta}{dz}$$

which yields

$$v_1(U_f, U_d, \dot{a}) = \frac{U_d b \sinh(\zeta) - \dot{a} b e^{2(\zeta - \xi_0)}}{c \sinh \zeta} \quad (2.20a)$$

$$v_2(U_f, U_d, \dot{a}) = \frac{U_f(a+b) \sinh(\zeta - \xi_0) + U_d b e^{-(\zeta - \xi_0)} + \dot{a} b e^{-2(\zeta - \xi_0)}}{c \sinh \zeta} . \quad (2.20b)$$

Recalling the Hele-Shaw equations (2.10), the pressure field is obtained from the velocity potential Φ to a constant:

$$p_1(U_f, U_d, \dot{a}) - \text{cst} = -\frac{12\mu_1}{h^2} \left(U_d c \cosh \xi \cos \eta + \frac{\dot{a}}{2} b e^{-2(\xi-\xi_0)} \cos 2\eta \right) \quad (2.21a)$$

$$p_2(U_f, U_d, \dot{a}) - \text{cst} = -\frac{12\mu_2}{h^2} \left(U_f c \cosh \xi \cos \eta - (U_d - U_f) b e^{\xi_0-\xi} \cos \eta - \frac{\dot{a}}{2} b e^{-2(\xi-\xi_0)} \cos 2\eta \right) . \quad (2.21b)$$

Estimating the Lagrangian of the flow

Finding the flow that verifies the principle of minimum dissipation of energy (P3-bis) is equivalent to minimizing the augmented Lagrangian (2.6). The terms concerning incompressibility of the flow are here obsolete since all considered flows are potential and divergence free. Remains the dissipation function \mathcal{D} , the rate of change of surface energy $\dot{\mathcal{E}}_s$ and the term imposing the far-field boundary condition $\mathcal{B}_f = -\int_{\mathcal{B}_\infty} \lambda(\vec{u} - \vec{u}_\infty) \cdot \vec{n} dS$.

The dissipation function \mathcal{D}

In the present analysis, we keep the TS assumption that the flow is fully captured by the Hele-Shaw solutions (2.17a). This assumption neglects the lubrication films between the droplet and the channel walls (top and bottom) and the boundary layer near the interface where the flow becomes fully 3D. Contributions from these two regions to the dissipation are for now omitted and will be treated later in Chapter 3.

Anyway, the dissipation function has contributions from the inner and outer flows:

$$\mathcal{D} = \frac{1}{2} \int_{\Omega_1} \mu_1 (\nabla \vec{u})^2 d\Omega_1 + \frac{1}{2} \int_{\Omega_2} \mu_2 (\nabla \vec{u})^2 d\Omega_2 . \quad (2.22)$$

In a Hele-Shaw cell, the shear is concentrated in the local transverse Poiseuille flows (2.10) because of the scale separation between the in-plane and transverse dimensions. Therefore, the velocity gradient simplifies to

$$\vec{\nabla} \vec{u} \approx \frac{6(h-2z)}{h^2} (U_x e_x \otimes e_x + U_y e_y \otimes e_y) , \quad (2.23)$$

where we used the notation $\vec{U} = U_x \vec{e}_x + U_y \vec{e}_y$.

By injecting (2.23) into the dissipation function \mathcal{D} , it gives

$$\begin{aligned} \mathcal{D}_1 &= \mu_1 \int_0^h \frac{36(h-2z)^2}{h^4} dz \int U_1^2 dx dy & \text{and} & & \mathcal{D}_2 &= \mu_2 \int_0^h \frac{36(h-2z)^2}{h^4} dz \int U_2^2 dx dy \\ &= \frac{6\mu_1}{h} \int_\xi \int_\eta U_1^2 g_\xi g_\eta d\xi d\eta & (2.24) & & &= \frac{6\mu_2}{h} \int_\xi \int_\eta U_2^2 g_\xi g_\eta d\xi d\eta . & (2.25) \end{aligned}$$

Here, we need to distinguish between the inner and outer flows because of the different viscosities μ_1 and μ_2 .

To compute the dissipation functions \mathcal{D}_1 and \mathcal{D}_2 , we only need an expression for U^2 , the square of the in-plane velocity field both for the inner and outer flows. U^2 is easily obtained using the complex velocity field v from equations (2.20) since $U^2 = v \cdot \bar{v}$, where $\bar{}$ represents the complex conjugate. We detail the computations for the outer flow only (subscripts $_2$) and state the result for the inner field flow (subscript $_1$).

Recalling the expression (2.20a) yields

$$U_2^2 = \frac{U_f(a+b) \sinh(\zeta - \xi_0) + U_d b e^{-(\zeta - \xi_0)} + \dot{a} b e^{-2(\zeta - \xi_0)}}{c \sinh \zeta} \times \frac{U_f(a+b) \sinh(\bar{\zeta} - \xi_0) + U_d b e^{-(\bar{\zeta} - \xi_0)} + \dot{a} b e^{-2(\bar{\zeta} - \xi_0)}}{c \sinh \bar{\zeta}} \quad (2.26)$$

and since the denominator $c \sinh \zeta \cdot c \sinh \bar{\zeta} = g_\xi g_\eta$, we have

$$g_\xi g_\eta U_2^2 = (U_f(a+b) \sinh(\zeta - \xi_0) + U_d b e^{-(\zeta - \xi_0)} + \dot{a} b e^{-2(\zeta - \xi_0)}) \times (U_f(a+b) \sinh(\bar{\zeta} - \xi_0) + U_d b e^{-(\bar{\zeta} - \xi_0)} + \dot{a} b e^{-2(\bar{\zeta} - \xi_0)}) . \quad (2.27)$$

Expanding this expression, we obtain

$$\begin{aligned} g_\xi g_\eta U_2^2 = & U_f^2(a+b)^2 \sinh^2(\xi - \xi_0) + U_d(U_d - U_f)b^2 e^{-2(\xi - \xi_0)} - U_f U_d a b e^{-2(\xi - \xi_0)} \\ & + U_f^2(a+b)^2 \sin^2 \eta \\ & + \dot{a}^2 b^2 e^{-4(\xi - \xi_0)} \\ & + \text{terms proportional to } \sin \eta, \cos \eta, \sin 2\eta \text{ or } \cos 2\eta \end{aligned} \quad (2.28)$$

To estimate the integral in (2.24), we start by integrating over a finite domain around the elliptic drop bounded by the ellipse $\xi = \xi_1$ to later on assume $\xi_1 \rightarrow \infty$. Since all periodic terms in $\cos \eta$, $\sin \eta$, etc... have no contribution to the overall integral, we obtain

$$\begin{aligned} \int_0^{2\pi} \int_{\xi_0}^{\xi_1} g_\xi g_\eta U_2^2 d\xi d\eta = & \frac{\pi}{4} U_f^2 c^2 e^{2\xi_1} - \frac{\pi}{4} U_f^2 \frac{(a+b)^3}{(a-b)} e^{-2\xi_1} + \pi U_d(U_d - U_f)b^2(1 - e^{-2(\xi_1 - \xi_0)}) \\ & - \pi U_f U_d a b (1 - e^{-2(\xi_1 - \xi_0)}) + \frac{\pi}{2} b^2 \dot{a}^2 (1 - e^{-4(\xi_1 - \xi_0)}) \end{aligned} \quad (2.29)$$

which simplifies to

$$\int_0^{2\pi} \int_{\xi_0}^{\xi_1} g_\xi g_\eta U_2^2 d\xi d\eta = \frac{\pi}{4} U_f^2 c^2 e^{2\xi_1} + \pi U_d(U_d - U_f)b^2 - \pi U_f U_d a b + \frac{\pi}{2} b^2 \dot{a}^2 \quad (2.30)$$

once all terms vanishing as $\xi_1 \rightarrow \infty$ are neglected.

Finally, by summing the contributions from the inner and outer flows \mathcal{D}_1 and \mathcal{D}_2 , we obtain

$$\begin{aligned} \mathcal{D} = & \frac{6\pi\mu_1}{h} \left(U_d^2 a b + \frac{1}{2} \dot{a}^2 b^2 \frac{4ab}{(a+b)^2} \right) + \\ & \frac{6\pi\mu_2}{h} \left(\frac{1}{4} U_f^2 c^2 e^{2\xi_1} + (U_d - U_f)^2 b^2 - U_f^2 b^2 - U_f U_d b(a-b) + \frac{1}{2} \dot{a}^2 b^2 \right) . \end{aligned} \quad (2.31)$$

The rate of change of surface energy $\dot{\mathcal{E}}_\gamma$

The translational component of the motion of the droplet does not modify the surface energy since it does not deform the interface. However, the elongation or contraction of the drop modifies its geometry. The overall surface \mathcal{S} of the pancake drop is well approximated by the formula

$$\mathcal{S} = 2 \cdot \pi ab + \frac{\pi}{2} h \cdot P \quad (2.32)$$

where P is the perimeter of the in-plane ellipse. Conservation of the volume implies that the in-plane surface area πab is kept constant throughout the motion of the drop. Hence, only the rate of change of the perimeter of the ellipse dP/dt contributes to the rate of change of the surface area $\dot{\mathcal{S}}$. We obtain

$$\dot{\mathcal{E}}_\gamma = \gamma \frac{\pi}{2} h \frac{dP}{dt} \quad (2.33)$$

The perimeter of an ellipse is equal to

$$\begin{aligned} P(\lambda, S) = & 4\sqrt{\frac{S}{\pi}} \frac{1}{\sqrt{\lambda}} E(\sqrt{1-\lambda^2}) \text{ for elongated ellipses } (\lambda < 1) \\ & 4\sqrt{\frac{S}{\pi}} \sqrt{\lambda} E(\sqrt{1-\frac{1}{\lambda^2}}) \text{ for flattened ellipses } (\lambda \geq 1) \end{aligned} \quad (2.34)$$

where E is the complete elliptic integral of the second kind.

The variables S and λ are separated and we can write the perimeter as

$$P(\lambda, S) = 4\sqrt{\frac{S}{\pi}} \cdot f(\lambda) \quad (2.35)$$

where the function $f(\lambda)$ is

$$\begin{aligned} f(\lambda) = & \frac{1}{\sqrt{\lambda}} E(\sqrt{1-\lambda^2}) \text{ for elongated ellipses } (\lambda < 1) \\ & \sqrt{\lambda} E(\sqrt{1-\frac{1}{\lambda^2}}) \text{ for flattened ellipses } (\lambda \geq 1) \end{aligned}$$

Figure 2.9 plots $f(\lambda)$. It shows that the circle ($\lambda = 1$, $\sqrt{S/\pi} = R$) has indeed the minimum perimeter of all ellipses and $f = \pi/2$ such that we recover $P = 2\pi R$.

Since the droplet is deforming while keeping its in-plane surface area S constant, we may express

$$\frac{dP}{dt} = 4\sqrt{\frac{S}{\pi}} \frac{df}{d\lambda} \dot{\lambda} \quad (2.36)$$

to finally obtain a simple expression for the rate of change of surface energy:

$$\dot{\mathcal{E}}_\gamma = \gamma 2\pi h \frac{df}{d\lambda} \cdot \left(\sqrt{\frac{S}{\pi}} \dot{\lambda} \right) \quad (2.37)$$

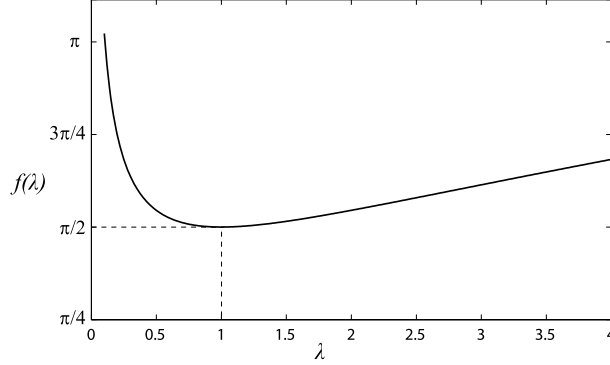


Figure 2.9: Plot of the $f(\lambda)$, highlighting the minimum perimeter of the circular case $\lambda = 1$

Effect of the far-field boundary condition \mathcal{B}_f

In the case of a Hele-Shaw cell, \mathcal{B}_f simplifies to

$$\mathcal{B}_f = h \int_0^{2\pi} p(\xi_1, \eta) \left[\vec{U}(\xi_1, \eta) - \vec{U}_f \right] \cdot \vec{n} g_\eta d\eta \quad (2.38)$$

due to the same scale separation argument used to express the dissipation function \mathcal{D} .

Although the velocity field \vec{U}_2 verifies the asymptotic far-field boundary conditions, \mathcal{B}_f is not equal to 0 because the far-field boundary conditions are never exactly met in the domain. The perturbations of velocity field due to the presence of the drop decay away from the drop but do not strictly vanish. In fact, they couple with the linear term $U_d c \cosh \xi \cos \eta$ of the pressure field to generate a non vanishing contribution in \mathcal{B}_f as $\xi \rightarrow \infty$. We find that this contribution is

$$\mathcal{B}_f = -\frac{6\pi\mu_2}{h} U_f (U_d - U_f) b(a + b) \quad (2.39)$$

The complete Lagrangian \mathcal{L}

Finally, the Lagrangian $\mathcal{L} = \mathcal{D} + \dot{\mathcal{E}}_\gamma + \mathcal{B}_f$ is equal to

$$\begin{aligned} \mathcal{L} = & \frac{6\pi\mu_1}{h} \left(U_d^2 ab + \frac{1}{2} \dot{a}^2 b^2 \frac{4ab}{(a+b)^2} \right) \\ & + \frac{6\pi\mu_2}{h} \left(\frac{1}{4} U_f^2 c^2 e^{2\xi_1} - U_f^2 (ab - b^2) - 2U_f U_d (ab + b^2) + U_d^2 b^2 + \frac{1}{2} b^2 \dot{a}^2 \right) \\ & + \gamma 2\pi h \frac{df}{d\lambda} \cdot \left(\sqrt{\frac{S}{\pi}} \dot{\lambda} \right). \end{aligned} \quad (2.40)$$

The term $U_f^2 c^2 e^{2\xi_1} / 4$ corresponds to the dissipation due to the uniform outer flow of velocity U_f in the entire domain. It depends neither on the droplet velocity U_d , nor on the deformation rate \dot{a} , nor on the geometry of the drop a and b . Hence, it is a constant which we will forget in the rest of the discussion.

Furthermore, we can define a non-dimensional Lagrangian L as $L = \mathcal{L}/(6\pi ab\mu_2 U_f^2/h)$:

$$L = \frac{\mu_1}{\mu_2} \left(U^2 + \frac{1}{8} \dot{\Lambda}^2 \frac{4}{\lambda^2(1+\lambda)^2} \right) + \left(U^2 \lambda - 2(1+\lambda)U - 1 + \lambda + \frac{1}{8} \dot{\Lambda}^2 \frac{1}{\lambda^2} \right) + \frac{4}{k^2 \text{Ca}} \frac{df}{d\lambda} \cdot \dot{\Lambda} \quad (2.41)$$

where $U = U_d/U_f$ is the relative velocity of the droplet compared to the outer flow, $\dot{\Lambda} = \sqrt{S/\pi} \dot{\lambda}/U_f$ is the elongation velocity relative to the outer flow velocity, $k = \sqrt{12S}/h$ is the transverse aspect ratio of the drop and $\text{Ca}_f = \mu_2 U_f/\gamma$ the capillary number based on the outer flow velocity U_f .

2.2.3 Comparison with the Taylor-Saffman results

Taylor and Saffman considered a bubble that is not allowed to deform, meaning that $\mu_1 = 0$ and $\dot{\Lambda} = 0$. In this case, the Lagrangian simplifies to

$$L = U^2 \lambda - 2(1+\lambda)U - 1 + \lambda. \quad (2.42)$$

We begin by recovering the relationship between the bubble velocity U and its aspect ratio λ . According to the principle of minimum dissipation (P3-bis), for any given λ , the bubble velocity that satisfies the Stokes equations and boundary conditions is the one that minimizes L with respect to U . Here, we emphasize the fact that solutions are minimum of the Lagrangian in terms of velocity field. Hence, we have

$$\frac{\partial L}{\partial U} = 2\lambda U - 2(1+\lambda) = 0 \quad (2.43)$$

such that the velocity of an elliptic bubble is

$$U(\lambda) = \frac{1+\lambda}{\lambda}. \quad (2.44)$$

This formula is identical to the one found by TS. For a circular bubble $\lambda = 1$, we obtain the classical result $U = 2$. Elongated bubbles ($\lambda < 1$) are faster while flattened ones ($\lambda > 1$) are slower.

Taylor and Saffman suggest that the solution ($U = 2, \lambda = 1$) is the one that minimizes energy dissipation amongst all possible flow fields and bubble shapes, and in particular amongst the family of solutions given by Eq. (2.44). Our analysis shows quite the contrary. In the (U, λ) phase space, the position ($U = 2, \lambda = 1$) is a saddle point of the Lagrangian and not a global minimum as shown on Fig. 2.10.a. In addition, along the particular trajectory $(U, 1/(U-1))$ defined by Eq. (2.44) which corresponds to the Taylor-Saffman family of solutions, $U = 2$ actually corresponds to a maximum of the Lagrangian as it can be seen on the plot of Fig. 2.10.b. This result is in contradiction with the intuition of TS.

This is not surprising since the principle of minimum dissipation selects a velocity field for a fixed shape of the domain boundaries. Hence, trying to apply this principle to find an appropriate shape of the drop does not stand on physical grounds. To correctly harvest

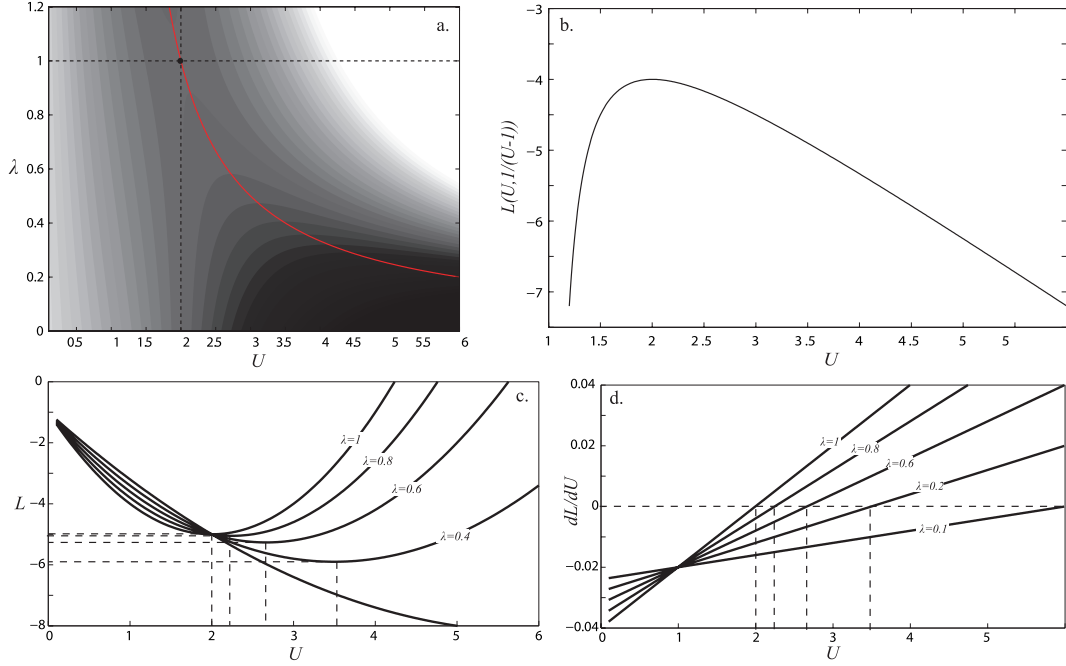


Figure 2.10: **a)** Plot of the non-dimensional Lagrangian L in the phase space (U, λ) . The value increases from dark to light regions. **b)** Plot of L along the particular trajectory $(U, 1/(U-1))$ of the phase space (U, λ) , in red in **a.** This trajectory corresponds to the TS family of solutions. **c)** Plots of L as a function of U for fixed droplet geometries $\lambda = 0.4, 0.6, 0.8$ and 1 . **d.)** Derivative of the L with respect to U for fixed droplet geometries $\lambda = 0.4, 0.6, 0.8$ and 1 .

information from the Lagrangian, one must assume a particular geometry (here fix λ) and look at the variations of L with respect to the parameters of the velocity field only, as illustrated on Fig. 2.10.c-d. For any given aspect ratio λ , we find that there exists a unique minimum of the Lagrangian in terms of bubble velocity, in agreement with Eq. (2.44).

2.2.4 The shape selection mechanism

A critical ingredient is missing in the reduced Lagrangian (2.43): bubble deformations. If we imagine that we were able to release a bubble of some geometry into the flow, say an elongated ellipse with $\lambda = 0.5$, then the flow would advect the bubble at some velocity U but also possibly deform the bubble progressively. An interesting initial shape is one that would not deform: it defines the stationary state of both the bubble's velocity and shape. Here, we imagine such an experiment. We assume the initial shape is one of the elliptic shapes identified as a possible solution by Taylor and Saffman and make the strong hypothesis that, as it deforms, the bubble keeps an elliptic shape.

This last assumption simplifies considerably the shape parameter space and is necessary for the problem to be tractable analytically. In practice, it is only a valid approximation

for nearly circular ellipses.

In this case, the time evolution of the bubble is fully captured by the Lagrangian (2.41), which simplifies to

$$L = \left(U^2 \lambda - 2(1 + \lambda)U - 1 + \lambda + \frac{1}{8} \dot{\Lambda}^2 \frac{1}{\lambda^2} \right) + \frac{4}{k^2 \text{Ca}} \frac{df}{d\lambda} \cdot \dot{\Lambda} \quad (2.45)$$

when $\mu_1 = 0$. This Lagrangian has two variables U and $\dot{\Lambda}$. The shape of the bubble (λ, k) and the flow properties Ca are parameters.

The stationary state, as defined above, is then obtained by finding the shape which does not deform. In other words, we are looking for (λ, k) such that the Lagrangian (2.45) has a minimum for $\dot{\Lambda} = 0$.

For example, a possible set of parameters is $(\lambda = 0.5, k = 0.5, \text{Ca} = 1)$. In this case, $df/d\lambda(\lambda = 0.5) = -0.8$ and the Lagrangian is

$$L = 0.5U^2 - 3U - 0.5 + 0.5\dot{\Lambda}^2 - 5\dot{\Lambda} \quad (2.46)$$

as plotted on Fig. 2.11.

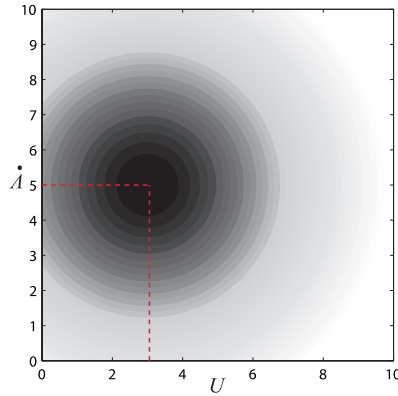


Figure 2.11: Lagrangian (2.46) plotted in the velocity field phase space $(U, \dot{\Lambda})$.

To find how this particular ellipse will move and deform in the flow, we need to find the minimum of L in the phase space of the velocity field $(U, \dot{\Lambda})$. The partial derivatives of L should both be zero at the minimum. Since

$$\begin{aligned} \frac{\partial L}{\partial U} &= U - 3 \\ \frac{\partial L}{\partial \dot{\Lambda}} &= \dot{\Lambda} - 5, \end{aligned}$$

we obtain that the bubble will move at $U = 3$ and deform towards the circular shape at an instantaneous elongational velocity $\dot{\Lambda} = 5$. Therefore, this particular shape is not stationary.

In the general case, the partial derivatives of the Lagrangian (2.45) are

$$\frac{\partial L}{\partial U} = 2\lambda U - 2(1 + \lambda) \quad (2.47a)$$

$$\frac{\partial L}{\partial \dot{\lambda}} = \frac{1}{4\lambda^2} \dot{\lambda} + \frac{4}{k^2 \text{Ca}} \frac{df}{d\lambda} \quad (2.47b)$$

such that the flow solution is

$$U = \frac{1 + \lambda}{\lambda} \quad (2.48a)$$

$$\dot{\lambda} = - \frac{16\lambda^2}{k^2 \text{Ca}} \frac{df}{d\lambda} \quad (2.48b)$$

These equations describe a path in the velocity field phase space $(U, \dot{\lambda})$ along which the system travels as the droplet is advect by the flow and deforms due to surface tension. This path is plotted on Fig. 2.12. For $\lambda > 1$, the path is located in the half space $\dot{\lambda} < 0$ while for $\lambda < 1$, it is the contrary. Since $\dot{\lambda}$ is proportional to $d\lambda/dt$, the system necessarily travels in the directions indicated by the red arrows along the path. It shows that the system always converges to $(U = 2, \lambda = 1)$ which is the circular drop configuration.

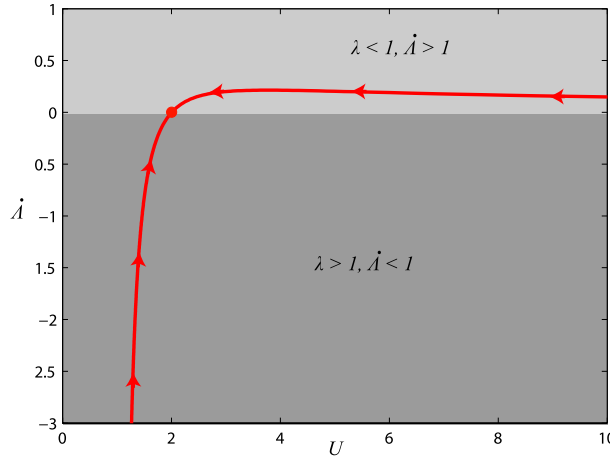


Figure 2.12: Plot (red curve) of the path defined by equations (2.48) in the velocity phase space $(U, \dot{\lambda})$.

Remarkably, the stationary state $(U = 2, \lambda = 1)$ is independent of the capillary number Ca and thereby of the interfacial tension γ . Even though interfacial tension is the driving mechanism, the system converges to the same state whatever the value of γ , no matter how small. In other words, the slightest amount of interfacial tension is sufficient to drive the bubble towards the circular shape configuration identified by Taylor and Saffman. The value of Ca will only select the time required for the relaxation to occur.

2.3 Summary and discussion of Chapter 2

We expressed a minimum principle for viscous two phase flows (P3-bis). Its Lagrangian formulation (2.6) was shown to be equivalent to the Stokes equations for two phase flows. When applied to the flow of a droplet in a Hele-Shaw cell, it demonstrated that

- for any shape of the drop, there is a minimum which dictates both how the drop deforms and translates;
- the circular bubble moving at twice the outer flow velocity is **not a minimum of energy dissipation** amongst all possible solutions;
- the circular bubble moving at twice the outer flow velocity is **a maximum of energy dissipation** amongst the family of solutions identified by Taylor and Saffman;
- interfacial tension is the mechanism that selects the bubble shape;
- the slightest amount of interfacial tension drives the bubble shape to deform into a circle.

However, the Taylor-Saffman solution has never been observed experimentally. In fact, studies on the motion of a bubble or a drop in Hele-Shaw cell [83, 84, 85] revealed a complete zoology of bubble shapes and measured bubble velocities either smaller or equal to the outer flow velocity.

A suggested explanation is the presence of lubricating thin films between the bubble and the walls of the Hele-Shaw cell, or a contact line along which the bubble interface intersects the walls. Indeed, Bretherton [86] in the first case and Tanner [87] in the second showed that these effects increase significantly the drag of a bubble moving in a capillary tube. Similar effects were shown to occur in a Hele-Shaw cell [51, 88, 89] and numerical studies [78, 77] revealed that they are sufficient to explain for the reduced bubble velocity. The surfactants used in the experiments to enhance the wetting of the outer fluid and to prevent droplet coalescence are also known to rigidify the interface [90, 91, 89] and can cause a significant increase in the drag of the droplet.

In Chapter 3, we briefly discuss the effects. Nonetheless, despite considerable efforts to model these secondary effects of interfacial tension, it is still impossible to predict the velocity of a bubble in a Hele-Shaw cell, and consequently in a 2D microchannel.

Chapter 3

Droplet trajectories in a Hele-Shaw cell with confinement gradients

“Liebnitz, offensé des soupçons que les Anglais avaient jeté sur ses travaux, leur proposa, comme une espèce de défi, le problème des trajectoires.”

D’Alembert, Eloge de Bernouilli, p. 24.

In the first section of this chapter, we rigorously derive an energy production-dissipation balance for open and confined viscous two phase flows from the minimum principle of Chapter 1. This energy balance is simpler to use than the minimum principle. However, it only identifies a family of potential solutions for the flow fields and a selection criterion is required to select the solution.

We then derive an equation for the motion and trajectory of a droplet pushed by an outer flow in a Hele-Shaw cell with confinement gradients. The predictions from the model are compared to the droplet trajectories measured experimentally in deformed Hele-Shaw cells.

Last, we reinterpret the terms that enter the energy production-dissipation balance as expressions of the work of different forces that apply onto the droplet. In particular, we identify the force due to the confinement gradient and the drag of the moving droplet which leads us to discuss the velocity of the droplet.

3.1 An energy production-dissipation balance

From the minimum principle (P3-bis) and its Lagrangian formulation (2.4), it is possible to derive an energy production-dissipation balance for viscous two phase flows from the minimum principle, analogous to the conservation of energy in closed conservative system. A similar balance was formulated and applied by Maxworthy [83] to the buoyant rise of a

bubble in a Hele-Shaw cell. Here, we provide a rigorous demonstration and include changes in the surface energy \mathcal{E}_γ of the interface.

Let's recall the Gateaux derivatives of the Lagrangian, equation (2.7):

$$\begin{aligned} \frac{\partial \mathcal{L}}{\partial \vec{u}} \delta \vec{u} = & \int_{\Omega_1} \mu_1 (\nabla \vec{u}) \cdot (\nabla \delta \vec{u}) d\Omega_1 + \int_{\Omega_2} \mu_2 (\nabla \vec{u}) \cdot (\nabla \delta \vec{u}) d\Omega_2 + \int_{S(t)} \gamma \kappa \vec{n} \cdot \delta \vec{u} dS + \int_{S(t)} \frac{\partial \gamma}{\partial \vec{n}} \vec{n} \cdot \delta \vec{u} dS \\ & - \int_{\Omega_1} p_1 \operatorname{div}(\delta \vec{u}) d\Omega_1 - \int_{\Omega_2} p_2 \operatorname{div}(\delta \vec{u}) d\Omega_2 - \int_{\mathcal{B}_\infty} \lambda \cdot \delta \vec{u} d\mathcal{B}_\infty \end{aligned} \quad (3.1)$$

From this derivative, we define the operator G that transforms any vector field \vec{x} into a scalar

$$\begin{aligned} G_{\vec{u}, p_1, p_2, \lambda}(\vec{x}) = & \int_{\Omega_1} \mu_1 (\nabla \vec{u}) \cdot (\nabla \vec{x}) d\Omega_1 + \int_{\Omega_2} \mu_2 (\nabla \vec{u}) \cdot (\nabla \vec{x}) d\Omega_2 + \int_{S(t)} \gamma \kappa \vec{n} \cdot \vec{x} dS + \int_{S(t)} \frac{\partial \gamma}{\partial \vec{n}} \vec{n} \cdot \vec{x} dS \\ & - \int_{\Omega_1} p_1 \operatorname{div}(\vec{x}) d\Omega_1 - \int_{\Omega_2} p_2 \operatorname{div}(\vec{x}) d\Omega_2 - \int_{\mathcal{B}_\infty} \lambda \cdot \vec{x} d\mathcal{B}_\infty \end{aligned} \quad (3.2)$$

and in which the scalars p_1 , p_2 , λ and the velocity field \vec{u} are parameters.

If the velocity field \vec{u} and the scalars p_1 , p_2 and λ are the fields \vec{u}^s , p_1^s , p_2^s and λ^s that minimize the Lagrangian (and thereby verify the Stokes equations), then the operator verifies

$$G_{\vec{u}^s, p_1^s, p_2^s, \lambda^s}(\vec{x}) = 0 \text{ for all vector fields } \vec{x}. \quad (3.3)$$

A particular case is obtained by taking $\vec{x} = \vec{u}^s$, the actual flow field that verifies the Stokes equation. It yields that the flow verifies the equation

$$\begin{aligned} \underbrace{\int_{\mathcal{B}_\infty} \lambda^s \cdot \vec{u}^s d\mathcal{B}_\infty}_{\substack{\text{power injected} \\ \text{by the stress tensor}}} = & \underbrace{\int_{\Omega_1} \mu_1 (\nabla \vec{u}^s)^2 d\Omega_1 + \int_{\Omega_2} \mu_2 (\nabla \vec{u}^s)^2 d\Omega_2}_{\text{viscous dissipation}} \\ & + \underbrace{\int_S \gamma \kappa \vec{n} \cdot \vec{u}^s dS + \int_{S(t)} \frac{\partial \gamma}{\partial \vec{n}} \vec{n} \cdot \vec{u}^s dS}_{\substack{\text{rate of change in } \mathcal{E}_\gamma \\ \text{due to advection} \\ \text{by } \vec{u}^s}} \end{aligned} \quad (3.4)$$

which is a balance between energy production and energy dissipation.

Here, we have shown that if the flow field \vec{u} is solution of the Stokes equation then it verifies the energy balance (3.4). However, the reciprocal is not true: a velocity field that verifies the energy balance (3.4) is not necessarily solution to the Stokes equation.

In that sense, the energy production-dissipation balance (3.4) is less powerful than the minimum principle (P3-bis). Nonetheless, analytically solving an equation is much more practical than performing a minimization, as illustrated in the following section which deals with droplet trajectories in confinement gradients.

Equation (3.4) has a large number of unknowns (velocity and pressure fields, position and shape of the droplet, etc...) and it can only be solved analytically if most of them are taken as parameters.

3.2 Geometry, velocity fields and assumptions

We consider a non-wetting pancake drop flowing in a nonparallel Hele-Shaw cell. We call h_0 the height of the chamber and dh the small amplitude height variations ($dh \ll h$). In his account of an oil drop moving towards the touching end of two slightly inclined plates, Hauksbee [38] mentions that the moving drop has a nearly circular pulley shape, closely resembling the one it would have if the plates were horizontal. Our own observations, discussed in Chapter 4 and 5, lead to the same conclusion but in the case of pancake drops. Small confinement gradients do not significantly deform the shape of the droplet. Consequently, we assume in our analysis that the droplet always has circular pancake shape of radius R . This assumption is also confirmed by theoretical arguments put forward by Laplace [45].

The outer fluid is forced to flow from left to right at an height-averaged velocity \vec{U}_f . As the droplet travels in the Hele-Shaw cell, the position of its center of mass $O(x_d, y_d)$ in the domain changes and its radius $R(x_d, y_d)$ varies as the droplet adapts to the local height $h(x, y) = h_0 + \delta h(x, y)$ of the Hele-Shaw cell. A relation between R and h is obtained by invoking the volume conservation of the droplet: $V \approx \pi R^2 \cdot h = \text{cste}$, an approximation valid for large pancake droplet and a slowly varying height of the Hele-Shaw cell.

The instantaneous velocity of the droplet \vec{U}_d may not be aligned with the input flow velocity $\vec{U}_f = U_f \vec{e}_x$. The angle $\phi = \cos^{-1}(\vec{U}_d \cdot \vec{U}_f / U_d U_f)$ identifies the direction of the droplet movement. Last, we define the polar coordinates (r, θ, z) attached to the center of mass of the droplet. All geometrical quantities are represented in Fig. 3.1.

3.2.1 Flow domains

As sketched on Fig. 3.1, the control volume is split into five different flow domains:

- Far from the transverse curved interface of the droplet, the Hele-Shaw approximation is valid. In these inner and outer far-field regions, the velocity field is well captured by a height-averaged potential flow analysis.

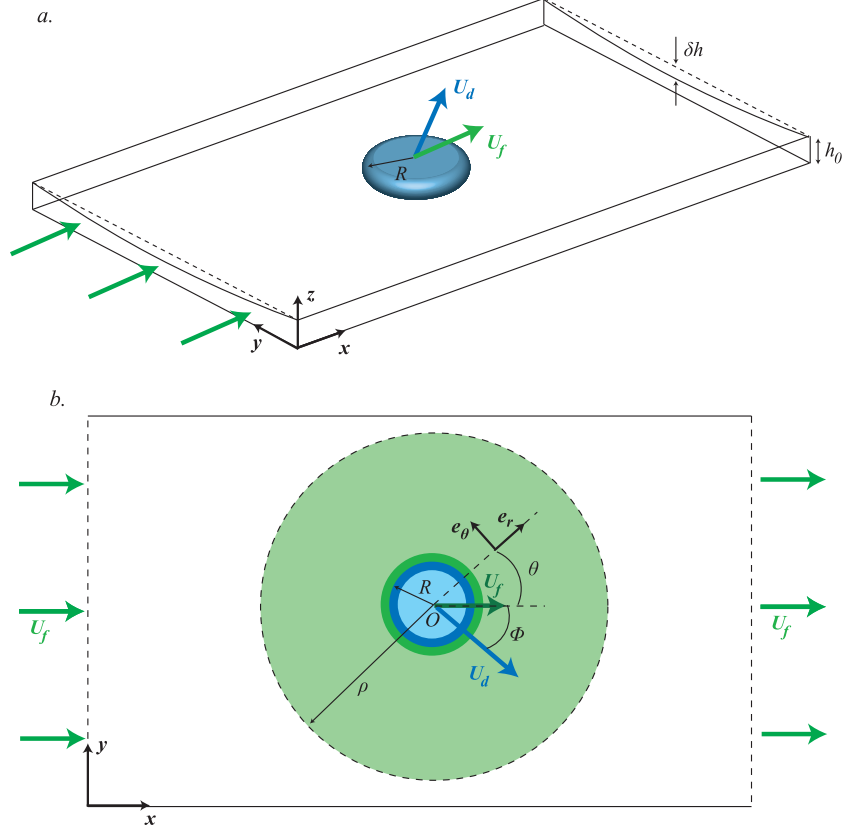


Figure 3.1: **a.** 3D sketch of the geometrical configuration: a pancake drop is moving at a velocity \vec{U}_d in an Hele-Shaw cell with confinement heterogeneities, pushed by an outer flow of velocity \vec{U}_f . **b.** Top-down projection with definitions of the main geometrical parameters and coordinate systems. The different colors correspond to the different flow domains: light green is the far-field outer flow, dark green is the near-interface outer flow, dark blue is the near-interface inner flow and light blue is the far-field inner flow. The thin lubrication films are not shown on this sketch.

- Near the interface however, the flow is fully 3D due to the presence of a transverse curved boundary. As a result, there are inner and outer near-interface boundary layers that extend a few gap widths $O(h_0)$ away from the interface.
- Last, the interface of the droplet deforms near the walls under viscous shear. There are thin lubrication films of outer fluid that form between the droplet and the channel walls.

Far-field flows

By definition, the flow field verifies the classical Hele-Shaw equations (2.10) in the far-field flow domains. For height variations of small amplitude ($\delta h \ll h_0$), the local height of the cell in the Hele-Shaw equations can be assumed everywhere as equal to h_0 . The flow

field in a Hele-Shaw cell with confinement gradients of small amplitude is therefore well approximated by the flow field in a parallel Hele-Shaw cell of height h_0 .

The far-field flow velocity is the superposition of the uniform outer flow, the flow around the circular droplet and the flow generated by the movement of the droplet. A potential flow analysis similar to the one used for the elliptic bubbles of Chapter 2 yields

$$U_{r,1} = U_d \cos(\theta - \phi) \quad (3.5a)$$

$$U_{r,2} = U_f \left(1 - \frac{R^2}{r^2}\right) \cos(\theta) + U_d \frac{R^2}{r^2} \cos(\theta - \phi), \quad (3.5b)$$

$$U_{\theta,1} = -U_d \sin(\theta - \phi) \quad (3.6a)$$

$$U_{\theta,2} = -U_f \left(1 + \frac{R^2}{r^2}\right) \sin(\theta) + U_d \frac{R^2}{r^2} \sin(\theta - \phi) \quad (3.6b)$$

and

$$p_1 = -\frac{\mu_1}{h_0^2} U_d r \cos(\theta - \phi) \quad (3.7a)$$

$$p_2 = -\frac{\mu_2}{h_0^2} \left[U_f \left(r + \frac{R^2}{r}\right) \cos \theta - U_d \frac{R^2}{r} \cos(\theta - \phi) \right] \quad (3.7b)$$

for the velocity and pressure fields, respectively.

Near-interface flows

Near the interface of the droplet, the Hele-Shaw approximation breaks down for two reasons. First, the flow becomes fully 3D because of the geometry of the droplet. Second, matching the inner and outer far-field flows requires four boundary conditions while the far-field inner and outer potential flows only provide a single adjustable parameter, the droplet velocity U_d . This mismatch between boundary conditions and adjustable parameters can only be solved by adding boundary layers that extend a few gap widths h_0 away from the interface.

To date, models only partially capture the flows in these boundary layers and analytical expressions for the velocity fields have only been derived for a solid cylinder [92].

Nonetheless, it is possible to estimate the viscous shear in these regions. The velocity scale is either U_f or U_d , depending on which of the two dominates. Experiments [84, 85] show that the droplet velocity is always smaller than the fluid velocity, pointing towards U_f as the correct velocity scale. The boundary layer has a single length scale, the channel height h_0 . Hence, the viscous shear $\nabla \vec{u}$ scales as U_f/h_0 .

Lubrication films

The movement of the droplet creates lubrication films between the droplet and the channel walls. These lubrication films, sketched in Fig. 3.2, are similar in nature to the Landau-Levich coating of a plate or to the Bretherton lubrication films [86] around a bubble moving

in a round capillary. Indeed, in its frame of reference, the droplet sees the walls moving backwards at a velocity $-\vec{U}_d$. Viscous shear then entrains outer fluid along with the walls, creating the lubrication films sketched in Fig. 3.2.a.

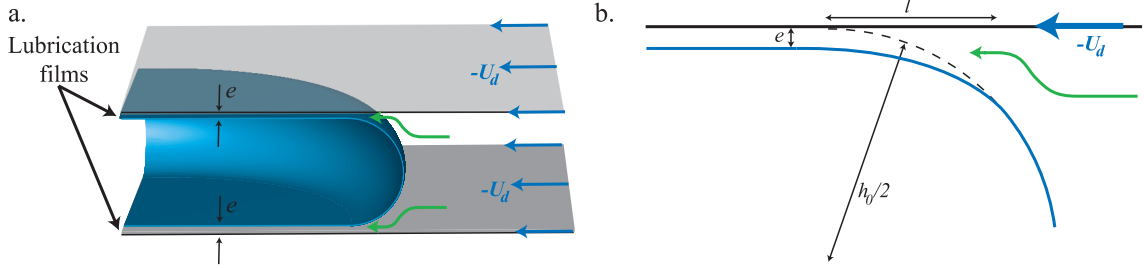


Figure 3.2: **a.** 3D sketch of the front half of a moving droplet in the reference frame of the droplet. The top and bottom walls are moving backward at a velocity $-\vec{U}_d$, dragging outer fluid along and depositing lubrication films of thickness e . **b.** Zoom on the film deposition region at the front of the droplet. The static interface of transverse curvature $h_0/2$ is deformed as outer fluid is dragged into the lubrication film. The deformed region has a length l and the deposited films have a thickness e .

The thickness e of the films is fixed by the competition between the viscous stresses that drag the outer fluid into the films and the capillary pressure that presses the fluid out of the films. Classically, a scaling law approach is used to estimate the thickness of the film e [43, 88].

The cap at the front end of the large pancake droplet has a curvature $h_0/2$ when it is static and at equilibrium. When the droplet is moving, it is deformed by the presence of the lubrication films in a small dynamic region of length l near the channel walls, as illustrated in Fig. 3.2.b. The Stokes equation then states that the pressure gradient ∇p balances viscous forces $\mu_2 \Delta u$. The pressure difference across the dynamic region is given by Young-Laplace equation (1.1). Assuming that the pressure inside the droplet is uniform, the pressure jump across the interface at the curved static cap is approximately $2\gamma/h_0$ while at the flat lubrication film, it is zero. Hence, ∇p is proportional to $\gamma/(h_0 l)$. Viscous forces $\mu_2 \Delta u$ are dominated by transverse shear stresses, which implies the scaling law $\mu_2 \Delta u \propto \mu_2 U_d / e^2$. Balancing pressure and viscous forces yields

$$\text{Ca}_d \propto \frac{e^2}{h_0 l} \quad (3.8)$$

in which $\text{Ca}_d = \frac{\mu_2 U_d}{\gamma}$ is the droplet based capillary number.

A second scaling law is obtained by estimating the curvature of the interface in the dynamic region. The change in curvature scales as l/e^2 and must be of order $h_0/2$ in order to match the static cap curvature. Hence,

$$\frac{l}{e^2} \propto \frac{1}{h_0} . \quad (3.9)$$

By combining these two scaling laws, we obtain estimates for the thickness e of the lubrication films and for the length l of the dynamic region:

$$\begin{aligned} e &\propto \text{Ca}^{2/3} h_0 \\ l &\propto \text{Ca}^{1/3} h_0 . \end{aligned} \quad (3.10)$$

While more detailed models of the lubrication films around a Hele-Shaw droplet are found in the literature [51, 88], the scaling laws (3.10) capture the essential physics and will serve the purpose of our discussion.

3.2.2 Control volume and simplifications

The control volume on which we apply the energy production-dissipation balance is a cylinder centered on the droplet and of radius ρ much larger than the droplet radius R .

The power \mathcal{P} injected by the stress tensor (2.9d) at the external boundaries of the control volume is the work that is required to flow the outer fluid at a mean velocity U_f . In a Hele-Shaw cell, the in-plane viscous shear stresses are always negligible compared to pressure gradients far from any vertical boundaries. Hence, \mathcal{P} reduces to the work of the pressure on the boundaries of the control volume. Also, we only consider variations of surface energy that are due to modifications of the droplet shape. The interfacial tension γ is assumed uniform and invariant of the droplet position.

As a result, the energy production-dissipation balance (3.4) becomes

$$\underbrace{\int_0^{2\pi} -p_2(\rho, \theta) U_{r,2} \rho d\theta}_{\substack{\text{power } \mathcal{W} \text{ injected} \\ \text{by the pressure}}} = \underbrace{\int_{\Omega_1} \mu_1 (\nabla \vec{u}^s)^2 d\Omega_1}_{\substack{\text{viscous dissipation } \mathcal{P}_1 \\ \text{inside the drop}}} + \underbrace{\int_{\Omega_2} \mu_2 (\nabla \vec{u}^s)^2 d\Omega_2}_{\substack{\text{viscous dissipation } \mathcal{P}_2 \\ \text{outside the drop}}} + \underbrace{\gamma \dot{S}}_{\substack{\text{rate of change in } \mathcal{E}_\gamma \\ \text{due to advection} \\ \text{by } \vec{u}^s}} . \quad (3.11)$$

3.3 Equation of motion

We now solve the simplified energy production-dissipation balance (3.11) by estimating each term individually. For the viscous dissipation, we estimate separately the contributions for each of the five flow domains identified above in Fig. 3.1.

3.3.1 Power injected into the control volume

The first term in the energy production-dissipation balance (3.11) is the power \mathcal{W} injected into the control volume, which amounts to the work of the pressure field on the boundary of the control volume. Taking the potential flow solutions (3.5a) and (3.7a) for the pressure field p_2 and radial flow velocity $U_{r,2}$, we obtain

$$\mathcal{W} = \frac{12\pi\mu_2}{h_0} \left(U_f^2 \rho^2 - (U_d - U_f)^2 \frac{R^4}{\rho^2} \right) \quad (3.12)$$

For a large control volume ($\rho \gg R$), it simplifies to

$$\mathcal{W} = \frac{12\pi\mu_2}{h_0} U_f^2 \rho^2 \quad (3.13)$$

3.3.2 Energy dissipation in the far-field flows

In the far-field flow domains, the potential flow approximations for the velocity field (3.5a) and (3.6a) apply. Recalling the expression (2.24) for the energy dissipation in this case yields the following two expressions

$$\begin{aligned} \mathcal{P}_{ff_1} &= \int \mu_1 (\nabla \vec{u}^s)^2 d\Omega_1 \\ &= \frac{12\mu_1}{h} \int \vec{U}_1^2 dx dy \end{aligned} \quad \text{and} \quad \begin{aligned} \mathcal{P}_{ff_2} &= \int \mu_2 (\nabla \vec{u}^s)^2 d\Omega_2 \\ &= \frac{12\mu_2}{h} \int \vec{U}_2^2 dx dy \end{aligned} \quad (3.14) \quad (3.15)$$

for the viscous dissipation of the far-field flows inside and outside the droplet.

Inside the droplet, the potential velocity is uniform and equal to \vec{U}_d (see Eqs. (3.5a) and (3.6a)). Hence, we have

$$\mathcal{P}_{ff_1} = \frac{12\pi\mu_1}{h} \vec{U}_d^2 R^2 \quad (3.16)$$

Outside the droplet, the flow field is a linear superposition of two potential flows: the flow around a static droplet with a imposed far-field velocity \vec{U}_f and the flow generated by the droplet moving at a velocity \vec{U}_d . As a result, the square of the Hele-Shaw velocity \vec{U}_2^2 contains terms in \vec{U}_f^2 and \vec{U}_d^2 as well as crossed terms $\vec{U}_f \cdot \vec{U}_d$. We find

$$\vec{U}_2^2 = \vec{U}_f^2 + (\vec{U}_f - \vec{U}_d)^2 \frac{R^4}{r^4} + 2\vec{U}_f^2 \frac{R^2}{r^2} \cos(2\theta) + 2U_f U_d \frac{R^2}{r^2} \cos(2\theta - \phi) \quad (3.17)$$

which has to be integrated over all θ and for r ranging between R and ρ . In the end, it yields

$$\mathcal{P}_{ff_2} = \frac{12\pi\mu_2}{h} \left(\vec{U}_f^2 \rho^2 - \vec{U}_f^2 R^2 + (\vec{U}_f - \vec{U}_d)^2 R^2 \right) . \quad (3.18)$$

3.3.3 Other sources of viscous dissipation

Near-interface dissipation

In the near-interface boundary layers, the complexity of the flow field rules out the possibility to compute analytically the viscous dissipation \mathcal{P}_{ni} in these regions. Consequently, we only derive scaling laws.

As established in Section 3.2.1, the amplitude of shear in the flow is given by the scaling law $\nabla u \propto U_{f,d}/h_0$. The volume of the near-interface bands scales as $h_0^2 \cdot R$. Since, the viscous dissipation in these regions scales as the square of the shear times the flow volume, we find

$$\mathcal{P}_{ni,2} \propto \mu_{1,2} U_{f,d}^2 R . \quad (3.19)$$

This scaling law shows that the viscous dissipation in the near-interface fluid bands is h/R smaller than the far-field viscous dissipation $\mathcal{P}_{1,2}$. Consequently, we can neglect this contribution in the case of large pancake drops.

Lubrication film dissipation

The velocity field in the established thin film region is uniformly equal to the wall velocity [43]: $\vec{u}(x, y, z) = -\vec{U}_d$ in the droplet's reference frame and $\vec{u}(x, y, z) = 0$ in the lab frame. No energy production or dissipation occurs in this region of the lubrication films.

In the dynamic region however, outer fluid is forced into the lubrication films which creates shears of amplitude $\nabla u \propto U_d/e$. The volume of the dynamic region around the droplet is proportional to $e \cdot l \cdot R$. Using these two estimates, we can express a scaling law for the viscous dissipation \mathcal{P}_{lf} in the dynamic region and by extension in the lubrication films:

$$\mathcal{P}_{lf} = 12\pi\beta\mu_2 \frac{U_d^2}{Ca_d^{1/3}} R , \quad (3.20)$$

with β a non-dimensional constant of proportionality.

3.3.4 Rate of change of surface energy

At last, confinement gradients are added into the model including the effect of height variations $\delta h(x, y)$ of the cell on the surface energy of the non-wetting pancake droplet. Although we assumed the in-plane circular shape of the droplet is invariant of the droplet position in the Hele-Shaw cell, its radius R must still adapt to account for local height variations of the cell: R becomes a function of the droplet's position (x_d, y_d) . The surface energy $\mathcal{E}_\gamma = \gamma S$ of the droplet then also varies with the droplet position (x_d, y_d) and surface energy gradients appear.

Over an infinitesimal time interval dt , the surface energy of the droplet changes of an amount $d\mathcal{E}_\gamma$ while its position translates over a distance $\vec{U}_d \cdot dt$. The rate of change of

surface energy $\dot{\mathcal{E}}_\gamma$ can then be expressed as

$$\begin{aligned}\dot{\mathcal{E}}_\gamma &= \frac{d\mathcal{E}_\gamma}{dt} = \vec{\nabla} \mathcal{E}_\gamma \cdot \frac{d\vec{x}}{dt} \\ &= \gamma \vec{\nabla} S \cdot \vec{U}_d ,\end{aligned}\tag{3.21}$$

when the interfacial tension γ does not vary with the position and velocity of the droplet. Here, we have also implicitly assumed that the shape of the droplet is independent of its velocity \vec{U}_d .

3.3.5 Equation of motion

All terms \mathcal{W} , \mathcal{P}_{ff_1} , \mathcal{P}_{ff_2} , \mathcal{P}_{lf} and $\dot{\mathcal{E}}_\gamma$ are then injected into the energy production-dissipation balance (3.11) to obtain an equation for the motion of a pancake in a Hele-Shaw cell with small heterogeneities in confinement:

$$\begin{aligned}\frac{12\pi\mu_2}{h_0} U_f^2 \rho^2 &= \frac{12\pi\mu_1}{h_0} \vec{U}_d^2 R^2 + \frac{12\pi\mu_2}{h_0} (\vec{U}_f^2 \rho^2 - \vec{U}_f^2 R^2 + (\vec{U}_f - \vec{U}_d)^2 R^2) \\ &\quad + 12\pi\beta\mu_2 \frac{\vec{U}_d^2}{\text{Ca}^{1/3}} R + \gamma \vec{\nabla} S \cdot \vec{U}_d .\end{aligned}\tag{3.22}$$

All terms in U_f^2 cancel out to yield the simplified equation

$$\frac{24\pi\mu_2}{h_0} \vec{U}_f \cdot \vec{U}_d R^2 = \frac{12\pi\mu_1}{h_0} \vec{U}_d^2 R^2 + \frac{12\pi\mu_2}{h_0} \vec{U}_d^2 R^2 + 12\pi\beta\mu_2 \frac{\vec{U}_d^2}{\text{Ca}^{1/3}} R + \gamma \vec{\nabla} S \cdot \vec{U}_d .\tag{3.23}$$

In a Hele-Shaw cell, we approximate the volume V of the droplet as $V \approx \pi R^2 \cdot h$. For large pancake droplets, the surface area S of the interface is dominated by the top and bottom circular surface: $S \approx 2\pi R^2$. Hence, we have $S(x_d, y_d) \approx 2V/h(x_d, y_d)$. It follows that

$$\dot{\mathcal{E}}_\gamma \approx -2\gamma \frac{V}{h_0^2} \vec{\nabla} h \cdot \vec{U}_d\tag{3.24}$$

which simplifies to

$$\dot{\mathcal{E}}_\gamma \approx -2\gamma \frac{\pi R^2}{h_0} \vec{\nabla} h \cdot \vec{U}_d\tag{3.25}$$

if we approximate the volume of the drop by $V \approx \pi R^2 h_0$.

Injecting the expression (3.25) into the balance equation (3.23) yields

$$\frac{24\pi\mu_2}{h_0} \vec{U}_f \cdot \vec{U}_d R^2 = \frac{12\pi\mu_1}{h_0} \vec{U}_d^2 R^2 + \frac{12\pi\mu_2}{h_0} \vec{U}_d^2 R^2 + 12\pi\beta\mu_2 \frac{\vec{U}_d^2}{\text{Ca}^{1/3}} R - 2\gamma \frac{\pi R^2}{h_0} \vec{\nabla} h \cdot \vec{U}_d .\tag{3.26}$$

This equation has three solutions. $\vec{U}_d = \vec{0}$ can be ruled out as unphysical. The orthogonality of the two vectors in the scalar production is possible although it is only a particular solution corresponding to special alignments and amplitudes of $\vec{\nabla}h$ and \vec{U}_f . The remaining solution is

$$\left(1 + \frac{\mu_1}{\mu_2} + \frac{\beta}{\text{Ca}^{1/3}} \frac{h}{R}\right) \vec{U}_d - 2\vec{U}_f - \frac{1}{6} \frac{\gamma}{\mu_2} \vec{\nabla}h = 0. \quad (3.27)$$

This equation describes the motion of a droplet flowing in the Hele-Shaw cell with confinement gradients of small amplitude.

It is noteworthy that while it is here easy to select the solution amongst the three possible flow fields, it may be more difficult in other cases. It is then necessary to use the minimum principle (P3-bis) on the family of solutions as a selection criterion.

3.4 Trajectory equation of the droplet

Let \mathcal{T} be the in-plane trajectory curve of a droplet in a nonparallel Hele-Shaw cell pushed by an outer fluid velocity $U_f \vec{e}_x$. The previous equation (3.27) contains information about both the trajectory \mathcal{T} of the droplet and the velocity at which the droplet travels along this trajectory.

By definition, the unit normal vector \vec{n} of \mathcal{T} is normal to the droplet velocity at all points on \mathcal{T} : $\vec{U}_d \cdot \vec{n} = 0$ as illustrated on Fig. 3.3.

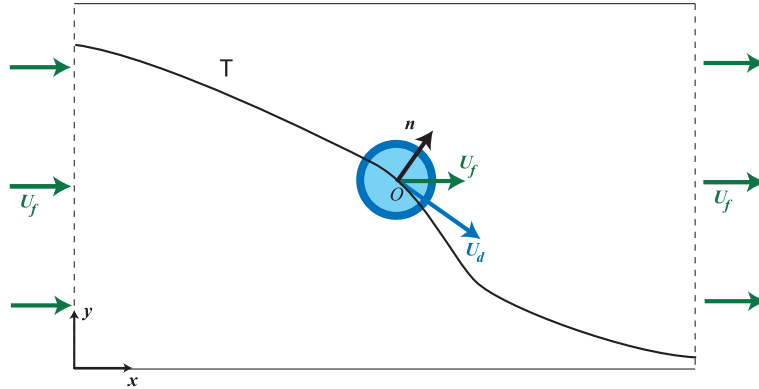


Figure 3.3: The solid black line is the droplet trajectory \mathcal{T} . Its normal vector \vec{n} is necessarily normal to the droplet velocity \vec{U}_d which defines the tangent to the trajectory.

By taking the scalar product of the equation of motion (3.27) with the normal vector \vec{n} , we obtain the equation

$$12\vec{U}_f \cdot \vec{n} + \frac{\gamma}{\mu_2} \vec{\nabla}h \cdot \vec{n} = 0 \quad (3.28)$$

for the trajectory \mathcal{T} of the droplet. This equation can also be written

$$12\text{Ca}_f \vec{e}_x \cdot \vec{n} + \vec{\nabla}h \cdot \vec{n} = 0 \quad (3.29)$$

recalling that $Ca_f = \mu_2 U_f / \gamma$ is the capillary number based on the outer flow velocity.

Remarkably, the trajectory of the droplet is independent of the velocity \vec{U}_d . Indeed, all terms associated with the *drag* of the droplet in equation (3.27), namely the terms proportional to \vec{U}_d , disappear with the scalar product $\cdot \vec{n}$. In particular, the unknown β vanishes and the equation for trajectory (3.29) is fully solvable knowing the experimental parameters Ca_f and $\vec{\nabla}h$.

3.5 Experiments in swollen microchannels

The first experiments on droplets flowing in a non-parallel Hele-Shaw cell were performed unknowingly in 2009 by a former undergraduate student, Hervé Turlier. To his surprise, he observed pancake water droplets moving through a long and wide microchannel along bent trajectories although they were pushed by a uniform unidirectional outer flow of silicone oil. Under the same flow conditions, he also recorded straight trajectories for the water droplets advected by paraffin oil. Figure 3.4 evidences the droplet trajectories by superposing successive images taken in each experiment.

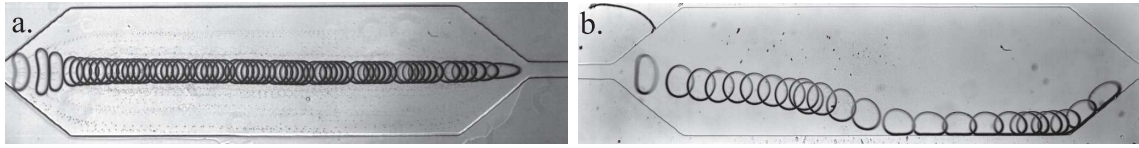


Figure 3.4: The microchannel consists of a flow focusing region for droplet production followed by a test section analogous to a Hele-Shaw cell: the channel height $h = 50 \mu\text{m}$ was much smaller than its width $w = 1 \text{ mm}$ and length $L = 4 \text{ mm}$. Water droplets are advected from left to right by a second carrier fluid. The trajectories of the droplets are visualized by superposing successive images taken using a high speed camera: **a)** straight trajectory for paraffin oil ($Q = 1.1 \mu\text{L}/\text{min}$ and $R = 100 \mu\text{m}$) **b)** bent trajectory with transverse migration toward the side wall for silicone V100 oil ($Q = 3.0 \mu\text{L}/\text{min}$ and $R = 130 \mu\text{m}$)

In these two experiments, the geometry and the hydrodynamic parameters are similar (equivalent droplet radius R and approximately equal capillary numbers Ca_f) and yet, the droplets behave differently in the two oils. The only difference in experimental conditions lies in the chemical composition of the oils used to advect the droplet.

It turns out that PDMS, the polymer out of which are made the device, swells when in contact with a wide range of organic solvents as shown by Lee *et. al.* [93]. In particular, it swells in contact with all silicone oils but not with paraffin oil. Consequently, in the same way a sponge deforms when wet, it is possible that the swelling of the PDMS deforms the channel geometry away its nominal *dry* shape.

In order to verify this hypothesis and measure the nature and amplitude of the deformations, we adapted an optical technique for measuring surface deformation called Free

Surface Synthetic Schlieren [94]. This method consists in observing a random pattern through a deforming surface and monitoring its optical distortion caused by refraction of light at the interface, as illustrated in Fig. 3.5. In this case, grainy scotch tape stuck under the test section served the purpose of the patterned surface. The experimental protocol is the following: starting from an initially dry channel, we fill it completely with oil and then let the liquid penetrate the PDMS and/or evaporate. Throughout the process, images of the scotch tape similar to the one shown on Fig. 3.5.b are regularly captured to obtain a movie of the distortions of the pattern. Although the movements are small, they are clearly visible on a space-time diagram of the channel cross-section (Fig. 3.5.c). The last step consists in reconstructing the deformed free surface(s) from the pattern distortions. The details of the method are published in Lab-On-a-Chip [95] and the paper can be found in Appendix C.

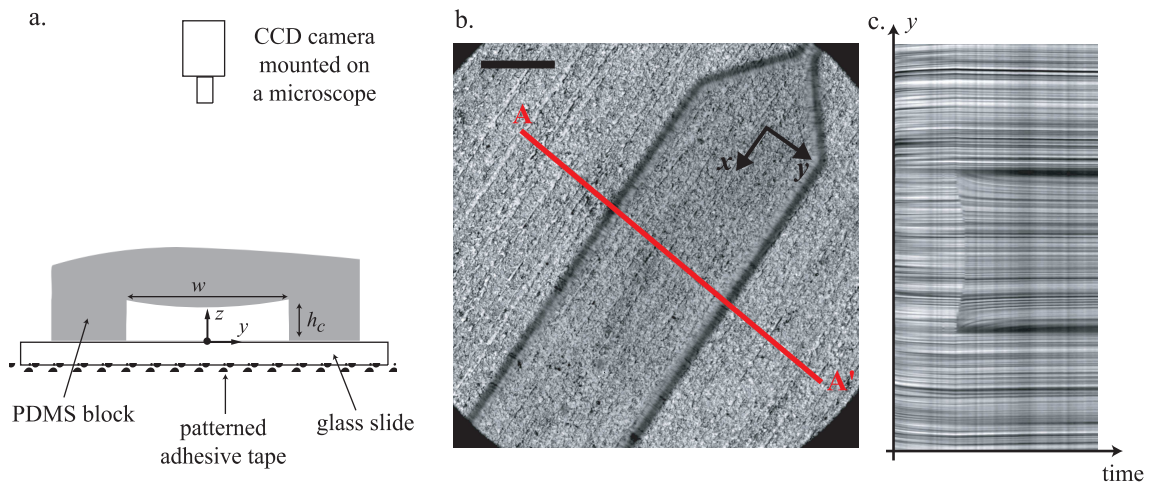


Figure 3.5: Illustration of the Free Surface Synthetic Schlieren method used to measure swelling induced microchannel deformations. **a.** Sketch of the experimental setup: the textured scotch tape is observed through the deforming microchannel with a camera mounted onto a microscope. **b.** Example of an image of the scotch tape. Scale bar is $500\ \mu\text{m}$. **c.** A space-time diagram of the pattern along the line AA' clearly evidences distortions in the image of the scotch tape by refraction at the deforming interface.

This study of the swelling induced channel deformation revealed that the swollen channel collapses along its centerline, as shown in Fig. 3.6.a. When filled with hexadecane for example, the roof of the channel features a subsidence $6\ \mu\text{m}$ in amplitude that is well fitted with a parabolic profile (see Fig. 3.6.b). The amplitude of the subsidence dh increases with the swelling coefficient of the oil used in the experiment and with the width W of the test section. Hence, we find that the test section is a Hele-Shaw cell with height variations of the form

$$h(x, y) = h_0 - dh \left(1 - \frac{4y^2}{W^2} \right) \quad (3.30)$$

and use this generic expression to derive the droplet trajectories predicted by the energy

production-dissipation.

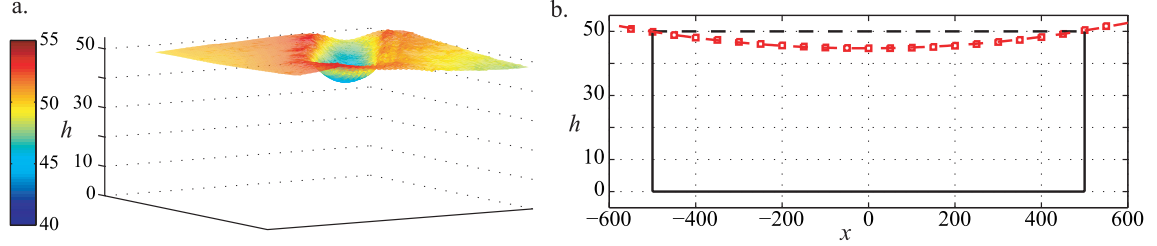


Figure 3.6: **a)** Height profile of the channel swollen with silicone oil, measured by Synthetic Schlieren as described in Dangla et. al. [95]. **b)** The transverse channel height profile averaged over the length of the test section from the Synthetic Schlieren measurements.

3.6 Comparing observed and predicted trajectories

Injecting the height profile (3.30) into the trajectory equation (3.29), we obtain

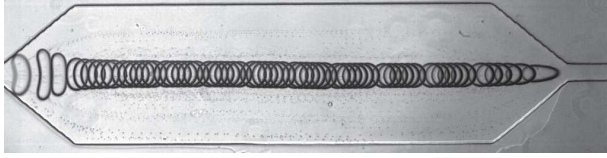
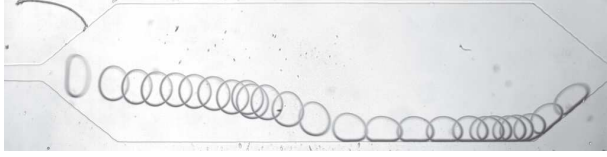
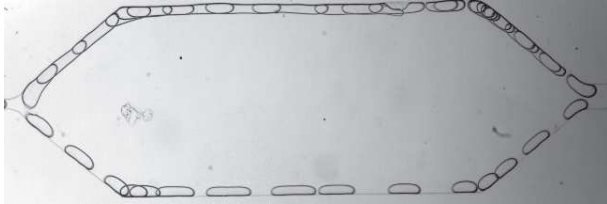
$$12\text{Ca}_f \frac{dy_d}{dx_d} - dh \frac{8y}{W^2} = 0.$$

The equation depends on a single non-dimensional number that we call the subsidence number $\text{Su} = dh/W \cdot 1/\text{Ca}_f$, once W is used a characteristic in-plane length scale for $x_d = W\bar{x}_d$ and $y_d = W\bar{y}_d$:

$$3 \frac{d\bar{y}_d}{d\bar{x}_d} - \text{Su}\bar{y}_d = 0. \quad (3.31)$$

The subsidence number Su measures the force exerted on the droplet by the channel deformations to the one due to the outer flow. For strong channel deformations ($\text{Su} \gg 1$), the equation simplifies to $d\bar{x}_d = 0$ meaning that the droplet is barely advected by the flow before it reaches the side walls of the channel. On the contrary, for strong flow advection ($\text{Su} \ll 1$), the equation simplifies to $d\bar{y}_d = 0$ and the droplet travels across the test section without being deflected by the channel deformations.

We can test these qualitative predictions by estimating the subsidence number for three experiments of water drops flowing in oils of different viscosities and swelling coefficients: hexadecane, a swelling solvent of low viscosity; silicone oil, a highly viscous swelling oil; and paraffin oil, a highly viscous non-swelling oil. The table below compares the three experiments.

Trajectory of a water droplet in paraffin oil				
				
Paraffin oil	$\mu_2 = 130$ cP $\gamma = 20$ mNm $U_f = 1.3$ mm/s	$Ca_f =$ $=$ $8.4 \cdot 10^{-3}$	$S = 1.00$ $dh = 0$ μ m $W = 1$ mm	$Su = 0$
Trajectory of a water droplet in silicon oil				
				
Silicone oil	$\mu_2 = 100$ cP $\gamma = 35$ mNm $U_f = 1.3$ mm/s	$Ca_f =$ $=$ $1.3 \cdot 10^{-2}$	$S = 1.08$ $dh = 6$ μ m $W = 1$ mm	$Su = 0.33$
Trajectory of a water droplet in hexadecane				
				
Hexadecane	$\mu_2 = 3.1$ cP $\gamma = 28$ mNm $U_f = 4$ mm/s	$Ca_f =$ $=$ $4.4 \cdot 10^{-4}$	$S = 1.14$ $dh = 8$ μ m $W = 1$ mm	$Su = 18$

Estimated subsidence number Su are in agreement with observed trajectories: for the non-swelling paraffin oil, $Su = 0$ and the droplet travels in a straight line across the microchannel while for the highly swelling and low viscosity hexadecane, $Su \gg 1$ and the droplet splits in two as it enters the test section and crosses the test section pressed against the side walls.

In the case of silicone oil, Su is order 1 and the water droplets follow bent trajectories that fall within the scope of this study. Hence, we use this configuration to further test our model quantitatively. The generic expression for the droplet trajectories is obtained by integrating the differential equation (3.31):

$$\frac{y_d}{W} = A \cdot \exp\left(\frac{Su}{3} \frac{x_d}{W}\right). \quad (3.32)$$

In this expression, A is the only fitting parameter once W and Su are taken from

the experimental conditions. The predicted trajectories are in excellent agreement with experimental data points along most of the trajectory, as shown on Fig. 3.7.

The model however fails to capture the boundary effects that occur as the droplet approaches the side walls or the narrowing exit of the test section. Indeed, we observe experimentally that the droplet accelerates its lateral migration when it is closer than a diameter away from the sidewalls while near the exit of the channel, the converging flow field tends to recenter the droplet.

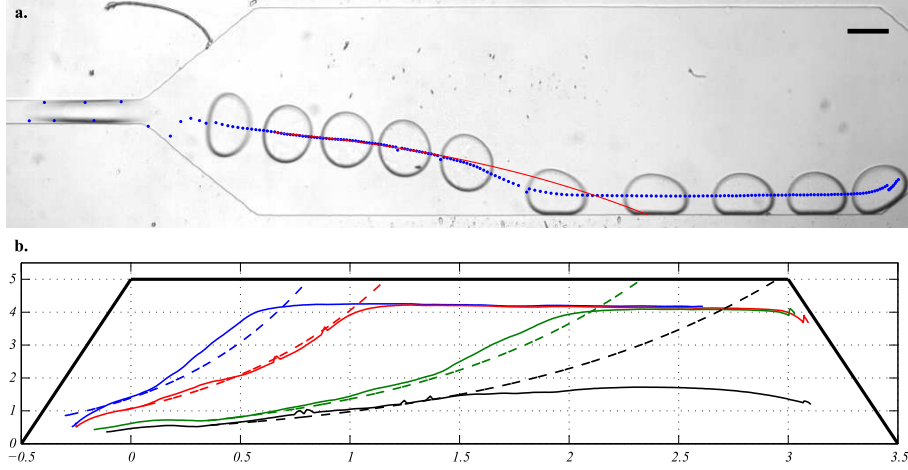


Figure 3.7: **a.** Superposition of an image of the drop in the test section with the experimentally measured trajectory (blue dots) and the fitted predicted trajectory (red solid line). Experimental conditions : flow rate $Q = 2.975\mu\text{L}/\text{min}$, droplet radius $R = 130\mu\text{m}$, $dh = 6\mu\text{m}$. Scaling bar : $200\mu\text{m}$ **b.** Measured and predicted trajectories from 4 different flow parameters: in blue, flow rate $Q = 2\mu\text{L}/\text{min}$, droplet radius $R = 116\mu\text{m}$, $S_u = 0.51$; in red, flow rate $Q = 2.3\mu\text{L}/\text{min}$, droplet radius $R = 123\mu\text{m}$, $S_u = 0.45$; in green, flow rate $Q = 3.1\mu\text{L}/\text{min}$, droplet radius $R = 124\mu\text{m}$, $S_u = 0.33$; in black, flow rate $Q = 3.7\mu\text{L}/\text{min}$, droplet radius $R = 119\mu\text{m}$, $S_u = 0.27$

3.7 Summary and discussion of Chapter 3

The good agreement between the predicted and measured trajectories indicates that the trajectory equation (3.29) captures correctly the effects of the outer flow and of the confinement gradients. The fact that the trajectory of the droplet is independent of the velocity U_d at which the droplet travels may seem surprising at first. However, it is a common feature of mechanical systems without inertia nor lift. For example, we can expect the trajectory of a bubble rising under gravity in a viscous flow [85] to be independent of the actual bubble velocity as well.

We finish by discussing different aspects concerning the main result of this chapter, the energy balance (3.23) and the resulting equation of motion (3.27).

3.7.1 Physical insight on the Taylor-Saffman result

We first observe that it is possible to recover the Taylor-Saffman result $\vec{U}_d = 2\vec{U}_f$ by keeping only the terms due to the potential flow fields in the balance of energy production-dissipation. Since Taylor and Saffman neglected the near-interface and lubrication film flow regions in their analysis, a balance between the power of the pressure forces \mathcal{W} from (3.13) and the viscous dissipation $\mathcal{P}_{ff_1} + \mathcal{P}_{ff_2}$ given by the expressions (3.16) and (3.18) contains all the physical ingredients were considered by TS. This balance corresponds to the equation

$$\frac{12\pi\mu_2}{h_0}U_f^2\rho^2 = \frac{12\pi\mu_1}{h}\vec{U}_d^2R^2 + \frac{12\pi\mu_2}{h}(\vec{U}_f^2\rho^2 - \vec{U}_f^2R^2 + (\vec{U}_f - \vec{U}_d)^2R^2) .$$

Hence, finding the droplet velocity amounts to solving the simplified equation

$$0 = \left[\left(1 + \frac{\mu_1}{\mu_2} \right) \vec{U}_d - 2\vec{U}_f \right] \cdot \vec{U}_d . \quad (3.33)$$

This vectorial equation has two solutions,

$$\vec{U}_d = \frac{2\mu_2}{\mu_1 + \mu_2}\vec{U}_f \text{ and } \vec{U}_d = \vec{0} . \quad (3.34)$$

The energy production-dissipation balance (3.4) then states that the solution to the Stokes equation is necessarily one of these two solutions. Here, we can rule out the solution $\vec{U}_d = \vec{0}$ as unphysical and we recover the Taylor-Saffman result $\vec{U}_d = 2\vec{U}_f$ when the inner fluid is gas ($\mu_1 = 0$).

This balance of energy production-dissipation provides physical insight on this surprising result. Indeed, naively, one could think that the bubble should move at the speed of the outer fluid: $\vec{U}_d = \vec{U}_f$. Let's assume this is the case. Then, the outer flow is uniform with a velocity \vec{U}_f everywhere in the Hele-Shaw cell. It dissipates energy over the entire control volume except inside the inviscid bubble: $\mathcal{P}_{ff_2} = 12\pi\mu_2/hU_f^2(\rho^2 - R^2)$. The energy injected in the system however is left unchanged: $\mathcal{W} = 12\pi\mu_2U_f^2\rho^2$. Since $\mathcal{P}_{ff_2} < \mathcal{W}$, we find that there is a deficiency in energy dissipation. There is more energy injected into the control volume than dissipated. The bubble must move at a different velocity than the outer fluid in order to account for this deficiency.

3.7.2 An interpretation of the energy production-dissipation balance in terms of forces

Equation (3.27) for the movement of a droplet in a Hele-Shaw cell was derived from a balance between the amount of energy injected in the system and the amount of energy dissipated by viscosity plus the energy stored as surface energy. This approach differs in its nature from the force balance usually considered to study droplets in Hele-Shaw cells [89, 63, 85, 96].

The force approach is based on the property that in Stokes flows, any volume of fluid is force free. Hence, the sum of the forces acting upon a droplet must be zero. In the absence of volume forces like gravity, only the pressure and viscous shear stresses at the interface contribute to the force balance. The classical methodology then consists in identifying the dominating terms in the pressure field and in the shear stresses around the droplet, like the contributions from the outer flow of velocity U_f or from the thin lubrication films, and integrating these contributions over the interface to obtain an expression for the *force* they each apply on the droplet.

To compare the two approaches, we notice that all the terms in the reduced equation (3.23) for the energy production-dissipation balance are in the form $\vec{F} \cdot \vec{U}_d$ and can therefore be interpreted as the work of a force \vec{F} that applies on the moving droplet:

$$\begin{aligned}
 & \underbrace{\frac{24\pi R^2 \mu_2}{h_0} \vec{U}_f}_{\text{propulsion force } \vec{F}_{U_f} \text{ from the outer flow}} \cdot \vec{U}_d + \underbrace{(-\gamma \vec{\nabla} S)}_{\text{force } \vec{F}_\gamma \text{ from the confinement gradients}} \cdot \vec{U}_d = \\
 & \underbrace{\left(\frac{12\pi R^2 \mu_1}{h_0} \vec{U}_d + \frac{12\pi R^2 \mu_2}{h_0} \vec{U}_d \right)}_{\text{drag force } \vec{F}_H \text{ due to the droplet induced flows in the Hele-Shaw cells}} \cdot \vec{U}_d + \underbrace{\frac{12\beta\pi R \mu_2}{\text{Ca}^{1/3}} \vec{U}_d}_{\text{drag force } \vec{F}_{lf} \text{ from the lubrication films}} \cdot \vec{U}_d . \quad (3.35)
 \end{aligned}$$

We recover a force balance equation: the driving forces \vec{F}_{U_f} and \vec{F}_γ from outer flow and the confinement gradient respectively are countered by the viscous drag \vec{F}_μ , sum of the two forces \vec{F}_H and \vec{F}_{lf} which originate from the flows in the Hele-Shaw cell and the lubrication films respectively.

This reinterpretation of the energy production-dissipation balance yields a simple expression for the force \vec{F}_γ that applies on a droplet in Hele-Shaw cell due to confinement gradients:

$$\vec{F}_\gamma = -\gamma \vec{\nabla} S . \quad (3.36)$$

This expression is of the form $F_\gamma = -\vec{\nabla} \mathcal{E}_\gamma$, as if the surface energy \mathcal{E}_γ behaves like a source of potential energy in the system. In the Hele-Shaw cell with small height variations studied above, we found $\vec{\nabla} S \approx -2\pi R^2/h_0 \vec{\nabla} h$. Consequently, the force that applies on the droplet in a deformed Hele-Shaw cell due to the confinement gradients is equal to

$$\vec{F}_\gamma \approx 2\gamma \frac{\pi R^2}{h_0} \vec{\nabla} h . \quad (3.37)$$

When the height variations of the Hele-Shaw cell occur over length scales larger than the size of the droplet, we can define locally the angle α between the top and bottom walls.

The magnitude of the force F_γ is then

$$|F_\gamma| \approx \gamma \frac{2 \tan \alpha \pi R^2}{h_0}, \quad (3.38)$$

in agreement with the expression (1.7) extracted from the seminal work of Laplace.

For the propulsive force F_d from the outer flow, we find using our energy dissipation approach

$$\vec{F}_{U_f} = \frac{24\pi R^2 \mu_2}{h_0} \vec{U}_f, \quad (3.39)$$

in agreement with previous analytical studies of the pressure stresses applied by the outer flow on a solid cylinder [92] and on a cylindrical droplet [89, 85] in a Hele-Shaw cell.

3.7.3 The viscous drag and velocity of a non-wetting droplet in a Hele-Shaw cell

We conclude with a discussion of the viscous drag force F_μ that applies on a droplet moving in a Hele-Shaw cell, an unsettled question in the literature. We illustrate the effect of the drag by comparing the velocity U_d of a droplet pushed by an outer flow of velocity U_f for the different suggested models.

While Taylor and Saffman [39] predict a velocity $U_d = 2U_f$ for an inviscid drop in a Hele-Shaw cell, measurements [83, 84, 97, 89, 85] always yielded significantly smaller velocities and suggest a scaling of the form $U_d \propto f(R/h) \text{Ca}_d^n \cdot U_f$ for the droplet velocity, with $n > 0$. From their experiments, Maruvada and Park [89] conclude $n \approx 2/3$ while Rabaud *et. al.* find instead a smaller decrease of the velocity, with $n \approx 1/2$.

Analytical studies [89, 63, 85] and numerical simulations [78] agree that the slow droplet velocity is due the presence of the lubrication films. At first, it is not obvious that lubrication increases the drag of the droplet. Lubrication is usually thought of as a mean to reduce friction at the walls. Also, in the case of a capillary tube, it was observed and demonstrated that the speed of a bubble with lubrication films actually exceeds the velocity it would have without them [98, 86, 12].

From our interpretation of the energy production-dissipation balance, we identify two contributions to the total drag force $F_\mu = F_H + F_{lf}$:

- a first term F_H which stems from the flows in the Hele-Shaw cell (including inside the drop) that are induced by the movements of the droplet

$$F_H = 12\pi\mu_1 \frac{R^2}{h_0} \vec{U}_d + 12\pi\mu_2 \frac{R^2}{h_0} \vec{U}_d \quad (3.40)$$

- a second F_{lf} that is due to the viscous dissipation in the dynamic regions of the thin lubrication films

$$F_{lf} = 12\beta\pi R\mu_2 \frac{\vec{U}_d}{\text{Ca}^{1/3}} \quad (3.41)$$

Our estimate for F_H is in agreement with the consensual expression $F_H = 12\mu\pi R^2/h_0 \cdot \mu U_d$ found in the literature [83, 89, 99, 85, 96] although here we have also taken into account the dissipation from the inner flow. Hence, if we balance F_H in the case of an inviscid droplet with the propulsive force from the outer flow F_{U_f} , we recover the Taylor-Saffman prediction $U_d = 2U_f$.

However, in the limit of small capillary numbers, the drag F_{lf} due to the thin films dominates the drag from the outer flow F_H . Indeed, the ratio of the two forces F_H/F_{lf} scales as $\text{Ca}_d^{1/3} R/h_0$. When $\text{Ca}_d^{1/3} \ll h/R$, F_{lf} dictates a velocity

$$\begin{aligned} \vec{U}_d &\propto \frac{R}{h_0} \text{Ca}_d^{1/3} U_f \\ &\propto \left(\frac{R}{h_0}\right)^{3/2} \sqrt{\text{Ca}_f} \vec{U}_f \end{aligned} \quad (3.42)$$

for a droplet pushed by an outer flow U_f . Our analysis yields an exponent $n = 1/3$ in agreement with previous studies that employed a force approach to estimate the effect of the dynamic region of the thin lubrication films [86, 100, 78]. Nonetheless, the exponent $n = 1/3$ is smaller than the ones obtained experimentally, meaning that the drag in the dynamic region of the lubrication films is not sufficient to explain the fast decrease of the droplet velocity with the capillary number Ca_d .

In a seminal article [89], Maruvada and Park (hereafter M&P) explain *the retarded motion of bubbles in Hele-Shaw cells*¹ as an effect of the surfactants in the outer phase, always present in experimental studies to enhance the wetting of the outer phase on the channel walls and to inhibit coalescence. Under certain conditions, surfactants are known to rigidify the interface, i.e. the usual slip boundary condition for a clean interface becomes a no-slip boundary condition [90, 91]. This change in boundary condition does not modify significantly the drag from the far-field flows F_H since in the case of a solid cylinder, its expression is also given by the equation (3.40) [92]. However, M&P notice that if the interface of the droplet is rigid, then viscous stresses are present everywhere in the lubrication films, even in the central region where the thickness of the film e is established. In this region, the continuous fluid is sheared between two parallel moving plates: the static channel wall on one side and the rigid droplet (or bubble) interface moving at the velocity U_d on the other. The authors estimate the shear stresses at the interface by a simple scaling argument

$$\mu \vec{\nabla} u \propto \mu \frac{U_d}{e} \quad (3.43)$$

Prior to the study by M&P, Bretherton had obtained the scaling for the thickness e of the lubrication films in the case of a rigid interface [86] by an asymptotic analysis. He showed that $e/h \propto \text{Ca}_d^{2/3}$ as in the case of the slip boundary condition. Hence, the nature of slip boundary condition at the interface only affects the prefactor. Injecting this result in the

¹Title of their article

scaling for the shear stress, M&P obtain

$$\mu \vec{\nabla} u \propto \mu \frac{U_d}{\text{Ca}^{2/3} h} \quad (3.44)$$

The shear stress applies over the entire surface of the films, of area $\propto R^2$. Therefore, the authors estimate the associated drag force on the drop as

$$F_{lf}^{\text{Maruvada}} \propto 2.01 \mu_2 \frac{\pi R^2}{h_0} \frac{\vec{U}_d}{\text{Ca}^{2/3}}. \quad (3.45)$$

Surprisingly, they omit the drag from the dynamic region of the films and conclude that the overall viscous drag on a circular droplet is

$$F_{\mu}^{\text{Maruvada}} = 12\pi\mu_2 \frac{R^2}{h_0} \vec{U}_d + 2.01\pi\mu_2 \frac{R^2}{h_0} \frac{U_d}{\text{Ca}^{2/3}} \quad (3.46)$$

which yields the scaling $U_d \propto \text{Ca}_d^{2/3} U_f$ at low capillary numbers, in qualitative agreement with their experimental measurements.

To explain their observed value $n \approx 1/2$, Rabaud *et. al.* also invoke the rigid boundary condition of the interface in the presence of surfactants but apply a model developed by Denkov *et. al.* to model the resulting drag force on the droplet. The main difference with the model of Maruvada and Park lies in the scaling law $e \propto \text{Ca}_d^{1/2} h_0$ for the thickness of the lubrication films. This scaling yields

$$F_{lf}^{\text{Denkov}} \propto \mu_2 \frac{\pi R^2}{h_0} \frac{\vec{U}_d}{\text{Ca}^{1/2}} \quad (3.47)$$

for the drag force due to the lubrication films, which translates to

$$\vec{U}_d^{\text{Denkov}} \propto \text{Ca}_d^{1/2} U_f$$

for the velocity of the droplet at small capillary numbers.

However, the scaling $e \propto \text{Ca}_d^{1/2} h_0$ derived by Denkov *et. al.* [63] disagrees with the scaling $e \propto \text{Ca}_d^{2/3} h_0$ obtained in most studies of lubrication in the case of a rigid interface, from the original estimation by Bretherton [86] to recent numerical and analytical investigations [101, 102]. To find the stationary shape of the lubrication films, Denkov *et. al.* explain *we applied the principle of minimal rate of energy dissipation* and argue that *this principle implies that the deformable surface of the wetting film (which is the only “free” internal variable in the system under consideration) would acquire a shape, which ensures minimal rate of energy dissipation* [63]. This reasoning appears to be a misuse of the minimum principle (P3) presented in Chapter 2 since, as we discussed, it does not select stationary states of a system. This contradiction could explain the different scaling found by Denkov *et. al.*

Finally, as suggested by I. Cantat [103], it is possible to derive an expression of the drag F_{μ} that encompasses all existing results, analytical, numerical and experimental, by

considering the drag both in the dynamic and established regions of the lubrication films for a rigid boundary condition. Going back to our energy production-dissipation balance, the central region of the lubrication films dissipates energy from the viscous shear of amplitude $\mu U_d/e$ in a volume that scales as $\pi R^2 e$. Taking the classic law $e \propto \text{Ca}_d^{2/3} h_0$ for the film thickness, we obtain a total dissipation in the lubrication films with a rigid boundary condition at the interface

$$\mathcal{P}_{lf} = \underbrace{12\beta_1\pi R\mu_2 \frac{\vec{U}_d^2}{\text{Ca}_d^{1/3}}}_{\text{dynamic region}} + \underbrace{12\beta_2\pi\mu_2 \frac{R^2}{h_0} \frac{\vec{U}_d^2}{\text{Ca}_d^{2/3}}}_{\text{established region}} \quad (3.48)$$

which translates to

$$F_\mu = 12\pi \frac{R^2}{h_0} \mu_2 \left[\left(1 + \frac{\mu_1}{\mu_2}\right) + \beta_1 \frac{h_0}{R} \text{Ca}_d^{-1/3} + \beta_2 \text{Ca}_d^{-2/3} \right] \vec{U}_d \quad (3.49)$$

in terms of the droplet drag. The droplet velocity follows easily as

$$\vec{U}_d = \frac{2\vec{U}_f}{\left(1 + \frac{\mu_1}{\mu_2}\right) + \beta_1 \frac{h_0}{R} \text{Ca}_d^{-1/3} + \beta_2 \text{Ca}_d^{-2/3}}. \quad (3.50)$$

For a clean interface or mobile surfactant laden interface, the established region of the lubrication films does not dissipate energy and $\beta_2 = 0$. At low capillary numbers, the droplet velocity scales then as $U_d \propto R/h_0 \cdot \text{Ca}_d^{1/3} U_f$ like in equation (3.42). For a rigid (or mixed) boundary condition, the established lubrication films are sheared and dissipate energy such that $\beta_2 > 0$. This source of energy dissipation dominates all other terms at very low capillary numbers that verify $\text{Ca}_d^{1/3} \ll \beta_2/\beta_1 \cdot R/h_0$. In this case, we recover the result by Maruvada and Park: $U_d \propto \text{Ca}_d^{2/3} U_f$. For higher values of the capillary number, dissipation in the dynamic and established regions of the lubrication films may still dominate dissipation from the far-field flows in the Hele-Shaw cell but contribute equally to the energy dissipation. We find a complex scaling for the droplet velocity

$$\vec{U}_d \propto \frac{2}{\beta_1 \frac{h_0}{R} \text{Ca}_d^{-1/3} + \beta_2 \text{Ca}_d^{-2/3}} \vec{U}_f. \quad (3.51)$$

An estimation in the form $U_d \propto \text{Ca}_d^n U_f$ over two to three decades in capillary number and thereby less than a decade $\text{Ca}_d^{1/3}$ can yield values of n between $1/3$ and $2/3$ which can explain the discrepancy in the experimental measurements [89, 63, 85].

Finally, given that the predicted drag (3.49) contains terms of order $\text{Ca}_d^{2/3}$, $\text{Ca}_d^{1/3}$ and Ca_d^0 , it can only be verified experimentally by covering a very wide range of low capillary numbers, over three decades at least. Hence it is a true experimental challenge.

Part II

Experimental study of droplet actuation with confinement gradients

In this second part of the manuscript, we implement confinement gradients in 2D microfluidic devices and demonstrate the key droplet operations that are production, transport, guiding and trapping.

Chapter 4

Guiding and trapping drops with rails and anchors

“Une petite citation par quelqu’un d’intelligent qui avait quelque chose d’intéressant à dire”.
Untel, souvenir.

As discussed in the introduction, the basic structure of a 2D microfluidic device is a Hele-Shaw cell, a channel in which droplets are free to move in any direction in the plane. This is the strength of the approach: it opens up new perspectives in droplet microfluidics by allowing a droplet to move around with minimal interactions with other droplets present in the channel. However, the 2D format of the device raises the issue of guiding the drops, a task which is mainly achieved with the channel walls in serial droplet microfluidics.

In this chapter, we demonstrate a passive technique for droplet guiding and trapping that relies on gradients of confinement and bypasses the need for solid side walls in a 2D microfluidic device.

4.1 Guiding and trapping in *serial* microfluidics

4.1.1 Guides

In *serial* microfluidics, guiding is not strictly speaking an issue since the droplets flow along the microchannel in one direction. It is only at branching junctions that a droplet is offered multiple routes and hence, guiding comes down to distributing droplets between the different outlets.

The typical branching configuration is a T- or a Y-junction as sketched on Fig. 4.1. A large amount of literature is devoted to understanding the natural behavior of a drop or a train of drops at such a junction. These studies were motivated by observations of periodic

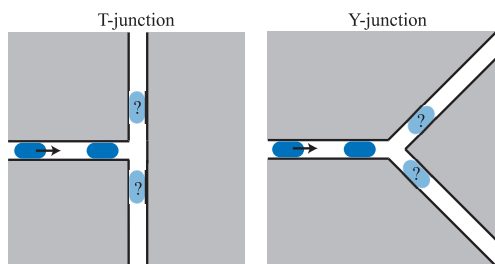


Figure 4.1: Sketch of a T- and Y-junction at which an oncoming train of droplets has two possible trajectories.s

or even chaotic distribution patterns of the droplets across the two outlets [104, 105]. Empirically, it was shown that a droplet chooses the branch with the lowest hydrodynamic resistance. As a result, when the branches do not contain any droplets, the shortest branch is chosen. However, because a droplet increases the hydrodynamic resistance of the branch it is in, the direction taken by a drop at the junction actually depends on the position of the other drops downstream in the network.

Careful modeling of these phenomena provides the necessary ingredients to elaborate passive strategies for traffic control. By playing with the geometry of the network, it is possible to split a train of drops in an ordered manner or to rearrange the drops in the train. Nonetheless, the behavior of a given device is sensitive to many flow parameters (channel geometry, drop size, fluid viscosities, interfacial tension, flow velocity, etc...) such that reproducibility is a critical issue.

This problem is robustly overcome by implementing active sorting techniques on chip. Strategies differ on the nature of the force used to push the drops into the selected branch. The most common approach [106] relies on two localized electrodes to apply a dielectrophoretic force on the drop, as shown on Fig. 4.2.a-c. While this approach allows kHz actuation, the actuation occurs only between the tip of the two electrodes and results in a local deflection of trajectory rather than a long-distance guiding of the droplet.

An alternative solution consists in using spatial modulations of temperature instead of electric fields to modify the trajectory of a droplet. Indeed, a gradient of temperature across a drop is known to create a Marangoni force that pulls the drop towards the hotter regions [107] and this effect has been used to move a droplet across a Hele-Shaw cell [108]. More recently, Selva *et. al.* integrated an addressable heating source at a Y-junction in a microfluidic device and demonstrated that temperature gradients could be used to drive drops towards the selected outlet branch [109]. However, they observed that the drop moved towards the coldest regions of the microchannel, in contradiction with the classical thermo-Marangoni effect. They later found that the temperature gradients are in fact inducing channel deformations alike to the chemical swelling described in Chapter 3 [110]. Consequently, Selva *et. al.* are effectively using confinement gradients to manipulate the drops. Nonetheless, the heating source is cumbersome and cannot easily scale to large 2D microfluidic devices.

A more flexible solution was developed by Maria-Luisa Cordero at LadHyx. It relies

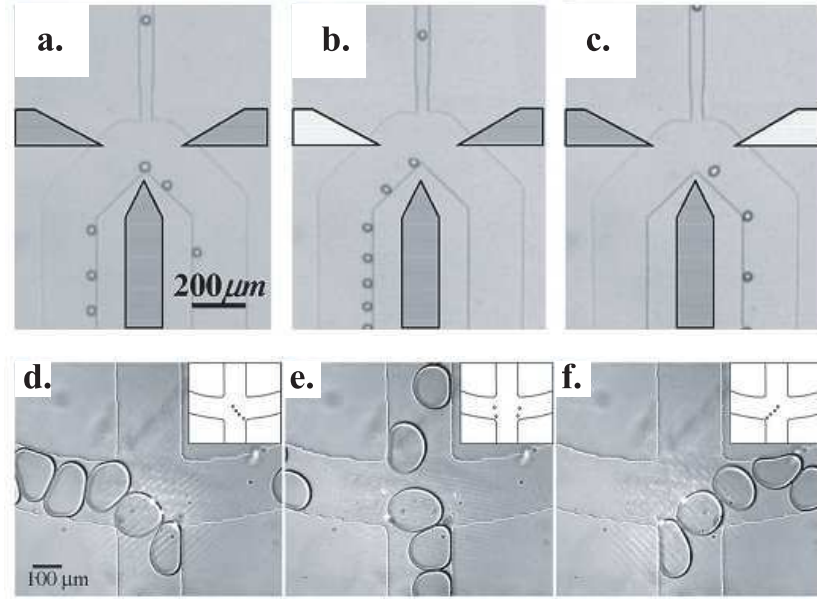


Figure 4.2: Two examples of active droplet distribution at a branch in a microfluidic network. **a-c)** Electrodes are used to apply a dielectrophoretic force on the droplets passing through the junction. The droplets are attracted towards the energized electrode colored in white and can either **a)** distribute randomly (no energized electrode), **b)** go left or **c)** go right. Reproduced from Ahn *et. al.* [106]. **d-f)** Multiple laser spots are focused in the device to form the patterns drawn on the insets of the images. When a drop approaches a laser spot, its interface heats up which creates thermo-solutal-Marangoni recirculations of the fluid in and around the drop. As a result, the drop is pushed away from the laser spot. [36]. Three patterns are used to send the drops **d)** to the left, **e)** up the center or **f)** to the right. Reproduced from Cordero *et. al.* [35].

instead on a soluto-Marangoni force induced by locally heating the interface of the drop with a focused laser. In this case, the actuation strongly modifies the behavior of the drops and deflects the trajectories over significant distances. Furthermore, the laser can be moved in real-time anywhere in the device, allowing for the complex operations featured in Fig. 4.2.d-f. to be implemented.

Initially, we considered the possibility of using mobile laser spots to control drops in 2D microfluidics. This would provide a microfluidic tool with ultimate versatility: a programmable 2D chamber in which droplets could be moved to any position following any desired trajectory. Unfortunately, soluto-Marangoni actuation by laser heating lacks robustness as it strongly depends on the surfactants covering the droplet and thereby on the chemical contents of the droplet itself.

4.1.2 Traps

Trapping drops in *serial* microfluidics comes down to solving the very annoying and incredibly frequent delivery-truck-in-a-one-lane-street (DTOLS) problem introduced at the

beginning of the manuscript. An obvious solution would be to have regularly spaced large parking spaces into which the garbage truck could shift away from traffic while awaiting its load of waste. Unfortunately, this solution is impractical in any city filled with disobedient drivers like Paris since 99 % of the time, the cleverly designed garbage truck parking spaces would be occupied by parked cars begging for a traffic ticket.

Fortunately, droplets are far less prone to breaking the law and the side pocket solution is not doomed to failure. The trick however is then in how to attract the droplets into the pockets and releasing them later on, as droplets are not known for their natural sense of initiative.

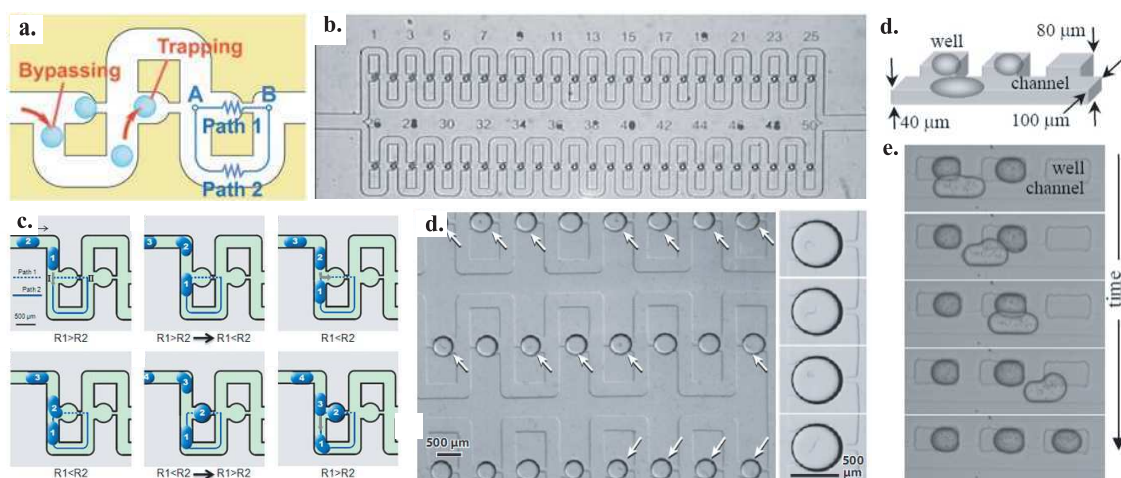


Figure 4.3: Three examples of droplet trapping in serial microfluidics. **a-b** The pocket-in-a-loop solution developed to trap microfluidic beads. Reproduced from Tan *et. al.*, PNAS 2006. **c-d** The pocket-in-a-loop solution applied to microfluidic droplets containing *C. Elegans*. Reproduced from Shi *et. al.*, Lab Chip 2008. **e-f** The interfacial tension based solution introduced by S. Fraden group. Reproduced from Shim *et. al.*, J Am Chem Soc, 2007.

To my knowledge, the first and very elegant strategy that addresses the DTOLS problem in microfluidics deals with the docking of large microfluidics beads [111]. In this approach, the pocket is combined with a loop to ensure that beads always enter empty pockets and flow around occupied ones as sketched in Fig. 4.3.a. When the pocket is empty, the hydrodynamic resistance of the pocket by-pass is smaller than the hydrodynamic resistance of the loop such that fluid flows mainly into the pocket. When the pocket is occupied by a bead, the by-pass is closed and the fluid flows through the loop. By placing many pockets in series, it is then possible to form an array of trapped beads (see Fig. 4.3.b). The beads can also be released, either by reversing the flow or by forming a vapor bubble in the pocket with a focused laser.

This design does not work exclusively with solid beads and it was later applied to trap droplets [112] as shown on Fig. 4.3.c-d. A number of improvements were then implemented

in order to make drops directly into the traps [113] or to create an array of drops with a concentration gradient [114].

Instead of relying on viscosity and hydrodynamic resistance, an alternative approach developed by Fraden *et. al.* utilizes the interfacial tension specific to drops as a mean to attract the droplets into the side pockets [115]. In this case, the pockets are closed but have a greater height than the main channel as illustrated by Fig. 4.3.e. The droplets, larger than the size of the main channel, are flowing confined by the channel walls. When a drop reaches a pocket, it expands into the cavity where it is less confined in order to reduce its surface energy. If the volume of the trap matches the volume of the droplet, the droplet is entirely withdrawn from the flow and prevents following droplets from entering the same trap. The main inconvenience of this approach however is that droplets cannot be easily ejected from the traps.

A noteworthy although trivial feature of all these trapping methods is that they preserve but reverse the order of the drops: the first droplet in the train ends up being at the tail of the array and vice versa. An approach for which order is not preserved is the DropSpot method developed by the Weitz group [116] who looked at the DTOLS problem with a new eye and asked the question: what if the garbage truck was the solution to droplet trapping? Indeed, the cars piled behind the garbage truck are nicely arrayed after all. They designed a device containing dozens of microfluidic channels with successive constrictions, as shown on Fig. 4.4. Owing to interfacial tension, the droplets resist going through the constrictions where they are more confined and a stop-and-go traffic jam motion appears in the channels. When the flow is stopped, the droplets then rearrange to occupy only the wide pockets where they minimize their surface energy.

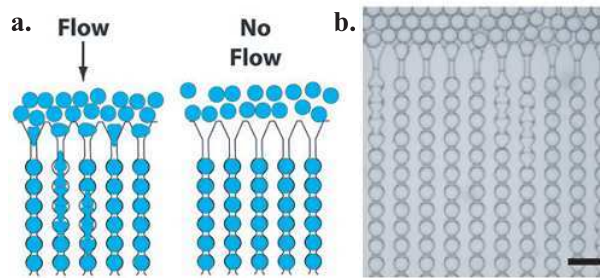


Figure 4.4: **a.** Schematics of the architecture and mechanism of a DropSpot microdevice. **b.** Image of the traffic jams forming in the microchannels with constrictions. Reproduced from Schmitz *et. al.* [116].

In summary, all passive trapping techniques developed to date are based on solid pockets designed to host one or a few droplets and they only differ in the strategy employed to attract the droplets into the pocket. Huebner *et. al.* showed that solid traps can be easily adapted to 2D microfluidics. In their study, they added a number of traps resembling the original format by Tan *et. al.* featured in Fig. 4.3.a inside a Hele-Shaw cell and thereby captured an array of drops as shown in Fig. 7 on our introduction. Nevertheless, this elegant solution departs from our paradigm of suppressing side walls in 2D microfluidic

devices.

4.2 Droplet manipulation by confinement gradients in the context of microfluidics

Overall, the unbounded geometry of a 2D microfluidic device calls for innovative strategies to guide and trap drops. Drawing on our understanding of droplet trajectories in non-parallel microchannels presented in Chapter 3, we designed Hele-Shaw cells with localized height variations that serve this purpose: rails and anchors.

Microchannels made using standard soft lithography techniques [6, 7, 117] necessarily have parallel top and bottom walls such that continuous confinement gradients cannot be fabricated. However, multilayer soft lithography enables to the prototyping of microfluidic devices with step changes in the channel height. Hence, this technique can be used to etch secondary structures inside a microfluidic Hele-Shaw cell that locally reduce (negative structures) or increase (positive structures) the height of the chamber, as illustrated in Fig. 4.5. The in-plane geometry of these structures can be whatever is needed, provided its in-plane size exceeds its depth or height.

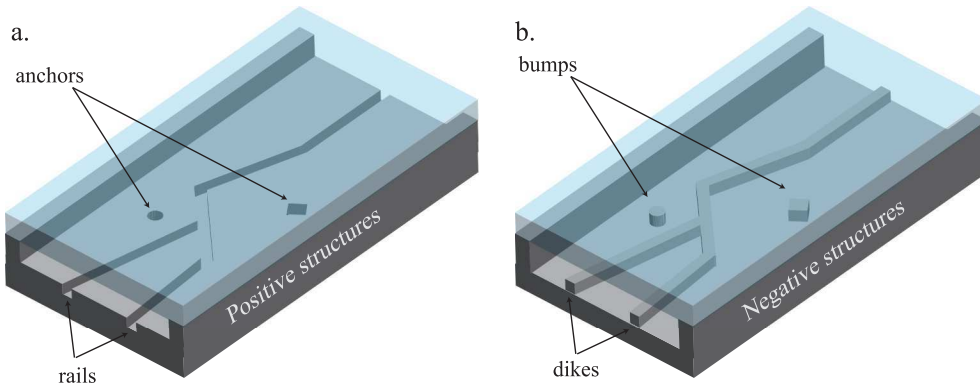


Figure 4.5: 3D representation of a 2D microchannel with various types of etched microstructures: **a.** positive structures like rails and anchors; **b.** negative structures like posts or dikes.

Recalling the rules of thumb established in Chapter 1 from energy arguments 1.7, we expect negative structures to repel non-wetting pancake drops because they locally increase confinement. In that sense, elongated dikes and bumps could be used to create regions of exclusions for the droplets in the 2D channel and serve the purpose of walls and posts. Reciprocally, positive structures like grooves or holes should attract the drops since they decrease confinement. In terms of energy, these structures are seen by the drops as valleys or wells of surface energy, respectively. Hence, we expect grooves to guide drops and holes to trap drops. Thereafter, we focus on these structures that we name rails and anchors.

4.3 Rails and anchors: proof of concept and applications

The paragraphs that follow summarize the results obtained in collaboration with Paul Abbyad for the Laboratoire d'Optique et Biosciences (LOB) at Ecole Polytechnique. They were published in a Lab-On-a-Chip article in 2010 [118] that is included at the end of this chapter.

First, we demonstrate that rails and anchors are able to guide and trap pancake droplets, respectively, and then investigate in more detail the trapping performance of an anchor against a train of droplets. We evidence a variety of trapping regimes that can be controlled using the outer flow. Last, we show how the large surface area of an anchored droplet that is in contact with the outer flow can be used to actively modify the chemical contents of the droplet. This feature allowed Paul Abbyad to design a microfluidic device to study the sickle cell disease.

4.3.1 Proof of concept

To test the guiding ability of rails, we fabricate microfluidic devices that contain a flow focusing module for droplet production and a Hele-Shaw cell with etched grooves of various geometries. In a first experiment, we flow large pancake droplets of radii $R \approx 200 \mu\text{m}$ into a chamber containing a sinusoidal rail of width and depth significantly smaller than the radius of the drops. As illustrated by Fig. 4.6, the drops are advected from left to right following the winding rail and not in a straight line as they would if the Hele-Shaw cell were perfectly flat.

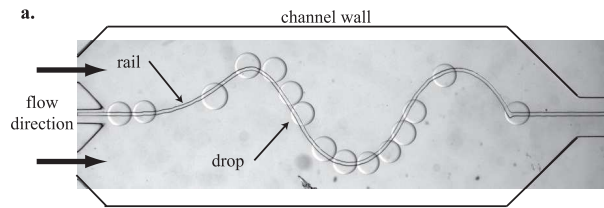


Figure 4.6: Microscope images of multiple water drops of radii $R \approx 200 \mu\text{m}$ guided from left to right along a sinusoidal rails ($50 \mu\text{m}$ in width and $50 \mu\text{m}$ in depth) in an external flow of fluorinated oil. The Hele-Shaw cell has a height of $h = 100 \mu\text{m}$

Similarly, we perform experiments with a Hele-Shaw cell containing an array of anchors $50 \mu\text{m}$ in depth and diameter and flow a large number of pancake drops through the chamber. As shown on Fig. 4.7, once droplet production stopped, an array of trapped drops remains in the channel. This experiment also reveals that an anchor is able to trap drops much larger than its own size. Here, the drops are approximately $300 \mu\text{m}$ in diameter, roughly six times the anchor's diameter.

In a third experiment, we trap a single drop on a single anchor against a continuous outer flow and observe how the droplet behaves as the outer flow increases in magnitude.

Figure 4.7 shows that the rear end of trapped drop aligns with the anchor and that the drop deforms under the drag from the outer flow. As the flow rate Q is increased from $4 \mu\text{L}/\text{min}$ to $12 \mu\text{L}/\text{min}$, the drop elongates more and more until it finally detaches from the anchor at $Q = 12.5 \mu\text{L}/\text{min}$. This defines the critical flow rate Q^* of outer flow velocity U^* above which the trapping force from the anchor is no longer sufficient to resist the drag from the outer flow.

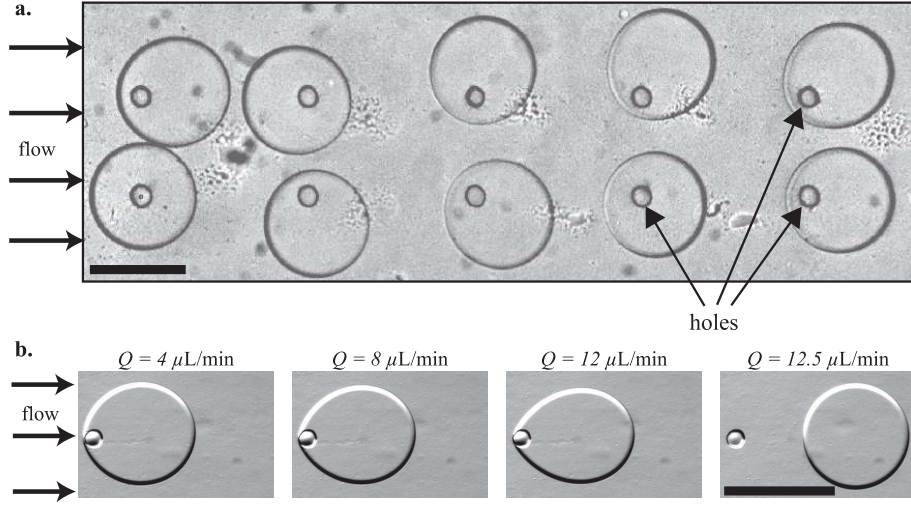


Figure 4.7: **a.** Image of an array of droplets trapped by anchors of $50 \mu\text{m}$ in depth and diameter in a Hele-Shaw cell of gap width $h = 35 \mu\text{m}$. **b.** Four images of a drop trapped by an anchors $100 \mu\text{m}$ in diameter and $50 \mu\text{m}$ in depth, in a Hele-Shaw cell of gap width $h = 50 \mu\text{m}$. The drop deforms more and more as the outer flow rate Q increases until it detaches at a critical flow rate $Q^* = 12.5 \mu\text{L}/\text{min}$.

Overall, these experiments evidence that small secondary structures like rails and anchors are able to significantly influence the dynamics and/or trajectory of large droplets flowing in a 2D microfluidic chamber. In practical applications however, multiple drops may be flowing inside the microchannel such that droplets will collide with one another. Therefore, we investigate how an anchor performs when a train of droplets rather than a single one is flown into the Hele-Shaw cell.

Figure 4.8.a illustrates the experimental setup: a regular stream of water droplets of radius $R \approx 180 \mu\text{m}$ is produced upstream of the microfluidic chamber of height $h = 50 \mu\text{m}$ that contains a single small anchor, $75 \mu\text{m}$ in diameter. The drops are advected through the Hele-Shaw cell by an outer flow of oil whose flow rate Q can be controlled independently of the droplet production. As expected, if the flow rate Q exceeds the critical flow rate $Q^* = 16.5 \mu\text{L}/\text{min}$ for this configuration, the droplets are not trapped by the anchor and they are regularly advected across the test section. However, within a range of flow rates $10 \mu\text{L}/\text{min} \leq Q < Q^*$ below the threshold Q^* , the stream enters a *buffering* mode: a single droplet is trapped by the anchor until the following one in the stream arrives, collides, and pushes it out of the hole, thus replacing it. This behavior is illustrated by the time

sequence shown in Fig. 4.8.b. If we decrease the flow rate Q further, the buffering mode switches to a parking mode: a unique droplet is held in place by the anchor and remains trapped even when following drops collide with it. This behavior is illustrated by the time sequence shown in Fig. 4.8.c.

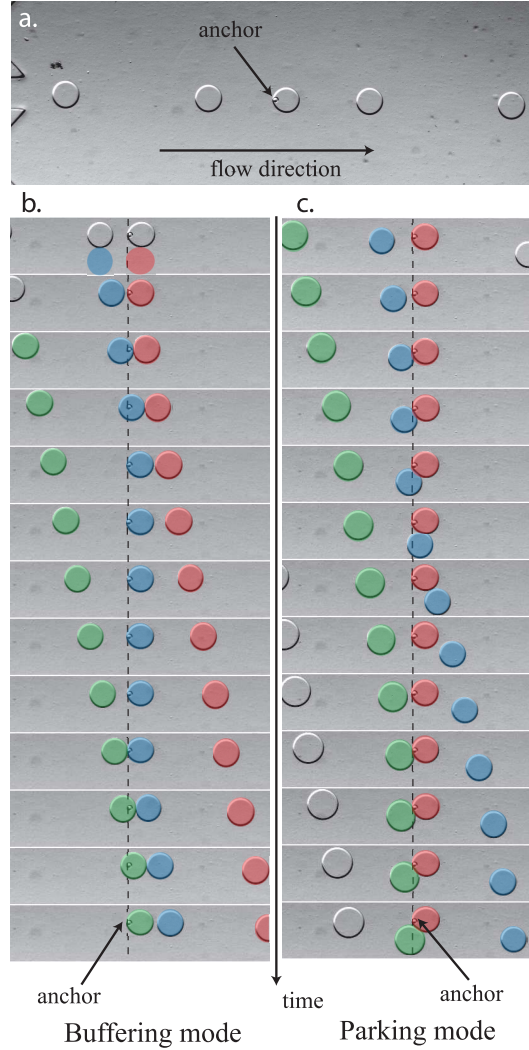


Figure 4.8: **a.** A stream of droplets of radius $R = 180 \mu\text{m}$ is flowing from left to right in a Hele-Shaw cell of height $h = 50 \mu\text{m}$ over a anchor $75 \mu\text{m}$ in diameter. **b.** For an outer flow rate $Q = 12 \mu\text{L}/\text{min}$, the stream exhibits a buffering mode (sequence frame rate: 1 frame per second) **c.** For $Q = 6 \mu\text{L}/\text{min}$, the stream exhibits a parking mode (sequence frame rate: 0.5fps). Droplets are artificially colored by image processing to ease the tracking of individual droplets.

This experiment reveals the flexibility of the anchors and rails, contrasting with the classical approaches that rely on solid walls spanning the height of the channel.

4.3.2 Controlling the chemical environment of an anchored drop

Another key asset of anchored droplets compared to classical solid traps [33] is the large surface area that an anchored droplet shares with the flowing outer liquid. This surface allows the efficient exchange of chemicals like gases between the droplet and the outer fluid. Furthermore, because flows are laminar in a Hele-Shaw cell, it is possible to have parallel streams of the outer liquid that contain different chemicals and thereby create a heterogeneous chemical landscape inside the 2D microfluidic device.

As shown in Fig. 4.9, we combined these two aspects to create an array of drops anchored in a heterogeneous chemical environment. To this end, we used a Hele-Shaw cell that has two inlets for the outer phase. One inlet is used to inject fluorinated oil with a low concentration of dissolved carbon dioxide gas while the other is used to inject oil with a higher concentration of CO_2 . If the flow rates are equal, the streams have equal width in the Hele-Shaw cell which is chemically split in two as sketched on Fig. 4.9. Hence, the two lines of anchored droplets are in a different chemical environment. The drops contain a pH indicator which reacts to the carbonic acid produced by the carbon dioxide dissolving in the water of the droplet. As a result, the droplets on the top become yellow while those on the bottom remain blue.

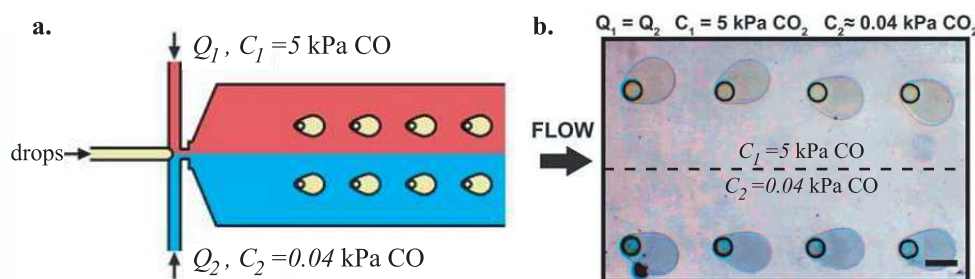


Figure 4.9: **a.** Schematic of the flows in the microfluidic chip for gas exchange. The flow rates and gas contents are annotated as follows: Q_1 flow rate of oil inlet one, Q_2 flow rate of oil inlet two, C_1 gas partial pressure of oil inlet one and C_2 gas partial pressure of oil inlet two. When $Q_1 = Q_2$, the two streams of oil split equally in the Hele-Shaw cell. **b.** Color image of trapped droplets containing the pH indicator bromothymol blue. The oil flow rates, Q_1 and Q_2 , are both held constant at $2 \mu\text{L}/\text{min}$. The upper oil stream contains 5 kPa dissolved CO_2 and the lower oil stream contains ambient dissolved CO_2 (0.04 kPa). The droplets exposed to the upper oil stream are acidic and yellow while those exposed to the lower oil stream are neutral and blue. The scale bar represents $200 \mu\text{m}$.

4.3.3 Application to the study of the sickle cell disease

Last, we briefly summarized the work of Paul Abbyad on the sickle cell disease, the details of which can be found in the article at the end of the chapter.

Sickle cell anemia is a genetic disease which causes the hemoglobin of the red blood cells to polymerize when deoxygenated. The red blood cells then take on a “sickle” shape, hence the name of the disease. Sickling is reversible and highly dependent on oxygen concentration. Red blood cells are exposed to cycles of oxygen rich and oxygen poor environments in vascular circulation and therefore, it is of biological importance to study the effect of these cycles on red blood cell sickling.

To this end, Paul designed a microfluidic chip similar to the one shown on Fig. 4.9 that enables the arraying of buffer droplets containing red blood cells and the flow of either oxygenated or deoxygenated fluorinated oils. By controlling the flow rates of these two oil streams, it is possible to control spatially and temporally the oxygen concentration of the droplets in the array and in particular to perform oxygenation/deoxygenation cycles *in vitro* that mimic the vascular circulation. This technique has promising applications in the search for new drugs to treat the sickle cell disease.

4.4 A model and measure of the trapping force

In this section, we summarize the results obtained in collaboration with Sungyon Lee concerning the theoretical modelling of the anchoring mechanism. These results are published Physical Review Letters [119]. The letter and detailed calculations are included at the end of this chapter.

The aim of the study is to measure and model for the force F_γ generated by an anchor. We use the drag force F_{U_f} from a controlled outer flow to probe the trapping mechanism. This allows us to measure experimentally the anchoring force. We also describe a simple theoretical model that yields a scaling law for F_γ in very good agreement with experimental measurements.

4.4.1 The force balance on an anchored drop

Consider a pancake droplet of radius R placed over an anchor of diameter d in a Hele-Shaw cell of height h with an outer mean flow of far-field height averaged velocity U_f . This configuration is sketched on Fig. 4.10 which shows an image of a large anchored droplet.

When the droplet is trapped and held still by the anchor, it is in a state of equilibrium such that the drag force F_{U_f} from the outer flow is exactly balanced by a trapping force F_γ of the anchor due to the local decrease in confinement. Experimentally, we observe that a droplet remains trapped on the anchor until the outer flow rate exceeds a critical value Q^* , which translates to a critical value U^* in terms of the outer flow velocity.

Conceptually, when the flow velocity is equal U_f^* , the drag force F_μ^* from the outer flow exactly matches the largest force F_γ^* that the anchor can apply on the drop. Hence, if we know how to express the drag force as a function of the outer flow velocity, then the measured value of the untrapping flow velocity U^* can be used to estimate the maximum trapping force F_γ^* of the anchor.

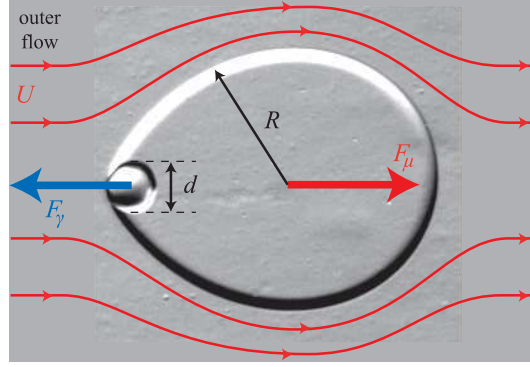


Figure 4.10: Two forces apply on an anchored droplet of radius R trapped by an anchor of diameter d in an outer flow of velocity U_f : F_γ , the trapping force from the anchor, balances F_{U_f} , the drag force from the outer flow. The scale bar represents $200 \mu\text{m}$.

4.4.2 A model and measure of the drag force F_d

We model the outer flow around the stationary pancake droplet using the classical height-averaged potential flow theory introduced in Chapter 2. The energy production-dissipation balance yielded an expression (3.39) for the force applied by a uniform outer flow on a pancake droplet. Here, we recall the classical force based approach. In a Hele-Shaw cell, the in-plane viscous shear stresses are negligible compared to the pressure gradients and the pushing force F_{U_f} reduces to the pressure drag around the droplet. Solving the Hele-Shaw equations (2.10) yields expressions

$$p_o = -24 \frac{\mu U_f}{h^2} \cdot x + \text{cst and} \quad (4.1a)$$

$$F_{U_f} = 24\pi \frac{\mu U_f R^2}{h} \quad (4.1b)$$

for the outer pressure field p_o at the interface and the resulting drag force F_{U_f} respectively. Asymptotic analyses of the full flow field in the case of a stationary inviscid bubble [89] and around a solid cylinder [92] confirms these expressions.

Nonetheless, the pushing force of an outer flow on a stationary pancake droplet in Hele-Shaw cell has never been measured. In a seminal article [73], G.I. Taylor shows that it is possible to extract the drag on a stationary droplet by analyzing the deformations of the drop due to the flow. Indeed, according to the Young-Laplace equation (1.1), the shape of the drop is directly related to the pressure jump across the interface. Thereby, it is related to the pressure field p_o in the outer phase and consequently to the drag force F_{U_f} .

Assuming the pressure around the droplet is captured by the expression above (4.1a), we solve the Young-Laplace equation. Using polar coordinates (r, θ) of origin positioned on the center of the droplet to describe the shape of the drop, we obtain an expression for the local deviations $\delta r(\theta) = r - R$ in the radius of the droplet from away from its equilibrium

value R :

$$\frac{\delta r}{R} = \frac{48}{\pi} \text{Ca}_f \frac{R^2}{h^2} (1 - \theta \sin \theta) \quad (4.2)$$

where $\text{Ca}_f = \mu U_f / \gamma$ is the capillary number based on the outer flow. In particular, it gives a scaling for the elongation L of the deformed droplet, equal to the ratio of the elongated length of the drop over its equilibrium diameter: $L \propto \text{Ca}_f R^2 / h^2$.

To verify this scaling, we performed several hundreds of experiments in which we measured the elongation of an anchored droplet while varying the channel height h , the anchor diameter d , the outer flow velocity U_f , the fluids used and thereby the viscosity μ and the interfacial tension γ . As a result, we covered almost two decades in flow based capillary number Ca_f . On Fig. 4.11, we plot $L \cdot h^2 / R^2$ versus Ca_f . The data collapses onto two distinct lines which both agree with the theoretical scaling $L \propto \text{Ca}_f R^2 / h^2$. The two groups of data points corresponds to the two different surfactants used in the experiments, which suggests that Marangoni effects are present at the interface.

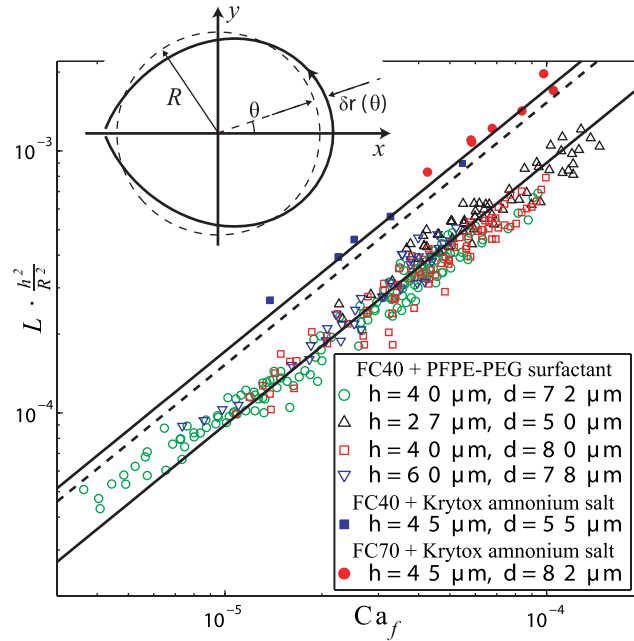


Figure 4.11: **Inset:** Sketch of the polar coordinates for the deformations $\delta r(\theta)$ from the static radius R . **Main panel:** Elongation $L = \delta r(0)/R$ of anchored droplets, rescaled by h^2/R^2 , as a function of the oil capillary number Ca_f for various channels, liquids and surfactants. The solid lines are a linear fits of the two distinct data groups while the dashed line is the theoretical prediction for equation (4.2).

Nevertheless, the elongation measurements are in agreement with the predicted scaling for the pressure variations around the droplet. Hence, it validates the scaling $F_{U_f} \propto \mu U_f R^2 / h$ for the drag force.

4.4.3 The theoretical estimate of the trapping force F_γ

The force F_γ applied by the anchor on the drop originates in the confinement gradient created by the hole in the Hele-Shaw cell. According to the result (3.36) obtained in Chapter 3, F_γ is proportional to the gradient in the surface area S of the droplet as it moves about the anchor: $F_\gamma = \gamma \cdot \vec{\nabla} S$.

In order to evaluate the magnitude of this force, we start by estimating the difference ΔS between the surface area of a droplet when it is over an anchor or away from the anchors. The shape of the droplet over the anchors is modeled as a circular pancake shape combined with a spherical cap extending in the anchor, which best describes the Surface Evolver rendering shown on Fig. 4.12.a.

The curvature of the spherical cap in the anchor has to match the curvature of the interface at the rim of the pancake. For a large pancake ($R \gg h$), this curvature is $2/h$, yielding a radius of curvature ρ of the spherical cap in the anchor $\rho = h/4$. If ρ is smaller than half the anchor diameter $d/2$, then the spherical cap fits entirely into the anchor. The droplet then fills the anchor until it touches the bottom of the hole. In this case, the depth of the anchor e plays an important role. If on the other hand ρ is larger than $d/2$, the spherical cap cannot enter completely into the anchor and, provided $e > d/2$, the droplet does not touch the bottom of the hole. This is the situation depicted in Fig. 4.12.a. Overall, the parameter $b = d/h$ determines the behavior of the drop and in the rest of the discussion, we consider the case of $b < 2$.

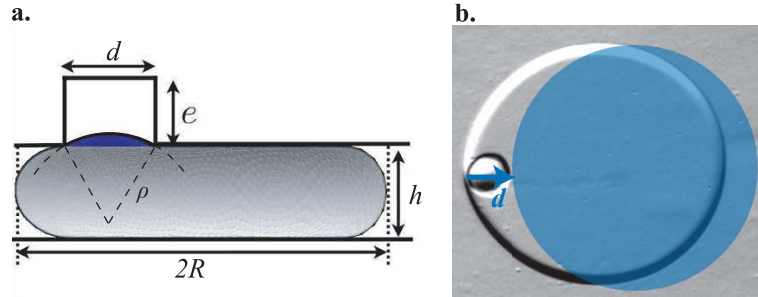


Figure 4.12: **a.** Surface Evolver [120] rendering of an anchored droplet of outer radius R inside a microchannel of height h over an anchor of diameter d . **b.** Illustration of the imaginary displacement of the droplet out of the anchor that is considered to estimated the gradient of surface area.

A geometric study of the shape shown on Fig. 4.12.a yields that the surface area of the droplet over the anchor is indeed smaller than the nominal surface area and we obtain the expression

$$\Delta S \approx -\frac{\pi}{2} b f(b) h^2 (1 + o(h/R)) \quad (4.3)$$

in which

$$f(b) = \frac{b}{2} - \frac{4}{3b} \left[1 - \left(1 - \frac{b^2}{4} \right)^{3/2} \right]. \quad (4.4)$$

Last, we estimate the gradient of surface area by observing that the change in surface area occurs as the droplet moves over a distance d equal to the diameter of the anchor, as illustrated on Fig. 4.12.b. Hence, we obtain

$$F_\gamma \propto \gamma \frac{\pi}{2} h f(b) . \quad (4.5)$$

4.4.4 Comparison with the measured trapping force

Balancing the theoretical expression for the two forces F_γ and F_{U_f} yields a predicted scaling law for the untrapping velocity

$$U_f^* \propto \frac{\gamma}{\mu} f(b) \frac{h^2}{R^2} \quad (4.6)$$

which can be written in terms of the critical capillary number Ca_f^* as

$$\text{Ca}_f^* \propto f(b) \frac{h^2}{R^2} . \quad (4.7)$$

Experimentally, we measured the untrapping flow velocity U_f^* for droplets of various radii R between $75 \mu\text{m}$ and 1 mm trapped by anchors of different dimensions $h = 27, 40, 45, 60 \mu\text{m}$ and $d = 50, 55, 72, 78, 80, 82 \mu\text{m}$. We also used two different oils (FC-40 and FC-70 fluorinated oils) for the outer fluid, of the viscosities $\mu = 4.1 \text{ cP}$ and 16 cP . To change the interfacial tension, we mixed two different surfactants (PEG-PFPE or Krytox ammonium salt) yielding $\gamma = 20 \text{ mN/m}$ and 10 mN/m respectively. In Fig. 4.13, we plot the collected data rescaled in terms of Ca_f^* and $f(b)h^2/R^2$. The data points all collapse on a single line, validating the scaling law (4.5) for the trapping force F_γ . In particular, it supports the use of d as the characteristic length scale to estimate the gradient of the droplet surface area.

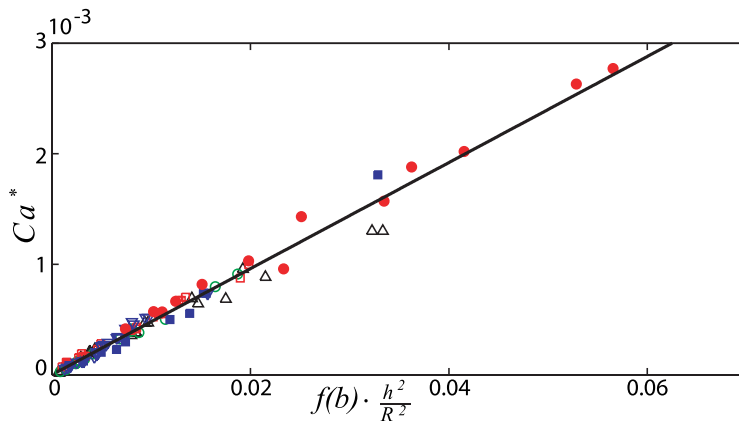


Figure 4.13: Critical capillary number Ca_f^* plotted against $f(b)h^2/R^2$ for the channel geometries, liquids and surfactants listed in the legend of Fig. 4.11. The solid line is a linear fit of the data.

Finally, using the characteristic values $h = 100 \text{ } \mu\text{m}$, $d = 100 \text{ } \mu\text{m}$ and $\gamma = 10^{-2} \text{ N/m}$, we find that the anchoring force F_γ is in the range of 100 to 1000 nN, orders of magnitude stronger than forces generated using optical tweezers [121] or dielectrophoresis (of the order of 10 nN) for example.

4.5 Towards addressable 2D droplet arrays

In a recent review [122], Pompano *et. al.* survey droplet compartmentalization and its applications. They distinguish bulk emulsions from arrays in which droplets have a specific spatial organization. They comment that “bulk emulsions are well suited for high-throughput analysis of initially equivalent droplets to obtain statistical data, such as for directed molecular evolution, screening for cellular behaviors by fluorescence-activated droplet sorting, or emulsion-based PCR” and argues that “for multiplexed experiments involving droplets of different compositions, such as large-scale screening of reaction conditions, indexing (spatial indexing in an array for example) is required”.

In my opinion, indexing is not sufficient to aim for applications which involve multiplexed experiments. Individual droplets in the array must also be accessible to readout obviously but also to combination, dilution, extraction, etc... In other words, the droplet array must be addressable. As argued in the introduction, if microtiter plates have become a lab standard, it is not just because they provide small volume arrayed equivalents of test tubes but also because the contents of the microwells are easily accessible by pipetting.

To date, most microfluidic droplet array technologies strongly lack accessibility. Digital microfluidics [29, 123] are an exception but at the cost of a complex and expensive technology which has yet failed to scale in number and volume with existing microwell technologies. The SlipChip [124, 125] developed by Ismagilov and co-workers is a clever approach to 2D droplet microfluidic that does not require an external flow of oil. Instead, droplets are stored in pockets etched into two glass plates which are held pressed together. By sliding one plate relative to the other, wells from one plate can be aligned with wells on the other to fuse droplets, allowing successive chemical reactions or dilutions to be performed on chip. Figure 4.14 reproduced from Du *et. al.* [124] illustrates the SlipChip mechanism. An inconvenient of this approach is that all droplets are actuated simultaneously and not selectively.

Our rails and anchors technology has potential for selective accessibility owing to what some might consider as its weakness: the droplets do not firmly interact with the etched structures such that they can derail from rails or break free from anchors. Above, we showed how easy it is to create a 2D droplet array with regularly patterned anchors. If we are then able to trigger local derailing or untrapping events in a controlled manner, then the array becomes selectively addressable.

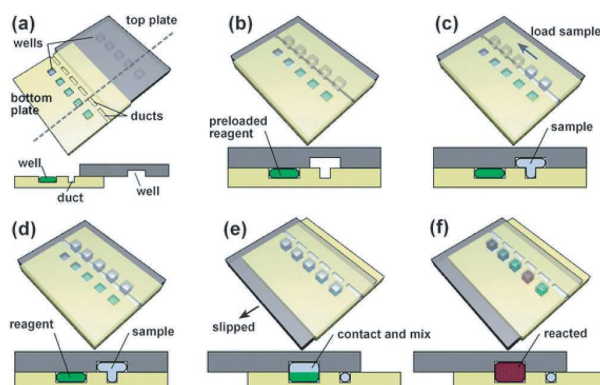


Figure 4.14: The SlipChip technology as presented by Du *et. al.* [124].

4.5.1 Combining rails and anchors with laser actuation

The original endemic technology of our microfluidic laboratory is droplet actuation by laser [35, 37]. To summarize the basic principle, when an infrared laser is focused on the interface of an aqueous droplet, it locally heats the water and locally changes the interfacial tension. The gradient of interfacial tension then induces flow and the droplet *swims* away from the laser.

Furthermore, the magnitude of the forced applied by the laser on the droplet was measured to be above 100 nN, a range similar to the range of forces applied by anchors and rails on droplets in our geometries. Hence, droplet actuation is an ideal candidate to implement active untrapping and derailing events.

Along with Etienne Fradet and Craig McDougall, we designed various 2D droplet microfluidic devices that allow selective manipulations within droplet arrays. This includes ordered arraying, selective removal and on-demand fusion of droplet pairs in a 2D format. This results were published in Lab-On-a-Chip [126] and the article included at the end of this chapter describes how each operation is implemented.

4.6 Summary and discussion of Chapter 4

Rails and anchors are simple and elegant techniques to guide and trap droplets in a 2D microfluidic device. Owing to their small size, they only weakly perturb the flow of external fluid but significantly interact with pancake droplets. The effect on a drop of an etched microstructure can be adjusted prior to an experiment by designing different shapes and during an experiment by varying the flow conditions. This versatility is especially useful in the case of anchors. Indeed, it is possible to switch the behavior of an anchor from holding multiple drops, a single drop or a buffering mode by simply changing the flow velocity.

In this study, we have only tested a few microstructure geometries. The idea of using confinement heterogeneities in 2D droplet microfluidic will certainly lead to other applications in the near future. Already, a few research groups across the world have adopted

this concept. The SMALL Lab at the University of Buffalo is combining rails and anchors [127, 128, 129] with other microfluidic components inside 2D devices. Allouch *et. al.* from LAAS in Toulouse have instead relied on posts and dikes to force fractures and exclusion zones in 2D crystals of bubbles, with possible applications to optical guides and resonators.

In the following chapter, we demonstrate how confinement gradients can be used to produce and propel droplets, paving the way for droplet microfluidic devices powered by surface energy only.

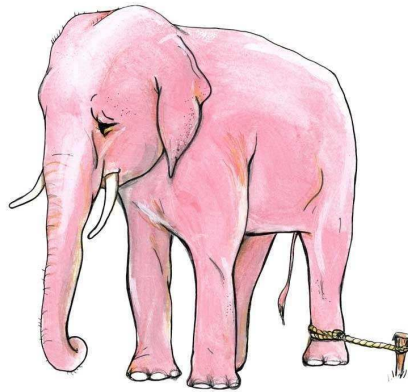


Figure 4.15: A striking similarity between droplets and elephants...

Published material

Rails and anchors: guiding and trapping droplet microreactors in two dimensions†‡

Paul Abbyad,^{§ab} Rémi Dangla,^{§a} Antigoni Alexandrou^b and Charles N. Baroud^{*a}

Received 14th June 2010, Accepted 4th October 2010

DOI: 10.1039/c0lc00104j

This paper presents a method to control the motion of nanolitre drops in a wide and thin microchannel, by etching fine patterns into the channel's top surface. Such control is possible for drops that are squeezed by the channel roof, by allowing them to reduce their surface energy as they enter into a local depression. The resulting gain in surface energy pulls a drop into the groove such that localized holes can be used as anchors for holding drops, while linear patterns can be used as rails to guide them along complex trajectories. An anchored drop can remain stationary indefinitely, as long as the driving flow rate is below a critical value which depends on the hole and drop sizes. By micro-fabricating holes into a grid pattern, drops can be arrayed and held in the observation field of a microscope against the mean carrier flow. Their contents can then be modulated by gas exchange with the flowing carrier oil. We demonstrate in particular how the pH or the oxygen levels within the drops can be controlled spatially and temporally, either by exposing rows of drops to two streams of oil at different gas concentrations or by periodically switching oil inputs to vary the gas concentration of drops as a function of time. Oxygen control is used to selectively deoxygenate droplets that encapsulate red blood cells from patients suffering from sickle cell disease, in order to study the polymerization of intracellular hemoglobin. Cycles of oxygenation and deoxygenation of anchored droplets induce depolymerization and polymerization of the hemoglobin, thus providing a method to simulate the cycling that takes place in physiological flows.

1. Introduction

Performing a large number of experiments in parallel has become increasingly important in molecular and cell biology. The most common laboratory tool for such parallelization is the multi-well plate, in which different reactions can take place in a large grid of independent wells. Experiments in such two-dimensional arrays simplify the observation, manipulation, and analysis of large data sets. For this reason, many emerging miniature devices aimed at replacing standard laboratory equipment have explored ways to organize experiments in an array format, for example in DNA-chips and cellular arrays.^{1,2}

Parallelization within the field of microfluidics is of great interest and continues to be explored through different approaches. For instance, the early work on collapsible channels led to the large-scale integration of microfluidic networks, in which isolated chambers were used to perform independent reactions.³ Other approaches involve for example a large number of independent microchannels that are replicated side by side, in view of integrating them with standard micro-pipette

instruments.⁴ Droplet microfluidics is particularly attractive for parallel experiments as the content of each drop is isolated and controlled. Furthermore, individual droplets can be transported, sorted, merged and divided.^{5–9} However, arraying droplets within microchannels must rely on immobilizing them in a controlled fashion in the presence of a mean flow that constantly pushes them downstream. Different groups have proposed ways to hold droplets stationary, either using localized laser heating^{10,11} or relying on microfabricated mechanical obstacles.^{12–16}

In the case of mechanical traps, the devices rely on the drop's resistance to being squeezed.^{12–16} Indeed, an unconstrained drop takes on a spherical shape in order to minimize its surface energy, which is equal to its surface area times its surface tension. Therefore, if a drop is placed in a region of low surface energy, it will resist leaving into a region where it will be squeezed. The resistance force is given by the gradient of the surface energy. This can be applied to block a droplet either by placing it in a pocket and pushing it with the mean flow against a small exit hole^{13,14,16} or by allowing it to expand into a chamber of increased dimensions compared to its surroundings.^{12,15} In all of the above cases, the drops were positioned in an array to maximize the number of drops in the microscope field of view.

However, holding a droplet can be performed using much weaker constraints than the ones described in the literature. As we detail below, flattened drops that are constrained by the top and bottom boundaries of the microchannel can be manipulated by imposing modulations of the channel height, *e.g.* by etching a pattern of holes and grooves into one of the microchannel surfaces. The technique that we present here relies on simple multi-layer photolithography, which allows any pattern to be

^aLaboratoire d'Hydrodynamique (LadHyX) and Department of Mechanics, Ecole Polytechnique, CNRS, 91128 Palaiseau, France. E-mail: baroud@ladhyx.polytechnique.fr

^bLaboratoire d'Optique et Biosciences (LOB), Ecole Polytechnique, INSERM U696, CNRS, 91128 Palaiseau, France

† Published as part of a LOC themed issue dedicated to French Research: Guest Editor Professor Jean-Louis Viovy.

‡ Electronic supplementary information (ESI) available: Six movie files illustrating the behaviors described in the paper. See DOI: 10.1039/c0lc00104j

§ These authors contributed equally to this work.

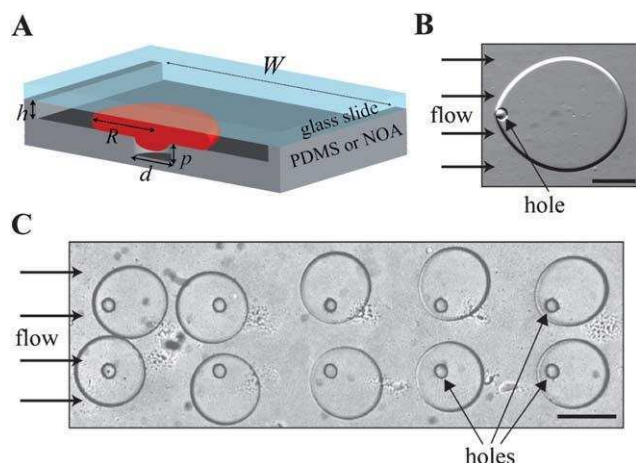


Fig. 1 (A) Sketch of the experimental device which defines the geometric parameters. (B) A water drop anchored to a hole in the channel roof with oil flowing left to right. (C) An array of anchored droplets. The scale bar represents 250 μm in all images.

drawn on the channel roof. In particular, a circular hole anchors a drop in place (Fig. 1A and B) and a series of patterned holes is used to obtain a droplet array (Fig. 1C and Movie S1†). Furthermore, linear grooves are used to guide drops in two-dimensions (2D) much like a rail is used to guide a train. The combination of rails and anchors therefore provides truly 2D manipulation of drops, far from the lateral walls of the microchannel and with minimal interactions between the drops. The simplicity of this approach ensures its robustness, since it relies on a balance between two well-understood physical mechanisms. Finally, the drops that are anchored in this way keep a large exchange area with the flowing external oil phase, which allows gas transfer between the oil phase and the stationary droplet as shown in Abbyad *et al.*¹⁷ This can be used to transport a continuous supply of oxygen for cell cultures in droplets or to provoke a temporal or spatial variation in gas content in a droplet array.

The body of the manuscript is divided into three parts. The Materials and methods section (Section II) explains the device fabrication and experimental protocol. The second part (Section III) discusses the physical principles and shows how droplets can be guided and anchored using etched patterns. It further quantifies the strength of an anchor point by measuring the critical flow rate of the carrier phase required to displace the drop from the anchor. In the third part (Section IV), the gas exchange with the carrier phase is used to impose variable conditions within an array of anchored drops, both in space, across different rows of the array, and in time. This work is motivated by the study of sickle-cell anemia and the gas-exchange techniques are used to induce red blood cell sickling in anchored droplets as shown in Section IVB.

II. Materials and methods

A. Microfluidic device fabrication

Chips of two different materials were used for the experiments. PDMS devices were used for the experiments on anchor strength and rails (Section III). For experiments involving gas exchange

(Section IV), chips were made of gas impermeable Norland Optical Adhesive 81 (NOA81). The fabrication procedures for both PDMS and NOA81 devices are explained briefly below.

Microfluidic devices with channel depth modulations were fabricated using the dry film photoresist soft lithography technique described by Stephan *et al.*¹⁸ since it enables rapid prototyping of multi-level structures. Here, the masters were etched in Eternal Laminar E8013 and Eternal Laminar E8020 negative films of thickness $33 \pm 2 \mu\text{m}$ and $49 \pm 2 \mu\text{m}$ respectively.

The fabrication procedure is as follows: (i) photoresist layers were successively laminated onto a clean glass slide using an office laminator at 100 °C until the desired height h of the main channel was reached. (ii) The photoresist film was exposed to UV through the photomask of the main network (test section, entrance and exit channels). (iii) Additional photoresist layers were laminated on top of the exposed film until the desired depth p of the anchors (or rails) was reached. (iv) The stack of photoresist films was again exposed to UV, through the photomask of the depth modulations aligned with the previous network. (v) Finally the full structure was developed by immersion in an aqueous bath of carbonate potassium at 1% mass concentration. PDMS (Dow Corning SYLGARD 184, 1/10 ratio of curing agent to bulk material) was then poured over the master and cured (2 hours at 70 °C). The PDMS device was sealed on a glass slide by plasma bonding to obtain a microchannel as sketched in Fig. 1.

Devices used for oil–droplet gas exchange were made of gas-impermeable photocurable glue, NOA, following the protocol described in Bartolo *et al.*¹⁹ Briefly, a PDMS mold was made from the master as described above. This PDMS mold was in turn used as a template to produce a PDMS stamp. Exposing the PDMS mold to gaseous 1H,1H,2H,2H-perfluorodecyltrichlorosilane (Alfa Aesar) for 3 hours in a sealed container ensured that the PDMS layers did not permanently bond during the curing process. The PDMS stamp was then pressed over a drop of Norland Optical Adhesive 81 (NOA81, Thorlabs) on a glass coverslide before exposure to a UV lamp (exposure for 40 seconds at a power of 7 mW cm⁻²). A thin layer of glue remained uncured on the surface due to the presence of oxygen, which allowed the device to be sealed with a glass slide with a second exposure to a UV source (exposure for 40 seconds at a power of 7 mW cm⁻²). To render the internal channel surface hydrophobic, a glass treatment chemical (Aquapel, PPG Industries) or 1H,1H,2H,2H-perfluorodecyltrichlorosilane (20 μL in 1 mL of FC-40) was flowed briefly through the microchannel.

B. Oxygen control

To vary its oxygen concentration, the oil was flowed through approximately 50 cm of gas permeable silicone tubing (0.3 mm internal diameter and 0.6 mm outer diameter, Helix) in a vial with a controlled oxygen atmosphere prior to entering the NOA microfluidic device. By varying the relative flow rates of nitrogen gas and air into the vial, the oxygen concentration in the vial could be adjusted from 0% to 21% oxygen (atmospheric oxygen percentage) *i.e.* from 0 to 21 kPa oxygen partial pressure (p_{O_2}). The flowing fluids equilibrated with the oxygen partial pressure in the vials through gas exchange across the silicone tubing. After the gas exchange vial, it is important to maintain a virtually gas-tight environment. Therefore low-gas permeability tubing made

of polyether ether ketone (PEEK, Upchurch) was used to connect the vial to the NanoPort (Upchurch) inlets of the microfluidic device.

C. Determination of on-chip oxygen concentration

The on-chip oxygen concentration in individual trapped microdroplets was determined using a fluorescence probe, ruthenium tris(dipyridyl) dichloride hexahydrate (RTDP) (Sigma-Aldrich), using a setup recently described in Abbyad *et al.*¹⁷ The fluorescence lifetime of the probe is proportional to the oxygen partial pressure and varies from 600 ns for 0 kPa oxygen to 380 ns for 21 kPa oxygen.

In contrast with our earlier study on flowing droplets, a slow drift to shorter lifetimes was observed when measurements were made on an anchored droplet over extended periods. The drift was not observed in the absence of excitation light or for a flowing stream of RTDP solution. Therefore, this drift is likely associated with production of an unknown photoproduct with a shorter lifetime that accumulates in the small volume of a droplet. Within the timescale of the experiments, the drift in lifetime was constant in time and was more substantial for smaller droplets. For a droplet with a diameter of 320 μm , the change in lifetime was 0.7 ns per second of illumination with excitation light. To minimize this drift, the excitation light was reduced to 0.5 second exposures every 2 seconds (for fast oxygen changes as in Fig. 5D) or every 20 seconds (for slow oxygen changes as in Fig. 5C). In the treatment of the lifetime data, a linear slope corresponding to the drift was subtracted to correct for the effect.

D. pH control

The pH of anchored droplets was altered by gas exchange with CO_2 dissolved in the carrier oil. To monitor the droplet pH, the indicator, bromothymol blue (Sigma-Aldrich), was dissolved in the aqueous phase (0.5 mg mL^{-1}) and the pH of the solution was adjusted to about 9 using sodium hydroxide. To dissolve CO_2 in the carrier oil, a solution of FC-40 with surfactant was placed for 30 minutes in an incubator with a controlled atmosphere containing 5 kPa CO_2 . The solution was then transferred to a gastight syringe (SGE).

E. Sickling of red blood cells

Blood samples were obtained from untreated sickle cell patients (Tenon Hospital, Paris) and stored at 4 $^{\circ}\text{C}$ using sodium citrate as an anti-coagulant. Samples were used within a week after extraction. Red blood cells were washed three times with PBS buffer (137 mM NaCl, 2.7 mM KCl, 8.0 mM Na_2HPO_4 , 1.5 mM KH_2PO_4 , 5.5 mM glucose, 2 mM CaCl_2 , pH 7.4) by sequential dilution and centrifugation (3000g). For experiments, the washed red blood cells were diluted 100–200 fold in D-PBS buffer (137 mM NaCl, 2.7 mM KCl, 8.0 mM Na_2HPO_4 , 1.5 mM KH_2PO_4 , 0.9 mM CaCl_2 , 0.5 mM MgCl_2 , pH 7.4, Invitrogen) and 35% v/v Optiprep (Sigma) to prevent cell sedimentation. Biocompatible surfactant, 0.5% dimorpholinophosphate-PFPE (DMP-PFPE)²⁰ in FC-40, was added to the oil. The microfluidic chip was heated to 30 $^{\circ}\text{C}$ using a heater plate, thus approaching physiological temperatures.

Polarization microscopy was used to detect intracellular hemoglobin fibers in red blood cells. Images were obtained with two crossed thin-film linear polarizers placed in the optical path of the microscope before and after the sample as described in Abbyad *et al.*¹⁷

III. Droplet anchoring by depth modulations

A. Physical background

The basic geometry of the test section is a thin microchannel of height h much smaller than its width W and length L , referred to as a Hele-Shaw cell in the fluid mechanics literature.²¹ It is filled with a fully wetting oil, in which case a thin film of oil prevents the water drops from being in direct contact with the channel walls. In this geometry, large drops (of volume greater than the largest sphere that can be inscribed in the channel $V_c = 4\pi/3(h/2)^3$) are constrained by the top and bottom walls of the channel such that they can only move in the plane of the Hele-Shaw cell. V_c is equal to 0.5 nL for a 100 micron high channel and typical droplet volumes used here were around 10 nL. Such drops adopt a flattened pancake shape, *i.e.* a rounded cylinder of radius R and height h , as sketched in Fig. 1A.

A consequence of the vertical confinement on the drops is that they become sensitive to depth modulations of the microchannel. Indeed, any interface between two fluids has a surface energy ϵ_γ , defined as the product between interfacial tension γ and the surface area of the interface. For a drop of constant volume, this surface energy is minimal for a spherical shape and it increases as the drop flattens into a pancake shape. Therefore, in a microchannel of non-uniform height, flattened droplets are captured by regions of reduced confinement which lower their surface energy.

By this mechanism, a hole, *i.e.* a circular region of increased channel height of diameter d and depth p , is able to trap a droplet. Indeed, when a droplet reaches the hole, it lowers its surface energy by partially entering into the cavity even if d is much smaller than the radius of the drop R , as sketched in Fig. 1A. The drop deforms and is held only locally, as if it were anchored to the hole. In that sense, a hole can be seen as a surface energy well in which the drop is trapped, in an analogy with particle trapping in potential energy wells. An external force is therefore necessary for the drop to detach from the anchor site.

In the presence of an external flow, the droplet is pushed by the hydrodynamic drag of the carrier phase and it will remain anchored only if the strength of the trap is sufficient to balance the drag from the flow. The trap strength can therefore be quantified by measuring the critical flow rate of the carrier phase Q_c above which the hole is no longer able to hold the droplet.

B. Determination of anchor strength

We measured the anchor strength experimentally using a PDMS microfluidic chip that enabled separate control of the size of the drops and the advection flow velocity, as sketched in the inset of Fig. 2. The design consisted of a main test section, a Hele-Shaw cell of height $h = 35 \mu\text{m}$ or $h = 50 \mu\text{m}$, $W = 3 \text{ mm}$, and length $L = 6 \text{ mm}$, which contained a single hole. It was connected upstream to a flow focusing device which produced water droplets in oil (FC-40 + 2% surfactant). The fluids were injected using syringe

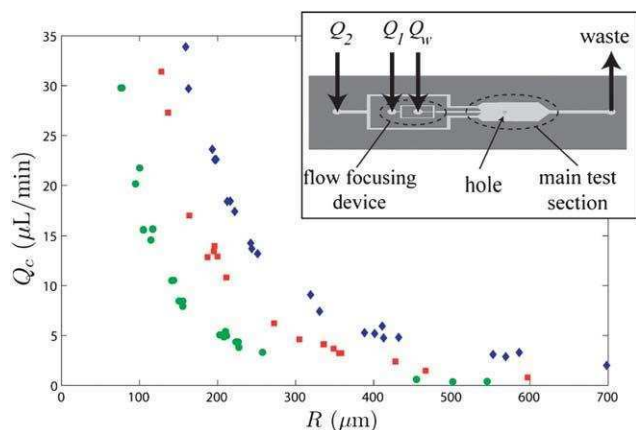


Fig. 2 Inset: sketch of the microfluidic chip featuring the flow focusing device for droplet production, the oil inlet for flow rate control and the Hele-Shaw cell with a single anchor for the measurement of the anchor strength. Main: critical flow rate Q_c as a function of droplet radius R for three channels and anchor geometries: $h = 35 \mu\text{m}$, $d = 50 \mu\text{m}$ and $p = 35 \mu\text{m}$ (green circles); $h = 50 \mu\text{m}$, $d = 75 \mu\text{m}$ and $p = 50 \mu\text{m}$ (red squares); $h = 50 \mu\text{m}$, $d = 100 \mu\text{m}$ and $p = 50 \mu\text{m}$ (blue diamonds).

pumps, at flow rates Q_w for water and Q_1 for the oil, which could be tuned to adjust the droplet size. A second oil inlet with a flow rate Q_2 also led to the test section. The total flow rate of the advecting oil in the test region was thus $Q_o = Q_1 + Q_2$.

Droplets of a given radius R were first produced at the flow focuser²² and flowed into the Hele-Shaw cell, at which point the entrainment flow rate Q_o was lowered to a value at which a single droplet was trapped by the hole. At this stage the flow of water was stopped to end the production of droplets and all droplets, except for the anchored droplet of interest, were flushed out of the test section by the carrier oil. The value of Q_o was then incrementally increased up to the critical value Q_c at which the anchored droplet was pushed out of the hole by the oil flow. For a given geometry of the test region (h, d, p), this protocol was repeated for droplets of various radii in order to determine the dependence of Q_c on R .

The results for three channel and hole geometries (h, d, p) are presented in Fig. 2. We observe that droplets are trapped by the holes at low flow rates and that they can be held in this stationary state indefinitely unless the flow rate is increased above a critical value Q_c . For a given hole geometry and droplet radius R , this threshold is well defined since fluctuations in successive measurements are below 5%. The strength of anchors displays a general trend: the critical flow rate Q_c decreases with R regardless of the channel and hole geometry. This trend is due to the increase in drag force with droplet radius R .²³ Furthermore, the experimental curves $Q_c(R)$ for the three geometries do not intersect, indicating that anchors can be ranked according to their trapping strength, independent of drop radius R . For example, for a channel of height $h = 50 \mu\text{m}$, the hole of diameter $d = 100 \mu\text{m}$ is a stronger anchor than the hole with diameter $d = 75 \mu\text{m}$. This is in agreement with the intuitive argument that the larger the hole, the more the surface energy decreases as the droplet deforms into it.

From this empirical analysis, anchors appear as a simple and robust device for trapping droplets in an external flow. In

addition, this technique is flexible and reversible since the flow rate can be tuned to below Q_c to anchor a droplet then increased above Q_c to flush it out after an experiment. Anchors are also omnidirectional, capable of anchoring a droplet regardless of the external flow direction.

C. Droplet interactions

In practical applications, multiple drops may be flowing inside the microchannel such that mobile droplets will collide with anchored ones. This raises the issue of droplet interactions which we explore here. Using the same microfluidic chip as in the previous section, we produced a continuous train of regularly sized droplets that flowed into the Hele-Shaw cell containing a single anchor. The total flow rate was adjusted by varying the secondary flow rate Q_2 .

As expected, if the total flow rate Q_o exceeded the critical flow rate Q_c , the droplets were not trapped by the anchor and they were regularly advected across the test section. However, within a range of flow rates below the threshold, the droplet train entered a *buffering mode*: a single droplet is trapped by the anchor until the following one in the train arrives, collides, and pushes it out of the hole, thus replacing it. This behavior is illustrated by the time sequence shown in Fig. 3A which shows droplets of radius $R = 180 \mu\text{m}$ flowing from left to right with an

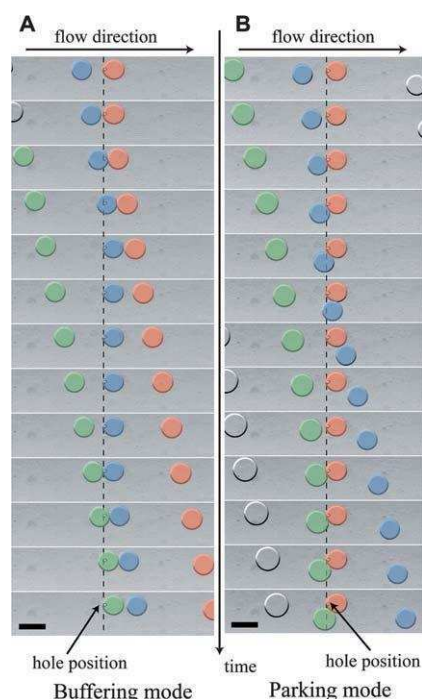


Fig. 3 Image sequences of a train of droplets of radius $R = 180 \mu\text{m}$ flowing from left to right in a Hele-Shaw cell of height $h = 50 \mu\text{m}$ over an anchor of diameter $d = 75 \mu\text{m}$. Droplets are artificially colored by image processing to facilitate tracking of individual droplets. (A) For $Q_o = 12 \mu\text{L min}^{-1}$, the train is in buffering mode (sequence frame rate: 1 frame per second). Droplets enter the Hele-Shaw cell at a rate of 15 droplets per minute. (B) For $Q_o = 6 \mu\text{L min}^{-1}$, the train enters into parking mode (sequence frame rate: 0.5 frames per second). Droplets enter the Hele-Shaw cell at a rate of 8 droplets per minute. The scale bars represent 500 μm .

oil flow rate $Q_o = 12 \mu\text{L min}^{-1}$. This flow rate was lower than the critical value $Q_c = 16.5 \mu\text{L min}^{-1}$ for this configuration. In the figure, the droplets are artificially colored by image processing to easily distinguish individual droplets. In the first 2 frames, the red drop is held stationary by the anchor when the blue drop arrives, advected by the external flow. The instant the two drops collide (frame 3), the red drop is pushed off the anchor and the blue drop takes its place. The blue drop is now stationary and anchored to the hole (frames 5–9) until the arrival of the next drop. This cycle can continue indefinitely, with each successive droplet replacing the previous droplet in the anchor (see Movie S2†).

If we decrease the flow rate Q_o further, the buffering mode switches to a *parking mode*: a unique droplet is held in place by the anchor and remains anchored as later drops collide with it. This behavior is illustrated by the time sequence shown in Fig. 3B which has the same geometrical configuration as Fig. 3A but with a lower oil flow rate, $Q_o = 6 \mu\text{L min}^{-1}$. Indeed, we observe that the red drop is held stationary by the anchor throughout the time sequence and resists collision with the incoming blue and green drops.

These modes illustrate the flexibility of the anchors as trapping devices as it is possible to switch from one mode to the other by varying the external flow rate. Applications are numerous: the buffering mode could be used to observe for a limited duration successive droplets at a fixed position, increasing the integration time for example in fluorescence experiments; the parking mode is useful to observe droplets for an extended period at fixed positions or to select a single droplet in a continuous train of droplets. This is of particular interest when studying a slow biological or chemical process in a droplet.

D. Drops on rails

Similar gain in surface energy is achieved when a pancake droplet encounters grooves that extend along one direction. In this case, however, the indentation only impedes movement along the direction perpendicular to the groove but not along the groove direction. In this way, a drop will be guided by the groove while being pushed by the external flow, as a train follows a rail. These rails can have much smaller widths than the radius of the droplet, as shown in Fig. 4A where a sinusoidal rail pattern guides droplets along its path. All the drops follow the path dictated by the micro-fabricated etch, although they do not necessarily remain centered on the rail, due to the drag force from the external oil flow. The velocity of the drops depends on the relative local orientation of the rail with respect to the direction of the mean oil flow. As seen in Movie S3†, the drops flow rapidly along sections where the rail is oriented in the same direction as the mean flow but more slowly in sections where the rail is strongly inclined relative to the mean flow.

Again, the simple microfabrication procedure allows complex rail networks to be implemented, as shown in the snapshot of Fig. 4B. In this image, drops that are of similar size as the rail width are guided into a complex distribution along the channel width. In this example, droplet–droplet interactions within the crowded central rail push some drops to take alternative paths between the inlet and the exit. If a drop “derails”, it will follow the mean flow until it reaches an available position in another rail. Drops spend variable amounts of time in the test section

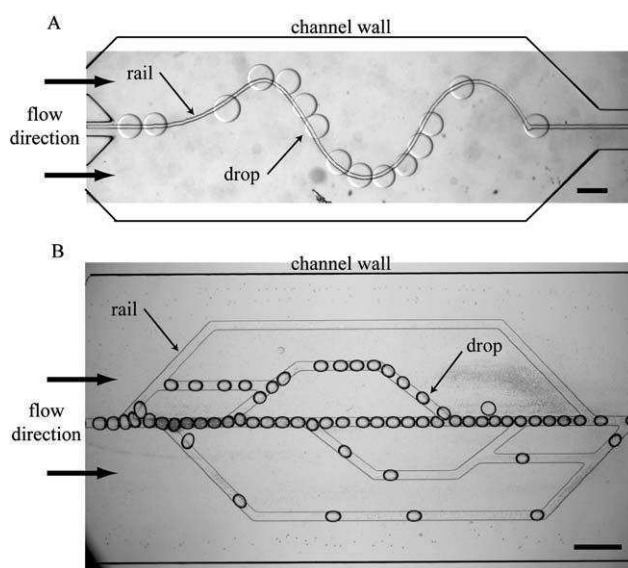


Fig. 4 Microscope images of multiple water drops guided from left to right along microfabricated rails ($50 \mu\text{m}$ in width and $50 \mu\text{m}$ in depth) in an external flow of fluorinated oil. (A) Large drops of radius $R \approx 200 \mu\text{m}$ follow a narrow sinusoidal rail inside a Hele-Shaw cell of height $h = 100 \mu\text{m}$. (B) Smaller drops of radius $R \approx 50 \mu\text{m}$ follow a complex network of rails with bifurcations and junctions inside a Hele-Shaw cell of height $h = 50 \mu\text{m}$. The scale bars represent $500 \mu\text{m}$.

since it takes longer to follow the off-centered paths as compared with the central rail.

These two examples of drops on rails demonstrate the basic functions of guiding drops in a 2D area. Drops will follow a micro-fabricated rail and this can be used to divide an initial sample into many parallel paths. Conversely, several input samples can be brought close together by designing drop inputs and rail patterns accordingly. Furthermore, the combination of rails and anchors provides a way to bring different initial samples into close proximity and to hold them in place, in order to facilitate their observation within a single image. Networks of interconnected rails can be used for complex operations by directing droplets at junctions. Droplets can be guided through a complex network of rails by passive means, for instance by relying on droplet–droplet interactions and rail geometry. An example of this crowding effect is visible in Fig. 4B, where some drops are pushed away from the central rail by their neighbors. Moreover, the guidance can also be determined actively by applying an external force that selects between two possible rails, for example through electric fields²⁴ or laser heating.⁸ In the rest of the manuscript, we focus on arrays of stationary droplets and show how the oil flow can be used to control the drop contents.

IV. Spatial and temporal control in droplet arrays

In two-phase microfluidic devices, the carrier oil serves both for the production and the transport of microdroplets. We have shown in a recent publication¹⁷ that the perfluorinated carrier oil can also be used as either a source or a sink for oxygen exchange in aqueous droplets. This approach can be generalized to many different gases due to their high solubility in perfluorinated oils. Below, we show how this gas exchange can be used to control the

contents of anchored droplet arrays. For gas exchange applications, the devices are made of a gas impermeable chip material, NOA photocurable glue, rather than gas permeable PDMS, to ensure that exchange occurs solely between the oil and aqueous phases.

A. Oil–droplet gas exchange

A train of droplets was produced at a flow focuser and transported to an array of anchors as shown in Fig. 5A. By working at

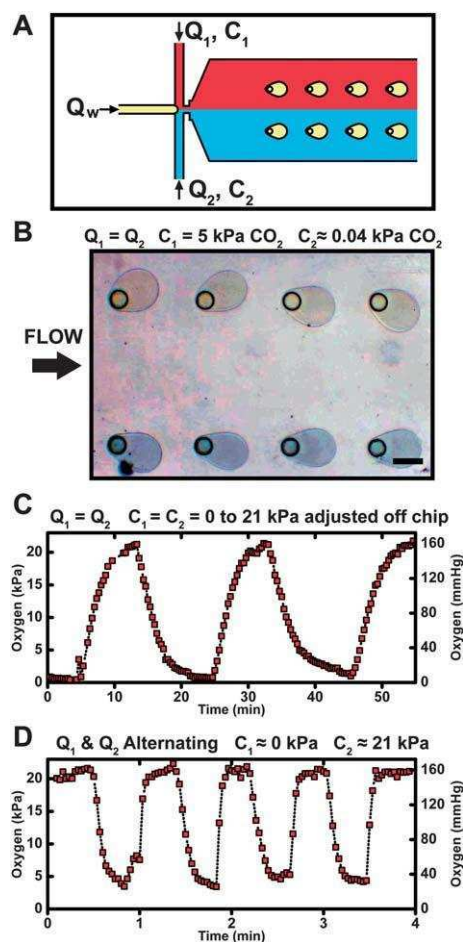


Fig. 5 (A) Schematic of the flows in the microfluidic chip for gas exchange. The flow rates and gas contents are annotated as follows: Q_w flow rate of aqueous phase, Q_1 flow rate of oil inlet one, Q_2 flow rate of oil inlet two, C_1 gas partial pressure of oil inlet one and C_2 gas partial pressure of oil inlet two. (B) Color image of trapped droplets containing the pH indicator bromothymol blue. The oil flow rates, Q_1 and Q_2 , are both held constant at $2 \mu\text{L min}^{-1}$. The upper oil stream, C_1 , contains 5 kPa dissolved CO_2 and the lower oil stream, C_2 , contains ambient dissolved CO_2 (0.04 kPa). The droplets exposed to the upper oil stream are yellow while those exposed to the lower oil stream are blue. The scale bar represents 200 μm . (C) Oxygen partial pressure (p_{O_2}) of an anchored droplet as determined by RTDP fluorescence lifetime while alternating the oxygen concentration upstream of the chip. The partial pressure of oxygen is varied from 0 kPa to 21 kPa. The flow rate is held constant at $Q_1 = Q_2 = 1 \mu\text{L min}^{-1}$. (D) Oxygen partial pressure (p_{O_2}) of a trapped droplet while alternating the flows of the two oil channels. The partial pressures of oxygen of the oil channels are $C_1 = 21 \text{ kPa}$ and $C_2 \approx 0 \text{ kPa}$. The two oil flows, Q_1 and Q_2 , are alternated between 0 and $8 \mu\text{L min}^{-1}$. In all cases, the height h of the anchor is 50 μm and its depth p is 50 μm .

flow rates in the parking mode range, anchored drops remained stationary despite the external flow of carrier oil. In this situation, the flowing oil can be used to control the gas content of the droplets while they remain in the observation area of the microscope. The control parameters of this experiment are the flow rates of the oil inputs, Q_1 and Q_2 , as well as their respective gas partial pressures, C_1 and C_2 . Controlling the flow rates and gas contents of the two incoming oil streams allows both spatial and temporal control of gas content in a droplet array.

For example, spatial variation of the dissolved gas content along the width of the channel is achieved by using two laminar oil streams at different dissolved gas concentrations. In our chip geometry, setting $Q_1 = Q_2$ and $C_1 \neq C_2$ results in the droplets in the upper part of the channel being exposed to a different gas partial pressure from those in the lower part as shown schematically in Fig. 5A. In the same microscope viewing area, the trapped droplets can thus be subjected to different gas conditions if advection dominates over diffusion. This situation corresponds to a large Peclet number $Pe = UL/D$, where U is the oil velocity, L is the distance between two droplets, and D is the diffusion coefficient of the gas molecules.

We demonstrate spatial control of the pH using two different concentrations of CO_2 in the two streams: $C_1 = 5 \text{ kPa}$ and $C_2 = 0.04 \text{ kPa}$ (ambient CO_2). A pH indicator, bromothymol blue, was dissolved in the aqueous phase and the indicator undergoes a color change from blue to yellow as the pH changes from 8 to 6. The initial pH of the aqueous phase was adjusted to 9 and therefore all droplets were blue as they were produced. The droplets were anchored in two rows, separated by 1 mm, along the length of the channel. The droplets in the upper row were exposed to a higher concentration of CO_2 , which dissolves in the droplet as carbonic acid. In a few seconds, the dissolved acid decreased the droplet's pH from 9 to 5 with a corresponding droplet color change from blue to yellow (Fig. 5B). The drops of the lower row were exposed to a far lower concentration of CO_2 and remained blue. Under these flow conditions, the large Peclet number, $Pe = 300$, indicates that the difference in CO_2 concentrations between the two streams remains sharp over the whole array.

Temporal control of droplet gas content is obtained by modulating the gas content of the carrier oil, which can be achieved in two different ways. The first is to vary the gas content of the flowing oil prior to entering the chip while keeping the flow rates Q_1 and Q_2 constant (Fig. 5C) and the second is to alternate the oil flow rates, Q_1 and Q_2 (Fig. 5D). We demonstrate how these two techniques induce oxygenation/deoxygenation cycles of a trapped droplet.

The droplet was monitored for close to an hour as the oxygen content was oscillated from ambient to zero oxygen content with a period of approximately 20 minutes (Fig. 5C). In this case, a single oil inlet was used and the flow was split equally into the two oil channels of the flow focuser ($Q_1 = Q_2$, $C_1 = C_2$). The oxygen concentration of the oil was changed prior to entering the chip using a gas exchange vial described in Section IIB, where the oil equilibrates to the vial's oxygen concentration by flowing through gas permeable tubing. To vary the oxygen content of the oil, the oxygen partial pressure in the vial was changed. The oxygen change in the anchored droplet was slow since it is limited by the equilibration time of the oil in the exchange vial.

Faster changes are possible by using two independent oil inlets at different oxygen concentrations ($C_1 \approx 0$ kPa and $C_2 \approx 21$ kPa) as shown in Fig. 5D. By alternating the oil flow rates Q_1 and Q_2 , oxygen changes in less than 10 seconds were readily attainable. The flows were modulated by using two different syringe pumps, an operation that could be automated to study the effect of cycling rate on a biological or chemical process. Furthermore, faster oscillations should be attainable by using faster flow rates or potentially by switching to pressure driven control systems.

The operations shown here demonstrate the most basic spatial and temporal control of gas content in droplet arrays. More complex operations, such as continuous gradients of oxygenation for example, can be obtained by combining the techniques described above or by adding more oil inlets with different gas contents. This opens the possibility of using a large array of droplets to perform dynamic assays over a range of conditions.

B. Sickling of red blood cells

To demonstrate the control and utility of gas exchange on anchored droplets, we show here experiments on the sickling of red blood cells. Sick cell anemia is a genetic disease due to a single mutation in hemoglobin.^{25,26} After oxygen is released in the tissues, a conformational change in mutant hemoglobin (HbS) exposes a hydrophobic residue on the surface of the protein that provokes its polymerization. This in turn leads to the red blood cells taking on a “sickle” shape, from which the name of the disease derives, and greatly losing their deformability provoking vaso-occlusions. Sickling is reversible and highly dependent on oxygen concentration. Red blood cells are exposed to cycles of oxygen rich and oxygen poor environments in vascular circulation and residual hemoglobin fibers are known to play a role in the dynamics of sickling.²⁷ Therefore, it is of biological importance to reproduce these cycles of oxygenation/deoxygenation to study its effect on red blood cell sickling. Anchored droplet arrays provide a tool to oscillate the oxygen partial pressure while continuously observing a small population of red blood cells.

Polarization microscopy was used to detect intracellular hemoglobin fibers based on their birefringence.²⁸ It is compatible with microfluidic approaches and we have recently shown that polarization microscopy can be used to visualize intracellular hemoglobin fibers in red blood cells encapsulated in flowing droplets.¹⁷ By observing the sample between crossed polarizers, red blood cells with dissolved hemoglobin appear dark while those with hemoglobin fibers rotate the polarization and therefore appear bright relative to the background.

By using flow conditions in the parking mode, droplets with encapsulated sickle red blood cells were trapped in an array of anchors. Two oil inputs were used to obtain a channel with varying oxygen concentration along its width (Fig. 6A). The same chip geometry as in Fig. 5B was used and droplets with sickle red blood cells were trapped in two rows along the length of the channel. The continuous flow of oil ($4 \mu\text{L min}^{-1}$) was enough to keep the cells in constant motion and suspension in the droplet. The droplets in the upper row have oxygen concentrations close to ambient and the cells appear dark with no indication of intracellular hemoglobin fibers (Fig. 6A, left and Movie S4†). In contrast, droplets in the bottom row were deoxygenated

and intracellular fibers appear as bright spots within the cells (Fig. 6A, right and Movie S4†). This spatial control of droplet oxygen content paves the way for experiments on multiple rows of droplets kept under different oxygen partial pressures to determine, for example, the critical oxygen concentration for hemoglobin polymerization.

The flow of deoxygenated oil into a test region containing a linear array of oxygenated droplets is shown in Fig. 6B and Movie S5†. The linear array contains droplets separated by $600 \mu\text{m}$. Initially, the droplets were oxygenated and the red blood cells inside all the drops appear dark. Deoxygenated oil was then flowed at a rate of $1 \mu\text{L min}^{-1}$ into the test region replacing the oxygenated oil. The droplets in the linear array are deoxygenated sequentially, with the red blood cells in droplets upstream appearing bright earlier than those downstream. The mean flow velocity was calculated to be 0.15 mm s^{-1} which means that the deoxygenated oil traveled between adjacent droplets in 4 seconds, which is consistent with the time interval for the dark to bright transition in sequential droplets. By controlling the flow rate and droplet spacing one can trigger a reaction in different droplets at different times. In this way, a single snapshot can yield information on the dynamics of a chemical process.

Finally, the oxygen concentration in a single trapped droplet can be oscillated to subject red blood cells to repeated cycles of oxygenation/deoxygenation (Fig. 6C and Movie S6†). Here the oxygen concentration was oscillated by alternating the flow from two oil inputs containing zero and ambient oxygen, respectively. The flow of oil in the test region is altered at $t = 5$ s to deoxygenated oil, at $t = 155$ s to oxygenated oil and finally at $t = 225$ s back to deoxygenated oil. The sickle red blood cells in the droplets undergo transitions from dark to bright that follow the changes of oxygen content in the oil. We observe a delay of approximately 30 seconds between the alternation of the oil flows (Q_1 and Q_2) and the dark to bright transitions of the red blood cells. This delay is due to the time required for the oil to travel from the inlet of the test region to the anchored droplet. The low oil flow used in this experiment, $1 \mu\text{L min}^{-1}$, is insufficient to keep the cells in constant suspension and the cells sediment at later times in the image sequence. Higher oil flows can be used if it is essential to keep cells in constant motion and suspension.

The experiments above demonstrate how anchored droplets can be used to study the effect of repeated sickling and de-sickling events on individual red blood cells. Also, by combining these cycles with spatial control of oxygen content, droplets with oscillating oxygen partial pressures can be viewed simultaneously with control droplets that undergo no oxygen variation. Future work will focus on more closely reproducing the conditions that red blood cells encounter in the vascular system, in particular, with respect to cycling rates, oxygen partial pressure and shear forces. Moreover, anchors and rails can be used to organize droplets of different contents in arrays. This will provide a means to study in a droplet array the effect of potential therapeutics on sickling under conditions that approximate those in the blood.

V. Summary and conclusion

In summary, we have demonstrated a robust way to guide and hold drops of a few nanolitres in a 2D area, without relying on

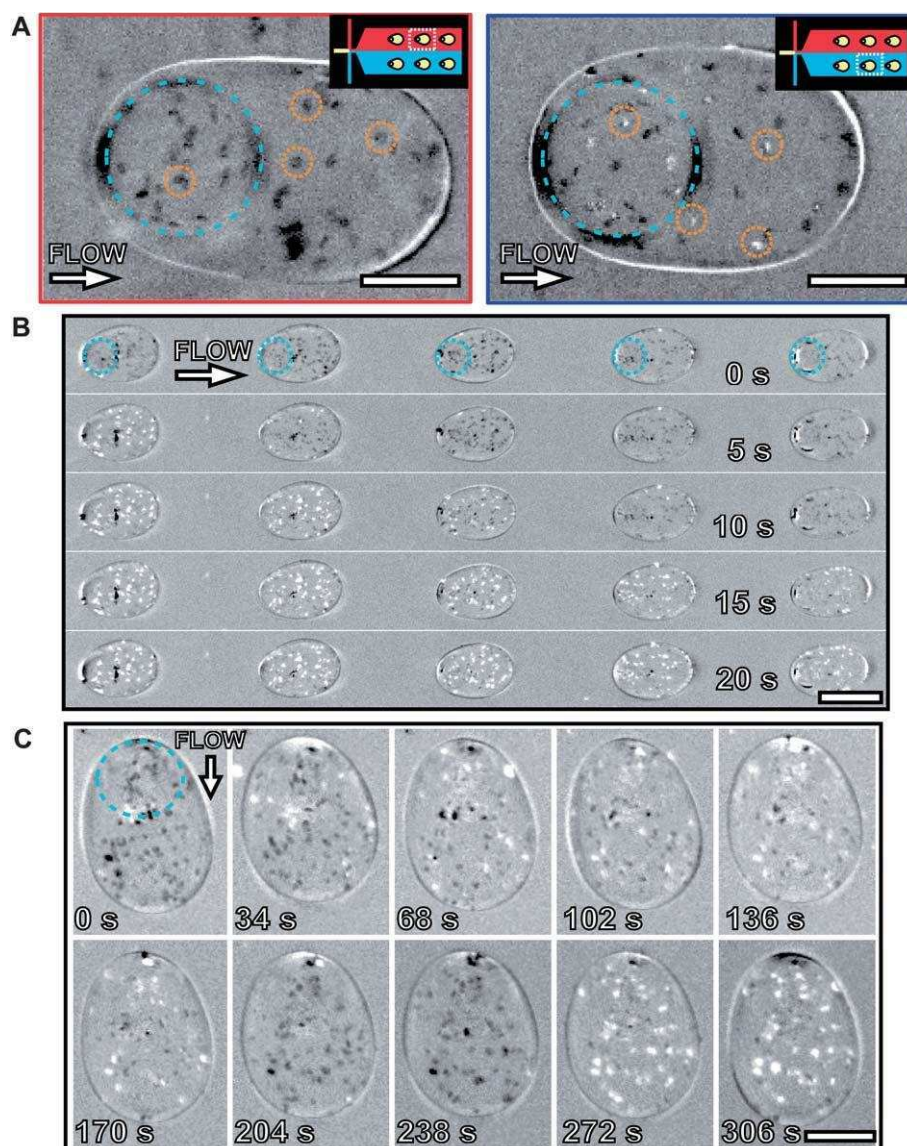


Fig. 6 (A) Simultaneous polarization microscopy images of anchored droplets in a stream of oxygenated oil (left) and deoxygenated oil (right). Images were taken with a $10\times$ objective and the background was subtracted. A few red blood cells in each image are circled in orange. The contour of the hole is outlined in blue. Using the notation defined in Fig. 5A: $Q_1 = Q_2 = 2 \mu\text{L min}^{-1}$ and the partial pressure of oxygen is equal to $C_1 = 21 \text{ kPa}$ and $C_2 = 0 \text{ kPa}$. The inset shows the droplet position in the channel. The scale bar represents $100 \mu\text{m}$. (B) Polarization microscopy image sequence showing the polymerization of intracellular hemoglobin in a linear array of anchored droplets as deoxygenated oil flows from left to right. Images were taken with a $4\times$ objective and the background was subtracted. The contour of the hole is outlined in blue in the first image. The oil flow rate is $1 \mu\text{L min}^{-1}$. The scale bar represents $200 \mu\text{m}$. (C) Polarization microscopy image sequence showing the polymerization and depolymerization of intracellular hemoglobin due to the alternating flows of the two oil channels. Images were taken with a $4\times$ objective and the background was subtracted. The contour of the hole is outlined in blue in the first image. The partial pressures of oxygen of the oil channels are $C_1 = 21 \text{ kPa}$ and $C_2 = 0 \text{ kPa}$. The flow changes are the following $t = 5 \text{ s}$: $Q_1 = 1 \rightarrow 0 \mu\text{L min}^{-1}$, $Q_2 = 0 \rightarrow 1 \mu\text{L min}^{-1}$; $t = 155 \text{ s}$: $Q_1 = 0 \rightarrow 1 \mu\text{L min}^{-1}$, $Q_2 = 1 \rightarrow 0 \mu\text{L min}^{-1}$; $t = 225 \text{ s}$: $Q_1 = 1 \rightarrow 0 \mu\text{L min}^{-1}$, $Q_2 = 0 \rightarrow 1 \mu\text{L min}^{-1}$. The scale bar represents $100 \mu\text{m}$. In all cases, the height h of the anchor is $50 \mu\text{m}$ and its depth p is $50 \mu\text{m}$.

the side walls or other structures within the microchannel. This was used to anchor drops subjected to continuous flow of the carrier phase, an important step for producing arrays of drops for lab on a chip applications. The anchor strength determines the maximum flow rate at which a droplet can be trapped. This strength depends on the hole geometry and the droplet size, such that the device can be loaded and emptied by changing the flow rate. Moreover, it can also be run in different modes which allow the observation of drops either sequentially in “*buffer mode*” or

for a long duration in “*parking mode*”. In parking mode, patterning the holes in a grid allows observation of a droplet array. Finally, guiding drops by rails was shown through linear structures of arbitrary shape.

We have also shown how the gas exchange between the flowing oil and the stationary droplet provides a way to modify the drop contents after anchoring. The gas exchange can be used to modify the pH or oxygen partial pressure within the drops, for example to produce a droplet array with variable conditions over

time and space. We used it to selectively provoke intracellular hemoglobin polymerization in certain droplets in an array, while temporal control was used to produce cycles of oxygenation and de-oxygenation on encapsulated populations of red blood cells. This spatial and temporal control can now be implemented to study the effect of medical treatments on the polymerization and de-polymerization of intra-cellular hemoglobin, while simulating the cyclic oxygen variations in flowing blood.

This technique should be compared with other approaches that have already been published for arraying drops. In contrast with methods that rely on transport in confined microchannels,^{12,13,15} the rails and anchors provide truly 2D arrays, which greatly reduces the interactions between drops and which allows several inputs to converge on a single test section. Gas control could thus be performed without resorting to a supplementary layer of microchannels. The other two-dimensional approach^{14,16} produces similar arrays but does not provide a method to selectively place droplets in selected traps. The integration of rails and anchors, possibly augmented with external actuation, would allow such selective positioning. Finally, all of these advances in arraying techniques should yield equivalent capabilities as drop deposition on a flat surface,^{29–31} while keeping the flexibility and functionality of droplet microfluidics.

Acknowledgements

Special thanks to François Lionnet for providing blood from sickle cell patients and Jean-Christophe Baret for providing the perfluorinated surfactant used in our studies. We would also like to thank Pierre-Louis Tharaux, Ashleigh Theberge and Samir Zard for helpful discussions. The authors also thank Caroline Frot for microfabrication assistance. This project was partially supported by Region Ile-de-France Nanosciences Competence Center and the CNRS Interdisciplinary Program “Interface Physique Chimie Biologie: soutien à la prise de risque”. P.A. acknowledges the financial support from CNRS and Ecole Polytechnique.

References

- 1 G. Ramsay, *Nat. Biotechnol.*, 1998, **16**, 40–44.
- 2 K. Appasani, *Bioarrays: from Basics to Diagnostics*, Humana Pr Inc, 2007.
- 3 T. Thorsen, S. Maerkl and S. Quake, *Science*, 2002, **298**, 580.
- 4 I. Meyvantsson, J. W. Warrick, S. Hayes, A. Skoien and D. J. Beebe, *Lab Chip*, 2008, **8**, 717–724.
- 5 M. Chabert, K. D. Dorfman and J. L. Viovy, *Electrophoresis*, 2005, **26**, 3706–3715.
- 6 G. Cristobal, J. P. Benoit, M. Joanicot and A. Ajdari, *Appl. Phys. Lett.*, 2006, **89**, 034104.
- 7 K. Ahn, J. Agresti, H. Chong, M. Marquez and D. A. Weitz, *Appl. Phys. Lett.*, 2006, **88**, 264105.
- 8 C. N. Baroud, M. R. de Saint Vincent and J.-P. Delville, *Lab Chip*, 2007, **7**, 1029–1033.
- 9 E. Brouzes, M. Medkova, N. Savenelli, D. Marran, M. Twardowski, J. Hutchison, J. Rothberg, D. Link, N. Perrimon and M. Samuels, *Proc. Natl. Acad. Sci. U. S. A.*, 2009, **106**, 14195.
- 10 M. L. Cordero, D. R. Burnham, C. N. Baroud and D. McGloin, *Appl. Phys. Lett.*, 2008, **93**, 034107.
- 11 E. Verneuil, M. L. Cordero, F. Gallaire and C. N. Baroud, *Langmuir*, 2009, **25**, 5127–5134.
- 12 J. Shim, G. Cristobal, D. R. Link, T. Thorsen, Y. Jia, K. Piattelli and S. Fraden, *J. Am. Chem. Soc.*, 2007, **129**, 8825–8835.
- 13 W. Shi, J. Qin, N. Ye and B. Lin, *Lab Chip*, 2008, **8**, 1432–1435.
- 14 A. Huebner, D. Bratton, G. Whyte, M. Yang, A. Demello, C. Abell and F. Hollfelder, *Lab Chip*, 2009, **9**, 692.
- 15 C. Schmitz, A. Rowat, S. Köster and D. Weitz, *Lab Chip*, 2009, **9**, 44–49.
- 16 Y. Bai, X. He, D. Liu, S. Patil, D. Bratton, A. Huebner, F. Hollfelder, C. Abell and W. Huck, *Lab Chip*, 2010, **10**, 1281–1285.
- 17 P. Abbyad, P. Tharaux, J. Martin, C. Baroud and A. Alexandrou, *Lab Chip*, 2010, **10**, 2505–2512.
- 18 K. Stephan, P. Pittet, L. Renaud, P. Kleimann, P. Morin, N. Ouaini and R. Ferrigno, *J. Micromech. Microeng.*, 2007, **17**, N69.
- 19 D. Bartolo, G. Degré, P. Nghe and V. Studer, *Lab Chip*, 2008, **8**, 274–279.
- 20 J. Clausell-Tormos, D. Lieber, J. C. Baret, A. El-Harrak, O. J. Miller, L. Frenz, J. Blouwolff, K. J. Humphry, S. Köster, H. Duan, C. Holze, D. A. Weitz, A. D. Griffiths and C. A. Merten, *Chem. Biol.*, 2008, **15**, 427–437.
- 21 H. Hele-Shaw, *Nature*, 1898, **58**, 520.
- 22 S. L. Anna, N. Bontoux and H. A. Stone, *Appl. Phys. Lett.*, 2003, **82**, 364–366.
- 23 J. Bush, *J. Fluid Mech.*, 1997, **352**, 283–303.
- 24 K. Ahn, C. Kerbage, T. Hynt, R. M. Westervelt, D. R. Link and D. A. Weitz, *Appl. Phys. Lett.*, 2006, **88**, 024104.
- 25 G. Serjeant, *Lancet*, 1997, **350**, 725–730.
- 26 M. Stuart and R. Nagel, *Lancet*, 2004, **364**, 1343–1360.
- 27 W. Eaton and J. Hofrichter, *Blood*, 1987, **70**, 1245–1266.
- 28 H. Sunshine, J. Hofrichter, F. Ferrone and W. Eaton, *J. Mol. Biol.*, 1982, **158**, 251–273.
- 29 F. Lemaire, C. Mandon, J. Reboud, A. Papine, J. Angulo, H. Pointu, C. Diaz-Latoud, C. Lajaunie, F. Chatelain and A. Arrigo, *PLoS One*, 2007, **2**, e163.
- 30 H. Kim, S. Vishniakou and G. W. Faris, *Lab Chip*, 2009, **9**, 1230–1235.
- 31 L. Muegherli, O. Burchak, L. Balakieva, A. Thomas, F. Chatelain and M. Balakirev, *Angew. Chem., Int. Ed.*, 2009, **48**, 7639–7644.

Trapping microfluidic drops in wells of surface energy

Rémi Dangla, Sungyon Lee, and Charles N. Baroud*

LadHyX and department of Mechanics, Ecole Polytechnique, CNRS, 91128 Palaiseau Cedex, France

(Dated: August 1, 2011)

A small hole etched in the top of a wide microchannel creates a well of surface energy for a confined drop. This produces an attractive force F_γ equal to the energy gradient, which is estimated from geometric arguments. We use the drag F_d from an outer flow to probe the trapping mechanism. When $F_d < F_\gamma$, the drop deforms but remains anchored to the hole. Its shape provides information about the pressure field. At higher flow velocities, the drop detaches, defining a critical capillary number for which $F_d = F_\gamma$. The measured anchoring force agrees with the geometric model.

When a spherical drop enters a channel whose height is smaller than the sphere diameter, the drop must squeeze and depart from its relaxed shape. The resulting deformation leads to an increase in its interfacial area A and a corresponding increase in free energy $E_\gamma = \gamma A$, with γ the interfacial tension. By this mechanism, the drop can store and transport this extra energy as it travels down the channel. Given the chance, it will tend to decrease its surface area in order to reduce its free energy. Variations in the level of confinement can therefore be used to apply a force on the drop by inducing gradients of the surface energy. The migration of droplets in such gradients has been known since Hauksbee [1] and exploited in several geometries [2–5], both for wetting and non-wetting drops.

A novel use of surface energy gradients was recently demonstrated in the context of microfluidics [6]. It consists of creating localized areas of reduced confinement by etching grooves into the top surface of a microchannel, in order to attract drops to particular locations. It was shown that the induced energy gradients are able to guide or anchor drops against a mean flow if the outer flow velocity is below a critical value, much as oranges are trapped at the bottom of a bowl by the gradient of gravitational potential energy.

We now turn to the physics behind such anchoring, namely the balance between the force due to surface energy gradient (\vec{F}_γ) and the hydrodynamic drag force (\vec{F}_d) due to the outer flow of oil. First, we estimate F_γ from the geometric study of a static drop. Then, we consider the conditions for which a drop remains anchored to the hole, namely $F_d < F_\gamma^*$ with F_γ^* the maximum force due to surface energy gradient. We analyze the shape of the elongated drops and extract a scaling law for the drag F_d . Last, we measure the threshold velocity above which the drop cannot be anchored, for which $F_d = F_\gamma^*$. This yields a direct measure of the maximum strength of the anchoring mechanism.

The experiments were conducted in PDMS microchannels (Dow Corning Sylgard 184), fabricated using dry film photoresist soft lithography techniques [6, 7]. The microchannel consists of a flow focusing junction to generate droplets, connected to a test section (width=3 mm) containing a single anchor of diameter between $d = 50$ and $82 \mu\text{m}$ and of depth between $e = 28$ and $45 \mu\text{m}$,

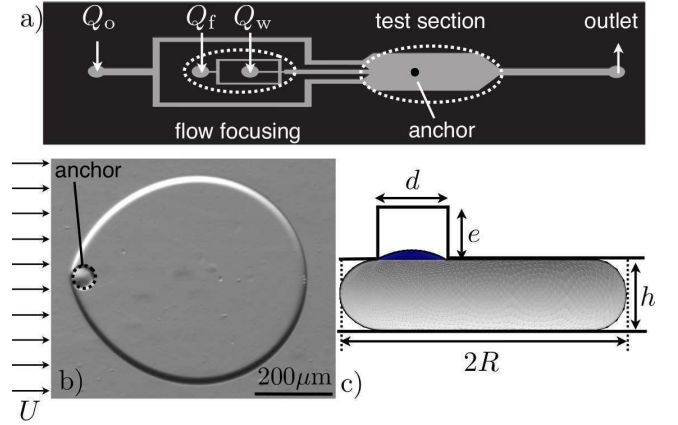


FIG. 1. **a.** Schematic of a microchannel that consists of a flow focuser to generate water drops in oil and of a test section with a single anchor. **b.** A top-down image of a pancake droplet held in place by an anchor against a mean external flow U . **c.** Surface Evolver rendering of an anchored droplet of outer radius R inside the microchannel of height h over an anchor of diameter d and of depth e .

as sketched in Fig. 1a. The channel height is constant everywhere else and ranges from $h = 28$ to $60 \mu\text{m}$.

The oil is injected with two syringe pumps, at flow rates Q_f in the flow-focusing junction and Q_o through the entrainment channel (see Fig. 1a). By injecting water at a flow rate Q_w , water droplets are formed and transported into the test section. Once a drop is trapped by the single anchor, the water flow is set to zero and Q_o is gradually increased until the droplet detaches at a critical flow rate Q^* . The experiment is repeated for different drop and channel parameters.

The continuous phase consists of a fluorinated oil (3M Fluorinert FC-40 or FC-70 of viscosities $\mu \approx 4.1 \text{ cP}$ and $\mu \approx 24 \text{ cP}$ at 25°C respectively). Contrary to alkanes or silicone oils, these oils do not swell the PDMS and the surfaces of the channel remain parallel even for large aspect ratios [9]. One of two different fluoro-surfactants, based on the molecules described in Ref. [8], is added to the oil phase at a concentration of 2%: the first is a PFPE-PEG molecule while the second has a simpler ammonium salt head group [8]. The water-oil interfacial

tension γ_e is measured via the pendant drop method. Independently of the oil type, the equilibrium value is found to be $\gamma_e = 20$ mN/m and $\gamma_e = 10$ mN/m for the PFPE-PEG and ammonium salt surfactants respectively. The time to reach these equilibrium values ranges from 30 minutes for the first surfactant, up to several hours for the second.

As illustrated in Fig. 1b, even small anchors are able to hold relatively large droplets. This implies that a droplet reduces its overall surface area, despite locally creating excess surface as it partially enters into the anchor. This can be verified by comparing the surface area of a circular pancake drop, in the absence of an anchor, to the modified area when the drop is above the anchor. The area of the unperturbed drop is estimated by modeling it as a circular cylinder of radius R_i , surrounded by the outer half of a torus of small radius $h/2$. This is strictly valid in the limit of $\varepsilon \equiv h/2R_i \ll 1$ and yields the area of the drop: $A_i = 2\pi R_i^2 [1 + \pi\varepsilon]$.

When a static droplet feels the presence of an anchor, it penetrates into it and forms a spherical cap whose local curvature equilibrates with the interface curvature far away. The parameter $b \equiv d/h$ determines the behavior of the drop: If $b > 2$, curvature equilibrium is reached only when the drop enters fully into the hole and the spherical cap flattens against the top, rendering the hole depth e an important parameter. Here, we will limit ourselves to the case of $b \leq 2$, in which the drop only partially enters into the hole. This situation is depicted in Fig. 1c, which features a Surface Evolver simulation of the drop shape in the absence of flow [10]. By matching the curvature of the spherical cap in the hole with the curvature of the interface far away $\mathcal{C} \approx 2/h + \pi/(4R)$ [11] and imposing the volume conservation of the droplet, a new value of R can be obtained. This yields a new value of the surface area of the drop A in the presence of the anchor. The change in surface area $\Delta A = A - A_i$ then corresponds to

$$\Delta A = - \left[\frac{\pi}{2} b S(b) + O(\varepsilon) \right] h^2, \quad (1)$$

where

$$S(b) \equiv \frac{b}{2} - \frac{4}{3b} \left[1 - \left(1 - \frac{b^2}{4} \right)^{\frac{3}{2}} \right]. \quad (2)$$

The dimensionless function $S(b)$ is positive for $0 < b \leq 2$, resulting in a negative ΔA and a decrease in E_γ . Therefore, even an asymptotically small anchor reduces the droplet surface energy, yielding $\Delta E_\gamma = \gamma \Delta A < 0$. For $b > 2$, the energy change remains negative but its value will depend on the hole depth; $S(b)$ does not fully capture the energy change in this case.

The magnitude of the force due to this change in surface area is equal to the gradient of surface energy. Estimating it therefore requires an estimate of the distance

over which the energy changes. Figure 1b shows that even a weak external flow aligns the edge of the drop with the anchor. This indicates that the gradients of surface energy appear only as the edge of the drop passes over the hole. Therefore, the characteristic length over which the energy changes is given by the hole diameter d and the force can be estimated as

$$F_\gamma^* \propto \frac{|\Delta E_\gamma|}{d} \approx \gamma \frac{\pi}{2} h S(b). \quad (3)$$

Having determined the anchoring force based on the static droplet geometry, we now consider the drag force \vec{F}_d , exerted by the outer flow, which tends to push the drop out of the anchor. Given the scale separation between the vertical (z) and in plane (x, y) dimensions, the test section of the channel is modeled as a Hele-Shaw cell [12]. Hence, the height averaged velocity field \vec{U} is potential and verifies Darcy's law

$$\vec{\nabla} p = - \frac{12\mu}{h^2} \vec{U}, \quad (4)$$

where the pressure p is invariant in the vertical direction.

The drag force \vec{F}_d acting on the droplet has two components: the pressure drag $\vec{F}_p = - \int p_o \vec{ds}$, defined as the outer pressure p_o at the interface applied on the surface elements \vec{ds} , and the viscous drag $\vec{F}_\mu = \int \mu \vec{\nabla} \vec{U} \cdot \vec{ds}$. Darcy's law (4) provides an estimate for the pressure as $p \propto \mu U R / h^2$, while viscous shear stresses $\mu \vec{\nabla} \vec{U}$ scale as $\mu U / h$ to the leading order. Since both the pressure and shear stresses act on the lateral drop surface ($\propto hR$), the pressure drag $F_p \propto \mu U R^2 / h$ is greater than the viscous drag $F_\mu \propto \mu U R$ by an order $R/h \gg 1$. One may therefore ignore the viscous drag and focus on the pressure drag.

This scaling argument has been validated by asymptotic analyses of the Hele-Shaw flow around a stationary inviscid bubble [13] and around a solid cylinder [14]. Those studies confirm the dominant role of pressure drag and provide expressions for p_o and \vec{F}_d as

$$p_o = - 24 \frac{\mu U}{h^2} \cdot x + \text{Cst}, \quad (5a)$$

$$\vec{F}_d = 24\pi \frac{\mu U R^2}{h}. \quad (5b)$$

In order to verify this expression for p_o , we analyze the shape of anchored droplets. Indeed, the Laplace equation gives a local relationship between the mean curvature of the drop \mathcal{C} and the pressure jump, $p_i - p_o$, across the interface. This provides an optical readout of the pressure variations through the drop shape. By defining $\delta r(\theta)$ as the local deviation from the radius R in the absence of flow (see Fig. 2), the Laplace equation reduces to

$$\gamma \left\{ \frac{2}{h} + \frac{\pi}{4} \frac{1}{R} \left[1 - \frac{1}{R} \left(\delta r(\theta) + \frac{d^2 \delta r}{d\theta^2} \right) \right] \right\} = p_i - p_o, \quad (6)$$

in the limit of $\delta r/R \ll 1$ [11].

Although Eq. (6) involves the pressure field within the droplet p_i , this field does not affect the deformations. In fact, the internal flow must satisfy potential flow theory to leading order and, given the static drop interface as the boundary, the only possible velocity field is the trivial $\vec{U} = \vec{0}$ with a constant p_i . Consequently, the shape deformations $\delta r(\theta)$ are mainly determined by the outer pressure p_o . Then, inserting the expression for p_o from Eq. (5a) in Eq. (6) yields

$$\frac{\delta r(\theta)}{R} = 15.3 \cdot Ca \cdot \frac{R^2}{h^2} (1 - \theta \sin \theta). \quad (7)$$

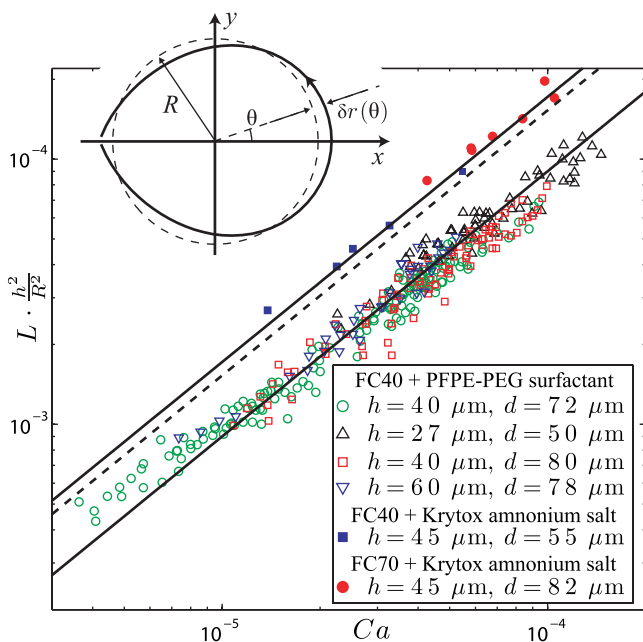


FIG. 2. **Inset:** Sketch of the polar coordinates for the deformations $\delta r(\theta)$ from the static radius R . **Main panel:** Elongation $L = \delta r(0)/R$ of anchored droplets, rescaled by h^2/R^2 , as a function of the oil capillary number Ca for various channels, liquids and surfactants. The solid lines are a linear fits of the two data groups, with slopes 9 ± 2 (PFPE-PEG surfactant) and 17 ± 1 (ammonium head group). The dashed line is the theoretical prediction of Eq. (7), with slope 15.3.

Equation (7) provides a scaling law for the drop elongation $L \equiv \delta r(0)/R \propto Ca R^2/h^2$. This scaling is verified in Fig. 2 where $L \cdot h^2/R^2$ is plotted vs. Ca for various channel geometries, liquid viscosities, surfactant types, and oil flow rates Q_o (or equivalently flow velocities $U_o = Q_o/(Wh)$). The data collapse onto two distinct lines which both verify the linear scaling, although with different prefactors. The value of the prefactor is only a function of the surfactant type and is independent of the other parameters.

Since the two surfactants exhibit different adsorption kinetics in a pendant drop experiment, they may also

reach different spatial distributions on the drop interface in the presence of an external flow [15]. Indeed, complex recirculation patterns are observed on the surface of our droplets, indicating that Marangoni stresses are present on the interfaces. The dependence of these stresses on the surfactant kinetics could explain the different prefactors that are observed in the elongation experiments.

Nevertheless, the drop shape is well described by Eq. (7), once the prefactor 15.3 is replaced by the slope of the linear fit from Fig. 2. The predicted deformations display a good agreement with the drop shape at different flow rates, as illustrated in Fig. 3. Given that the pressure deforming the drop is linear in x , the drop shape obtained in this flow is akin to a 2D pendant drop, where the hydrostatic pressure also decreases linearly with height.

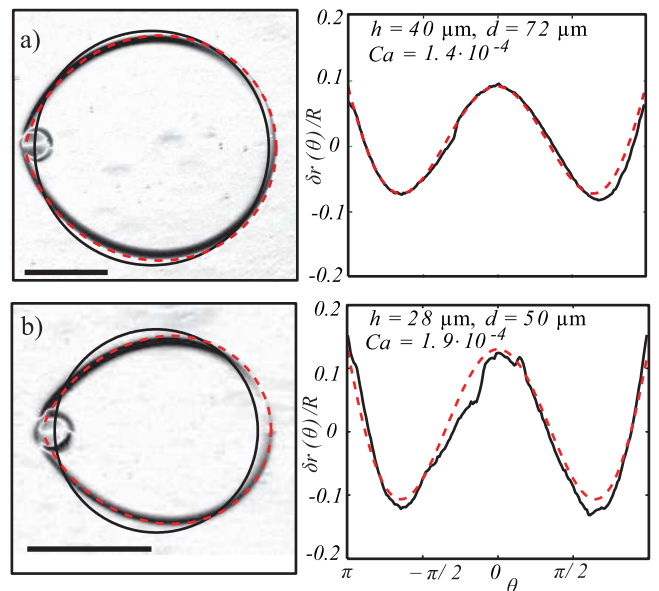


FIG. 3. **Left:** Images of anchored droplets deformed by the flow of oil. The dashed lines show the prediction from Eq. (7), while the solid line shows the equivalent circle of radius R . Scale bars represent $200 \mu\text{m}$. **Right:** Comparison between the deformations $\delta r(\theta)/R$ extracted from the microscope images on the left (solid line) and the theoretical curve (dashed line) obtained from Eq. (7), using 9 as a prefactor.

The elongation and shape measurements of Fig. 2&3 verify the amplitude of the pressure variations along the drop and, thereby, the scaling for the pressure drag in Eq. (5b): $F_d \propto \mu U \cdot R^2/h$. We can now obtain the anchor strength by finding the maximum oil velocity U^* that the anchored droplet can resist and by using the force equilibrium $F_\gamma = F_d(U^*)$. This yields the scaling

$$Ca^* \propto S(b) \frac{h^2}{R^2}, \quad (8)$$

where $Ca^* \equiv \mu U^*/\gamma$.

The experimental results agree with this theoretical prediction, as seen in Fig. 4 which displays the value

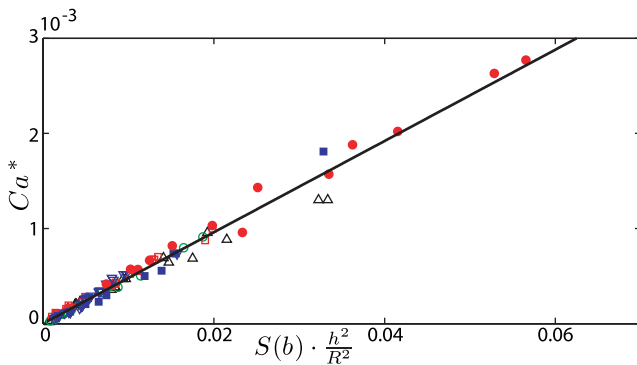


FIG. 4. Critical capillary number Ca^* plotted against $S(b)h^2/R^2$ for the channel geometries, liquids and surfactants as listed in the legend of Fig. 2. The solid line is a linear fit of the data.

of Ca^* for all channels, liquids, and surfactants. The data all collapse on a single linear law, thus confirming the scaling law (3) for the anchoring force F_γ^* , which is derived from purely geometric arguments. In particular, it supports the use of d as the characteristic length scale in F_γ^* . The actual value of the anchoring force can be estimated by reintroducing the numerical prefactor of Eq. (5b). It yields values of F_γ^* in the range of 100-1000 nN, depending on the geometric parameters h and d .

These results verify that the gradient of surface energy and the hydrodynamic drag due to the external fluid are indeed the dominant competing physical mechanisms that determine the ability to anchor a droplet. In this respect, anchoring droplets in wells of surface energy resembles other methods of trapping in energy wells, such as electrostatic cups [16] or optical tweezers [17], where the maximum restoring force is given by the maximum energy gradient. Below this limit, deviations from the equilibrium shape or position provide information about the magnitude of the opposing forces at play in all three examples. In the present case, the drop shape depends on the surfactant type, in addition to the global force balance, which may yield information about the physical chemistry at the free interface.

An important distinction between the anchors and other trapping mechanisms resides in the source of energy: while most systems rely on an external field, the energy here is contained in the droplet itself. The typical values of surface energy therefore increase the range of attainable forces up to several hundred nN. This value can be further increased by etching larger and deeper holes, thus exploring the regime $b > 2$. In this case, the drop extends fully into the hole into a spherical or cigar shape and the gain in surface energy is maximized. Although this limit is not studied here, such devices would exert very large anchoring forces.

In terms of applications, anchors are simple and efficient passive devices to hold drops stationary, even in

the presence of an outer flow. Parallelization is straightforward and enables easy production of droplet arrays for chemical or biomedical studies. The array format has gained in popularity recently since it provides a direct microfluidic equivalent to classic multiwell plates which are ubiquitous in biological applications. A key benefit over existing methods is the continuous flow of outer liquid, which can be used to control the chemical environment of the trapped droplets and their content, both in space and time. A wide range of chemical and biomedical applications follows, from protein crystallization to the study of sickle cell anemia [6]. Finally, more controlled droplet placing can be achieved by combining the passive “rails and anchors” approach with active forcing of individual droplets, for example using a focused laser [18].

We thank François Gallaire and Matthias Nagel for fruitful discussions, Caroline Frot for the microfabrication. Estelle Mayot provided invaluable surfactant help and Wiebke Drenckhan and Anniina Salonen helped with the surface tension measurements. S.L. was funded by a Chateaubriand fellowship and the Direction des Relations Extérieures of Ecole Polytechnique.

* baroud@ladhyx.polytechnique.fr

- [1] F. Hauksbee, Phil. Trans. Roy. Soc. **27**, 395 (1710).
- [2] É. Lorenceau and D. Quéré, J. Fluid Mech. **510**, 29 (2004).
- [3] T. Metz, N. Paust, C. Muller, R. Zengerle, and P. Koltay, Sensors and Actuators A **143**, 49 (2008).
- [4] P. Renvoisé, J. Bush, M. Prakash, and D. Quéré, Europhys. Lett. **86**, 64003 (2009).
- [5] T. Metz, N. Paust, R. Zengerle, and P. Koltay, Microfluidics Nanofluidics **9**, 341 (2010).
- [6] P. Abbyad, R. Dangla, A. Alexandrou, and C. N. Baroud, Lab Chip **11**, 813 (2010).
- [7] K. Stephan, P. Pittet, L. Renaud, P. Kleimann, P. Morin, N. Ouaini, and R. Ferrigno, Micromechanics and Microeng. **17**, N69 (2007).
- [8] J. Clausell-Tormos, et al., Chemistry & Biology **15**, 427 (2008).
- [9] R. Dangla, F. Gallaire, and C. N. Baroud, Lab Chip **10**, 2032 (2010).
- [10] K. Brakke, *Surface Evolver manual*, <http://www.susqu.edu/facstaff/b/brakke/evolver/evolver.html> (2008).
- [11] C. Park and G. Homsy, J. Fluid Mech. **139**, 291 (1984).
- [12] G. I. Taylor and T. G. Saffman, J. Mech. Appl. Math. **12**, 265 (1959).
- [13] S. Maruvada and C. Park, Phys. Fluids **8**, 3229 (1996).
- [14] J. Lee and Y. Fung, J. Fluid Mech. **37**, 657 (1969).
- [15] V. Levich, *Physicochemical Hydrodynamics* (Prentice Hall, Englewood Cliffs, N.J., 1962).
- [16] M. Krishnan, N. Mojarad, P. Kukura, and V. Sandogh-dar, Nature **467**, 692 (2010).
- [17] A. Ashkin, Proc. Nat. Acad. Sci. **94**, 4853 (1997).
- [18] E. Fradet, et al., Lab Chip **Submitted** (2011).

Detailed derivations

In this short letter, the details of the calculations are left out. Here, we explain how the equations (6) and (7) that describe the shape of an anchored droplet are derived. Let's recall expression (5a) for the pressure field around a circular droplet:

$$p_o = -24 \frac{\mu U}{h^2} \cdot x + \text{Cst} . \quad (4.8)$$

The Laplace equation dictates how the droplet responds to this pressure field, by relating the curvature of the interface \mathcal{C} to the pressure jump $p_i - p_o$ across the interface:

$$\gamma \mathcal{C} = p_i - p_o , \quad (4.9)$$

where p_i and p_o are the inner and outer pressure fields respectively.

The curvature \mathcal{C} of a large non-wetting pancake droplet is derived in Appendix B and expressed as a function of the channel height h and the in-plane curvature of the interface $\mathcal{C}_{//}$:

$$\mathcal{C} = \frac{2}{h} + \frac{\pi}{4} \mathcal{C}_{//} \quad (4.10)$$

The in-plane shape is expressed in polar coordinates via the function $r(\theta)$. The in-plane curvature is then given by

$$C = \frac{r^2 + 2(r')^2 - rr''}{(r^2 + (r')^2)^{3/2}} = \frac{1}{r} \frac{1 + 2(r'/r)^2 - r''/r}{(+ (r'/r)^2)^{3/2}} . \quad (4.11)$$

Next, we assume that the droplet is only slightly deformed, meaning that its in-plane shape is a approximately circle of radius R with small perturbations $\delta r(\theta)$ ($\delta r \ll R$). The previous expression simplifies to

$$\begin{aligned} C &= \frac{1}{R} \left(1 - \frac{\delta r}{R}\right) \left(1 - \frac{\delta r''}{R}\right) \\ &= \frac{1}{R} \left(1 - \frac{1}{R}(\delta r + \delta r'')\right) \end{aligned}$$

by keeping order 1 terms in $\delta r/R$ only.

Finally, we can inject the curvature back into the Laplace equation and get equation (6) of the paper

$$\gamma \left(\frac{2}{h} + \frac{\pi}{4} \frac{1}{R} \left[1 - \frac{1}{R} \left(\delta r + \frac{d^2 \delta r}{d\theta^2} \right) \right] \right) = p_i - p_o \quad (4.12)$$

Because the Darcy prediction for the inner pressure p_i is a constant, we can assume that

$$p_i - p_o = 24 \frac{\mu U}{h^2} R \cos \theta + \text{Cst} \quad (4.13)$$

which can be inserted in the previous equation. We then obtain the following second order differential equation

$$\delta r + \frac{d^2 \delta r}{d\theta^2} = -24 \frac{4}{\pi} \frac{\mu U}{\gamma} \frac{R^2}{h^2} R \cos \theta . \quad (4.14)$$

We recognize the equation of an harmonic oscillator forced at the resonance frequency. Hence, we look for a solution of the form $\delta r(\theta) = A\theta \sin \theta$. With this assumption, we have

$$\begin{aligned} \delta r(\theta) &= A\theta \sin \theta \\ \frac{d\delta r(\theta)}{d\theta} &= A(\sin \theta + \theta \cos \theta) \\ \frac{d^2 \delta r(\theta)}{d\theta^2} &= A(\cos \theta + \cos \theta - \theta \sin \theta) \end{aligned}$$

which, once inserted back into equation (4.14) yields

$$2 \cdot A \cdot \cos \theta = -24 \frac{4}{\pi} \frac{\mu U}{\gamma} \frac{R^2}{h^2} R \cos \theta . \quad (4.15)$$

which must balance the right hand side of the differential equation.

In the end, we obtain

$$\begin{aligned} A &= - \frac{48}{\pi} \frac{\mu U}{\gamma} \frac{R^2}{h^2} \cdot R \text{ and} \\ \delta r(\theta) &= - \frac{48}{\pi} \frac{\mu U}{\gamma} \frac{R^2}{h^2} \cdot R \theta \sin \theta \end{aligned} \quad (4.16)$$

as the solution of the differential equation, which we know is unique.

Notice however that this expression is slightly different than the one used in the article. This is because of a discrepancy in the definition of R , the droplet radius. In the paper, R is the radius of the drop when it is undeformed by the flow and circular. In the derivations above, R is the radius of the circle best fitting the deformed droplet. Notice that the two definitions are not identical, especially since the deformations δr of (4.16) have a volume contribution.

The droplet is incompressible and by applying the volume conservation, we can transform the R in equation (4.16) into the R of the paper to obtain equation (7):

$$\delta r(\theta) = \frac{48}{\pi} \frac{\text{Ca} R^2}{h^2} \cdot R (1 - \theta \sin \theta) \quad (4.17)$$

Cite this: DOI: 10.1039/c1lc20541b

www.rsc.org/loc

PAPER

Combining rails and anchors with laser forcing for selective manipulation within 2D droplet arrays†

Etienne Fradet,^a Craig McDougall,^b Paul Abbyad,^c Rémi Dangla,^a David McGloin^b and Charles N. Baroud^{*a}

Received 21st June 2011, Accepted 26th September 2011

DOI: 10.1039/c1lc20541b

We demonstrate the combination of a rails and anchors microfluidic system with laser forcing to enable the creation of highly controllable 2D droplet arrays. Water droplets residing in an oil phase can be pinned to anchor holes made in the base of a microfluidic channel, enabling the creation of arrays by the appropriate patterning of such holes. The introduction of laser forcing, *via* laser induced thermocapillary forces to anchored droplets, enables the selective extraction of particular droplets from an array. We also demonstrate that such anchor arrays can be filled with multiple, in our case two, droplets each and that if such droplets have different chemical contents, the application of a laser at their interface triggers their merging and a chemical reaction to take place. Finally by adding guiding rails within the microfluidic structure we can selectively fill large scale arrays with monodisperse droplets with significant control over their contents. In this way we make a droplet array filled with 96 droplets containing different concentrations of fluorescent microparticles.

1 Introduction

Performing a set of independent reactions in a two-dimensional (2D) array format is a standard approach for implementing a large number of parallel assays. This is the case for instance in multi-well plates, DNA or protein chips, and many other genomic technologies. Droplet microfluidic techniques have aimed to replicate such a 2D format in recent years, since the ability to keep a drop stationary allows the long term observation of its contents, in addition to providing combinatorial measurements on a single image. Patterning a 2D area with different droplets is straightforward when using surface microfluidic manipulations, *e.g.* through electro-wetting¹ or surface acoustic waves.² More classical drop deposition techniques have also been used to produce arrays of distinct droplets for combinatorial enzymatic studies³ or for polymerase chain reaction (PCR).⁴

Producing arrays of droplets in microchannels has proved more challenging, in part due to the standard methods for forming drops: both T-junctions and flow-focusing devices rely on the presence of a strong flow of the carrier fluid,⁵ so that holding the drops in an array requires a method to stop their motion against the outer flow. This has been achieved through

innovative designs of the microfluidic geometries and operating protocols, leading to different methods to array drops: quasi-2D arrays were formed by winding a linear path in the plane of the microchannel. Drops flowed in series in this microchannel and were blocked at particular locations, for example by having side pockets in the channel,^{6,7} by flowing the drops into parallel dead-end microchannels,⁸ or into parallel corrugated channels.⁹ These devices however suffer from strong droplet interactions since the drops are tightly confined into linear motion by the channel walls, which can make their operation difficult. Some authors reduced these interactions by increasing locally the channel width and depth.¹⁰ Real 2D arrays, in which droplet interactions are weak, were formed by placing obstacles in a wide microchannel¹¹ and the obstacles could be designed to hold one, two or more drops.^{12,13}

More recently, Abbyad *et al.*¹⁴ demonstrated the manipulation of drops in 2D by using *rails* and *anchors*, which correspond to grooves that are etched on the surface of the microchannel. In this approach, drops are squeezed by the top and bottom boundaries of the microchannel, which increases their surface energy. By partially entering into the grooves, the drop reduces its surface energy. This creates a gradient of surface energy at the edge of the grooves, which leads to an attractive force pulling it into the region with larger depth. This was used to guide drops along linear paths (a *rail*) or to hold them stationary in an *anchor*.¹⁴

The current challenge is therefore to pattern a 2D area with a heterogeneous droplet population, either by selectively placing a drop at the desired location, selectively extracting a drop, or selectively initiating a chemical reaction. To date, none of the methods for arraying drops allow for such controlled operations.

^aLaboratoire d'Hydrodynamique (LadHyX) and Department of Mechanics, Ecole Polytechnique, CNRS, 91128, Palaiseau, France. E-mail: baroud@ladhyx.polytechnique.fr

^bElectronic Engineering and Physics Division, University of Dundee, Nethergate, Dundee, DD1 4HN, UK

^cLaboratoire d'Optique et Biosciences (LOB), Ecole Polytechnique, INSERM U696, CNRS, 91128 Palaiseau, France

† Electronic supplementary information (ESI) available. See DOI: 10.1039/c1lc20541b

Instead, random filling is used in most cases and there exists no mechanism for selectively extracting a particular drop. While random distribution of drops can yield useful information in the case of two droplet species,¹³ it quickly becomes limiting when there are many species to be studied simultaneously. Here we demonstrate how the controlled filling, extraction, or reactions can be performed by combining the *rails* and *anchors* approach with the selective manipulation through laser-induced local heating.^{15–17} The *rails* and *anchors* provide a passive, robust and simple 2D guidance and trapping of drops, while the mobile laser spot adds an intelligent and versatile selectivity.

After the materials and methods section (Section 2), we turn to the physical ingredients that determine the different forces in Section 3. This is followed by demonstrations of drop extraction in Section 4. Filling an array with a controlled drop population is then demonstrated by showing how to build an array of drops which displays a gradient of concentration (Section 5). Finally, we demonstrate how to trigger local reactions on demand (Section 6).

2 Materials and methods

Microfluidic device fabrication

All experiments were conducted in PDMS microchannels (Dow Corning Sylgard 184) sealed onto glass slides by plasma bonding. The fabrication procedure relies on dry film photoresist soft lithography techniques¹⁸ which enable rapid prototyping of multi-level structures. The multilayer masters were etched in stacks of Eternal Laminar E8013 and Eternal Laminar E8020 negative films (of thickness $35 \pm 2 \mu\text{m}$ and $50 \pm 2 \mu\text{m}$ respectively) depending on the desired thickness of the main channel and patterns.

The successive steps were the following: (i) photoresist layers were successively laminated onto a clean glass slide using a PEAK Photo Laminator (PS320) at a temperature $T = 100^\circ\text{C}$ until the desired height h of the main channel was reached; (ii) The photoresist stack was exposed to UV (Hamamatsu Lightningcure LC8) through a photomask of the base channel (comprising a test section, droplet generation devices and entrance and exit channels); (iii) Additional photoresist layers were laminated on top of the exposed stack until the desired depth p of the patterns (anchor holes and/or rails) was reached; (iv) The stack of photoresist films was exposed again to UV, through the second photomask featuring only the patterns to be added onto the base channel. Finally, the full structure was developed by immersion in an aqueous bath of carbonate potassium at 1% mass concentration.

Furthermore, in order to render the internal channel surface hydrophobic, a surface treatment was applied: A dilute solution of 1H,1H,2H,2H-perfluorodecyltrichlorosilane (Sigma-Aldrich) in FC40 oil (3M Fluorinert) (20 μL in 1 mL of FC40) was flowed through the microchannel for approximately 5 min. The channel was then rinsed with pure FC40 to remove the residue chemicals remaining in the bulk.

Chip design and operation

The common architecture of the microfluidic chip was a base channel with a blank 'test section' onto which rail and anchor

patterns were etched. The base channel consisted of one (Sections 4–5) or two (Section 6) droplet generation devices discharging into a wide main test section. The system then emptied into a single outlet channel. The height of the base channel h was 100 μm everywhere. Channels upstream of the test section had widths ranging from 100 to 200 μm . The test section was a rectangle of dimensions $10 \times 3 \text{ mm}$ (Sections 4 and 6) or $20 \times 4.5 \text{ mm}$ (Section 5).

Various patterns of rails and anchors could then be added onto the base test section depending on the desired applications. Section 4 relied on a regular square array of small circular holes of diameter $d = 50 \mu\text{m}$ and depth $p = 35 \mu\text{m}$. For Section 6, only two rows of holes with a diameter $d = 200 \mu\text{m}$ were used. The pattern designed for Section 5 was a complex combination of rails, ranging in width from 50 μm to 200 μm , combined with square anchors of 120 μm a side.

Throughout the study, the continuous phase was FC40 oil (3M Fluorinert) of viscosity $\mu = 4.1 \text{ cP}$ containing fluorinated surfactants for both emulsion stabilization and improvement of the wetting conditions. Experiments described in Sections 4 and 5 used a Krytox (Dupont) ammonium salt,¹⁹ at 0.5% mass concentration, while those in Section 6 used a PEG-based surfactant at 0.01% mass concentration.¹⁹ Two inlets of oil were required: one at a flow rate Q_o for the droplet generation and one at a flow rate Q_e to adjust droplet entrainment in the test section independently of the droplet generation.

Different aqueous solutions were used as the dispersed phase and were injected at a flow rate Q_w : Section 4 uses pure water droplets; in Section 5 a solution of water containing fluorescent beads (Invitrogen green fluorescent beads, 1 μm) at a volume fraction of 0.4%. In Section 6, the two aqueous solutions consisted of a solution of FeCl_3 at 0.27 M and a solution of KSCN at 0.8 M. The interfacial tension γ between a pure water drop and the FC40 solution was measured to be $\sim 20 \text{ mN m}^{-1}$. We observed however that the contents of the drops, such as the chemicals of Section 6 or the fluorescent beads, could have an impact and reduce this value in some cases.

A system of computer controlled syringe pumps (Cetoni neMESYS) was used to control the different flow rates (Q_w , Q_o and Q_e) in real time.

Optical setup and laser operation

The optical arrangement employed for droplet manipulation makes use of a 1480 nm continuous wave infrared laser source (Fitel Furukawa FOL1424) and a commercial inverted microscope system (Nikon TE2000) equipped with epifluorescent illumination (Exfo X-cite 6210C). A pair of galvanometric mirrors (Cambridge Technologies 6210H) permitted beam positioning in the microchannels to be controlled by a mouse click using in-house Labview programs. Following the galvanometric mirror, the laser beam was both expanded appropriately (to overfill the back aperture of the microscope objective) and relayed to the back aperture of the objective by a 4f conjugate lens system and an appropriate dichroic mirror (OCTAX). The laser power was measured to be 200 mW in the focal plane of the microscope objective. The described system provided an approximately diffraction limited spot at the focal plane whose position was readily computer controlled by the user. A camera

was used to image the field of view *via* a sideport and record monochrome video at typical frame rates of 60 frames per second (Photron Fastcam 1024 PCI). Alternatively, a digital SLR camera (Nikon D70) was used to capture color images *via* the front camera port of the microscope. Whilst the laser spot wavelength was outside the range of both cameras, the spot location was visible as a dark shadow on the computer screen.

3 Physical ingredients

Guiding and trapping drops in our devices are based on manipulating three forces of different physical origins, as sketched in Fig. 1: The force due to the surface patterning F_γ , the entrainment force due to the flow of the outer fluid F_d , and the force due to the laser heating F_l . Below we discuss the main attributes of each of these forces.

Force due to surface patterning

The surface energy of a droplet can be written as $E_\gamma = \gamma A$, where γ is the interfacial energy and A the surface area of the droplet. While γ can be considered as nearly constant over the course of an experiment, A can vary significantly as the droplet changes its shape. An unconfined drop will take a spherical shape in order to minimize its surface area while the confinement can be used to force the drop to take a flattened “pancake” shape of height nearly equal to the microchannel height h . In the plane of the microchannel, one can describe the drop by its radius R ; in the case when $R \gg h$, the main contribution to the surface area is given by the top and bottom boundaries of the droplet and we can write $A \approx 2\pi R^2$, with a small correction due to the area around the drop in the vertical direction.

When the channel height is locally modified, for instance by etching a groove into one of the surfaces, the drop enters into the groove. This always leads to a reduction of the total surface area of the drop,²⁰ thus reducing its surface energy. Removing the drop from the region of low surface energy therefore requires a force F_γ , whose magnitude is given by the gradient of the energy and always pointing towards the energy minimum. Dangla *et al.*²⁰ estimate this anchoring force as $\gamma\Delta A/d$, where ΔA is the difference in surface area between the drop over the groove and away from it, and d is a characteristic length scale over which

the energy changes. They measure forces in the range of 100–600 nN for similar geometries to the ones presented here.

For a circular groove, a geometric calculation shows that F_γ does not depend on the drop size in the case when $R \gg h$. This is not the case however in the case of a rail, where F_γ scales linearly with the drop radius R .

Force due to the outer flow

The flow of the outer fluid applies a drag force F_d on the droplet through hydrodynamic drag. This force is always directed in the direction of motion of the outer fluid. Its magnitude scales as $F_d \sim \mu_o UR^2/h$, where μ_o is the outer fluid viscosity and U is the velocity of the outer fluid. F_d therefore increases with the flow velocity and depends strongly on the size of the droplet.

For given drop and channel geometries, we can measure a critical velocity beyond which $F_d > F_\gamma$ at which point the drop cannot be held anymore. For velocities below this critical velocity, a drop in an anchor is deformed from its circular shape (Fig. 1(a)). Conversely, a drop that is in a rail is pushed along the rail due to the existence of a component in the tangent direction F_d' of the drag force (Fig. 1(b)). Once the critical velocity is reached, drops cannot be held anymore and they are de-pinned by the outer flow.¹⁴ An important regime concerns velocities that are slightly below the critical velocity. In this regime, the anchor strength is sufficient to hold one droplet stationary but not two, since the net drag force experienced by the touching pair increases while the anchoring force remains constant. Abbyad *et al.*¹⁴ identified a range of velocities where drops enter into a ‘buffering’ mode, in which an incoming drop replaces the drop that was previously anchored. This buffering regime will be used below to determine the occupation of anchor sites in the experiments.

Force due to the laser heating

The final force F_l that we must consider is due to the localized heating by a focused laser.²¹ When the water–oil interface is heated locally, variations in surface tension lead to the creation of a flow along the interface, which in turn leads to flow inside and outside the droplet.¹⁶ The net effect on the droplet is a “pushing” force, by which the laser heating forces the droplet away from the laser position. This has been used in one-dimensional (1D) microchannels to sort or buffer drops, or change the order in which they flow.¹⁷ The magnitude of F_l was measured²¹ in confined microchannels to be in the range of 100–300 nN. Verneuil *et al.* also observed that the contributions to the force are dominated by the flows along the thin films between the drop and the lateral channel walls, which implied that the force depended on the drop size in that case.²¹ Finally, the direction of the force due to the laser heating is determined by the direction of the thermo-capillary flows. In the case studied by Verneuil *et al.*,²¹ the presence of surfactants in the continuous phase implied that laser produced a repulsive force, by inducing anomalous thermo-capillarity. There are however no measurements of the magnitude or size dependence of F_l in the absence of lateral walls.

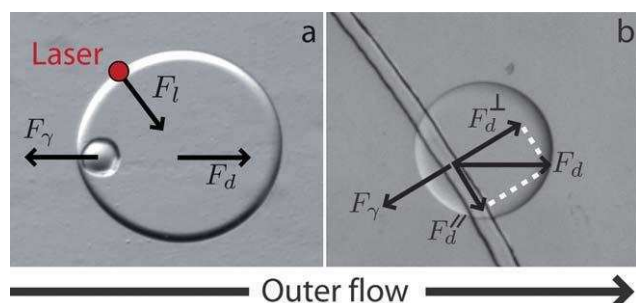


Fig. 1 Forces acting on a drop in the presence of surface patterning: The anchoring force due to the surface patterning F_γ , the drag force due to the flow of the outer fluid F_d , and the force due to the laser heating F_l . (a) The case of an anchor. (b) In the case of a rail, the unbalanced force due to the drag parallel to the rail F_d' leads to motion along this direction.

4 Extracting a drop from an array of holes

The force balance described above can now be used to selectively remove a drop from an anchor site, by adding the laser-induced force to the drag force from the fluid flow. An example implementation is shown in Fig. 2 and in ESI movie S1.† In this experiment, drops are initially formed in a flow-focusing geometry and flowed into the test section, which is patterned with a square lattice of holes. Some drops become anchored at the hole positions, filling the lattice in a random fashion. The water flow is then stopped and the oil flow rate is held constant at $Q_o = 2 \mu\text{L min}^{-1}$.

Once the lattice is filled (Fig. 2(a)), the laser focus is selectively positioned within the test section. If the laser is focused inside the droplet, it can remove it from the anchor. This allows the user to select a position on the computer screen and to remove the corresponding drop at that particular position. The oil flow rate then transports the drop away from the array and out of the microchannel (Fig. 2(b)). Fig. 2(c) shows an 'X' pattern formed using this method.

This device can be operated in two different regimes. In the current regime, small anchors and a weak oil flow rate are used, therefore requiring a high laser power ($P_{\text{laser}} = 200 \text{ mW}$) to remove the drops. Alternatively, lower laser powers can be used by increasing the flow rate to work closer to the critical anchoring velocity. In that case however, extracted drops interact with their neighbours and can lead to a buffering mode, in which drops downstream of the extracted drop also get unpinned.

5 Selectively filling an array

Here, the ability to sort and subsequently fill a two-dimensional array with droplets of a uniform size is presented. The methodology is again based upon the combination of creative chip design, which combines rails and anchors of different strengths, and highly localised laser induced forcing for derailing the drops. By superimposing anchors onto rails, droplets may be guided directly to the anchor sites where they become trapped on these 'storage rails'. The presented method involves first selectively filling these storage rails and then allowing the droplets to assemble into the desired array by entering into a buffering mode through an increase of the carrier oil flow rate.

To construct an array of droplets, we use a chip test section composed of 6 rails, each of which is periodically superimposed with 16 anchor sites, producing a 96 drop array. The rail sorting portion of this test section is shown in Fig. 3(a) which demonstrates active switching of droplets between rails, achieved by employing laser-induced forces as described above. In the

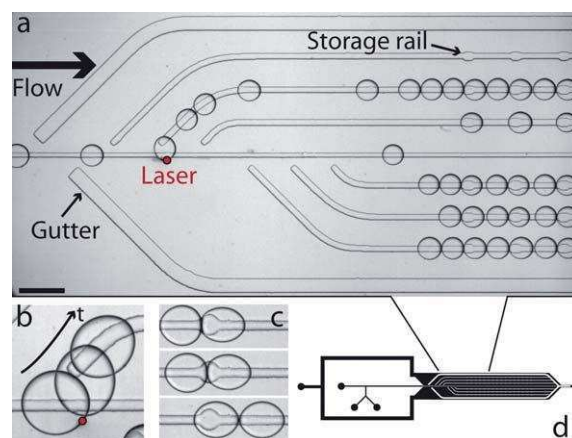


Fig. 3 (a) Test region ($20 \times 4.5 \text{ mm}$, $h = 100 \mu\text{m}$) for building an array of droplets. All rails are $50 \mu\text{m}$ deep. The central default rail is $50 \mu\text{m}$ wide. The side gutter rails used to filter out large droplets are $200 \mu\text{m}$ wide. The 6 storage rails are $75 \mu\text{m}$ wide and the anchor sites superimposed on these rails are $120 \mu\text{m}$ squares. The image shows the fifth rail being filled (see movie S2 for full sequence†). The scale bar is $600 \mu\text{m}$. (b) Superposition of three images showing a drop leaving the default rail into a storage rail. (c) Once the storage rails are filled the entrainment flow rate Q_e is increased to initiate a buffering mode whereby the droplets self arrange into an array of one droplet trapped at each anchor site. (d) A schematic of the complete chip design illustrates the droplet formation portions of the chip relative to the test region.

absence of the laser, droplets are guided along the central rail to the exit of the chip by default. The selective derailing operation is demonstrated in Fig. 3(b) and ESI movie S2.† To fill the array, rails are filled in sequence, row by row, beginning with the right-most junction to the left-most junction. Any order can be used however, even working on a drop-by-drop basis.

Selective filling of the array, in addition to anchoring the drops in place, depends upon several key design features which are highly sensitive to droplet size. Consequently, the device geometry is constructed specifically for a given droplet size. For this experiment the chips (shown in Fig. 3(d)) are designed for droplets of a $150 \mu\text{m}$ radius.

The first of these features is designed to ensure that all droplets placed on the array are of the same size. Such steps are necessary, as droplet monodispersity is not guaranteed for transient stages of droplet production, nor for all flow rates. Droplets are only placed in the array when the laser is used to direct them there. Furthermore, droplets below the size of interest cannot be derailed from the central rail, due to the limit on the maximum deflection achievable with the employed laser power. Small



Fig. 2 Selectively extracting drops. (a) The array of holes ($d = 50 \mu\text{m}$ and $p = 35 \mu\text{m}$) is initially filled with water drops. (b) The laser is focused on the water–oil interface, pushing the drops out of the anchor. (c) An 'X' is patterned with the remaining droplets. Scale bar is $400 \mu\text{m}$.

droplets are therefore guided out of the chip and never reach the storage rails. To ensure droplets of a size larger than those under study are also eliminated, two side gutters are placed upstream and redirect large droplets along the side of the test section. Therefore, large droplets are prevented from entering the array portion of the chip as the gutter rails provide an energetically favorable alternative route. These features ensure that only droplets of the desired size are available for active laser forcing onto the array rails.

The remaining features are concerned with filling the storage rails. Once a droplet passes the two side gutters, it enters the rail switching area and is available for sorting into the storage rails containing square anchor sites. As can be seen in Fig. 3(b), the storage rails have been designed to be wider than the central guide rail and there is a gap between the storage rails and the central default rail. This intentional gap is to avoid junction sites, where the local width reaches a maximum value. This leads to junctions behaving as anchor sites from which drops cannot be removed. Upon deflection by the laser, the droplet sees the wider side rail as an energetically favorable route and leaves the default rail as illustrated in both Fig. 3(b) and ESI movie S2.†

Once sorted onto the storage rails, the droplet encounters anchor sites and becomes trapped. The dimensions of the anchors have been chosen for the given droplet radii so that they may hold one droplet parked stationary against the mean flow. However, the anchor site is intentionally too weak to hold multiple droplets stationary. Consequently, under the correct external flow conditions the droplets will enter into a buffering regime. It is noteworthy that whilst the storage rails are being filled with droplets, the apparent channel cross section available for the oil to flow through decreases due to the stationary droplets. Such a reduction causes an increase in the velocity that must be taken into account when filling the anchor sites, to prevent all the droplets from being swept out of the array. Therefore, the entrainment oil flow rate Q_e is reduced from 40 to 20 $\mu\text{L min}^{-1}$ during the filling period as the storage rails become populated, while the small oil (Q_o) and water (Q_w) flow rates are maintained at a steady 0.5 and 0.18 $\mu\text{L min}^{-1}$ respectively. This ensures that all rails are completely filled with monodisperse droplets during the filling procedure. Once this procedure is completed, the entrainment flow rate Q_e is increased slowly to 70 $\mu\text{L min}^{-1}$ to initiate the desired droplet buffering regime (Fig. 3 (c)). Under these conditions arrays of 96 droplets may be constructed in a controlled manner at a rate of approximately 1 min per rail for droplet sorting and a further minute for droplet buffering into a complete array.

Whilst maintaining the droplet size for a given chip design, this methodology may be extended to droplets of varying composition. An example of such a controlled filling appears in Fig. 4, where an array of 96 anchored droplets with an increasing concentration of fluorescent beads is shown. In the chip used here, a mixer was positioned before the T-junction used for droplet formation, allowing the composition of the droplets to be altered in time. To modify the composition of the droplets, a stream of pure water is mixed with a concentrated bead solution in pure water (0.4% by volume). For the various rails of the array, the ratio of pure water to bead solution is altered by varying the relative flow rates whilst maintaining an overall flow rate of 0.18 $\mu\text{L min}^{-1}$ for the mixture. This ensures that the

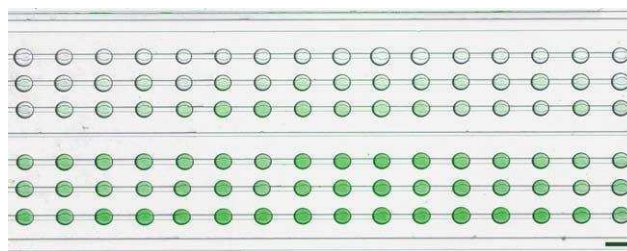


Fig. 4 A superposition of bright-field and fluorescent images of a 96 anchor array. The droplet composition has been altered from pure water to a solution of water and green fluorescent beads to create a gradient. The droplet volume is 7 nL each. The scale bar is 300 μm .

droplets are of uniform size. For the top rail, droplets are composed entirely of pure water and the flow rate of the bead solution is set to zero. For each row, moving down the array, the flow rate of the bead solution is increased in 0.005 $\mu\text{L min}^{-1}$ increments whilst the water rate is decreased by the same amount.

The filling protocol begins with the top rail, which is filled with droplets containing pure water. The laser is then removed, causing all droplets to follow the default central path to the drain. The droplet composition is then altered to the concentration required for the next rail and allowed to reach a steady state before filling of that rail commences. To do so we translate the laser to the correct position for the new rail and direct droplets into the storage rail. Once the rail is filled with droplets, the laser is again removed and the droplet composition altered. The remaining storage rails are filled in this stepwise manner, changing the droplet formation specifically for each rail and using the laser to position the droplets onto the rails.

6 Controlled initiation of chemical reactions at anchor sites

Our final demonstration of the power of the technique is to carry out the loading of two droplets into the anchor sites and then use laser induced merging of droplets to enable controlled chemical reactions within selected droplet pairs. This can be done at a location predefined by the anchor position and it indicates the potential of this method as an analysis and assaying tool.

We make use of an array of anchors in the chip test section. A key point here is that the anchor holes are designed to be twice as wide as the droplet diameters, so that each can accommodate two droplets. In this situation, where the holes are larger than the droplet, an outer flow rate of 80 $\mu\text{L min}^{-1}$ removes one drop per trap while in the experiment presented in Section 4, an outer flow rate of 10 $\mu\text{L min}^{-1}$ detaches all the drops.

To initiate a chemical reaction we must load droplets with different contents into each hole site. We choose droplets with FeCl_3 and KSCN , which react to form a colored liquid from two colorless ones. We begin by generating one species of droplets from the top flow focusing junction and fill the anchor sites ($Q_o^{\text{top}} = 7 \mu\text{L min}^{-1}$, $Q_w^{\text{top}} = 0.1 \mu\text{L min}^{-1}$). Initially this leads to two droplets occupying each anchor site, since the holes are twice as big as the droplets (Fig. 5(a + b) and supplementary movie S3†). We then increase the oil flow rate ($Q_o^{\text{top}} = 80 \mu\text{L min}^{-1}$, $Q_w^{\text{top}} = 0 \mu\text{L min}^{-1}$) to wash out one of each pair, thus leaving one

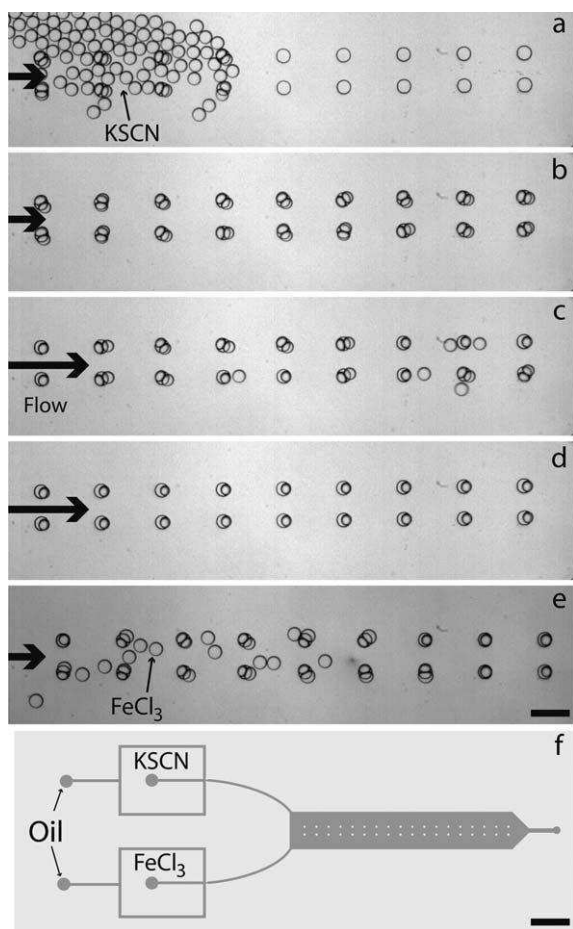


Fig. 5 (a + b) Filling first species into anchor holes. (c + d) Emptying one droplet from each trap to leave one drop per anchor site. (e) Bringing in the second species droplets to anchor holes. The scale bar is 400 μm . (f) Schematic of channel used, illustrating dual inlets for the two different chemical species. The test section (containing the anchors) is 100 μm high, 1 cm long and 3 mm wide. The anchor holes have a height of 50 μm and a diameter of 200 μm . The scale bar is 3 mm.

droplet per site (Fig. 5(c + d)). We then introduce droplets containing the second species from the bottom flow focusing device (Fig. 5(e)). Here lower flow rates than for the first droplets are used to prevent accidentally knocking any further droplet out of the holes: $Q_{\text{o}}^{\text{bottom}} = 5 \mu\text{L min}^{-1}$, $Q_{\text{w}}^{\text{bottom}} = 0.05 \mu\text{L min}^{-1}$. A loaded array, with two droplets per trap site, each with different contents, is shown in Fig. 6(a).

Having established the ability to fill the holes with droplets we can then use laser induced droplet merging¹⁵ to start the chemical reaction. With the control we have over the positioning of the laser this means that we can target a specified droplet pair in the array. The power used is 200 mW, and a dwell time at the droplet interface of 100 ms is required before any fusion takes place when laser position is well placed.

The process of laser initiated droplet merging is shown in Fig. 6(b) and ESI movie S4,[†] where we choose to react the droplets such that they form a 'W' pattern. The track of the laser is shown by the solid and dashed lines in Fig. 6(b), which correspond to a time $t = 117 \text{ ms}$ after the merging of the drops at the top-center location. Fig. 6(c) shows the final state where only

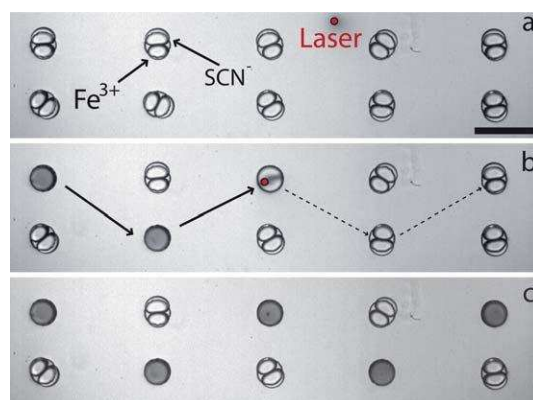


Fig. 6 Laser induced merging of droplets in anchor sites. (a) Filled droplet array. Laser spot is shown as a red dot. (b) The laser is scanned in the pattern shown. As it stops on the droplet-droplet interface it initiates fusion and a chemical reaction takes place. The solid line shows where the beam has been, the dashed line its future path. (c) The laser completes its path leaving 5 anchor points with a reaction product and all other droplets undisturbed. Scale bar is 400 μm .

the droplets illuminated by the laser have undergone the reaction.

7 Summary and discussions

In summary, we have demonstrated the first device that allows a selective patterning of a 2D array with microfluidic droplets. This is performed either through selectively filling or emptying the array, or by triggering a chemical reaction on demand. The approach relies on combining the rails and anchors approach, which provides robust passive manipulation, and the localized heating from the laser which adds selectivity and local actuation.

Both of these approaches are highly scalable, independent of the microchannel material and rely on very simple micro-fabrication: the rails and anchors are produced using lithographic techniques and can easily be densified over wide areas. The design of the test section is nearly common to all of the devices, which only differ in the pattern of rails and anchors that are designed for a specific application. This further simplifies the fabrication in large quantities for commercial applications. As for the optical heating, any number of operations can be performed with single beam by simply scanning the laser focus or by using holographic techniques to split one beam into a complex pattern.²² The tight focus of the laser allows manipulation of individual droplets, even in very dense arrays, providing a clear advantage over electrical or acoustic methods.

The throughput of the devices presented here is appropriate for many applications that require a high level of control, since all of the experiments presented here lasted less than a few minutes using purely manual control of the flow rate and the laser position. This duration can be further reduced through use of an automated time-sharing of the laser heating, which can produce many operations simultaneously, or through optimization of the device designs. In the case of the droplet extraction for instance, a different pattern of anchors or the addition of gutter rails would allow the device to function at higher oil velocity, therefore allowing much faster sorting of the drops.

Increasing the throughput in the case of the array filling depends on the ability to derail rapidly moving drops. This will be realizable by improving the tolerance on the micro-fabrication process, which would allow the distance between the side-rails and the central rail to be better calibrated for the drop sizes. By optimizing this distance, drops can be derailed with a minimal deflection, which would allow us to work at higher flow rates.

Finally, future work will have to investigate the effect of the laser heating on the contents of the droplets, as well as ways to minimize these effects such as pulsing the laser source. While we expect that the heating can damage some proteins or sensitive biological material, it should still allow DNA or chemical manipulation without any significant artifacts.

8 Acknowledgments

Special thanks to Estelle Mayot for providing the perfluorinated surfactants used in our studies. The authors also thank Caroline Frot for microfabrication assistance. This project was partially supported by a 'Royal Society International Joint Project'. D. M. is a Royal Society University Research Fellow. The authors finally acknowledge the financial support from CNRS and Ecole Polytechnique.

References

- 1 S. K. Cho, H. Moon and C. J. Kim, *J. Microelectromech. Syst.*, 2003, **12**, 70–80.
- 2 A. Wixforth, *Superlattices Microstruct.*, 2003, **33**, 389–396.
- 3 L. Mugherli, O. N. Burchak, L. A. Balakireva, A. Thomas, F. Chatelain and M. Y. Balakirev, *Angew. Chem. Int. Ed.*, 2009, **48**, 1433–1435.
- 4 H. Kim, S. Vishniakou and G. W. Faris, *Lab Chip*, 2009, **9**, 1230–1235.
- 5 C. N. Baroud, F. Gallaire and R. Dangla, *Lab Chip*, 2010, **10**, 2032–2045.
- 6 H. Boukellal, S. Selimovic, Y. Jia, G. Cristobal and S. Fraden, *Lab Chip*, 2009, **9**, 331–338.
- 7 W. Shi, J. Qin, N. Ye and B. Lin, *Lab Chip*, 2008, **8**, 1432–1435.
- 8 P. Laval, N. Lisai, J. B. Salmon and M. Joanicot, *Lab Chip*, 2007, **7**, 829–834.
- 9 C. H. J. Schmitz, A. C. Rowat, S. Koester and D. A. Weitz, *Lab Chip*, 2009, **9**, 44–49.
- 10 J. Shim, G. Cristobal, D. R. Link, T. Thorsen, Y. Jia, K. Piattelli and S. Fraden, *J. Am. Chem. Soc.*, 2007, **129**, 8825–8835.
- 11 A. Huebner, D. Bratton, G. Whyte, M. Yang, A. J. deMello, C. Abell and F. Hollfelder, *Lab Chip*, 2009, **9**, 692–698.
- 12 Y. Bai, X. He, D. Liu, S. N. Patil, D. Bratton, A. Huebner, F. Hollfelder, C. Abell and W. T. S. Huck, *Lab Chip*, 2010, **10**, 1281–1285.
- 13 A. Huebner, C. Abell, W. T. S. Huck, C. N. Baroud and F. Hollfelder, *Anal. Chem.*, 2011, **83**, 1462–1468.
- 14 P. Abbyad, R. Dangla, A. Alexandrou and C. N. Baroud, *Lab Chip*, 2011, **11**, 813–821.
- 15 C. N. Baroud, M. R. de Saint Vincent and J. P. Delville, *Lab Chip*, 2007, **7**, 1029–1033.
- 16 C. N. Baroud, J. P. Delville, F. Gallaire and R. Wunenburger, *Phys. Rev. E*, 2007, **75**, 046302.
- 17 M. L. Cordero, D. R. Burnham, C. N. Baroud and D. McGloin, *Appl. Phys. Lett.*, 2008, **93**, 034107.
- 18 K. Stephan, P. Pittet, L. Renaud, P. Kleimann, P. Morin, N. Ouaini and R. Ferrigno, *J. Micromech. Microeng.*, 2007, **17**, N69–N74.
- 19 J. Clausell-Tormos, D. Lieber, J. C. Baret, A. El-Harrak, O. J. Miller, L. Frenz, J. Blouwolff, K. J. Humphry, S. Köster and H. Duan, *et al.*, *Chem. Biol.*, 2008, **15**, 427–437.
- 20 R. Dangla, S. Lee and C. N. Baroud, *Phys. Rev. Lett.*, 2011, **107**, 124501.
- 21 E. Verneuil, M. L. Cordero, F. Gallaire and C. N. Baroud, *Langmuir*, 2009, **25**, 5127–5134.
- 22 D. G. Grier, *Nature*, 2003, **424**, 810–816.

Chapter 5

Producing and transporting drops with wedges

In this last chapter, we address the question of producing droplets in a 2D microfluidic device using confinement gradients. To this end, we rely on devices of geometry similar to the one drawn in Fig. 5.1. It consists of an inlet channel of rectangular cross-section that leads to a wide reservoir whose top and bottom walls are inclined at an angle α . This wedged geometry provides a constant confinement gradient in the microfluidic chamber.

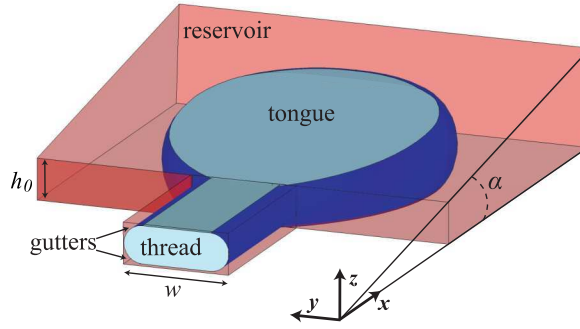


Figure 5.1: 3D sketch of a device during operation. The non-wetting dispersed phase is pushed through the inlet channel (width w and height h_0) into a wide reservoir containing a stationary continuous phase. The top wall of the reservoir is inclined at an angle α . Fluid from the continuous phase remains in the corners of the inlet channel, forming gutters connected to the reservoir while the dispersed phase forms an elongated tongue in the reservoir.

The device is initially filled with the liquid which will form the continuous phase (oil or water) and its surface is treated to provide good wetting for this liquid. The dispersed phase (water or oil) is then injected at a flow rate Q into the reservoir through the inlet channel. Owing to the non-wetting character of the dispersed phase, we expect the injected liquid to form an elongated thread in the inlet channel while leaving out corner gutters

of continuous phase [64]. Once the thread reaches the reservoir, lateral confinement is suddenly released and the liquid should expand into a tongue, as sketched in Fig. 5.1.

The equation (3.38) from Chapter 3 shows that a pancake drop in a non-parallel Hele-Shaw cell feels a force $F_\gamma \approx 2\gamma \tan \alpha \pi R^2 / h_0$ that propels it towards regions of least confinement. This force here pulls the tongue away from the inlet channel and we investigate if it could induce droplet production.

5.1 Device microfabrication

All devices were made in PDMS (polydimethylsiloxane) using soft lithography techniques. The novelty in the microfabrication lies in the construction of the reservoir whose top wall is inclined at an angle α .

A first approach, most used for this study, consists in making a mold which has a region inclined at the desired angle. To do so, the mold was fabricated in a two-step procedure: i) the injection nozzles and all channels upstream were obtained using the dry film photoresist soft lithography technique [117]; ii) the sloped reservoir was constructed by bonding glass cover slips using NOA81 optical glue (Norland Optical Adhesive). The microfabrication stages are detailed below and illustrated on Fig. 5.2.

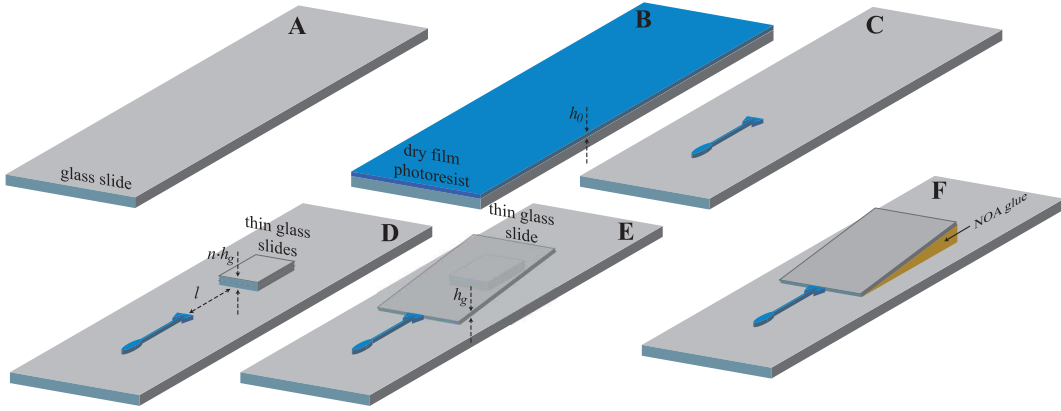


Figure 5.2: Sketch of the successive microfabrication steps required to produce a device with a sloped reservoir.

Starting from a standard glass slide 1.1 mm in thickness (stage A), three layers of dry film photoresist ($1 \times$ Eternal Laminar E8013 and $2 \times$ Eternal Laminar E8020 negative films of thickness $31 \pm 2 \mu\text{m}$ and $49 \pm 2 \mu\text{m}$ respectively) are successively laminated using an office laminator at a temperature of 100°C until the desired channel height $h_0 \approx 130 \mu\text{m}$ is reached (stage B). The photoresist film is then exposed to UV through a photomask of the injection network. The nozzle structures are developed by immersion in an aqueous bath of carbonate potassium at 1% mass concentration (stage C). To make the sloped reservoir, n square thin cover slips 1 cm a side and $h_g \approx 130 \mu\text{m}$ in thickness are glued using NOA adhesive to the base slide at a distance l from the nozzles (Stage D). Then,

another thin glass slide is placed just against the nozzle and rested on top of the glass pillar from the previous step (Stage E). Consequently, the glass slide is inclined compared with the base structure, at an angle given by the relation $\tan \alpha = n \cdot h_g / l$. Last, the gap between the inclined slide and the base slide is filled with NOA adhesive by capillary suction and reticulated with UV (Stage F). For devices with structures etched into the reservoir, dry film photoresist structures are added to the sloped glass slide prior to gluing.

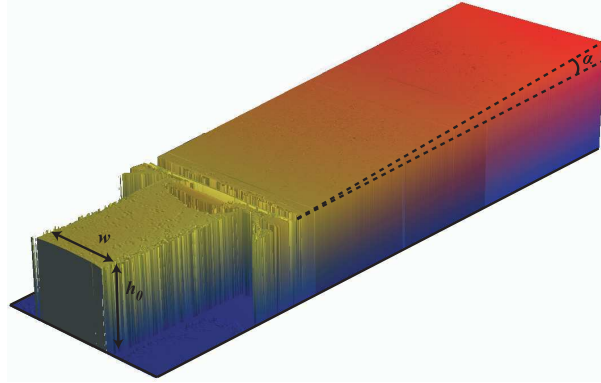


Figure 5.3: Measured height profile of an injection nozzle of dimension $h_0 = 130 \mu\text{m}$, $w = 250 \mu\text{m}$ and $\alpha = 2.6^\circ$

The topography of the mold was obtained using an optical profilometer (Veeco Wyco NT1100). These measurements verified that the height of the reservoir increased linearly downstream of the injection nozzle, as illustrated by Fig. 5.3.

The channels were then replicated in PDMS (Dow Corning SYLGARD 184, 1/10 ratio of curing agent to bulk material), poured over the master and cured 2 hours at 70°C . Finally, the PDMS is cut off and sealed on a glass slide by plasma bonding to obtain a device with a sloped reservoir.

This microfabrication protocol has the advantage of producing devices with a known and reproducible reservoir slope α . However, the minimum height of the channels is limited by the thickness of the cover slip used to make the sloped reservoir at $h_0 = 130 \mu\text{m}$.

A second approach relies instead on the deformability of the PDMS to produce *inflatable* devices which have reservoirs of any height and controllable slope at the nozzles. In this case, a flat mold of the device is fabricated using the standard dry film photoresist soft lithography techniques. For example, a $15 \mu\text{m}$ layer of photo-resist is laminated and exposed to UV through a photomask corresponding to both the inlet channel and the main reservoir. The structures are then etched, replicated in PDMS and sealed onto a glass slide to form the microfluidic device, as described above.

At this stage, the reservoir is flat. In order to create the slope of the reservoir, the device is pressurized above atmospheric pressure by connecting it to a programmable pressure source (Fluidgent MFCS-8C) via a dedicated pressure inlet in the chip design. Because PDMS is elastic (Young modulus $E \approx 1 \text{ GPa}$), the wide roof of the reservoir bends outwards [130]. This creates an apparent slope at the nozzles as illustrated on Fig. 5.4 and

the slope angle α can be controlled by varying the imposed pressure in the reservoir p_o . The deformations are most significant in the reservoir because of its high width to height aspect ratio. Comparatively, the narrow geometry of the inlet channels is not affected by the pressure stresses.

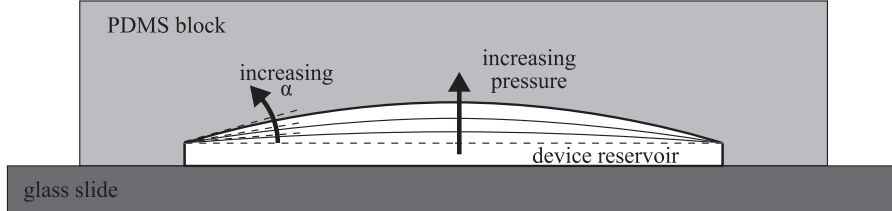


Figure 5.4: Sketch of the evolution of the geometry of an *inflatable* device. The PDMS top wall of the reservoir bends outwards and therefore connects with the side walls with a slope α that increases with the inner pressure p_o .

Although this method is easy to implement, the dependence of α on the imposed pressure showed some variations from device to device. We believe this is due to differences in the elastic property of the reservoir roof which depends both on the Young-Modulus and on the exact thickness of the PDMS above the reservoir.

5.2 Experimental observations

5.2.1 A control experiment

In a first control experiment, we inject distilled water at a flow rate $Q = 1 \mu\text{L}/\text{min}$ through an inlet of dimensions $w = 100 \mu\text{m}$ and $h_0 = 130 \mu\text{m}$ into a flat reservoir ($\alpha = 0^\circ$) filled with FC-40 fluorinated oil + 2% of PEG-PFPE surfactant. In this case, the top and bottom walls of the reservoir are parallel and there is no gradient of confinement. We observe that a circular tongue grows indefinitely into the reservoir and does not break off, as shown in Fig. 5.5.

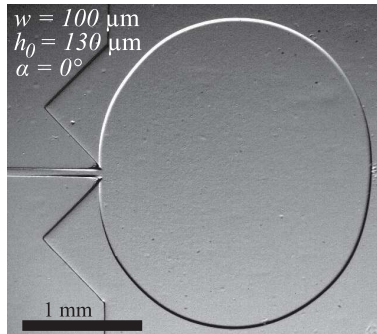


Figure 5.5: Photograph of a water tongue growing in a flat reservoir filled with FC-40 fluorinated oil.

5.2.2 A generic scenario for droplet production

Next, we repeat this experiment in a device which has its ceiling inclined with respect to the floor at a small angle $\alpha \approx 1.2^\circ$, as illustrated in Figs. 5.6.a-c.

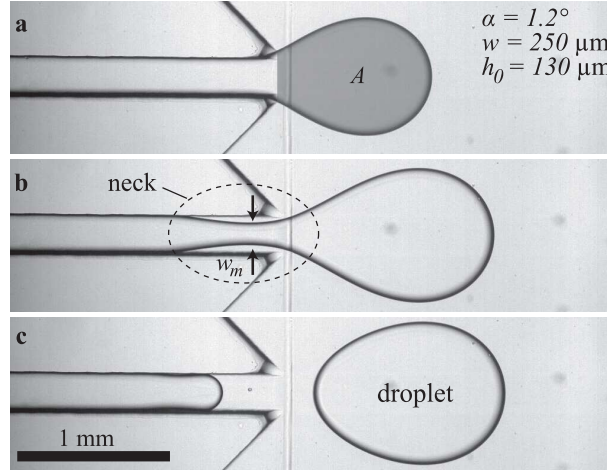


Figure 5.6: Photographs of a water tongue growing under continuous fluid injection at $Q = 1 \mu\text{L}/\text{min}$ in a sloped reservoir of dimensions $w = 250 \mu\text{m}$, $h_0 = 130 \mu\text{m}$ and $\alpha = 1.2^\circ$ filled with FC-40 fluorinated oil + 2% PEG-PFPE surfactant.

In this case, the thread expands into an elongated tongue resembling a 2D pendant drop upon entering into the reservoir (Fig. 5.6.a). The tongue's equivalent radius $R = \sqrt{A/\pi}$, where A is the projected surface area, grows until it reaches a critical value R^* . At this point the thread locally forms a neck of width w_m (Fig. 5.6.b) that progressively shrinks before suddenly pinching off when $w_m \approx h_0$, thus liberating a pancake droplet of radius R_d . It is noteworthy that the neck systematically appears upstream of the nozzle, inside the injection channel. The drop then spontaneously moves away from the nozzle (Fig. 5.6.c), propelled by the confinement gradient.

This scenario is generic to all of the sloped nozzles that we have investigated, spanning angles in the range $0.5^\circ < \alpha < 4.5^\circ$, widths from $100 < w < 500 \mu\text{m}$, operated at flow rates $Q = 0.04$ to $40 \mu\text{L}/\text{min}$. Overall, these experiments demonstrate that the confinement gradient of the wedged geometry is able to produce and transport droplets in a Hele-Shaw cell.

5.2.3 Influence of α , fluid properties and the injection flow rate on R_d

These experiments also reveal a strong dependence of R_d on the value of the slope of the reservoir. Indeed, a slope $\alpha = 0^\circ$ yields a *drop of infinite radius* while for $\alpha = 1.2^\circ$, we observe that R_d is approximately 5 times the reservoir height h_0 . The decrease in R_d with α is illustrated on Fig. 5.7.a which displays images of drops produced with nozzles of

identical width $w = 250 \mu\text{m}$ and height $h_0 = 130 \mu\text{m}$ but varying slopes $\alpha = 0.5, 1.2, 2.4$ and 4.5° .

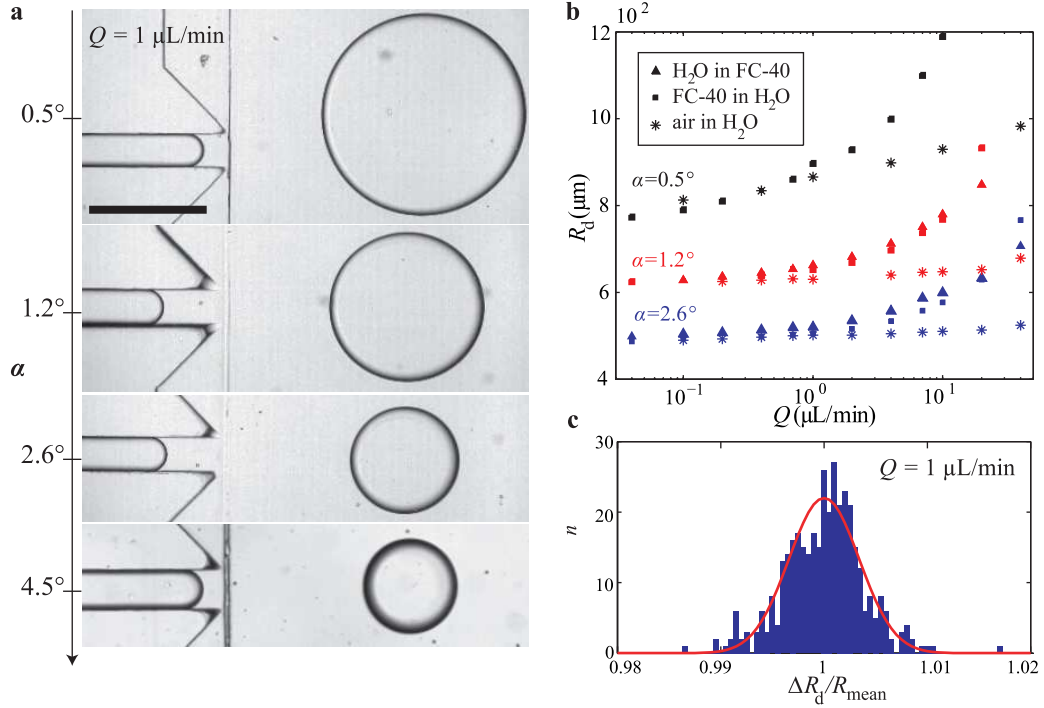


Figure 5.7: **a.** Images of drops captured immediately after they are produced from nozzles of identical height h_0 and width w but varying slopes $\alpha = 0.5, 1.2, 2.4$ and 4.5° . **b.** Plots of R_d versus the injection flow rate Q for three different channels with varying slopes (blue points for $\alpha = 2.6^\circ$, red points for $\alpha = 1.2^\circ$ and black points for $\alpha = 0.5^\circ$) and for three different fluid pairs (\blacksquare for FC-40 drops in water + 2% SDS, \blacktriangle for water drops in FC6-40 + 2% PEG-PFPE surfactant and $*$ for air bubbles in water + C_6E_{12} at the critical micellar concentration). **c.** Distribution of the size variations ΔR_d normalized by the mean drop size R_{mean} fitted with a gaussian of standard mean deviation $\sigma = 0.21\%$.

On the contrary, the injection flow rate Q appears to play only a weak role in the droplet production mechanism since we observe that it does not modify significantly the drop size. As shown on the log-lin plot of R_d versus Q of Fig. 5.7.b, we find that a 1000 fold increase in flow rate, from $0.04 \mu\text{L/min}$ to $40 \mu\text{L/min}$, only doubles the size of liquid drops and increases the radius of air bubbles by 25% at most. In addition, the drop size decreases towards a finite value that we call R_d^0 as Q tends to 0. This also indicates that the injection flow rate does not play a key role in the drop production mechanism, unlike with flow focusing [131] or T-junction devices [132].

Another key observation is that the sizes of the drops and bubbles produced at low flow rates are the same for all the fluid pairs investigated. Air bubbles in water have a radius R_d indistinguishable from that of water drops in oil and oil drops in water. Yet, these fluids have different viscosities and interfacial tensions, as listed in the table below.

Therefore, it appears that the mechanism for droplet formation is also independent of the fluid properties.

Last, we evaluate the monodispersity of the drops by measuring with a high resolution Spot camera (2048×2048 pixel resolution) the radii of several hundreds of drops produced sequentially by a nozzle of dimensions $w = 250 \mu\text{m}$, $h_0 = 130 \mu\text{m}$ and $\alpha = 1.2^\circ$ at a flow rate $Q = 1 \mu\text{L}/\text{min}$. We find that the device immediately reaches excellent monodispersity since the radii of the first few drops are within 5% of the long-time average R_{mean} . In addition, the size distribution shown in Fig. 5.7.c reveals a steady-state polydispersity index of the produced emulsions of 0.2%, an order of magnitude better than other microfluidic systems.

Continuous phase	Viscosity μ_c (cP)	Dispersed phase	Viscosity μ_d (cP)	Interfacial tension γ (mN/m)
$\text{H}_2\text{O} + \text{C}_6\text{E}_{12}$ ¹ at 1 CMC ²	1	Air	$2 \cdot 10^{-2}$	50 ± 2
$\text{H}_2\text{O} + \text{SDS}$ ³ at 1% mass concentration	1	FC-40 oil (3M)	4.1	12 ± 2
FC-40 oil (3M) + PEG-PFPE [133, 134, 135] at 1% mass concentration	4.1	H_2O	1	7 ± 1

¹ C_6E_{12} = hexaethylene glycol monodecyl ether, provided by the LPS.

² CMC = critical micellar concentration.

³ SDS = sodium dodecyl sulfate.

5.2.4 Recap of the experimental observations

Overall, the experimental observations reveal the following properties of droplet production in the wedged geometry of Fig. 5.1:

- minute inclination angles α , smaller than 0.5° , are sufficient to trigger droplet production
- pinching systematically occurs upstream of the nozzle, inside the injection channel
- the drop size R_d decreases with increasing α
- drops of finite size R_d^0 are produced as the injection flow rate Q approaches zero.
- R_d is weakly sensitive to Q
- at low flow rate, R_d is independent of the fluid properties

In the following section, we identify a physical mechanism that captures all these properties.

5.3 A novel mechanism for droplet formation

The following model for droplet production is unconventional as it relies neither on a force balance nor on a stability criterion.

The systematic observation in our experiments of the collapse of the thread inside the inlet channel suggests that the thread plays a key role in the droplet production mechanism. By studying the equilibrium of the thread upstream of the injection nozzle instead of the tongue in the reservoir, we identify a minimum \mathcal{C}^* of the mean curvature of a confined non-wetting fluid thread below which there no longer exists equilibrium shapes of the interface. We show that the tongue in the reservoir forces the curvature of the thread in the inlet channel to decrease beyond \mathcal{C}^* value, at which point the thread is forced out of equilibrium and collapses, releasing a droplet in the reservoir.

5.3.1 The minimum curvature of a confined non-wetting thread at equilibrium

Consider a thread of non-wetting fluid confined in an infinitely long channel with a rectangular cross section of width w and height h_0 . Next, imagine that by some mechanism we are able to impose an overpressure in the inner phase compared to the outer phase, i.e. $\Delta p = p_i - p_o > 0$.

The thread then inflates inside the channel until part of its interface eventually presses and flattens against the channel walls. The rest of the interface, referred to as the *free interface* according to the definitions introduced in Chapter 1, bends in the corners of the channel and forms gutters of outer fluid, as sketched on Fig. 5.8.a. An equilibrium shape of the thread is reached as soon as the curvature \mathcal{C} of the free interface verifies the Young-Laplace equation (1.1): $\gamma\mathcal{C} = p_i - p_o$. Calling $r = 1/\mathcal{C}$ the radius of curvature of the gutters, this equation is equivalent the equilibrium condition $\gamma/r = p_i - p_o$.

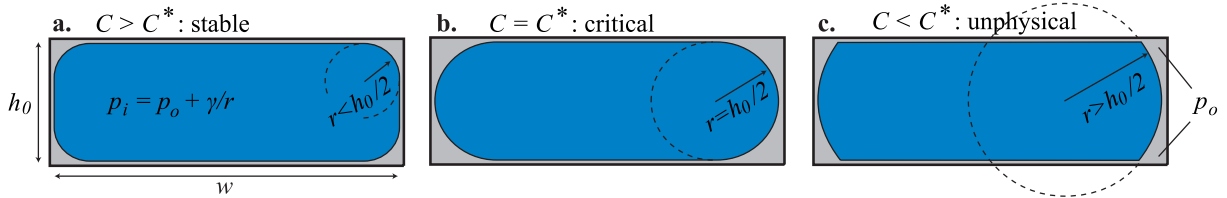


Figure 5.8: Sketches of the cross-sectional shape of an infinitely long non-wetting thread confined inside a rectangular channel. **a.** For high inner pressures p_i inside the thread, the interface flattens against the channel walls except near the corners where it bends and forms corner gutters with a strong curvature \mathcal{C} and small radius of curvature $r = 1/\mathcal{C}$. **b.** When \mathcal{C} decreases to the critical value $\mathcal{C}^* = 2/h_0$, then $r = h_0/2$ and the inner fluid completely detaches from the channel side walls. **c.** When $\mathcal{C} < \mathcal{C}^*$, the shape of the interface is unphysical. The interface must adjust its mean curvature by bending in the plane of the channel which eventually leads to pinching and collapse of the thread.

Hence, decreasing the pressure p_i inside the thread decreases the equilibrium curvature \mathcal{C} of the thread and thereby increases the radius r of the gutters. However, r is limited by confinement and cannot exceed $h_0/2$. Indeed, as illustrated by Fig. 5.8.b, the case

$r = h_0/2$ is a critical configuration of the thread for which the free interfaces of the top and bottom gutters meet at mid-height in the channel. Increasing the radius of curvature r of the gutters beyond $h_0/2$ leads to the unphysical situation of a kinked interface at the channel wall, as represented in Fig. 5.8.c.

The upper bound $r < h_0/2$ imposed by the confinement on the radius of curvature of the gutters implies a lower bound $\mathcal{C}^* = 2/h_0$ on the curvature of the thread below which there does not exist any equilibrium shape of the thread. Equivalently, the condition $r < h_0/2$ for the existence of an equilibrium shape of the interface translates to a lower bound $\Delta p^* = 2\gamma/h_0$ on the imposed Laplace pressure jump at the interface.

Identical considerations apply to the non-wetting thread confined in the semi-infinite inlet channel of our experiments. Consequently, the thread upstream of the nozzle can only be at equilibrium if its curvature exceeds $\mathcal{C}^* = 2/h_0$ or equivalently if the Laplace pressure jump across its free interface in the gutters is greater than $\Delta p^* = 2\gamma/h_0$.

5.3.2 Equilibrium of the thread attached to the tongue in the reservoir

In practice, the thread in the inlet channel is directly connected to the tongue in the reservoir. Hence, we must consider the equilibrium of the entire interface, composed of the tongue in the reservoir and the thread in the inlet channel.

To this end, we consider a tongue of size R attached to the thread in the inlet and assume the entire system is at equilibrium. If it is effectively the case, then there are no flows in either phases and the pressures p_o and p_i in the continuous and dispersed phases are constant. The Laplace equation (1.1) then implies a constant mean curvature of the free interface, everywhere around the thread in the inlet channel and over the tongue in the reservoir. In other words, the mean curvature of the thread \mathcal{C}_1 is necessarily equal to the mean curvature of the tongue \mathcal{C}_2 . As a result, the shape of the tongue in the reservoir imposes its curvature \mathcal{C}_2 to the thread in the inlet channel. We already foresee a critical configuration, when \mathcal{C}_2 becomes smaller than the critical value $\mathcal{C}^* = 2/h_0$ below which equilibrium shapes for the thread inside the inlet channel no longer exist.

Shape and mean curvature of the tongue

In order to estimate the curvature \mathcal{C}_2 of the tongue in the reservoir, we need to model its geometry. To this end, we define a function $y(x)$ that describes the shape of the tongue in the horizontal (x, y) plane of the reservoir, of origin O at the injection nozzle as sketched in Fig. 5.9. The function $y(x)$ must verify two geometric constraints: a continuity condition at the nozzle tip $y(0) = w/2$ and tangent continuity at the apex of the tongue $dy/dx(x = L) = dy/dx(y = 0) = \infty$, where L is the length of the tongue. However, tangent continuity is not required at the nozzle tip ($x = 0$) because of the sharp angle of the channel side walls.

As discussed in Appendix B, the mean curvature of the tongue \mathcal{C}_2 has two local contributions: the curvature $\mathcal{C}_{//}(x, y)$ of the projected shape in the (x, y) plane and the vertical

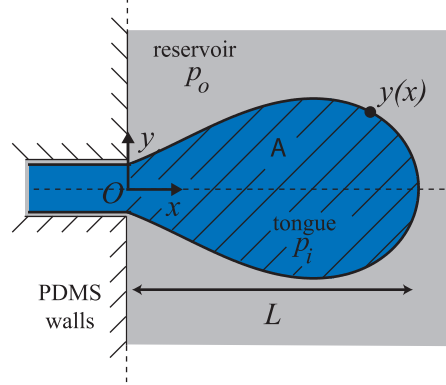


Figure 5.9: Sketch of the coordinate system used to describe the tongue shape.

transverse curvature $\mathcal{C}_\perp(x, y)$. For a non-wetting tongue, the latter is constrained by the top and bottom walls of the reservoir, of local height $h(x, y)$, with a correction that depends on the local in-plane curvature $\mathcal{C}_\parallel(x, y)$ in order to verify the condition of constant mean curvature [51]. Under these conditions,

$$\mathcal{C}_\perp(x, y) = \frac{2}{h(x, y)} + \left(\frac{\pi}{4} - 1\right) \cdot \mathcal{C}_\parallel(x, y) \quad (5.1)$$

and consequently, the mean curvature is given by

$$\mathcal{C}_2 = \mathcal{C}_\perp(x, y) + \mathcal{C}_\parallel(x, y) = \frac{2}{h(x, y)} + \frac{\pi}{4} \mathcal{C}_\parallel(x, y) . \quad (5.2)$$

This equation closely resembles the expression (1.5) of the curvature of a non-wetting pancake drop found by Laplace [45]. Its derivation is detailed in the Appendix. Constant curvature then implies that

$$\mathcal{C}_\parallel(x, y) + \frac{8}{\pi} \frac{1}{h(x, y)} = \text{cst} . \quad (5.3)$$

In the case of a reservoir of constant height $h(x, y) = h_0$, the in-plane curvature is then also constant. Therefore, the tongue adopts a circular shape at equilibrium, which is in agreement with experimental observations as shown by Fig. 5.5. Its mean curvature is given by

$$\mathcal{C}_2 = \frac{2}{h} + \frac{\pi}{4} \frac{1}{R} \quad (5.4)$$

in which R is the equivalent radius $R = \sqrt{A/\pi}$ extracted from the projected surface area A of the tongue.

In the case of a Hele-Shaw cell with walls tilted at an angle α , the height of the channel increases linearly with x from h_0 at the nozzle tip: $h(x, y) = h_0 + \tan(\alpha)x$. Assuming small height variations over the length of the tongue ($\sqrt{\tan \alpha} \ll 1$), Eq. (5.3) expands and simplifies to

$$\mathcal{C}_\parallel(x, y) = \mathcal{C}_\parallel^0 + \frac{8 \tan(\alpha)x}{\pi h_0^2} , \quad (5.5)$$

with $\mathcal{C}_{//}^0$ the curvature at the nozzle.

It is noteworthy that this shape equation is identical to the one describing the shape of a 2D pendant drop [136]. For such drops, the curvature increases linearly away from the needle tip due to gravity. This analogy points out the existence of a characteristic length $l_\alpha = \sqrt{\pi/(8 \tan \alpha)} h_0$, equivalent to the classical capillary length $l_g = \sqrt{\rho g / \gamma}$ for pendant drops [43].

However, while l_g is a function of the fluid properties (densities ρ and interfacial tension γ), the length scale l_α depends entirely on the geometry of the sloped reservoir (initial height h_0 and angle α) and is independent of the fluids involved. Consequently, the tongue shape does not depend on the fluid properties, not even on interfacial tension although it is the cause of the specific shape of the tongue.

Continuing our analysis, the droplet shape can then be described by the unique equation

$$\bar{\mathcal{C}}_{//}(\bar{x}, \bar{y}) = \frac{\bar{y}''}{(1 + \bar{y}'^2)^{3/2}} = \bar{\mathcal{C}}_{//}^0 + \bar{x}, \quad (5.6)$$

once all lengths are made non-dimensional by the characteristic length l_α : $x = l_\alpha \cdot \bar{x}$, $y = l_\alpha \cdot \bar{y}$ and $\mathcal{C}_{//} = \bar{\mathcal{C}}_{//}/l_\alpha$. The two geometric boundary conditions become

$$\bar{y}(\bar{x} = 0) = \bar{w} = \frac{w}{2l_\alpha} \text{ and } \bar{y}'(\bar{y} = 0) = \infty.$$

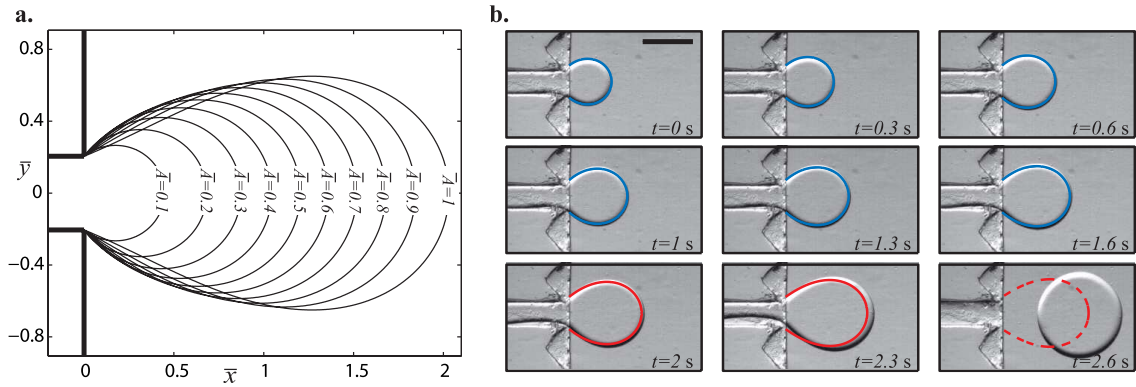


Figure 5.10: **(A)** Universal tongue shapes for various surface areas \bar{A} , attached to a nozzle of non-dimensional width $\bar{w} = 0.2$. **(B)** Image sequence of the production of a water droplet in a reservoir of FC40 + PEG-PFPE from a nozzle whose dimensions are $h_0 = 130 \mu\text{m}$, $w = 250 \mu\text{m}$ and $\alpha = 1.2^\circ$. Solid lines are the predicted shapes for the water tongue growing in the reservoir: in blue, the shapes have a mean curvature \mathcal{C} that verifies the stability criterion $\mathcal{C} > 2/h_0$; in red, the equilibrium shapes violate this criterion. Scale bar is $500 \mu\text{m}$.

Equation (5.6) is a second order differential equation in $\bar{y}(\bar{x})$ with two boundary conditions and a shape parameter $\bar{\mathcal{C}}_{//}^0$, the in-plane curvature at the nozzle. Consequently, for

any value of $\bar{\mathcal{C}}_{//}^0$, there is at most one solution for the tongue shape. Or equivalently, given a value of the tongue non-dimensional surface area $\bar{A} = A/l_\alpha^2$, there is also a unique $\bar{\mathcal{C}}_{//}^0$ and shape that verify Eq. (5.6). Using MatLab, we can then generate the family of shapes the tongue takes as it grows from a nozzle, as illustrated by Fig. 5.10.A.

These shapes can be compared to experimental observations. Figure 5.10.B displays 9 successive images of a tongue growing at a flow rate $Q = 1 \mu\text{L}/\text{min}$ into a sloped reservoir, along with predicted shapes (solid lines). A single fitting step at $t = 0$ is used to produce the series of theoretical shapes: the surface area A is extracted from the experimental image at $t = 0$ and the corresponding theoretical shape is computed. The predicted time evolution of the tongue shape and surface area $A(t)$ are then obtained by assuming the volume of the tongue $V(t) \approx h_0 \cdot A(t)$ increases linearly at the flow rate $Q = 1 \mu\text{L}/\text{min}$ used in the experiment. Figure 5.10.B shows the 8 predicted geometries corresponding to the experimental timesteps of the image acquisition. Excellent agreement is observed until necking of the thread appears after $t = 1.6 \text{ s}$.

The critical size of the tongue

From Eq. (5.6), we also obtain numerically the relationship between the mean curvature \mathcal{C}_2 and the surface A of the tongue. In particular, we can study whether \mathcal{C}_2 decreases below the critical curvature $\mathcal{C}^* = 2/h_0$ of the tongue. At the nozzle, the mean curvature is given by $\mathcal{C} = 2/h_0 + \pi/4 \cdot \mathcal{C}_{//}^0$ using Eq. (5.2). Hence, the critical curvature $\mathcal{C}_2 = \mathcal{C}^* = 2/h_0$ is reached when $\mathcal{C}_{//}^0 = 0$. Figure 5.11.a plots $\bar{\mathcal{C}}_{//}^0$ versus \bar{A} for 5 different nozzle widths \bar{w} . We observe that $\bar{\mathcal{C}}_{//}^0$ always decreases below zero as \bar{A} increases.

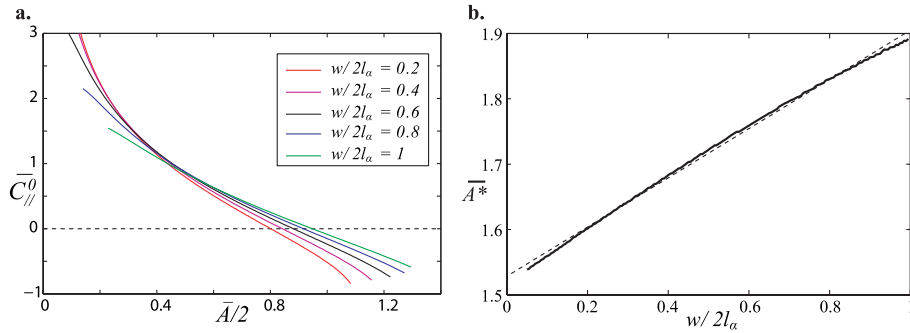


Figure 5.11: **a.** Plot of $\bar{\mathcal{C}}_{//}^0$ vs $\bar{A}/2$ for 5 different nozzle widths \bar{w} ranging from 0.2 to 1. **b.** Evolution of the critical tongue surface area \bar{A}^* as a function of the nozzle width \bar{w} .

The critical size \bar{A}^* for which $\mathcal{C}_2 = \mathcal{C}^*$ is extracted from Fig. 5.11.a and plotted on Fig. 5.11.b for \bar{w} ranging from 0.1 to 1, a range that includes all experimental conditions investigated. We find that \bar{A}^* increases slightly with the nozzle width and the trend is well captured by a linear fit. As a result, we approximate the critical tongue size by

$$\bar{A}^* = 1.53 + 0.38\bar{w} \quad (5.7)$$

which translates back to

$$A^* = 0.60 \left(1 + 0.2 \sqrt{\tan(\alpha)} \frac{w}{h_0} \right) \frac{h_0^2}{\tan \alpha} \quad (5.8)$$

using dimensional quantities.

In terms of equivalent radius $R = \sqrt{A/\pi}$, we find

$$R^* = 0.44 \sqrt{1 + 0.2 \sqrt{\tan(\alpha)} \frac{w}{h_0}} \frac{h_0}{\sqrt{\tan \alpha}}. \quad (5.9)$$

For small angles α , this expression simplifies to

$$R^* = 0.44(1 + 0.1 \sqrt{\tan(\alpha)} \frac{w}{h_0}) \frac{h_0}{\sqrt{\tan \alpha}}, \quad (5.10)$$

by expanding the square root.

5.3.3 Beyond R^* , a system out of equilibrium

As soon as the tongue in the reservoir exceeds the critical size R^* , the system composed of the tongue attached to the thread in the inlet channel is out of equilibrium. This statement differs in meaning from saying *the system is in a state of unstable equilibrium* since here there no longer exists equilibrium shapes of the interface for the thread. In that sense, the key mechanism for droplet production mechanism is not an instability, like the Rayleigh-Plateau instability that occurs for non-confined liquid threads [137, 138].

Indeed, in the case of the Rayleigh-Plateau instability, there exists an infinite number of equilibrium shapes for the thread: the Delaunay surfaces [139] of constant mean curvature detailed in Appendix B, amongst which the straight cylinder is one particular example. The rupture of the thread then occurs because these equilibrium states are maximums of surface energy and therefore unstable [137, 138].

When $R > R^*$, the curvature of the thread in the inlet channel cannot decrease to the value imposed by the tongue. Because of the Laplace law (1.1), this curvature imbalance leads to a pressure imbalance between the thread and the reservoir. Assuming that the pressure in the dispersed phase remains constant, the pressure of the continuous phase in the gutters is then lower than the pressure of the continuous phase in the reservoir. This drives a reverse flow into the gutters which is responsible for the necking of the thread upstream of the nozzle.

The necking implies an inflexion of the thread interface. This locally decreases the curvature of the thread to the value imposed by the tongue in the reservoir and locally restores equilibrium. Nonetheless, the rest of the thread upstream of the neck remains out of equilibrium and continues to suck continuous phase into the gutters. As a result, the necking region extends farther and farther into the inlet channel and the width of the neck decreases until it reaches the critical value $w_m = h_0$. At this instant, the neck has a circular transverse shape and is no longer confined by the channel walls. It is then

similar to a cylindrical fluid column which is prone to develop a Rayleigh-Plateau type of instability [131, 140].

The same happens if the pressure in the continuous phase is assumed to remain constant. Indeed, in this case, the pressure of the dispersed phase in the thread exceeds the pressure in the tongue. The dispersed phase flows from the thread to the tongue which can only lead to a necking of the thread. In practice, neither the pressure fields are constant but both effects are complementary and eventually lead to the release of the droplet in the reservoir.

5.3.4 A scenario for droplet formation

Using the three results discussed above, namely that

- the mean curvature of a confined thread at equilibrium has a lower bound
- the mean curvature of the fluid tongue in a sloped reservoir decreases below this lower bound
- once out of equilibrium, the thread necessarily collapses

we lay out the theoretical scenario that leads to droplet formation in a sloped reservoir.

Prior to reaching the reservoir, the non-wetting fluid thread is confined in all directions and the curvature of the advancing spherical cap at the tip of the thread largely exceeds the minimum equilibrium curvature \mathcal{C}^* .

As soon as the thread reaches the sloped reservoir, confinement is suddenly released in the plane and slowly in transverse direction. The thread forms a liquid tongue that elongates under the force from the confinement gradient and adopts the shape of a 2D pendant drop.

If the injection flow rate of the continuous phase is small (the meaning of small is discussed in the next section), the tongue grows in a quasi-static manner from small equilibrium shapes to larger equilibrium shapes. The good agreement between the computed and observed shapes shown on Fig. 5.10.b corroborates this quasi-static assumption. As the size of the tongue increases, its curvature \mathcal{C}_2 decreases and with it the curvature \mathcal{C}_1 of the thread.

Eventually, the curvature of the tongue reaches the critical value \mathcal{C}^* below which there no longer exist equilibrium shapes for the thread in the inlet channel. In other words, the slow decrease in the confinement of the tongue drives the thread out of equilibrium. It is noteworthy that in this configuration, the tongue itself is at equilibrium and there even exist larger equilibrium shapes with lower curvatures.

In order to locally adjust its curvature to match the tongue curvature, the thread forms a neck upstream of the nozzle which irremediably thins as more and more fluid from the reservoir is sucked into the gutters. Eventually, the neck narrows down to an unconfined cylindrical column prone to the Rayleigh-Taylor instability. The column suddenly collapses and a droplet is released in the sloped reservoir.

The newly formed droplet is then pushed away from the nozzle by the confinement gradient in a manner similar to the movement of Hauksbee's drops of oil of oranges.

5.4 Confronting the model to the experimental observations

In the light of this model scenario, we can interpret the experimental observations listed above and compare the predicted thresholds for droplet formation with our measurements.

Observation 1: pinch-off occurs in the inlet channel

First of all, the mechanism for droplet formation presented above immediately explains why the rupture of the dispersed phase systematically occurs inside the inlet channel. This peculiar property is not observed in other classical methods of droplet production at nozzles, like dripping or ink jet-printing. This is because in these cases, droplet formation occurs when the volume of fluid outside the nozzle becomes unstable. Here, the tongue of fluid in the reservoir is actually at a stable equilibrium while the thread inside the nozzle is driven out of equilibrium.

The measured evolution of the width w_m of the neck upstream of the nozzle also corroborates the suggested scenario for collapse of the thread. Figure. 5.12 plots w_m as a function of the time t initialized when necking appears for a nozzle of dimensions $w = 250 \mu\text{m}$, $h = 135 \mu\text{m}$ and slope $\alpha = 0.5^\circ$. The drop is produced at a constant flow rate $Q = 1 \mu\text{L}/\text{min}$ and images of the necking regions captured at 60 frames per second. We observe a regular decrease of the neck width during approximately 3 seconds until $w_m = 130 \mu\text{m}$. At this instant, the thread collapses and the droplet is released in the reservoir. Pinch-off occurs in less than 1/60th of a second since not even a single image of the final collapse is captured.

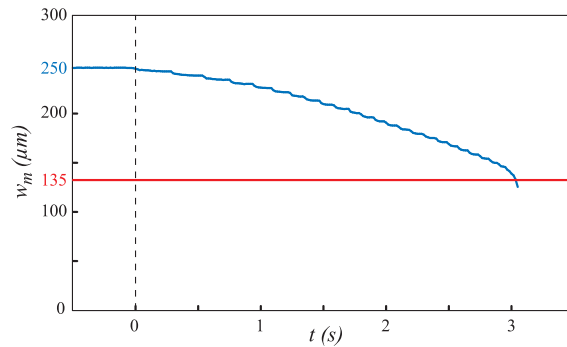


Figure 5.12: Measured width w_m of the thread of water upstream of nozzle of dimensions $h_0 \approx 135 \mu\text{m}$, $w = 250 \mu\text{m}$ and $\alpha = 0.5^\circ$ during formation of a droplet at a flow rate $Q = 1 \mu\text{L}/\text{min}$.

The break-up process clearly takes place in two stages, the second significantly faster than the first. A similar process was described by Garstecki *et. al.* [131] and others [141] for the droplet formation at a flow focusing junction. The authors also observed a sudden collapse of the thread when the width of the neck matched the height of their channel, a phenomenon which was attributed to the Rayleigh-Plateau instability. Here, the sudden collapse is due to the same phenomenon while the slow decrease corresponds to the growth

of the neck due to the reverse flow of continuous phase in the gutters once the tongue exceeds the critical size R^* .

Observation 2: drop size R_d decreases with α and is independent of the fluid properties

Second, the model is in agreement with the experimental observation that droplet formation does not occur in a flat reservoir. Indeed, when the walls of the reservoir are parallel, the curvature of the tongue \mathcal{C}_2 decreases as

$$\mathcal{C}_2 = \frac{2}{h_0} + \frac{\pi}{4} \frac{1}{R} \quad (5.11)$$

as its radius R increases such that it only reaches the critical value $\mathcal{C}^* = 2/h_0$ asymptotically when R tends to infinity. The tongue may then grow indefinitely without driving the thread out of equilibrium.

Conversely, we showed that the curvature of the tongue reaches \mathcal{C}^* for finite sizes R^* in the case of a wedged reservoir. From a numerical analysis, we obtained the approximation

$$R^* = 0.44(1 + 0.1\sqrt{\tan(\alpha)}\frac{w}{h_0})\frac{h_0}{\sqrt{\tan \alpha}} \quad (5.12)$$

for the critical tongue size which initiates collapse of the thread. Qualitatively, this expression captures the decrease of the drop size R_d as the slope α increases, a trend illustrated on Fig. 5.7.a. However, as shown on Fig. 5.13 which compares measured drop radii R_d with the predicted critical radii R^* for different reservoir slopes α , the expression (5.12) of R^* underestimates R_d .

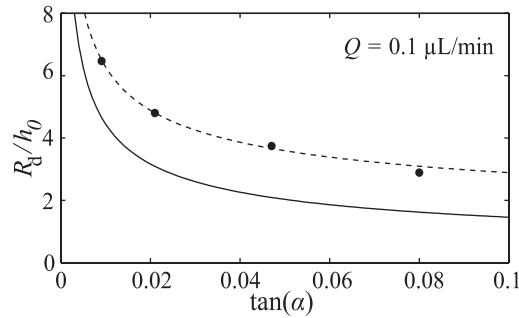


Figure 5.13: Measured radii R_d (circles) compared with the predictions of equations (5.12) (solid line) and (5.13) (dashed line) for drops produced at a nozzles of inlet dimensions $h_0 = 135 \mu\text{m}$, $w = 250 \mu\text{m}$ at a flow rate $Q = 1 \mu\text{L}/\text{min}$.

A cause for this discrepancy is the fact that R^* only predicts the size of the tongue for which necking is initiated. In particular, it fails to consider the volume of liquid from the neck that is absorbed by the droplet. Given that this volume is proportional to w , the expression (5.12) is modified by an empirical correction of the prefactor of the term in

w/h_0 that accounts for the effect of the inlet width. The best fit yields

$$R_d^f = 0.44(1 + 2.2\sqrt{\tan(\alpha)}\frac{w}{h_0})\frac{h_0}{\sqrt{\tan \alpha}}. \quad (5.13)$$

This expression for the radius of the produced drops shows excellent agreement with the measurements of R_d in our devices, as shown by the dashed line on Fig. 5.13. Finally, both equations (5.12) and (5.13) are in agreement with the peculiar property that the droplet size is independent at low flow rates of the fluid used in the experiments. Indeed, these equations express R^* and R_d^f as a function of the nozzle dimensions h_0 , w and α only.

Remarkably, although interfacial tension is at the root of the mechanism for droplet formation, its actual value has no effect on the size of the produced drops.

Observation 3: drops of finite size are produced at infinitesimal flow rates and R_d is weakly dependent of Q

The presented mechanism for droplet formation is based on an equilibrium analysis of the thread+tongue system and is strictly valid only in the absence of a continuous inflow of the dispersed phase in the inlet channel. As such, it automatically explains why the drop size decreases to a finite value R_d^0 as the flow rate Q tends to zero in our experiments.

The presence of a continuous inflow of the dispersed phase implies a viscous pressure drop in the thread and tongue, which is in contradiction with the equilibrium assumption of constant pressure fields in both phases and thereby constant curvature over the interface. Yet, we can estimate the effect of the flow by comparing the viscous pressure drop Δp_μ in the vicinity of the nozzle to the variations Δp_γ of the Laplace pressure that occur as the tongue grows in the reservoir.

The pressure gradient ∇p_μ due to a constant flow rate Q in a rectangular channel of dimensions h_0 and w scales as $\nabla p_\mu \propto \mu Q / wh_0^3$. The region of the inlet channel where the necking occurs has a length which amounts to a few channel widths w . Hence, the viscous pressure drop of interest scales as $\Delta p_\mu \propto \mu Q / h_0^3$.

When the tongue grows in the reservoir, changes in the curvature of the interface are mainly due to an increase in the radius R of the tongue. As a result, the Laplace pressure variations are of order γ/R . An estimate for the size of the tongue is given by the critical tongue size R_d which scales as $h_0/\sqrt{\alpha}$ using equation (5.13). Consequently, we have $\Delta p_\gamma \propto \gamma\sqrt{\alpha}/h_0$.

Comparing Δp_μ to Δp_γ defines a new capillary number Ca_α based on the reservoir slope α and flow rate Q of the continuous phase:

$$\text{Ca}_\alpha = \frac{\mu Q}{\gamma h^2 \sqrt{\alpha}} \quad (5.14)$$

For a typical low flow rate experiment, $Q = 6 \mu\text{L}/\text{min} = 10^{-10} \text{ m}^3/\text{s}$, $\mu \approx 10^{-3} \text{ Pa}\cdot\text{s}$, $\gamma \approx 10^{-2} \text{ Nm}$, $h_0 \approx 10^{-4} \text{ m}$ and $\alpha \approx 10^{-2}$ such that Ca_α is of order 10^{-2} . The viscous pressure drop is negligible compared to the Laplace pressure variations during the experiment.

This simple scaling law explains the qualitative trends of Fig. 5.7.b. For flow rate below say $1 \mu\text{L}/\text{min}$, Ca_α is much smaller than 1 and the drop size is well captured by the quasi-static model suggested above. For stronger flow rates $Q \approx 50 \mu\text{L}/\text{min}$, the viscous pressure becomes significant and has a stabilizing effect. Indeed, it increases the pressure of the dispersed phase in the thread relatively to the downstream tongue and thereby increases the curvature of the interface in the thread compared to the quasi-static case.

Last, Ca_α is in agreement with the observed trend that the flow has a stronger effect for low reservoir slopes. Indeed, decreasing α increases Ca_α .

Observation 4: drops are highly monodisperse

In light of the previous results, we can qualitatively explain the high monodispersity of the drops.

First of all, the drop size is weakly sensitive to variations in the injection flow rate. As a result and contrary to what has been observed with flow focusing devices [142], flow rate oscillations from the syringe pumps do not affect droplet production significantly. Second, the drop size is independent of the hydrodynamic properties (viscosity and surface tension) of the fluids. Hence, the performance of the device is unaffected by temperature variations or aging of the fluids which may occur over long period of times.

Second, the production mechanism is due to equilibrium properties of the thread upstream of the nozzle and inside the injection channel. This region of the interface is never in direct interaction with flows that may occur in the reservoir. Consequently, the droplet formation mechanism is insensitive to what is occurring in the reservoir and especially to the movements of the drops previously released in the device. This explains why the drops are monodisperse from the first to the last. This last statement is true only if the tongue grows sufficiently slowly that it never ends up pushing other droplets previously formed in the reservoir. Indeed, once there is contact between the tongue and a droplet in the reservoir, the shape of the tongue deviates from the equilibrium pendant drop geometry described above and its mean curvature is modified.

Overall, modeling droplet formation as an out of equilibrium collapse of the thread forced by the tongue in the reservoir explains all the phenomena and trends observed with our devices, in addition to giving a valid estimate for the size R_d of the produced drops. As such, it appears as the correct mechanism for droplet production.

5.5 Comparison with a classical force argument

Nevertheless, in the sloped reservoir, a force imbalance could also be responsible for droplet formation. The expressions (1.7) extracted from the seminal analysis of Laplace and (3.38) obtained in Chapter 3 from an energy approach can be used to estimate for the force F_γ

that applies on the tongue in the reservoir due to the confinement gradient:

$$F_\gamma \approx 2\gamma \frac{\tan \alpha A}{h_0} \text{ where } A \text{ is the surface area of the tongue.} \quad (5.15)$$

This force pulls the tongue away from the nozzle. The opposing force is the interfacial tension which holds the tongue attached to the thread. In Chapter 1, we recalled that this *capillary traction* is equal to the interfacial tension γ times the length of the interface on which it applies. Here, the *capillary traction* applies on a cross-sectional perimeter of the thread whose length P is a weighted sum of the height h_0 and width w of the inlet channel: $P = a_1 h_0 + a_2 w$. Equilibrating the two forces yields a critical tongue surface area A_f for which the force from the confinement gradient exceeds the capillary traction

$$2\gamma \frac{\tan \alpha A_f}{h_0} = \gamma(a_1 h_0 + a_2 w) . \quad (5.16)$$

This translates in terms of its equivalent radius R_f to

$$R_f \propto \frac{h_0}{\sqrt{\tan \alpha}} \sqrt{1 + \frac{a_2 w}{a_1 h_0}} . \quad (5.17)$$

This equation gives a scaling for the size of the produced drops very similar to the one obtained in equation (5.12) from an equilibrium analysis of the thread. The similarity in the two results questions whether the mechanism for droplet formation based on the equilibrium analysis of the thread is effectively distinct from the force balance approach, or whether the two are equivalent formulations of the same physical mechanism.

To answer this question, we imagine another configuration in which droplet formation would be triggered by driving a thread out of equilibrium and for which a force argument would not apply or lead to a different scaling for the drop size. The two main ingredients necessary for droplet formation to occur following the mechanism presented above are

- a confined thread of a non-wetting fluid
- directly connected to a less confined volume of the same fluid.

As the less confined volume of fluid grows, its curvature decreases which drives the thread out of equilibrium. The simplest geometry that combines these two ingredients is a square capillary of size h that leads to an unbounded domain.

5.5.1 The non-wetting pendant drop

With this geometry, when the non-wetting dispersed phase reaches the end of the channel, it is completely unconfined and expands in all direction in a spherical cap as shown on Fig. 5.14.a. The curvature of the spherical cap is inversely proportional to the radius R of the cap and equal to $2/R$. As a result, it reaches the critical curvature $\mathcal{C}^* = 2/h$ for the thread in the square channel when

$$R^* = h . \quad (5.18)$$

Here again, the critical radius is independent of the properties of the fluids considered. In the absence of volume forces, we are unable to identify a force that pulls the droplet away from the thread. Hence, a force balance would predict that the drop can grow indefinitely in opposition with the thread collapse mechanism.

We perform such an experiment with a glass capillary tube with an inner width of $100\text{ }\mu\text{m}$ immersed in a bath of hexadecane with 2% Span80 surfactant. When water is injected at a constant flow rate $Q = 0.2\text{ }\mu\text{L}/\text{min}$ through the capillary previously filled with hexadecane, it does not wet the walls as shown on Fig. 5.14.a. As predicted, the water forms a spherical cap as soon as it reaches the end of the capillary. It then grows until its radius reaches $R_c \approx 105\text{ }\mu\text{m}$ at which point necking appears significantly upstream of the nozzle. The thread rapidly collapse and a droplet is released in the bath of hexadecane. Remarkably, the measured value at which necking appears is in excellent agreement with the prediction $R = h = 100\text{ }\mu\text{m}$, which suggests that the thread collapse mechanism is the one at play.

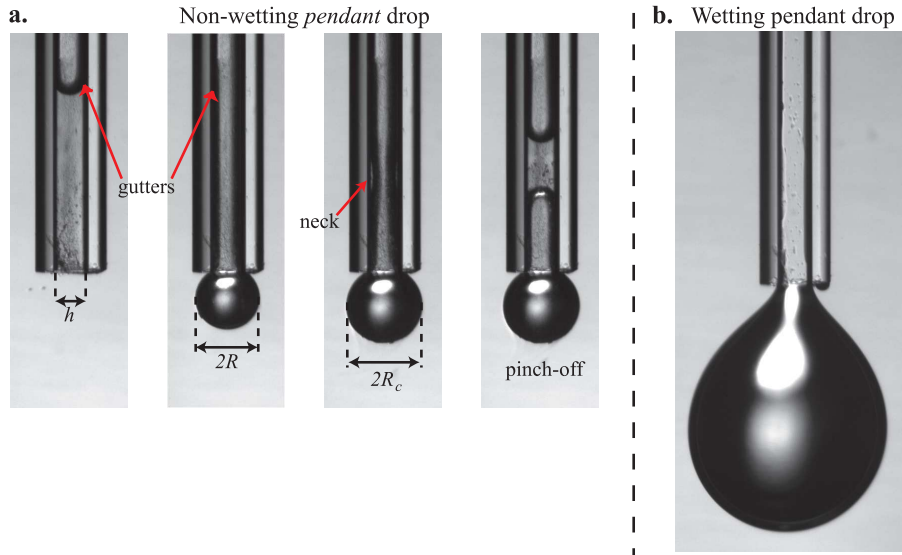


Figure 5.14: **a.** Images of a drop of water forming in hexadecane+Span80 at the tip of a square capillary for non-wetting boundary conditions of the thread inside the capillary. **b.** Last image before pinch-off of a pendant water drop in hexadecane+Span80 for wetting boundary condition of the water thread inside the capillary.

Nonetheless, the density mismatch $\Delta\rho = 200\text{ kg}/\text{m}^3$ between the two liquid used introduces a bias in the experiment and the water drop is also pulled down by gravity. Hence, the drop could also have detached under its own weight. Rayleigh and later contributors [143, 144, 145] showed that the critical size R_g of a pendant drop hanging from a tube of diameter h can be approximated by the formula

$$R_g \approx \left(\frac{h}{l_g}\right)^{1/3} l_g \text{ where } l_g = \sqrt{\frac{\gamma}{\Delta\rho g}} \text{ is the capillary length.} \quad (5.19)$$

The expression predicts a maximum size $R_g = 460 \mu\text{m}$ for the pendant drop at the tip of our square capillary, a value significantly larger than the $R^* = 100 \mu\text{m}$ predicted by the equilibrium condition of the thread in the capillary which we effectively measured in the experiment.

To further support our argumentation, we alter the wetting condition by filling the capillary with water before placing it in the bath of hexadecane. In this case, the water wets the inner walls of the capillary which automatically kills the mechanism for droplet formation based on the collapse of the non-wetting thread. Water is then injected at a constant flow rate and a pendant drop significantly larger than the drop produced for non-wetting conditions is formed as shown on Fig. 5.14.b. This last experiment identifies the critical size R_g for which weight exceeds the capillary traction of the interface. We measure $R_g \approx 530 \mu\text{m}$, a value close to the prediction $460 \mu\text{m}$.

Overall, this simple non-wetting pendant drop experiment indicates that the mechanism for droplet formation based on the out of equilibrium collapse of the thread inside the capillary is not necessarily equivalent to the usual force based mechanism. In the case of the sloped reservoir, the scalings obtained from the two approaches are identical such that it is more difficult to identify the one at play. However, as shown on Fig. 5.10, the tread collapses although there exists shapes for larger tongues that verify the force equilibrium.

Hence, we believe that the drop detaches before the force imbalance occurs due to the out of equilibrium collapse of the thread in the inlet channel. The force F_γ then propels it away from the nozzle.

5.6 Nozzle parallelization for emulsion production

A key asset of our method of droplet production is the weak sensitivity of the drop size to perturbations in flow rate and variations in the fluid properties. This property not only guarantees high monodispersity of the emulsion produced from a single nozzle but also allows nozzles to be parallelized in a straightforward manner. This is demonstrated first with a chip capable of producing an emulsion with a gradient of chemical content and then with an inflatable device producing highly monodisperse droplets at kHz frequencies from 256 nozzles operated in parallel in a 2 cm^2 reservoir.

5.6.1 Emulsions with chemical gradients

The controlled production of emulsions with heterogeneous contents has many potential applications in chemistry where screening the phase space of chemical concentration is required [146], or in biology to perform different genetic tests in parallel [15]. A general view of our chip used to produce an aqueous emulsion with a gradient in the chemical content of the droplets is shown on Fig. 5.15.

Three solutions of water dyed with red, yellow and blue food coloring are injected from three inlets into an hexagonal dispatching unit displayed in Fig. 5.16.a. This geometry of the channel network splits each colored stream into three: one stream never in contact

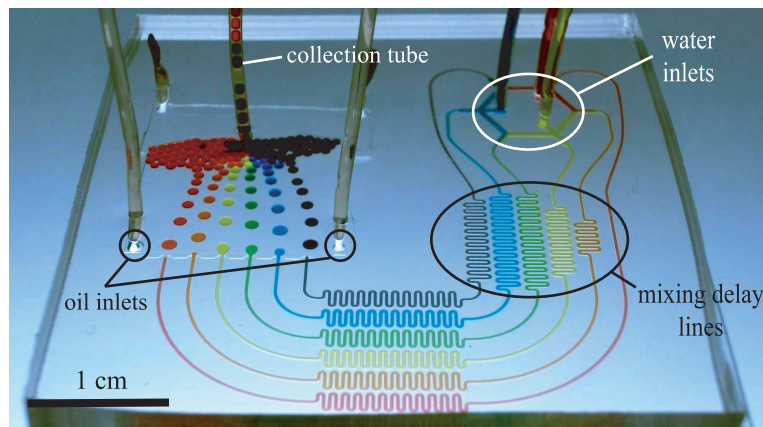


Figure 5.15: Photograph of the rainbow chip operating at flow rates of $12 \mu\text{L}/\text{min}$ for the colored stream of water and $10 \mu\text{L}/\text{min}$ for the fluorinated oil streams. Scale bar is 1 cm.

with the two other colored streams, and two streams that combine with each one of the other two colors. Hence, it forms six streams colored with the rainbow gradation purple-blue-green-yellow-orange-red. Sinuous delay lines are used to ensure complete mixing of the colors upstream of the droplet production region.

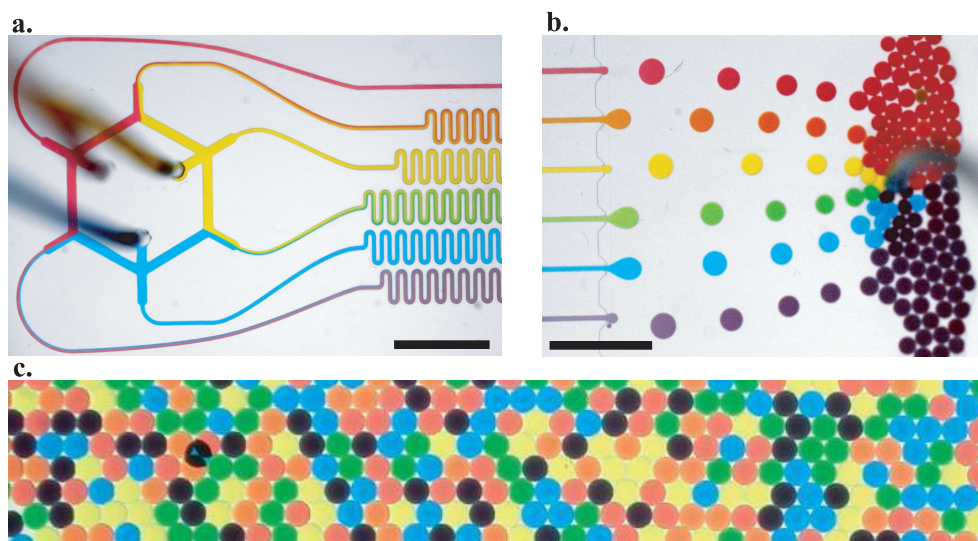


Figure 5.16: **a.** Photograph of the hexagonal dispatching unit and the delay lines that produced the rainbow gradation of dyes. **b.** Photograph of the sloped reservoir and the six streams of rainbow colored droplets produced by injecting the aqueous solutions at $6 \mu\text{L}/\text{min}$ each. **c.** Photograph of the collected emulsion. Scale bars are 5 mm.

The six channels then lead to six nozzles of identical dimensions $h_0 = 135 \mu\text{m}$ and $w = 250 \mu\text{m}$ placed side by side in a reservoir sloped at an angle $\alpha \approx 1.2^\circ$ and filled with FC-40 fluorinated oil + 2% PEG-PFPE surfactant. Each nozzles produces a monodisperse

droplet stream of a given color which spontaneously flows away from the nozzle due to the confinement gradient (see Fig. 5.16.b). The emulsion collected in a collection container and shown in Fig. 5.16.c displays excellent monodispersity, even though the dyes interact with the surfactant in the fluorinated oil such that the interfacial tension varies from nozzle to nozzle.

A first method to collect the emulsion is to force the droplets out of the reservoir through a tube and into a collection container by continuously injecting fluorinated oil in the reservoir from two additional inlet, as shown on Fig. 5.15. A second solution is to partially cut open the roof of the reservoir, allowing the water drops to rise by buoyancy into a syringe filled with fluorinated oil, as demonstrated on Fig. 5.17.

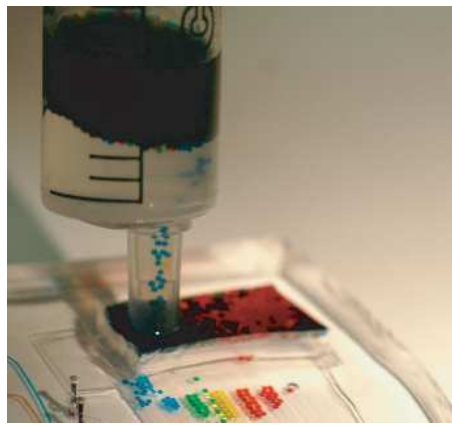


Figure 5.17: Photograph of the colored water drops rising by buoyancy into an FC-40 syringe.

Compared with existing designs that rely on classical droplet production geometries [15, 146, 147], the current devices are much simpler to design. Because there are no hydrodynamic interactions between the produced droplets and the nozzles, techniques developed for continuous flow microfluidics to produce gradients of solute in the dispersed phase can be used without modification upstream of the emulsification nozzles. From a practical point of view, the device complexity is also reduced as only inlets and channels for dispersed phase are required. Last, the device are also simpler to operate and can cover a wide range of flow rate, from 0.5 to 50 $\mu\text{L}/\text{min}$ in the example discussed above.

5.6.2 High throughput emulsification

Massive parallelization can be achieved in order to reach high throughput emulsification or to efficiently divide a microliter sample into a multitude of droplets which are held on chip. We demonstrate this capability with the inflatable device featured in Fig. 5.18 which contains 256 nozzles of dimensions $h_0 = 15 \mu\text{m}$ and $w = 50 \mu\text{m}$ placed side by side around a central circular reservoir 1.5 cm in diameter.

We recall the concept of inflatable devices which is detailed in Section 5.1. The device is initially filled with the continuous phase, water + 2% SDS in this case, and a small

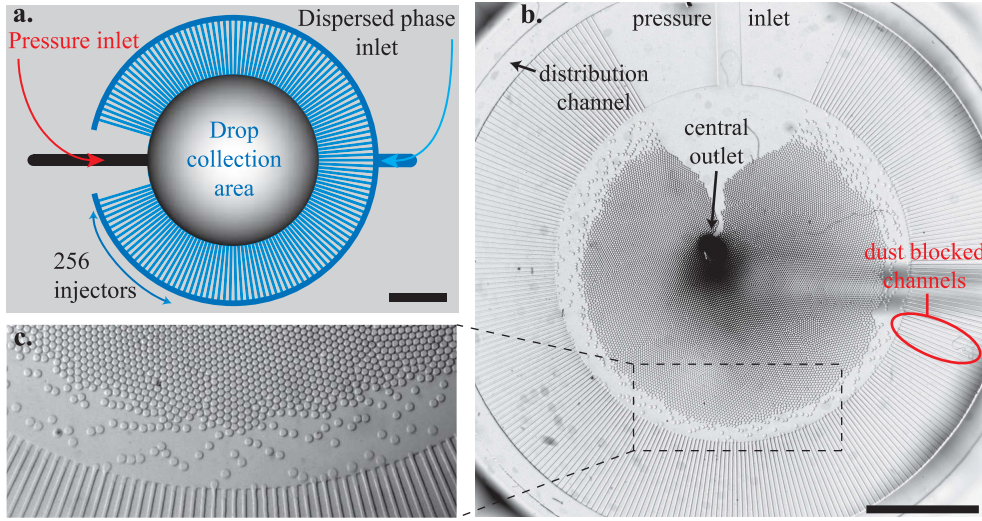


Figure 5.18: **a.** Sketch of the device architecture featuring the inlet for the dispersed phase which distributes to 256 nozzles via a peripheral distribution channel and an inflatable circular central reservoir. **b.** Image of the device during operation, producing 225 pL drops of FC-40 in water at frequency of 1.47 kHz from a 20 $\mu\text{L}/\text{min}$ influx of the dispersed phase. The drops are collected out of the chip at the outlet located at the center of the reservoir. **c.** Zoom on the nozzles. Scale bars are 5 mm.

overpressure (between 10 and 200 mbar) is applied inside the device using a pressure controller and a dedicated pressure inlet in the reservoir. This inflates the reservoir and creates a slope at the nozzles.

At this stage, the dispersed phase (FC-40 fluorinated oil) is injected at constant flow rate into the device from a single inlet which is distributed across all nozzles using large distribution channel circling the reservoir. All nozzles then produce streams of droplets that are advected by the confinement gradient towards the center of the reservoir. For example, using an overpressure $p = 100$ mbar and a flow rate of 20 $\mu\text{L}/\text{min}$, we produce droplets of 226 pL in volume at a frequency of 1470 drops/second. The drops can either be held on chip to form a dense array of monodisperse drops as shown on Fig. 5.19 or collected by placing an outlet tubing at the center of the reservoir.

One advantage of using inflatable devices is that the slope can be controlled with the overpressure. As a result, the size of the produced droplets can also be modulated by varying the overpressure. For example, for pressures of 50, 100, 150 and 200 mbar, we create droplets of spherical radius equal 41, 39, 37.5 and 36.5 μm . On Fig. 5.20, we plot the distribution of the measured radii of droplets for these 4 different pressure. The dispersion never exceeds 3%, a remarkable achievement given the rudimentary architecture of the device.

Because droplet production in a wedged reservoir only requires to flow the dispersed phase, the architectural limitations encountered when scaling up cross-flow geometries like the T-junction or flow focuser [148, 149, 150] are suppressed and massive parallelization is

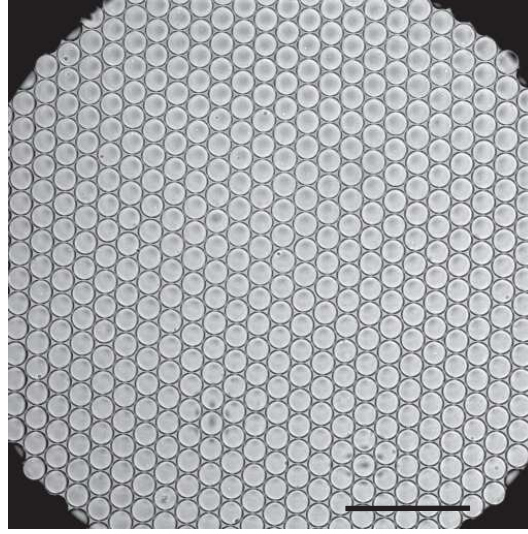


Figure 5.19: Brightfield image of an emulsion produced from 200 parallel nozzles and held on chip in a square inflatable reservoir. Scale bar is 400 μm .

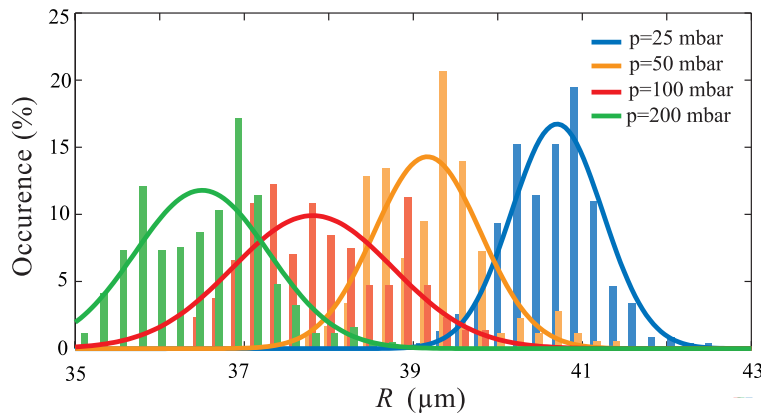


Figure 5.20: Histograms of the radii of droplets measured in the center of the reservoir where the drops are spherical for four overpressures of 25, 50, 100 and 200 mbar.

straightforward. Furthermore, the weak sensitivity of the droplet size to flow rate variation means that the device performance is unaffected by partial clogging. On Fig. 5.18.b for example, a few inlet channels on the right side of the reservoir are blocked by dust. Yet, neighboring nozzles operate normally and the flow of the dispersed phase is simply redistributed over the remaining unclogged nozzles.

5.6.3 High throughput emulsification with a micropipette

Last, because the droplet size does not vary significantly with the flow rate, we are able to operate the device shown on Fig. 5.18 by relying only on a hand-held micropipette to inject the dispersed phase.

The device is initially filled with the continuous phase (water + SDS) and the tip of the 100 μL micropipette is inserted in the inlet for the dispersed phase. The device is pressurized at 50 mbar to create the slope in the reservoir. Then, 20 μL of sample (FC-40 fluorinated oil) are slowly injected into the device. The injection process takes about 30 s, implying an average flow rate of 40 $\mu\text{L}/\text{min}$ that distributes across the 256 nozzles. Figure 5.21 illustrates the process. In the end, the sample is split into approximately 20,000 monodisperse droplets of volume around 250 pL and the droplets are held on chip in a large 2D array format.

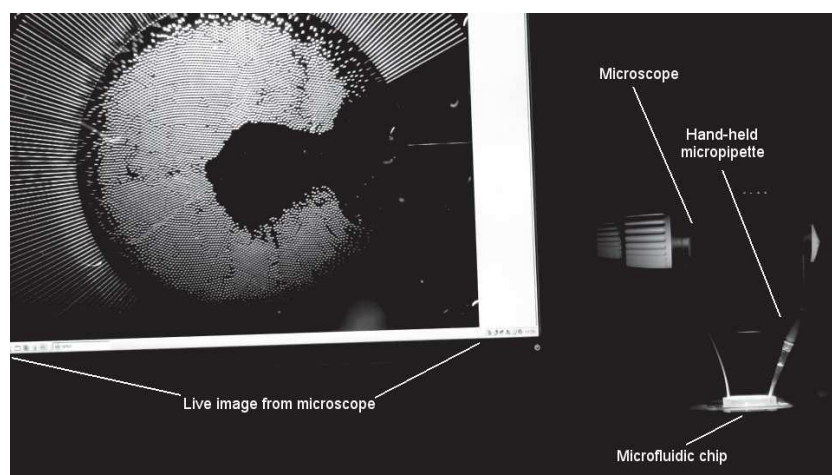


Figure 5.21: Photograph of the experimental setup used to demonstrate high throughput emulsification with a hand-held micropipette. The chip at the bottom right of the image is placed under a microscope which is used to monitor what happens in the sloped reservoir. The live image is shown on the computer screen on the left. The device is operated by injecting 20 μL of fluorinated oil in the reservoir filled with water + 2% SDS with a hand-held 100 μL micropipette, which creates thousands of droplets in the reservoir.

Non-inflatable devices of identical geometry are currently being developed. In practice, this device could be fully operated manually. Typically, the user would hold the microchip in one hand and inject the dispersed phase with the other using a micropipette. The sample would then be split into thousands of droplets held and arrayed on a transportable microchip, effectively droplet Lab-on-a-Chip technology out of the lab.

5.7 Discussion and summary of Chapter 5

Overall, the key asset of our method over classical techniques of droplet production in microfluidics, like the T-junction [8] or the flow focusing [9] geometries, is that it does not require a forced flow of the outer phase:

- it simplifies the design of the devices by suppressing the need for oil inlets and channels

- it improves the robustness of the droplet formation mechanism to perturbations in the flow and the fluid properties.
- it makes droplet microfluidics accessible to manual operation

The step [151] emulsification technique (initially named MC emulsification) developed by Nakajima *et. al.* in the early 2000's for droplet microfluidic applications shares this property with our method of droplet production. The basic geometry of an injection nozzle for step emulsification is similar to the one we have developed. A rectangular inlet channel leads to a wide reservoir whose height suddenly increases in a step like structure. Figure 5.22 illustrates droplet formation at a step emulsification nozzle. The dispersed phase, which has to be non-wetting like with our devices, expands to form a tongue which grows until it reaches the step in the reservoir. At this point, it expands a second time into a spherical drop which immediately breaks away from the tongue.

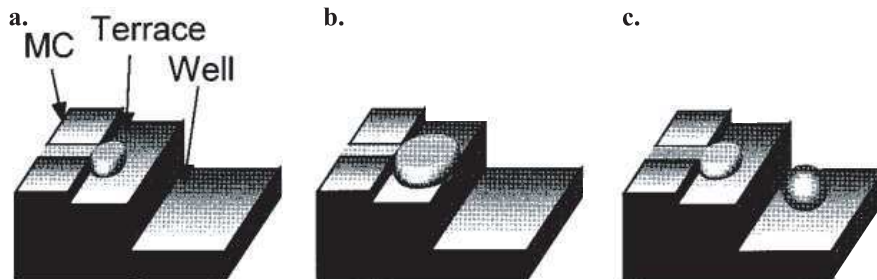


Figure 5.22: .

In contrast with our approach however, an outer flow of the continuous phase required to move the droplet away from the nozzle since there are no confinement gradients to propel the newly formed droplet. In our inclined reservoirs, the slope also prevents droplets already present in the reservoir from coming near the nozzles. It thereby limits perturbations of the droplet formation mechanism and allows the monodispersity of the emulsion to reach values below 1%.

Over the past ten years, Kobayashi and collaborators have investigated numerous variations of their step emulsification geometry, by changing the position and the height of the step [152] and by parallelizing nozzles in lines and stacks to form an emulsification membrane [153]. Their approach was adapted by others who added co-flowing streams of the continuous phase in the inlet channel to reach smaller droplet sizes [154, 155] or controlled the injection flow rate to enable on-demand droplet production [156].

Despite the prolific literature on step emulsification, the physical mechanism for droplet formation has only been partially identified [157]. It is understood the Laplace pressure jump at the interface decreases when the droplet expands beyond the step and that this effect is responsible for the droplet formation. However, how exactly it triggers the collapse of the liquid upstream of the droplet remains in debate.

We believe that the novel mechanism identified in Section 5.3 also applies to the case in step emulsification. Indeed, the main ingredient for droplet formation to occur following

this mechanism, namely a confined thread of a non-wetting fluid directly connected to a less confined volume of the same fluid, is present at the nozzle. In a step emulsification device, the confinement is suddenly released and the tongue is completely deconfined like in the case of the square capillary studied in Section 5.5. We obtained for this configuration that the diameter D of the produced drops should be $D \approx 2h$ with h is the height of the inlet channel. This simple prediction is in qualitative agreement with most of the observations in the literature [153, 158, 155] which report droplet diameters two to three times the inlet channel height. A quantitative analysis is currently underway to further support this result.

Overall, it appears that droplet production by *deconfinement* has been implemented before with numerous geometries: in membrane emulsification, in step emulsification or even recently in a particular T-junction geometry [159]. The mechanism above could potentially explain droplet formation in all of these devices.

Perspectives

The tools introduced in Chapter 4 and Chapter 5, namely the rail, the anchor and the wedge, enable all of the key operations required for a 2D droplet microfluidic platform without the need for an external flow of oil. By relying on gradients on confinement only, we are able to produce, transport, guide and trap droplets. Hence, we can imagine a new generation of droplet microfluidic devices that are simpler to operate than flow powered serial droplet microfluidics and less expensive than electrode based digital microfluidics.

To illustrate this statement, we designed a proof of concept device that achieves on-demand chemical reaction by coalescing two single droplets containing reactants. The device architecture and its operation is shown on Fig. 5.23. It consists in a wedged reservoir of height $h_0 \approx 130 \mu\text{m}$ and slope $\alpha \approx 1.2^\circ$ with two separate inlet channels of identical width $w = 200 \mu\text{m}$ that are used to inject the two different reactants. In the roof of the sloped reservoir are etched oblique rails that link the injection nozzles to an anchor. In the example of Fig. 5.23, the chemical reaction is a complexation between Fe^{3+} cations and SCN^- anions that produces $\text{Fe}(\text{SCN})^{2+}$ of a deep red color.

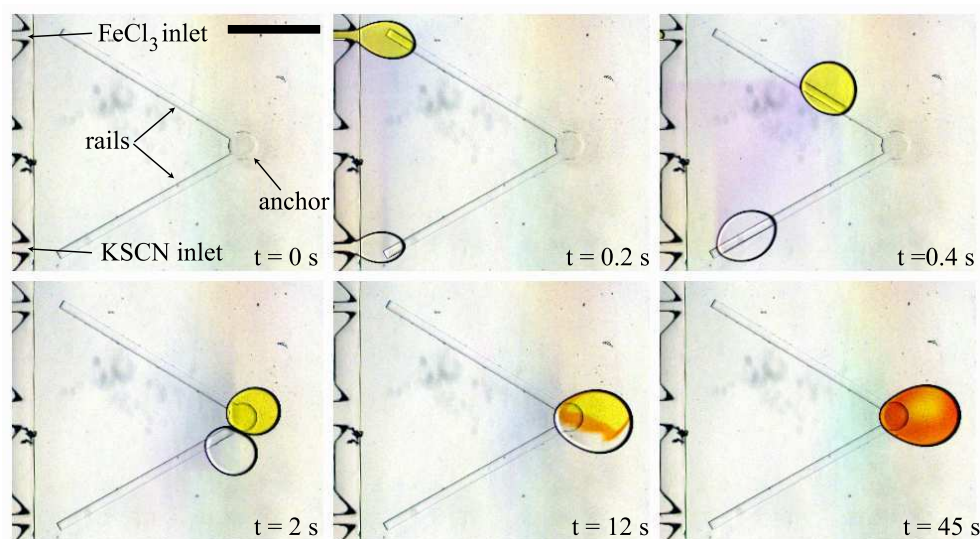


Figure 5.23: Successive images of a passive microfluidic device powered by confinement gradients only enables a controlled chemical reaction between two unique droplets containing different reactants.

The operating protocol is the following. To start the experiment, a single drop is produced from each nozzle by injecting 170 nL at 50 $\mu\text{L}/\text{min}$ during 0.2 s using a programmable syringe pump. Following this initial injection step, the syringe pump stops and the rest of the experiment takes place without any imposed flow. Each droplet detaches and is propelled by the confinement gradients while being guided towards the anchor site by the oblique rail.

We observe that the droplet containing KSCN is slower than the FeCl_3 droplet. This difference in velocity is due to the interactions between the chemical and the interface which modify the interfacial tension γ of the two droplets. Yet, because here the propulsion force due to the confinement gradients (3.36) and the guiding/trapping force from the rails/anchors (4.5) are both proportional to γ , the trajectory of the droplet is in the end independent of the actual value of the interfacial tension. The path that the drops follow in the device is fully dictated by geometry. For a given device architecture, it varies with the size of the droplets only.

Since the two drops have identical volumes in our experiment, they are equally guided by the rails. The faster drop is trapped by the anchor and waits until the slower one arrives, at which point the conjugate action of the slope and the rails presses the two drops together. It eventually leads to coalescence and initiates the chemical reaction.

Here, the anchor diameter and the droplet size are chosen such that the anchor is sufficiently strong to hold the merged droplet in place, thus allowing long term observation of the reaction product. Alternatively, a weaker anchor or larger droplets can be used to automatically release the merged droplet which can then flow to another anchor site and merge with third droplet to perform a chemical reaction with multiple steps.

The current example provides similar functionality and performance to digital microfluidic devices: a chemical reaction is triggered on-demand in a few seconds and using sub- μL sample volumes. In contrast however, the operations are here *hard-wired*, therefore not requiring any programming. Furthermore, our devices are entirely made of polymer with no active elements. Consequently, there are inexpensive and easy to replicate using molding methods. As such, it is well suited for diagnostics and other applications that require a robust, disposable, drop-on-demand platform, and for which digital microfluidics is prohibitively complex.

Finally, this device demonstrates that our droplet production method is able to cover the entire range of droplet production frequency, from the single drop on-demand to the high-throughput emulsification. In fact, we are also currently investigating the possibility of multiplexing nozzles to the thousands by stacking devices similar the one shown on Fig. 5.18.

In conclusion, we are confident that the versatility and the flexibility of the tools we have developed over the last three years will lead to numerous applications in the near future.

Appendix A

Potential flow generated by a deforming elliptical cylinder

In this first appendix, we identify the family of potential flow fields that transform one ellipse to its closest relative of equal surface area. To this end, we consider a particular ellipse of surface area $S = \pi R^2 = \pi ab$, with a and b being the main axis of the ellipse. We recall the formulas for the focal distance $c = \sqrt{a^2 + b^2}$ and the eccentricity $e = c/a$ of the ellipse.

A.1 The kinematic boundary condition

We perturb the ellipse towards another ellipse of equal surface area. The new ellipse has main axis of length $a + \delta a$ and $b - a/b\delta a$.

In the x, y plane, the original ellipse is defined by the equation

$$\frac{x^2}{a^2} + \frac{y^2}{b^2} = 1 \quad (\text{A.1})$$

The perturbed ellipse lies at a distance $(\delta x, \delta y)$ from the original one and it verifies the equation

$$\frac{(x + \delta x)^2}{(a + \delta a)^2} + \frac{(y + \delta y)^2}{(b + \delta b)^2} = 1 \quad (\text{A.2})$$

such that $(\delta x, \delta y)$ verify

$$\frac{x}{a^2}\delta x + \frac{y}{b^2}\delta y + \frac{\delta a}{a}\left(\frac{y^2}{b^2} - \frac{x^2}{a^2}\right) = 0 \quad (\text{A.3})$$

We can express this equation in the elliptic coordinates of the original ellipse, defined by $x = c \cosh \xi \cos \eta$ and $y = c \sinh \xi \sin \eta$. The original ellipse lies on the line of iso- ξ for $\xi = \xi_0 = 1/2 \log(a + b)/(a - b)$. The displacement translates to

$$\delta x = c \sinh \xi \cos \eta \delta \xi - c \cosh \xi \sin \eta \delta \eta \quad (\text{A.4})$$

$$\delta y = c \cosh \xi \sin \eta \delta \xi + c \sinh \xi \cos \eta \delta \eta \quad (\text{A.5})$$

such that the equation becomes

$$\frac{c^2 \cosh \xi_0 \cos \eta}{a^2} (\sinh \xi_0 \cos \eta \delta \xi - \cosh \xi_0 \sin \eta \delta \eta) + \frac{c^2 \sinh \xi_0 \sin \eta}{b^2} (\cosh \xi_0 \sin \eta \delta \xi + \sinh \xi_0 \cos \eta \delta \eta) + \frac{\delta a}{a} \left(\frac{y^2}{b^2} - \frac{x^2}{a^2} \right) = 0$$

and rearranges into

$$c^2 \left(\frac{\cosh \xi_0 \sinh \xi_0 \cos^2 \eta}{a^2} + \frac{\cosh \xi_0 \sinh \xi_0 \sin^2 \eta}{b^2} \right) \delta \xi + c^2 \left(\frac{\sinh^2 \xi_0 \cos \eta \sin \eta}{b^2} - \frac{\cosh^2 \xi_0 \cos \eta \sin \eta}{a^2} \right) \delta \eta + \frac{\delta a}{a} \left(\frac{y^2}{b^2} - \frac{x^2}{a^2} \right) = 0$$

We can recall the properties $a = c \cosh \xi_0$ and $b = \sinh \xi_0$ to simplify the equation

$$\begin{aligned} \left(\frac{b}{a} \cos^2 \eta + \frac{a}{b} \sin^2 \eta \right) \delta \xi + \left(\frac{b^2}{b^2} - \frac{a^2}{a^2} \right) \sin \eta \cos \eta \delta \eta + \frac{\delta a}{a} \left(\frac{y^2}{b^2} - \frac{x^2}{a^2} \right) &= 0 \\ \left(\frac{b}{a} \cos^2 \eta + \frac{a}{b} \sin^2 \eta \right) \delta \xi + \frac{\delta a}{a} (\sin^2 \eta - \cos^2 \eta) &= 0 \\ \left(\frac{b}{a} + \left(\frac{a}{b} - \frac{b}{a} \right) \sin^2 \eta \right) \delta \xi + \frac{\delta a}{a} \cos(2\eta) &= 0 \\ \frac{1}{ab} (b^2 + c^2 \sin^2 \eta) \delta \xi + \frac{\delta a}{a} \cos(2\eta) &= 0 \end{aligned}$$

On the left hand side, we can recognize a familiar expression: $g_\xi(\xi_0)g_\eta(\xi_0) = b^2 + c^2 \sin^2 \eta$. Finally, we get

$$\delta \xi = \frac{b}{g_\xi g_\eta} \cos(2\eta) \delta a \quad (\text{A.6})$$

As a result, we know that the deformation from the original ellipse to the perturbed ellipse only involves varying ξ and not η . This means that the ellipse deforms along lines of iso- η . The length of the displacement δr is necessary to compute a velocity. It is defined as

$$\delta r = \sqrt{\delta x^2 + \delta y^2}$$

Since the displacement is along lines of iso- η , it simplifies to

$$\delta r = g_\xi |\delta \xi|. \quad (\text{A.7})$$

Hence, we find that the displacement to perturb the ellipse is

$$\vec{\delta r} = \frac{b}{g_\eta} \cos(2\eta) \delta a \vec{e}_\xi$$

Therefore, the velocity at the boundary of the ellipse is given by

$$\boxed{U_\xi = \frac{b}{g_\eta} \cos(2\eta) \dot{a}} \quad (\text{A.8})$$

where we define $U_\xi = \delta r / \delta t$ and $\dot{a} = \delta a / \delta t$.

A.2 The velocity potential

The velocity boundary condition given above is simple. It looks like the boundary condition of a quadripolar flow. We suggest to take the complex potential

$$w = -\frac{\dot{a}}{2}be^{-2(\zeta-\xi_0)} \quad (\text{A.9})$$

where $\zeta = \xi + i\eta$.

In this case, we have

$$\phi = -\frac{\dot{a}}{2}be^{-2(\xi-\xi_0)} \cos 2\eta \quad (\text{A.10})$$

$$\psi = \frac{\dot{a}}{2}be^{-2(\xi-\xi_0)} \sin 2\eta \quad (\text{A.11})$$

We can then express the velocity field

$$\begin{aligned} U_\xi &= \frac{1}{g_\eta} \frac{\partial \psi}{\partial \eta} \\ &= \frac{\dot{a}}{g_\eta} be^{-2(\xi-\xi_0)} \cos 2\eta \end{aligned}$$

which, at the boundary of the ellipse in $\xi = \xi_0$, yields

$$U_\xi = \frac{\dot{a}}{g_\eta} b \cos 2\eta , \quad (\text{A.12})$$

matching the boundary condition derived above.

Hence, by uniqueness of the solution for the Laplace equation, we have found that

$$\boxed{w = -\frac{\dot{a}}{2}be^{-2(\zeta-\xi_0)}} \quad (\text{A.13})$$

Appendix B

The shape of a non-wetting pancake droplet

In this second appendix, we study the equilibrium shape of a non-wetting droplet placed between two horizontal plates at a distance h from one another. When the volume V of droplet is smaller than the volume $V_c = \pi/6 \cdot h^3$ of largest inscribed sphere between the plates, it is not confined by the plates and its equilibrium shape is a sphere, as if it were in an unbounded domain.

However, as soon as $V > V_c$, the droplet must flatten against the solid walls. This configuration has been explicitly studied before in the asymptotic limit of very large droplets [45, 51, 50], in which case the droplet has a pancake shape. Here, we provide an analytical description of the intermediate regime, when the volume of the droplet is larger but of the order of V_c .

As discussed in Chapter 1, when a non-wetting droplet is squeezed between solid walls, we distinguish the regions of the interface that are pressed against the walls (i.e. the constrained interface) from the rest of the interface (i.e. the free interface) which verifies the Young-Laplace equation (1.1).

At equilibrium, the Young-Laplace equation implies that the mean curvature \mathcal{C} of the free interface is constant everywhere around the droplet. Hence, the free interface is a surface of constant mean curvature, i.e. a CMC or minimal surface. Furthermore, given the in-plane rotational symmetry of the confining geometry, the shape of the free interface has rotational symmetry in the plane as well. As a result, the free interface of a non-wetting droplet squeezed between parallel plates is necessarily a surface of revolution of constant mean curvature whose axis is transverse to the plates.

B.1 Delaunay surfaces

Surfaces of revolution with a constant mean curvature were first studied, characterized and classified by Charles-Eugène Delaunay in 1841 [52] and are today called Delaunay surfaces. The sphere, the cylinder or the catenoid are classical examples surfaces of revolution with

a constant mean curvature. Two other groups of surfaces called unduloïds and nodoïds complete the family of Delaunay surfaces.

In his seminal work, Delaunay demonstrates that the generatrix of a surface of revolution with a constant mean curvature is necessarily the track of the focus of a conic rolling on the axis of the surface of revolution, a curve called a Delaunay's roulette. Reciprocally, the surface of revolution whose generatrix is a Delaunay's roulette has a constant mean curvature. We illustrate on Fig. B.1 how to obtain a roulette by rolling an ellipse and how to construct the associated surface of revolution. There are three families of conics, hence three families of roulettes and thereby three families of Delaunay surfaces:

- if the conic is a parabola, the roulette is the ordinary catenary and the Delaunay surface is a catenoid.
- if the conic is an ellipse, the roulette is an elliptic catenary and the Delaunay surface is an unduloïd.
- if the conic is a hyperbola, the roulette is a hyperbolic catenary and the Delaunay surface is a nodoïd.

The cylinder is a particular member of the unduloïd family. Its generatrix is a straight line and therefore the roulette obtained by tracking the center of circle rolling on the axis of the cylinder. The sphere is an asymptotic member of both unduloïd and the nodoïd family, a case we discuss later on.

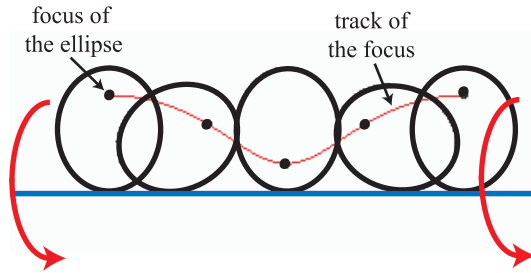


Figure B.1: An elliptic catenary is obtained by tracking the focus of an ellipse rolling on a straight line. The elliptic catenary is the generatrix of the surface of revolution while the line onto which it rolled is the axis of revolution. An undulated cylinder is obtained by rotating this elliptic catenary.

All of Delaunay's surfaces, except for the catenary, can be described by the following sets of parametric equations in which $t = [-\infty, \infty]$ and $\theta = [-\pi, \pi]$ are two independent parameter:

- when the generatrix is the elliptic catenary obtained by rolling an ellipse of major

and minor axis a and b , the Delaunay surface is the set of points

$$\begin{aligned}\frac{x(t)}{a} &= \sqrt{1-e^2} \sqrt{\frac{1-e\cos t}{1+e\cos t}} \cdot \cos \theta \\ \frac{y(t)}{a} &= \sqrt{1-e^2} \sqrt{\frac{1-e\cos t}{1+e\cos t}} \cdot \sin \theta \\ \frac{z(t)}{a} &= (1-e^2) \cdot \int_0^t \frac{du}{\sqrt{1-e^2\cos^2 u}(1+e\cos u)}\end{aligned}\tag{B.1}$$

in which $e = \sqrt{a^2 - b^2}/a < 1$ is the eccentricity of the ellipse.

- for the hyperbolic catenary obtained by rolling an hyperbola of major and minor axis a and b , we have

$$\begin{aligned}\frac{x(t)}{a} &= \sqrt{e^2-1} \sqrt{\frac{e-\cos t}{e+\cos t}} \cos \theta \\ \frac{y(t)}{a} &= \sqrt{e^2-1} \sqrt{\frac{e-\cos t}{e+\cos t}} \sin \theta \\ \frac{z(t)}{a} &= (e^2-1) \cdot \int_0^t \frac{du}{\sqrt{e^2-\cos^2 u}(e+\cos u)}\end{aligned}\tag{B.2}$$

in which $e = \sqrt{a^2 + b^2}/a > 1$ is the eccentricity of the hyperbola.

Hence, the family of Delaunay's roulettes and the resulting family of Delaunay's surface are essentially a one-parameter family of shapes which are scanned by varying the eccentricity parameter e . The parameter a is only a scaling factor. In Fig. B.2, we displays cuts in the (x, z) plane of eight different Delaunay surfaces obtained from MatLab using the equations above. We scan through the family of unduloïds and nodoïds by varying e from 10^{-3} to 5.

From Fig. B.2, we conclude that:

- the cylinder is the unduloïd obtained by taking $e = 0$ in equation (B.1).
- the sphere, or actually a collection of touching sphere, is the asymptotic limit of the unduloïd when $e \rightarrow 1$ and the asymptotic limit of the nodoïd when $e \rightarrow 1$.
- the tangent plane of an unduloïd is never perpendicular to the axis z , or equivalently $dz/dx \neq 0$ everywhere on the generatrix of an unduloïd.

B.2 Non-wetting pancake droplets

The analysis above shows that the free interface of a droplet squeezed between two plates parallel to the (x, y) plane and at a distant h from one another is necessarily a slice of thickness h of a Delaunay surface, i.e. the z -axis is bounded between values z_1 and $z_1 + h$ in Fig. B.2.

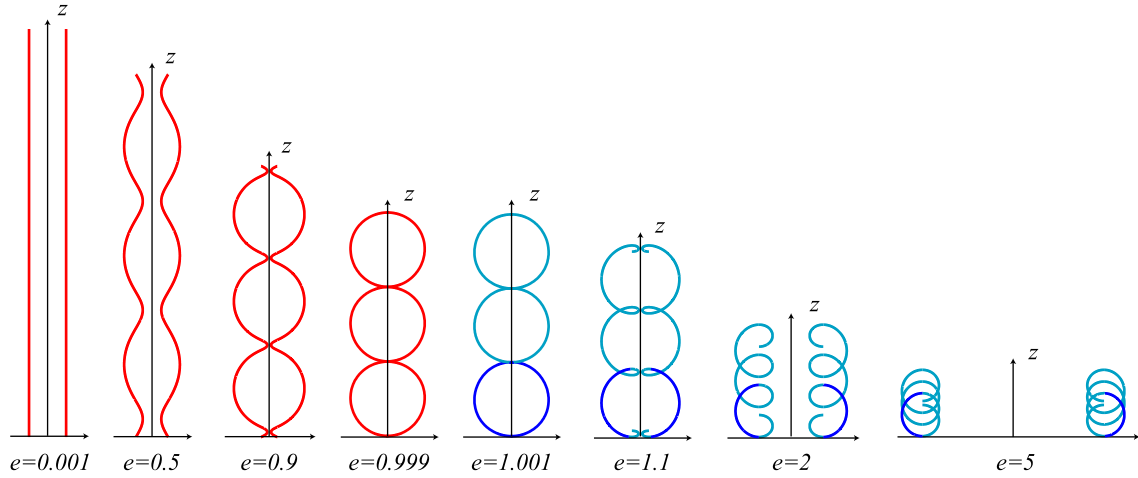


Figure B.2: Eight different members of the unduloid and noid families of Delaunay surfaces, obtained by taking different values of e in equations (B.1) and (B.2). The shape of a pancake droplet squeezed between two plates is a slice of a Delaunay surface, between $z = 0$ and the dotted line for example. The non-wetting condition of the droplet imposes that the dotted line intersects the generatrix tangentially. It is impossible for unduloids drawn in red and possible at multiple z positions for noids in blue. The interface of the pancake must bend outwards and can therefore only be the noid slices in dark blue.

The non-wetting condition of the droplet imposes that the free interface must connect to the solid walls at a contact angle $\theta_\gamma = \pi$. This translates to the condition that the tangent of the generatrix of the Delaunay surface at $z = z_1$ and $z = z_1 + h$ must be perpendicular to the z -axis, or equivalently that $dz/dx = 0$.

As shown on Fig. B.2, unduloids never verify such a condition over their entire surface. Hence, the interface of a non-wetting pancake droplet cannot be a portion of an unduloid. On the contrary, for every $e > 1$ and thus for every noid shape, there exists an infinite number of positions z ordered periodically for which the generatrix verifies $dz/dx = 0$. We call such positions *flats*. Between three or more flats, the generatrix crosses itself, meaning that the surface intersects itself. Such surfaces are unphysical for a droplet and hence, the slice can only be between two successive flats of the generatrix.

Between two successive *flats*, the generatrix is either convex and bends towards the main axis Oz of the surface or concave and bends outwards. A convex portion corresponds to $\theta_\gamma = 0$, a perfectly wetting liquid bridge, while a concave portion verifies the non-wetting condition $\theta_\gamma = \pi$. As a result, we obtain that the free interface of a non-wetting pancake droplet can only be a concave portion of a noid between two *flats* of its generatrix.

Such portions are identified in dark blue on Fig. B.2. We notice that by varying the parameter e , we modify simultaneously the height h and radius R of the non-wetting noid slice and cover the entire range of the shape parameter h/R for pancake droplets. When $e \rightarrow 1$, h/R tends towards its maximum value 2 obtained with the sphere. When

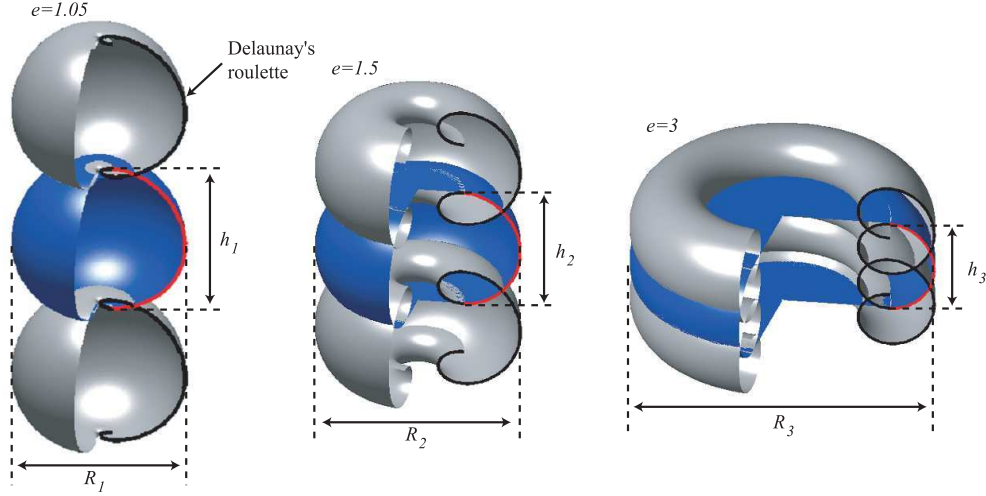


Figure B.3: Three different pancake shapes are constructed as slices of noidoids from different values of e . The larger e , the smaller the aspect ratio h/R of the pancake.

$e \rightarrow \infty$, the slice widens and flattens more and more and $h/R \rightarrow 0$. Figure B.3 extracts three different pancake shapes from slices of noidoids in 3D.

Since noidoids are the only surface of revolution with a constant mean curvature whose generatrix has *flats* (the classic catenary not discussed here has none), the slices discussed above are the only possible equilibrium shapes for the free interface of a non-wetting pancake droplet.

B.3 The curvature of a pancake droplet

Having identified the exact shape of a non-wetting pancake, we are able to compute its curvature \mathcal{C} . In the parametric descriptions (B.1) and (B.2), the curvature \mathcal{C} of the Delaunay surface is simply equal to $1/a$. Once x , y and z are made non-dimensional using a , we have $a\mathcal{C} = 1$. Hence, for a given value of e , we compute analytically the distances between two flats of the generatrix. This gives us a value of the non-dimensional thickness $\bar{h} = h/a$ of the pancake. We also extract the non-dimensional radius $\bar{R} = R/a$ of the pancake. We can then plot \bar{h} as a function of \bar{h}/\bar{R} , which is equivalent to plotting $h\mathcal{C}$ versus h/R . The result is shown on Fig. B.4.

As expected, we obtain for the sphere for a sphere of radius R and diameter $h = 2R$, $h\mathcal{C} = h \cdot 2/R = 4$. For very large pancakes, Laplace [45] derived an asymptotic expression

$$\mathcal{C} = 2/h + \frac{\pi}{4} \frac{1}{R} \quad (\text{B.3})$$

which transforms into the expression

$$h\mathcal{C} = 2 + \frac{\pi}{4} \frac{h}{R} \quad (\text{B.4})$$

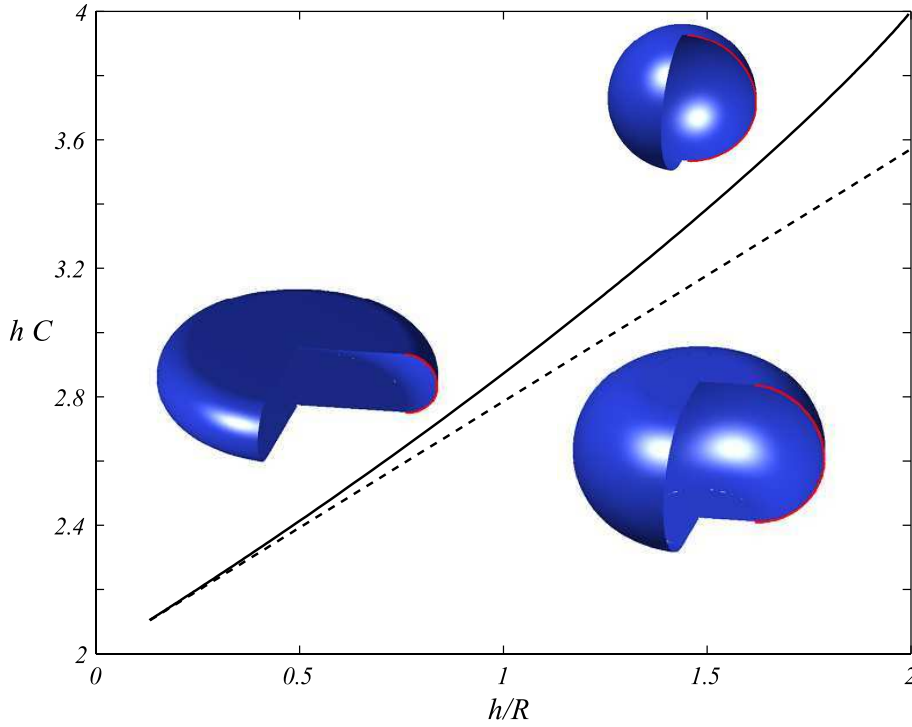


Figure B.4: Plot of the curvature \mathcal{C} scaled with the height of the pancake h versus the aspect ratio h/R of the pancake. The dotted line is the asymptotic prediction (B.3) found by Laplace.

which can be compared to the numerical prediction of Fig. B.4. We find that the curvature of pancakes of intermediate aspect ratio tends towards this asymptotic limit when $h/R \rightarrow 0$.

B.4 The asymptotic curvature of a pancake droplet

In this last section, we rederive and comment the expression

$$\mathcal{C} = \frac{2}{h} + \frac{\pi}{4}\mathcal{C}_{//} , \quad (\text{B.5})$$

for the mean curvature of a large non-wetting pancake drop with small in-plane deformations, in which $\mathcal{C}_{//}$ is the local in-plane curvature of the interface.

This expression is analogous to the expression obtained by Laplace for the curvature of a large pancake drop at equilibrium. Two hundred years later, Park&Homsy [51] extended Laplace's result to include small in-plane deformations of the droplet using asymptotic analysis. Here, we explain the physical origin of the puzzling $\pi/4$ prefactor in front of the otherwise logical in-plane curvature $\mathcal{C}_{//}$.

Our analysis detailed below allows a decomposition of the curvature into its transverse and in-plane components:

$$\mathcal{C} = \underbrace{\left[\frac{2}{h} + \left(\frac{\pi}{4} - 1 \right) \mathcal{C}_{//} \right]}_{\text{transverse curvature}} + \underbrace{\mathcal{C}_{//}}_{\text{in-plane curvature}}. \quad (\text{B.6})$$

From this decomposition, we find that

- the in-plane curvature is equal $\mathcal{C}_{//}$, as expected intuitively.
- the $\pi/4$ prefactor originates from a correction of the transverse curvature

We explain the correction of the transverse curvature as follows. Given the scale separation between the in-plane and transverse dimensions ($h \ll R$), the curvature is dominated by the transverse curvature. Hence, the 0th order curvature \mathcal{C}^0 in terms of h/R is given by

$$\mathcal{C}_0 = \underbrace{\frac{2}{h}}_{\text{transverse curvature}} + \underbrace{0}_{\text{in-plane curvature}}. \quad (\text{B.7})$$

Indeed, the transverse shape of the free interface is best approximated by a half circle at this stage. The in-plane curvature $1/R$ is h/R smaller than the transverse curvature. As a result, it can only be captured by computing the 1st order corrections \mathcal{C}^1 of the curvature. To be correct, this correction must also include 1st order correction to the transverse shape and transverse curvature. We find that \mathcal{C}^1 is given by

$$\mathcal{C}_1 = \underbrace{\left(\frac{\pi}{4} - 1 \right) \mathcal{C}_{//}}_{\text{transverse curvature}} + \underbrace{\mathcal{C}_{//}}_{\text{in-plane curvature}}, \quad (\text{B.8})$$

solving the mysterious origins of $\pi/4$.

Onto the tedious calculations. We consider the general configuration of a roughly circular pancake drop confined between two parallel plates, as observed a Hele-Shaw cell or a 2D microfluidic device, and assume arbitrary wetting conditions at the walls. We use cylindrical coordinates (r, θ, z) centered on the center of mass of the droplet and define the non-dimensional coordinates $\bar{r} = r/R$ and $\bar{z} = 2z/h$. The interface of the droplet is then described by the set of points $(f(\theta, z), \theta, z)$, with $f(\theta, z)$ an algebraic function.

Using differential geometry, we obtain the expression

$$\mathcal{C} = - \left(1 + \frac{f_\theta^2}{f^2} \right) \frac{f_{zz}}{(1 + f_\theta^2/f^2 + f_z^2)^{3/2}} + (1 + f_z^2) \frac{1 + 2 \frac{f_\theta^2}{f^2} - \frac{f_{\theta\theta}}{f}}{f(1 + f_\theta^2/f^2 + f_z^2)^{3/2}} + \frac{2}{f} \frac{\frac{f_\theta}{f} f_z f_{\theta z} - f_z^2 \frac{f_\theta^2}{f^2}}{(1 + f_\theta^2/f^2 + f_z^2)^{3/2}} \quad (\text{B.9})$$

for the mean curvature \mathcal{C} of a surface defined in cylindrical coordinates.

In the case of a surface with rotational symmetry, the function f depends on z only and all derivatives in θ are zero. The curvature is then

$$\mathcal{C} = - \frac{f_{zz}}{(1 + f_z^2)^{3/2}} + \frac{1}{f \sqrt{1 + f_z^2}}, \quad (\text{B.10})$$

in agreement with classic results [160].

The expression (B.9) can be simplified in the case of a large pancake droplet by using the scale separation between the in-plane and transverse dimensions ($\epsilon = h/2R \ll 1$). The function $f(\theta, z)$ is decomposed into two parts

$$f(\theta, z) = R \cdot \rho(\theta) + \frac{h}{2} \cdot F(\theta, z) \quad (\text{B.11})$$

The first term, $R \cdot \rho(\theta)$, describes the in-plane shape of the drop. The second term, $h/2 \cdot F(\theta, z)$, describes how the interface locally spans the height of the channel, from the bottom to the top wall. In order to verify the wetting conditions at the walls, the function F must verify the following boundary conditions

$$f(\theta, \bar{z} = 0) = 0 \quad (\text{B.12a})$$

$$f_z(\theta, \bar{z} = 0) = 0 \quad (\text{B.12b})$$

$$f_z(\theta, \bar{z} = 1) = \tan(\alpha) \quad (\text{B.12c})$$

$$(\text{B.12d})$$

where α is the contact angle ($\alpha = \pi/2$ in the non-wetting case).

Next, we define the non-dimensional curvature $\bar{\mathcal{C}} = h/2 \cdot \mathcal{C}$ and develop the $F(\theta, z)$ in terms of $\epsilon = h/R$ as

$$F(\theta, z) = F^{00}(\theta, z) + \epsilon F^{10}(\theta, z) + o(\epsilon) . \quad (\text{B.13})$$

Once injected into the expression (B.9) for the curvature, we obtain an asymptotic development for the curvature $\bar{\mathcal{C}}$

$$\begin{aligned} \bar{\mathcal{C}}_0 + \epsilon \bar{\mathcal{C}}_1 = & \underbrace{-\frac{F_{\bar{z}\bar{z}}^0}{(1 + (F_{\bar{z}}^0)^2)^{3/2}}}_{\text{dominant term}} + \\ & \underbrace{\left[-\left(\frac{F_{\bar{z}}^1}{(1 + (F_{\bar{z}}^0)^2)^{3/2}} \right)_{\bar{z}} + R\mathcal{C}_{//}(\theta) \frac{1}{\sqrt{1 + (F_{\bar{z}}^0)^2}} + \frac{\rho_{\theta} F_{\bar{z}}^0 F_{\theta\bar{z}}^0 - \rho_{\theta}/\rho (F_{\bar{z}}^0)^2}{\rho^2 (1 + (F_{\bar{z}}^0)^2)^{3/2}} \right]}_{\text{1st order term}} \cdot \epsilon \end{aligned} \quad (\text{B.14})$$

in which $\mathcal{C}_{//} = (1 + 2\rho_{\theta}^2/\rho^2 - \rho_{\theta\theta})/(R\rho)$ is the in-plane mean curvature of the droplet and the curvature of the function $R \cdot \rho$. This equation is strictly valid only when $(\rho_{\theta}/\rho)^2 \ll \epsilon$, which means that the in-plane shape of the pancake drop is roughly circular and evolves smoothly.

Balancing dominant terms: At the 0th order, equation (B.14) becomes

$$\bar{\mathcal{C}}_0 = -\frac{F_{\bar{z}\bar{z}}^0}{(1 + (F_{\bar{z}}^0)^2)^{3/2}} \quad (\text{B.15})$$

The right hand side is simply the curvature of the function F^0 in the (e_r, e_z) plane. Hence, the dominant curvature is the transverse curvature, as expected. The Hele-Shaw approximation implies that pressure and curvature are invariant in the z direction. Hence, $\bar{\mathcal{C}}_0$ is z -invariant and we find that F^0 describes a circular arc in the (e_r, e_z) plane. Last, the boundary conditions defines the value of the curvature such that

$$\bar{\mathcal{C}}_0 = \frac{1}{\sin \alpha} , \quad (\text{B.16a})$$

$$F^0(\theta, \bar{z}) = \sqrt{\frac{1}{\sin^2 \alpha} - \bar{z}^2} - \frac{1}{\sin \alpha} . \quad (\text{B.16b})$$

Balancing 1st order terms: At the 1st order in ϵ , equation (B.14) becomes

$$\bar{\mathcal{C}}_1 = - \left(\frac{F_{\bar{z}}^1}{(1 + (F_{\bar{z}}^0)^2)^{3/2}} \right)_{\bar{z}} + RC_{//} \frac{1}{\sqrt{1 + (F_{\bar{z}}^0)^2}} + \frac{\rho_\theta}{\rho^2} \text{frac} F_{\bar{z}}^0 F_{\theta \bar{z}}^0 - \rho_\theta / \rho (F_{\bar{z}}^0)^2 (1 + (F_{\bar{z}}^0)^2)^{3/2} . \quad (\text{B.17})$$

Recalling the assumption that $(\rho_\theta / \rho)^2 \ll \epsilon$ and the fact that $F_\theta^0 = 0$, we notice that the last term on the right hand side is negligible. Using the solution (B.16b) for $F^0(\theta, \bar{z})$, we can replace $1 + (F_{\bar{z}}^0)^2$ by

$$1 + (F_{\bar{z}}^0)^2 = \frac{1}{1 - \tan^2 \alpha \bar{z}^2} \quad (\text{B.18})$$

everywhere in the equation for $\bar{\mathcal{C}}_1$ above. It yields

$$\bar{\mathcal{C}}_1 = - \left[(1 - \sin^2 \alpha \bar{z}^2)^{3/2} F_{\bar{z}}^1 \right]_{\bar{z}} + RC_{//} \sqrt{1 - \sin^2 \alpha \bar{z}^2} . \quad (\text{B.19})$$

Because $\bar{\mathcal{C}}_1$ is \bar{z} invariant, we can integrate a first time treating $\bar{\mathcal{C}}_1$ as a constant:

$$(1 - \sin^2 \alpha \bar{z}^2)^{3/2} F_{\bar{z}}^1 = \frac{RC_{//}}{2} (\bar{z} \sqrt{1 - \sin^2 \alpha \bar{z}^2} + \frac{\sin^{-1}(\sin(\alpha) \bar{z})}{\sin \alpha}) - \bar{\mathcal{C}}_1 \bar{z} + \text{Cste} . \quad (\text{B.20})$$

The symmetry condition $F_{\bar{z}}^1(\bar{z} = 0) = 0$ imposes $\text{Cste} = 0$. Furthermore, since the contact angle boundary condition at the solid walls $F_{\bar{z}}(\bar{z} = 1) = \tan \alpha$ is fully captured by $F^0(\bar{z})$, $F_{\bar{z}}^1$ must verify the condition $F_{\bar{z}}^1(\bar{z} = 1) = 0$. As a result, we obtain from (B.20) that

$$\bar{\mathcal{C}}_1 = \frac{RC_{//}}{2} (\cos \alpha + \frac{\alpha}{\sin \alpha}) . \quad (\text{B.21})$$

We can finish the derivations by integrating (B.20) to find an expression for F^1 :

$$F^1 = \frac{RC_{//}}{2} \left[\frac{\bar{z} \sin^{-1}(\sin(\alpha) \bar{z})}{\sqrt{1 - \sin^2 \alpha \bar{z}^2}} - \left(\frac{\cos \alpha}{\sin^2 \alpha} + \frac{\alpha}{\sin^3 \alpha} \right) \frac{1}{\sqrt{1 - \sin^2 \alpha \bar{z}^2}} \right] + \text{Cste} . \quad (\text{B.22})$$

Since $F^1(\bar{z} = 0) = 0$, we have

$$\text{Cste} = \frac{RC_{//}}{2} \left(\frac{1}{\sin^2 \alpha} + \frac{\alpha}{\cos \alpha \sin^3 \alpha} \right) . \quad (\text{B.23})$$

As a result,

$$F^1 = \frac{RC_{//}}{2} \left[\frac{\bar{z} \sin^{-1}(\sin(\alpha)\bar{z})}{\sqrt{1 - \sin^2 \alpha \bar{z}^2}} + \left(\frac{\cos \alpha}{\sin^2 \alpha} + \frac{\alpha}{\sin^3 \alpha} \right) \left(\frac{1}{\cos \alpha} - \frac{1}{\sqrt{1 - \sin^2 \alpha \bar{z}^2}} \right) \right]. \quad (\text{B.24})$$

Results: We recover the mean curvature \mathcal{C} by summing the dominant and the 1st order terms: $h/2\mathcal{C} = \bar{\mathcal{C}}_0 + \epsilon\bar{\mathcal{C}}_1$. We obtain

$$\mathcal{C} = \frac{1}{\sin \alpha} \frac{2}{h} + \frac{\mathcal{C}_{//}}{2} \left(\cos \alpha + \frac{\alpha}{\sin \alpha} \right) \quad (\text{B.25})$$

This expression is in agreement with Laplace's result for perfectly circular pancake droplets and with Park&Homsy for slightly deformed pancake droplets.

In particular, for the non-wetting case ($\alpha = \pi/2$), we recover the result (B.5)

$$\boxed{\mathcal{C} = \frac{1}{h} + \frac{\pi}{4}\mathcal{C}_{//}} \quad (\text{B.26})$$

Appendix C

Published paper: *Microchannel deformations due to solvent-induced PDMS swelling*, LOC 2010

Microchannel deformations due to solvent-induced PDMS swelling†

Rémi Dangla,^a François Gallaire^b and Charles N. Baroud^{*a}

Received 23rd February 2010, Accepted 24th June 2010

DOI: 10.1039/c003504a

The compatibility of polydimethylsiloxane (PDMS) channels with certain solvents is a well known problem of soft lithography techniques, in particular when it leads to the swelling of the PDMS blocks. However, little is known about the modification of microchannel geometries when they are subjected to swelling solvents. Here, we experimentally measure the deformations of the roof of PDMS microchannels due to such solvents. The dynamics of impregnation of the solvents in PDMS and its relation to volume dilation are first addressed in a model experiment, allowing the precise measurement of the diffusion coefficients of oils in PDMS. When Hexadecane, a swelling solvent, fills a microchannel 1 mm in width and 50 μm in height, we measure that the channel roof bends inwards and takes a parabolic shape with a maximum deformation of 7 μm . The amplitude of the subsidence is found to increase with the channel width, reaching 28 μm for a 2 mm wide test section. On the other hand, perfluorinated oils do not swell the PDMS and the microchannel geometry is not affected by the presence of perfluorodecalin. Finally, we observe that the trajectories of droplets flowing in this microchannel are strongly affected by the deformations: drops carried by swelling oils are pushed towards the edges of the channel while those carried by non-swelling oils remain in the channel center.

I. Introduction

In recent years, polydimethylsiloxane (PDMS) has emerged as the material of choice for rapid, low cost fabrication of microfluidic channels. This is due to the many advantages of PDMS, particularly its transparency and biocompatibility, in addition to the development of standard protocols for its fabrication.^{1,2} This has allowed an explosion of interest in microfluidics by reducing the costs and complexity of fabricating microchannels.

However, PDMS presents a few characteristics which can limit its usefulness. It is a rubber elastic material³ with a low Young's modulus $E \sim 1$ MPa and a high Poisson ratio $\nu = 0.5$, making microchannels highly flexible and compliant. As a result, structures of extreme aspect ratios are difficult to fabricate: tall pillars bend and buckle while wide microchannels sag and collapse.⁴ Additionally, recent studies have shown that even stable geometries may significantly deform when the imposed flow pressures reach 10^5 Pa.^{5–7}

A second drawback arises from the porous nature of PDMS, which leads to compatibility issues with some solvents.⁸ Indeed, the absorption of certain liquids in the polymer matrix can lead to departures from the dry geometry of a microchannel. The rubber-like PDMS expands when a swelling solvent diffuses into the material, in an analogous fashion to heat diffusion and thermal expansion in elastic solids. The extent of the swelling of an isolated sheet is characterized by the swelling coefficient at saturation S_∞ which measures the ratio of its swollen length over

its dry length. Typical values of S_∞ are in the range of 1.05 to 1.20, meaning that solvents can induce strains of up to 20%.⁸

Deformations of this magnitude have also been reported for PDMS microchannels, by observing the changes in the size and shape of the channels on microscopy images.^{9,10} However, quantitative measurements of the microchannel deformation in the third dimension have proved difficult to obtain, although such information is of major importance for any microfluidic application that relies on a precise knowledge of the flow profile, for example when the shear stress on the wall must be known.¹¹

In this paper, we study the deformation of PDMS microchannels when placed in contact with swelling oils. The swelling characteristics of the oils (S_∞ and the diffusion coefficient D) are first determined by analyzing the size of isolated PDMS sheets in a bath of oil. The height profile of microchannels is then obtained, when those are placed in contact with a swelling oil, and compared with the case of non-swelling solvents. The measurements are achieved by adapting an optical method, initially developed for fluid free surfaces,¹² which compares the displacement of a pattern between two images (*before* and *after*). Finally, we demonstrate that the swelling is responsible for deviations of droplet trajectories as they flow in a deformed microchannel.

Below, we begin by describing the experimental setup and protocol in Section II. This is followed, in Section III, by an explanation of the synthetic Schlieren method which is used to obtain the channel deformations. The results are presented in three parts: First the swelling characteristics of the oils are presented, followed by the shape of microchannels when in contact with these oils. Finally, we demonstrate the effect of the deformation on the motion of droplets in swollen channels.

II. Experimental setup and protocol

The microfluidic devices are fabricated in PDMS (Dow Corning SYLGARD 184, 1/10 ratio of curing agent to bulk material)

^aLadHyX and department of Mechanics, Ecole Polytechnique, CNRS, 91128 Palaiseau Cedex, France. E-mail: baroud@ladhyx.polytechnique.fr
^bLaboratory of Fluid Mechanics and Instabilities (LFMI), Ecole Polytechnique Fédérale de Lausanne (EPFL), CH-1015 Lausanne, Switzerland

† Electronic supplementary information (ESI) available: Derivations of eqn (4) and eqn (5), supplementary data and supplementary movie. See DOI: 10.1039/c003504a

using standard soft lithography techniques.^{13,14} They are sealed onto a glass slide of thickness $h_g = 1.1$ mm by plasma bonding. The microchannels have a nominal height of $h_c = 50$ μm and the PDMS blocks have a global thickness h_p between 4 and 5 mm, as sketched in Fig. 1. Two solvents, hexadecane or perfluorodecalin (PFD), are used as the swelling and non-swelling oils in the microchannel experiments. They are injected into the channel by capillary suction, by depositing a drop at one of the channel entrances. The test sections whose deformations are measured have a length $L = 6$ mm and widths w of either 1 mm, 1.5 mm or 2 mm. They are connected to the entrance and exit through the main channel which is 100 μm in width.

The height profile of a test section is measured using a synthetic Schlieren approach, in which the surfaces of the PDMS act as lenses that refract a fixed pattern. By analyzing the image of this pattern seen through the PDMS, before and after the swelling, the local curvature of the surfaces can be reconstructed. This method has previously been used to observe deformations of a single free liquid surface¹² but works with any deformed refracting interface. Schematically, the refracted image is compared to a reference image using a Digital Image Correlation (DIC) algorithm to determine the apparent displacement field $\delta\vec{r}$ of the pattern, which is related to the gradient of the

height profile of the deformed surface. The deformations are then reconstructed by numerically integrating the slope thus measured in two dimensions.

The imaged pattern is obtained by fixing adhesive tape (3M Scotch Magic Tape) under the glass slide, as sketched in Fig. 1, and using its inherent texture. These patterns are visualized through a channel's test section using a digital camera mounted on a low magnification ($3\times$ to $5\times$) stereo microscope with backlighting. A typical image is shown in Fig. 2.a, where the microchannel walls are visible, in addition to the grainy texture to be tracked. The field of observation is a square, 3 mm to 5 mm in width depending on magnification, and the microscope's objective is at a distance $H \approx 7$ cm from the PDMS block. The DIC analysis to obtain the apparent displacement field is performed using the commercial software *DaVis* (LaVision). Multipass iterations with a decreasing window size and a 50% overlap are used for the computations of the correlation functions, leading to a displacement field defined on a 128×128 grid, with a spatial resolution ranging between 24.2 μm and 40.8 μm .

The experimental protocol consists of first preparing a microchannel and placing it on the apparatus described above. The field of observation is chosen such that the test section and the inlet channel are visible, then a reference image of the pattern is taken, as shown on Fig. 2.a. The solvent is then allowed into the microchannel and the device is monitored for 5 h by taking an image every 3 min. During this time, the solvent diffuses into the solid and evaporates into the atmosphere, leading to continuous variations of the observed pattern. These variations can be followed in Fig. 2.b which shows a space-time diagram extracted from a typical experiment. On this image, the horizontal axis represents time and the vertical axis gives the gray values measured along the line $A-A'$ in each image. Pattern displacements, which are a result of swelling induced surface deformations, can be qualitatively visualized in this way (see also movie in the ESI†).

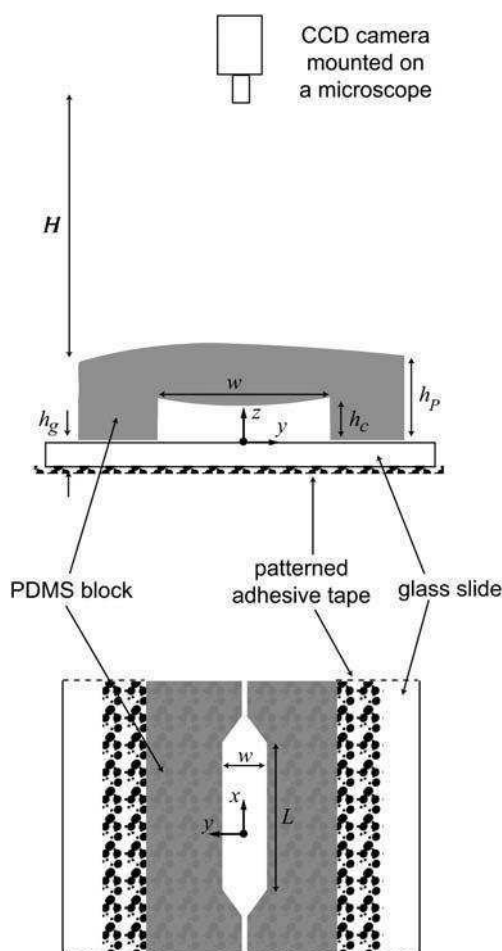


Fig. 1 Cross-section (top) and top view (bottom) of a microchannel test section, displaying the synthetic Schlieren experimental setup. The cross-section is not to scale.

III. Surface reconstruction

A typical experiment can be divided into two distinct periods, as pointed out on the spatio-temporal graph. During period 1, from $t = 0$ to $t = 90$ min in the example of Fig. 2.b, the channel is filled with solvent and the pattern displacements are due to the deformation of the top PDMS–air interface only. Indeed, the optical indices of glass ($n_g = 1.47$), PDMS ($n_{\text{PDMS}} = 1.42$) and of the solvents ($n_{\text{hexa}} = 1.43$, $n_{\text{PFD}} = 1.30$) are all close together. Therefore, the bottom two interfaces (glass–solvent and solvent–PDMS) disappear and the channel walls become invisible as long as the channel is filled.

The situation in period 1 is therefore strictly identical to the one described by Moisy *et al.*¹² Because the camera is far above the microchannel ($w/H \ll 1$), rays passing by the field of observation and reaching the objective are all nearly parallel. As they pass through the deformed interface, they are refracted at an angle proportional to the local slope of the interface. Hence, a point I of the pattern is actually seen by the camera as the point I' , at a distance $\delta\vec{r}_1$ from its original position, as sketched in Fig. 3.a. The slope of the top surface is given by the gradient of the height deformations $\vec{\nabla}h_p$ and, for small deformations ($h_p/h_p \ll 1$), it is related to the apparent displacement field $\delta\vec{r}_1$ by

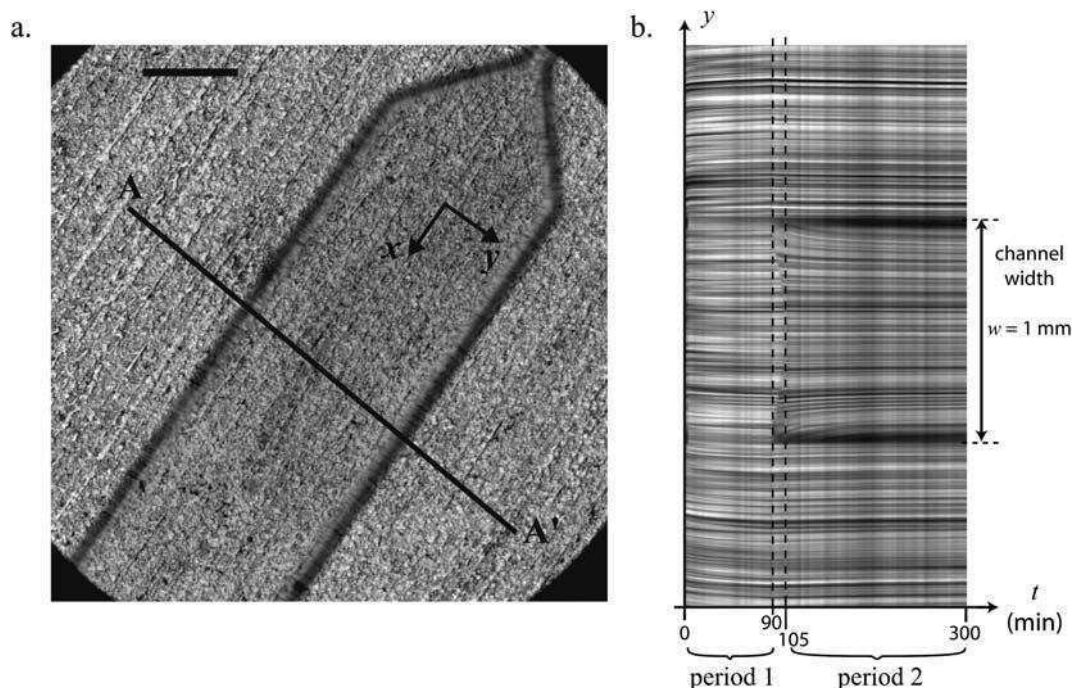


Fig. 2 a. Reference image of a channel taken before a swelling experiment, featuring the main test section of width $w = 1$ mm and the narrow inlet channel. The scale bar represents $500 \mu\text{m}$. b. Space-time diagram showing the evolution of the pixel gray values along the axis ($A - A'$) of the reference image. The channel is filled with hexadecane from $t = 0$ min to $t = 90$ min and it is empty after $t = 105$ min.

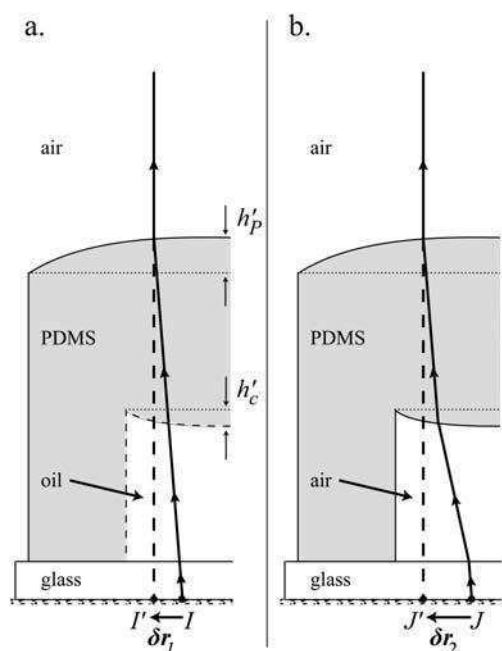


Fig. 3 Refraction of light rays by a deformed microchannel. The initial geometry is sketched by the dotted lines. a: The channel is filled with a solvent of matching optical index. The two bottom interfaces (dashed interfaces) disappear. The ray passing by I is refracted by the top surface and is seen as passing by I' , inducing the apparent displacement $\delta\vec{r}_1$. b: The channel is filled with air. The ray is refracted by three interfaces, including two potentially deformed surfaces. Point J has an image at J' , inducing the apparent displacement $\delta\vec{r}_2$.

$$\vec{\nabla} h'_p = \left(\frac{1}{H} - \frac{1}{h_1^*} \right) \delta\vec{r}_1, \quad (1)$$

where $h_1^* = (1 - n_{\text{air}}/n_{\text{PDMS}})(h_p + n_{\text{PDMS}}/n_{\text{oil}} \cdot h_c + n_{\text{PDMS}}/n_g \cdot h_g)$.

When using a stereomicroscope, this relation is modified by the fact that the optical axis of the microscope \vec{n} is not aligned with the vertical axis \vec{z} of the channel. The resulting viewing angle θ , typically around 10° , is characterized by its projections θ_x and θ_y on the in-plane axis (\vec{x}, \vec{y}) . A consequence of this non-alignment is a blur in the image near the vertical wall. To limit this drawback, the channel is aligned with the viewing angle, *i.e.* setting $\theta_y = 0$. A second consequence is a correction to the relationship between the apparent displacement field $\delta\vec{r}_1$ and the refracting interface slope $\vec{\nabla} h'_p$, yielding

$$\vec{\nabla} h'_p = \left(\frac{1}{H} - \frac{1}{h_1^*} \right) \cdot (\delta\vec{r}_1 - \delta_\theta \vec{x}), \quad (2)$$

where $\delta_\theta = h_c [\tan(\sin^{-1}(1/n_{\text{oil}} \sin \theta)) - \tan \theta]$. This small correction does not modify the qualitative features but improves the homogeneity of the measured deformation.

Period 1 is followed by a short transition period, from $t = 90$ min to $t = 105$ min, during which the microchannel is partially empty. This translates to a sudden reappearance of the channel walls and to complex movements of the patterns on Fig. 2.b. However, the channel remains in contact with the swelling solvent during the transition (see movie in the ESI†).

The second period begins when the microchannel is completely emptied due to absorption and evaporation, at $t = 105$ min in Fig. 2.b. During period 2, the PDMS block is no longer in contact with the swelling agent and the geometry relaxes back to

its initial shape, as observed on the space–time diagram. Again, the first image in period 2 is compared with the initial reference image by DIC analysis and yields a second displacement field $\delta\vec{r}_2$.

During this period, the pattern is refracted by two deformed surfaces: the air–PDMS interface which forms the channel roof and the PDMS–air interface on top of the block, in addition to the flat glass–air surface, as sketched in Fig. 3.b. One must therefore write that the total displacement $\delta\vec{r}_2$ is the sum of three elementary displacements and it is related to the gradients of both surface deformations $\vec{\nabla}h'_p$ and $\vec{\nabla}h'_c$, which yields

$$\vec{\nabla}h'_c = -\left(\frac{1}{h_2^*} - \frac{1}{H}\right)\delta\vec{r}_2 + \frac{1/h_2^* - 1/H}{1/h_3^* - 1/H}\vec{\nabla}h'_p, \quad (3)$$

where $h_2^* = (1 - n_{PDMS}/n_{air})(h_c + n_{air}/n_{glass} \cdot h_g)$ and $h_3^* = (1 - n_{air}/n_{PDMS})(h_p + n_{PDMS}/n_{air} \cdot h_c + n_{PDMS}/n_g \cdot h_g)$. Here, effects of the viewing angle θ are already accounted for by the term $\rightarrow \vec{\nabla}h'_p$ coming from eqn (2).

Calculating the shape of the channel roof therefore depends on the knowledge of the shape of the top PDMS surface, which we extract from the displacement field $\delta\vec{r}_1$, at the end of period 1. The numerical integration method provided by Moisy *et al.*¹⁵ is performed twice, first using eqn (2) to reconstruct the profile of the top PDMS surface h'_p , then on eqn (3) to reveal the channel's height profile h'_c , thereby reconstructing the complete geometry of the swollen microchannel.

The overall measurement accuracy and absolute error are a combination of system and DIC uncertainties, the latter being well documented in the literature for Particle Image Velocimetry.¹⁶ The interrogation windows were chosen so that the image of the patterned tape satisfies the criterion of 5 “dots” per interrogation window. The feature size is around 10 pixels, thus exceeding the optimal size of 2–3 pixels. Hence, DIC has an uncertainty of 5% approximately and induces an absolute error of 0.5 μm on the reconstructed height profile. Uncertainties in the experimental apparatus lie in the measurement of the effective heights (h_1^* , h_2^* , h_3^*) and in the estimation of the viewing angle θ_x . For the former, the glass slide and the microchannel have precise nominal heights and the PDMS block is measured for each channel with of precision of 0.1 mm. In addition, we measure a viewing angle $\theta_x = 9^\circ \pm 1^\circ$ for our setup. This leads to an overall accuracy estimated at 10%.

IV. Results

A. Characteristics of the diffusion and the dynamics of swelling

To characterize the amplitude of PDMS swelling by solvents, Lee *et al.*⁸ measured the swelling coefficient S_∞ for a number of organic solvents: this coefficient is defined as the ratio of the length L_∞ of a PDMS piece saturated by the solvent over its initial length L_0 before swelling. We conduct similar measurements for hexadecane, silicone V100 oil and paraffin oil. A thin square of PDMS (1 cm \times 1 cm \times 1 mm) is placed inside a Petri dish filled with the solvent of choice and is photographed during more than 12 h using a digital camera and a macro objective. On each image (3008 \times 2000 pixels, 1100 pixels/cm), the width $L(t)$ of the PDMS square is measured and compared to the reference value L_0 to yield the amplitude and dynamics of swelling.

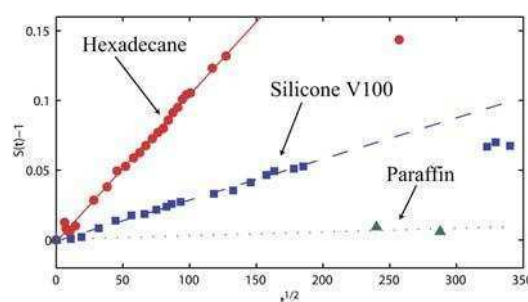


Fig. 4 Plots of the isotropic swelling coefficient $S(t)$ for hexadecane (●), silicone oil (■) and paraffin oil (▲) as a function of \sqrt{t} . The lines correspond to a linear fit before saturation.

The dynamics of swelling is linked to the absorption of the solvent into PDMS, which is a diffusive process, characterized by a diffusion coefficient D .¹⁷ Modeling solvent diffusion and the deformations induced by local swelling in a thin PDMS sheet shows that the length of the sheet $L(t)$ evolves as

$$\frac{L(t)}{L_0} - 1 = (S_\infty - 1) \frac{2}{d} \sqrt{\frac{Dt}{\pi}}, \quad (4)$$

where d is the thickness of the PDMS sheet (see ESI for the derivation of this equation†). Eqn (4), which is valid before saturation occurs, can be used to estimate the diffusion coefficient D .

Accordingly, the transient swelling ratio $S(t) = L(t)/L_0$ is plotted as a function of \sqrt{t} for hexadecane, silicone and paraffin oils in Fig. 4. The swelling coefficient at saturation S_∞ is evaluated from the steady state values of $S(t)$. Swelling is observed for hexadecane and silicone oil only. Next, the values of $[S(\sqrt{t}) - 1]$ are fitted with a linear law for early times. Fig. 4 shows a good agreement between the data points and the linear fit for both swelling oils, which validates the theoretical model used to compute eqn (4). Hence, the slope β of the fit can be used to evaluate the diffusion coefficient D of the solvent:

$$D = \pi \left(\frac{\beta d}{2(S_\infty - 1)} \right)^2. \quad (5)$$

The extracted values for S_∞ and D are listed in Table 1. They show good agreement with previous measurements for other carbon or silicone chains.^{8,18–20}

The diffusion coefficient D is useful to estimate the time τ necessary for the microchannel to reach its swollen steady state. It is reasonable to assume that the system locally reaches its equilibrium shape when the PDMS has swollen over a layer of

Table 1 Swelling coefficients S_∞ and diffusion constant D

	S_∞	$D/\text{m}^2 \text{ s}^{-1}$
PFD	1.00 ^a	none
Paraffin oil	1.00 \pm 0.01	none
Silicone V100	1.08 \pm 0.01	10 \pm 1 $\times 10^{-12}$
Hexadecane	1.14 \pm 0.01	44 \pm 4 $\times 10^{-12}$
n-Heptane	1.34 ^a	13–70 $\times 10^{-12}$ ^b

^a Extracted from ref. 8. ^b Extracted from ref. 20.

thickness comparable to that of the microchannel height h_c . This will occur over a time determined by the diffusion of oil into PDMS, $\tau \propto h_c^2/D$. For a 50 μm -deep microchannel swollen with hexadecane or silicone oil, τ is on the order of 5 min, which is very short compared to the duration of period 1. We may therefore assume that our measurements of the microchannel deformations correspond to the swollen steady state.

B. Microchannel deformations

We follow the experimental protocol of Section 2 and perform an experiment using hexadecane on a test section of width $w = 1$ mm. Eqn (2) is first integrated taking $\theta_x = 9^\circ$ to obtain the relative deformation of the top PDMS surface, which is shown in Fig. 5.b. This surface bends outwards away from the glass wall, with an amplitude of 10 μm above the microchannel. While these deformations are negligible for a PDMS block of thickness

$h_P \approx 4$ mm, they become significant when compared with the thickness of a second microchannel which may be stacked over the first one, for instance in multilayer microfluidic devices.²

Next, the height profile of the channel h'_c is computed using eqn (3) at the beginning of period 2. This is done by injecting the deformations h'_p , obtained at the end of period 1. The assumption that the top surface of the block has not significantly changed during the transition between the two periods is justified by noting that the pattern movements are small during this time lapse, as seen on the space–time plot of Fig. 2.b. The resulting swollen height profile h'_c is shown in Fig. 5.a. The roof of the test section is found to deform into the microchannel, displaying a transverse subsidence whose amplitude varies between 6 μm and 7 μm along the x -axis.

On the other hand, the narrow 100 μm -wide injection channel is not significantly deformed by swelling ($h'_c/h_c < 1\%$), while the subsidence rapidly increases with the channel width in the

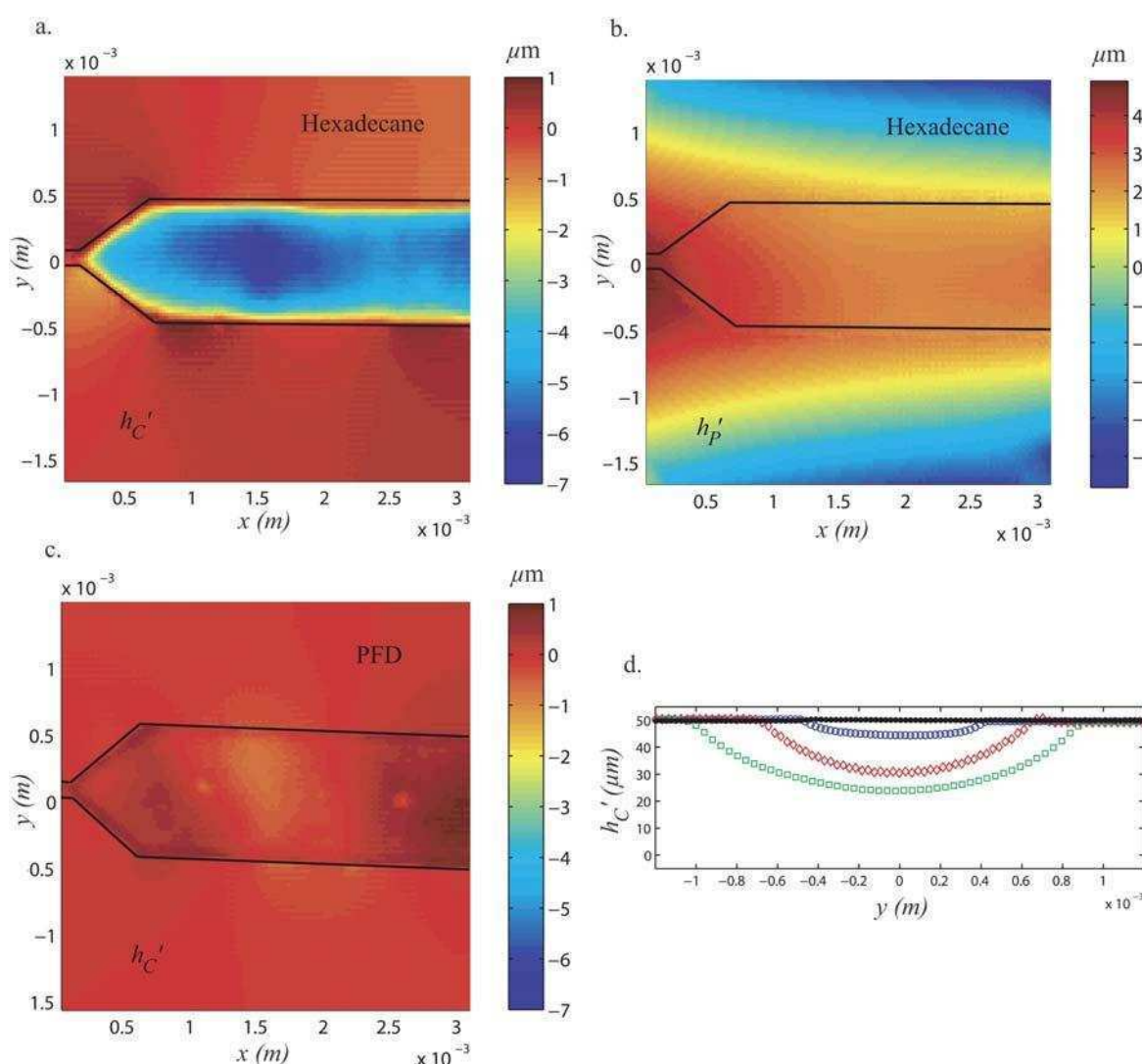


Fig. 5 Deformations of microchannels measured by the Synthetic Schlieren method. The position of the channel is outlined by solid lines. (a) Height profile h'_c of the roof of the test section swollen by hexadecane. (b) Height profile h'_p of the top surface of the PDMS block swollen by hexadecane. (c) Height profile h'_c the test section roof after PFD injection. (d) Transverse height profiles $h'_c(y)$ of the main test sections averaged along the x -axis for channels of widths 1 mm (\circ), 1.5 mm (\diamond) and 2 mm (\square) swollen by hexadecane, and for a channel of width 1 mm after PFD injection (\bullet).

diverging region, indicating that deformations are highly dependent on the channel's local aspect ratio $\alpha = w(x)/h_c$, in agreement with ref. 6.

To further investigate the influence of the channel's width, we perform experiments on test sections of width $w = 1.5$ mm and $w = 2$ mm. Again, we measure a subsidence of the channel roof, as seen on the height profiles (see ESI for figures†). The deformations for the three widths investigated are compared by averaging the subsidence along the length of the channel, in the x direction. The resulting profiles are plotted on Fig. 5.d and we observe that the amplitude of the deformations increases from $7\text{ }\mu\text{m}$ for $w = 1$ mm to $20\text{ }\mu\text{m}$ and $28\text{ }\mu\text{m}$ for $w = 1.5$ mm and $w = 2$ mm, respectively. In addition, an experiment on a 3 mm wide test section reveals that parts of the channel collapse, indicating that the deformations are larger than $50\text{ }\mu\text{m}$ for this width.

In contrast, the observed deformations are below the noise level of $0.5\text{ }\mu\text{m}$ when the experiments are performed using the non-swelling PFD, as shown on Fig. 5.c. This is further confirmed since the height variations that are observed are mostly located near the channel edges where the vertical walls blur the images and introduce further errors into the DIC analysis. The averaged height profile for this case is also plotted in Fig. 5.d, showing no discernible height variation along the y -axis. This control experiment confirms that the deformations measured using hexadecane are indeed due to the swelling of the PDMS block.

C. Effect of deformations on droplet trajectories

The effect of depth variations on the flow in a microchannel has already been studied in the case of single phase flows. Indeed, slight deformations in the channel geometries have been shown to significantly influence the flow within it, for instance in the production of three-dimensional flow profiles,²¹ in the amplification of the Taylor–Aris dispersion for pressure driven flows²² or in the modification of the pressure *vs.* flow rate relationship.⁷ Here, we observe the effect of the subsidence on the transport of droplets as they travel in the 1 mm wide test section. To this end, drops of water in oil are produced in a flow-focusing geometry⁹ which is operated in a regime to produce large drops. In this way, the drops are flattened when they flow through the test section and are thus sensitive to the height variations.

We chose silicone oil (swelling solvent) and paraffin oil (non-swelling) as the carrier fluids for the study of droplet dynamics because these oils enable controlled droplet formation and injection under identical hydrodynamic and capillary conditions. Indeed, the two liquids have similar viscosities ($\nu_{sil} = 100\text{ cP}$ and $\nu_{par} = 130\text{ cP}$) and interfacial tensions ($\gamma_{sil} = 0.25\text{ N m}^{-1}$ and $\gamma_{par} = 0.25\text{ N m}^{-1}$). Drops are made and transported by the two fluids while keeping the flow rates and droplet radii similar, as shown on Fig. 6.

If the test section's geometry is unperturbed, droplets are expected to follow straight trajectories along the channel's centerline as they would in a perfect Hele–Shaw cell.^{23,24} This behavior is indeed observed in Fig. 6.a which displays the trajectory of a water droplet in paraffin oil by superposing successive images of the droplet train. These drops follow the centerline of the channel and exit without feeling the presence of the side walls.

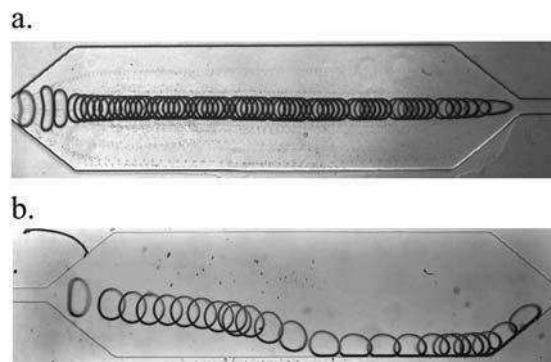


Fig. 6 Water droplets are advected from left to right along the large microchannel by a second carrier fluid. By superposing a few successive images taken using a high speed camera, the trajectories of the droplets are qualitatively visualized: (a) straight trajectory for paraffin oil ($Q = 1.1\text{ }\mu\text{L min}^{-1}$ and $R = 100\text{ }\mu\text{m}$). (b) bent trajectory with transverse migration toward the side wall for silicone V100 oil ($Q = 3.0\text{ }\mu\text{L min}^{-1}$ and $R = 130\text{ }\mu\text{m}$).

In contrast, drops carried by Silicone oil follow different trajectories, as shown in Fig. 6.b. These drops begin to deviate from the channel centerline as they enter the diverging section and they flow out of the test section along the side wall. Drops flowing at different flow rates make contact with the side walls at different locations, with faster drops advancing further before touching the sides. However, all drops deviate from the centerline before exiting the channel.

The physical reason for the trajectory modification can be understood in simple intuitive terms by considering the surface energy of the drop: Although the volume of each drop is fixed after its formation, its surface area varies as its shape changes. Recall that the smallest surface area for a drop of a given volume is given by a spherical shape, such that a flattened drop has an increased surface area and consequently an increased surface energy. By moving towards the side of the channel, where the subsidence is minimum, the drop minimizes its surface area by approaching a spherical shape. The migration of the drops towards the side walls therefore corresponds to a migration to the area of minimum confinement and minimum surface energy.

V. Summary and discussion

The synthetic Schlieren method developed to measure the deformations of PDMS microchannels only requires a low magnification microscope and adhesive tape. It is a simple and cost effective alternative to confocal or fluorescence microscopy with comparable resolution and precision. It is however limited to volatile liquids for two reasons. First, period 1 is excessively long for non-volatile liquids and the channel is not revealed in reasonable time. Second, the deformations of the microchannel are obtained at the beginning of period 2 when the liquid fully leaves the channel, and not when the channel is filled with the solvent at the end of period 1. The assumption that the roof of the channel has not deformed during this time is only valid if the transition period is short, which is the case for volatile liquids only.

The auxiliary experiment used to measure the swelling characteristics of a solvent into PDMS is easy to implement. Through an analysis of the time evolution of the PDMS sheet, this

experiment gives access to the swelling coefficient S_{∞} and also to the diffusion coefficient D of the oil, which is a key parameter in estimating the time necessary for establishment of a swollen steady state.

Finally, the swelling of PDMS by a solvent induces a subsidence of the microchannel. The amplitude of the deformations increases with the width of the channels, exceeding 50% of the channel's thickness for the widest channel measured here. This subsidence modifies the trajectories of pancake droplets and pushes them towards the sides of the wide test section, where the channel has a maximum depth. This behavior can be intuitively explained by energy arguments and a precise prediction of the trajectory based on such arguments is the subject of our current research.

Acknowledgements

The authors are grateful to Basile Audoly for help in deriving the model which leads to eqn (4) and Hervé Turlier for developing the microchannel geometry.

References

- 1 D. Duffy, J. McDonald, O. Schueller and G. Whitesides, *Anal. Chem.*, 1998, **70**, 4974–4984.
- 2 M. A. Unger, H. P. Chou, T. Thorsen, A. Scherer and S. R. Quake, *Science*, 2000, **288**, 113–116.
- 3 J. C. Lotters, W. Olthuis, P. H. Veltink and P. Bergveld, *J. Micromech. Microeng.*, 1997, **7**, 145–147.
- 4 C. Y. Hui, A. Jagota, Y. Y. Lin and E. J. Kramer, *Langmuir*, 2002, **18**, 1394–1407.
- 5 M. A. Holden, S. Kumar, A. Beskok and P. S. Cremer, *J. Micromech. Microeng.*, 2003, **13**, 412–418.
- 6 T. Gervais, J. El-Ali, A. Gunther and K. F. Jensen, *Lab Chip*, 2006, **6**, 500–507.
- 7 B. S. Hardy, K. Uechi, J. Zhen and H. P. Kavehpour, *Lab Chip*, 2009, **9**, 935–938.
- 8 J. Lee, C. Park and G. M. Whitesides, *Anal. Chem.*, 2003, **75**, 6544–6554.
- 9 S. L. Anna, N. Bontoux and H. A. Stone, *Appl. Phys. Lett.*, 2003, **82**, 364–366.
- 10 S. Vanapalli, A. Banpurkar, D. Ende, M. Duits and F. Mugele, *Lab Chip*, 2009, **9**, 982–990.
- 11 E. Young and C. Simmons, *Lab Chip*, 2010, **10**, 143–160.
- 12 F. Moisy, M. Rabaud and K. Salsac, *Exp. Fluids*, 2009, **46**, 1021–1036.
- 13 J. C. McDonald, D. C. Duffy, J. R. Anderson, C. D. T., H. Wu, O. J. A. Schueller and G. M. Whitesides, *Electrophoresis*, 2000, **21**, 27–40.
- 14 K. Stephan, P. Pittet, L. Renaud, P. Kleimann, P. Morin, N. Ouaini and R. Ferrigno, *J. Micromech. Microeng.*, 2007, **17**, N69–N74.
- 15 F. Moisy and M. Rabaud, *Free-Surface Synthetic Schlieren (FS-SS): a tutorial*, 2008.
- 16 M. Raffel, C. E. Willert, S. T. Wereley and J. Kompenhans, *Particle Image Velocimetry*, Springer, 1998.
- 17 E. Sultan and A. Boudaoud, *J. Appl. Mech.*, 2008, **75**, 051002.
- 18 E. Favre, P. Schaetzel, Q. Nguyen, R. Clement and J. Neel, *J. Membr. Sci.*, 1994, **92**, 169–184.
- 19 M. Chandak, Y. Lin, W. Ji and R. Higgins, *J. Appl. Polym. Sci.*, 1998, **67**, 165–175.
- 20 C. Zhao, J. Li, Z. Jiang and C. Chen, *Eur. Polym. J.*, 2006, **42**, 615–624.
- 21 E. Lauga, A. Stroock and H. Stone, *Phys. Fluids*, 2004, **16**, 3051–3062.
- 22 D. Dutta, A. Ramachandran and D. T. Leighton, *Microfluid. Nanofluid.*, 2006, **2**, 275–290.
- 23 G. I. Taylor and T. G. Saffman, *Q. J. Mech. Appl. Math.*, 1959, **12**, 265–279.
- 24 A. R. Kopf-Sill and G. Homsy, *Phys. Fluids*, 1988, **31**, 18–26.

Supplementary Information

for

Microchannel deformations due to solvent-induced PDMS swelling

Rémi Dangla

LadHyX and department of Mechanics, Ecole Polytechnique, CNRS 91128 Palaiseau Cedex, France

François Gallaire

*Institut de Génie Mécanique, Faculté des Sciences et Techniques de l'Ingénieur,
Ecole Polytechnique Fédérale de Lausanne, Switzerland*

Charles N. Baroud*

LadHyX and department of Mechanics, Ecole Polytechnique, CNRS 91128 Palaiseau Cedex, France

(Dated: May 21, 2010)

*baroud@ladhyx.polytechnique.fr

I. TRANSIENT EXPANSION OF A SWELLING PDMS SHEET

Here, we detail the calculations for determining the swelling characteristics of a solvent from the deformations it induces on a PDMS sheet. The swelling coefficient S_∞ and the diffusion coefficient D are obtained by comparing the observed time evolution of the length $L(t)$ of a PDMS sheet immersed in a bath of the solvent to a theoretical model. It is closely related to the method of sorption mass measurements described by J. Crank [1], which relies on the time evolution of the mass of the sheet. The method requires a precise prediction of the transient swelling geometry of the polymer sheet. To this end, we solve the coupled problems of solvent diffusion and induced mechanical strain. First, we compute the diffusion of the swelling solvent in the initial geometry, which we then deform by evaluating the local swelling expansion.

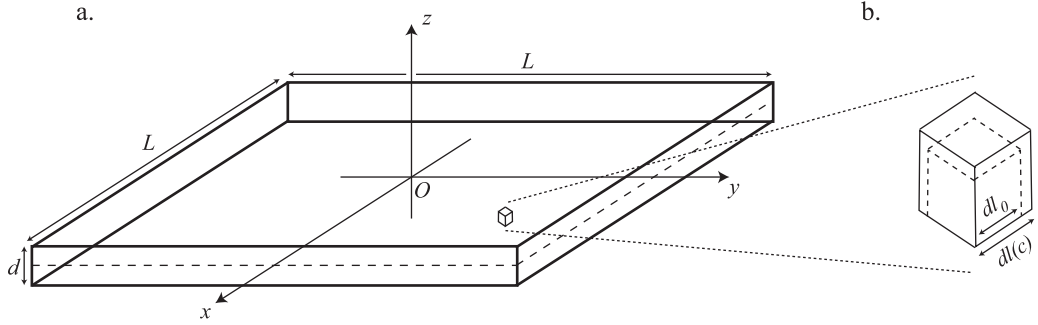


FIG. 1. **a.** Sketch of the thin square PDMS sheet and definition of the reference frame $(Oxyz)$. **b.** Illustration of the local swelling expansion of a stress-free infinitesimal cube due to a solvent concentration c .

In the following derivations, we consider a square plane sheet of height d small compared to its width L ($d \ll L$). The center O of the coordinate system is taken as the center of symmetry of the sheet. The (x, y) -directions are along then in-plane directions while the z -direction is along the transverse direction, as sketched on Fig. 1.a.

A. Solvent diffusion and local swelling ratio s

The diffusion process of the solvent is characterized by a concentration at saturation c_∞ and a diffusion coefficient D . In this model, we assume that D is independent of the solvent concentration, such that $c(\vec{x}, t)$ verifies the classical diffusion equation with saturated boundary conditions

$$\frac{\partial c}{\partial t} = D_s \vec{\nabla}^2 c(\vec{x}, t) \text{ in } \Omega, \quad c = c_\infty \text{ on } \partial\Omega, \quad (1)$$

where Ω and $\partial\Omega$ are the inner volume and the boundaries of the sheet, respectively.

The local swelling induced by the solvent is quantified through the local swelling ratio $s(\vec{x}, t)$. It is defined as the ratio between the size $dl(c)$ of a stress-free, infinitesimal cube at the concentration $c(\vec{x}, t)$ over its dry size dl_0 (see Fig. 1.b).

Next, we make an analogy with linear thermoelasticity. In the same way that thermal strain is assumed to be proportional to the temperature field T [2], we make the assumption that the local swelling ratio $s(\vec{x}, t)$ varies linearly with the concentration field of the solvent $c(\vec{x}, t)$. In addition, it saturates at S_∞ , yielding

$$s(\vec{x}, t) - 1 = \frac{c(\vec{x}, t)}{c_\infty} (S_\infty - 1). \quad (2)$$

Therefore, the swelling ratio $s(\vec{x}, t)$ also verifies the classical diffusion equation with saturated boundary conditions :

$$\frac{\partial s(\vec{x}, t)}{\partial t} = D \vec{\nabla}^2 s(\vec{x}, t) \text{ in } \Omega, \quad s = S_\infty \text{ on } \partial\Omega. \quad (3)$$

For a thin plane sheet, there is a scale separation between in-plane (x, y) and transverse z coordinates. This allows us to model the diffusion process as a one dimensional problem in the transverse direction and to treat the

concentration field as a function of z and t only. In this case, the solutions for equations (1) and (3) can be found in textbooks [1]. They are

$$\begin{aligned} \frac{c(z, t)}{c_\infty} &= 1 - \frac{4}{\pi} \sum_{n=0}^{\infty} \frac{(-1)^n}{2n+1} \cos \frac{(2n+1)\pi z}{d} \exp \left(-\frac{D(2n+1)^2 \pi^2 t}{d^2} \right), \\ \frac{s(z, t) - 1}{S_\infty - 1} &= 1 - \frac{4}{\pi} \sum_{n=0}^{\infty} \frac{(-1)^n}{2n+1} \cos \frac{(2n+1)\pi z}{d} \exp \left(-\frac{D(2n+1)^2 \pi^2 t}{d^2} \right). \end{aligned} \quad (4)$$

Plots of this concentration field $c(z, t)$ are shown on Fig. 2.a for different values of time t .

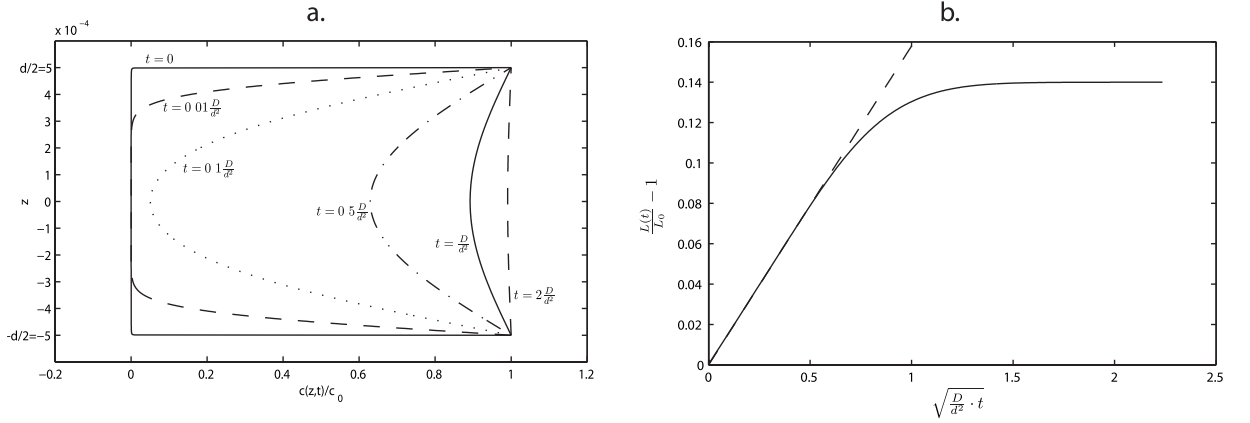


FIG. 2. **a.** Concentration profiles $c(z, t)$ plotted using equation (4) for different times $t = [0, 0.01, 0.1, 0.5, 1, 2] \cdot D/d^2$. **b.** Plots of the overall strain $L(t)/L_0 - 1$ for $S_\infty = 1.14$ as a function of $\sqrt{d^2 \cdot t/D}$, the square root of the nondimensional time: using the exact solution from equation (15) (solid line) and using the initial time approximation from equation (16) (dashed line).

B. The swollen geometry

To estimate the transient swelling geometry, we recall the analogy with linear thermoelasticity and rely on the classical models that relate a given strain to mechanical stresses [2]. In our case, the concentration profile $c(z, t)$ imposed by diffusion induces a local swelling ratio $s(\vec{x}, t)$, which can be expressed as a swelling strain : $\underline{\underline{\epsilon}}^s = (s(z, t) - 1)\underline{\underline{\mathbb{I}}}$. This strain tensor is not geometrically compatible: there does not exist any physical displacement field $\vec{\xi}(\vec{x}, t)$ that creates such a strain. In particular, it violates the second compatibility equation

$$\frac{\partial^2 \epsilon_{yy}^s}{\partial z^2} + \frac{\partial^2 \epsilon_{zz}^s}{\partial y^2} \neq 2 \frac{\partial^2 \epsilon_{yz}^s}{\partial y \partial z}. \quad (5)$$

As a result, the observed strain $\underline{\underline{\epsilon}}$ has to be different from the natural swelling strain $\underline{\underline{\epsilon}}^s$ and it induces internal mechanical stresses $\underline{\underline{\sigma}}$ according to the Hook relation [2]:

$$\underline{\underline{\sigma}} = 2\mu(\underline{\underline{\epsilon}} - \underline{\underline{\epsilon}}^s) + \lambda Tr(\underline{\underline{\epsilon}} - \underline{\underline{\epsilon}}^s)\underline{\underline{\mathbb{I}}}. \quad (6)$$

We recall the thin sheet limit ($d \ll L$) to assume problem invariance in the (x, y) plane. When used along with the compatibility equations, this limits the strain tensor to the form

$$\underline{\underline{\epsilon}} = \begin{pmatrix} \gamma(t) & 0 & 0 \\ 0 & \gamma(t) & 0 \\ 0 & 0 & f(z, t) \end{pmatrix}, \quad (7)$$

where $\gamma(t)$ and $f(z, t)$ are the unknowns to be determined.

Plugging this strain into equation (6), the stress tensor becomes

$$\begin{aligned}\sigma_{xx} &= \sigma_{yy} = 2\mu[\gamma(t) - (s(z, t) - 1)] + \lambda[2(\gamma(t) - (s(z, t) - 1)) + (f(z, t) - (s(z, t) - 1))] , \\ \sigma_{zz} &= 2\mu[f(z, t) - (s(z, t) - 1)] + \lambda[2(\gamma(t) - (s(z, t) - 1)) + (f(z, t) - (s(z, t) - 1))]\end{aligned}\quad (8)$$

and shear components are zero.

At this point, we assume that the solid responds instantaneously to the variations of swelling strain induced by the diffusion process. Hence, the stress tensor must verify the equation of statics $\vec{\text{div}} \underline{\underline{\sigma}} = 0$ with unconstrained boundary conditions. This yields

$$\begin{aligned}\langle \sigma_{xx} \rangle_z &= \langle \sigma_{yy} \rangle_z = 0 , \\ \sigma_{zz} &= 0 , \forall z ,\end{aligned}\quad (9)$$

where the $\langle \cdot \rangle_z$ operator is the mean in the z -direction. At each time t , these equations lead to a coupled linear system in terms of $f(z)$ and γ

$$\begin{aligned}2(\lambda + \mu)(\gamma - \langle s - 1 \rangle_z) + \lambda(\langle f \rangle_z - \langle s - 1 \rangle_z) &= 0 , \\ (2\mu + \lambda)(f(z) - (s - 1)) + 2\lambda(\gamma - (s - 1)) &= 0 ,\end{aligned}\quad (10)$$

which has a unique set of solutions

$$\begin{aligned}\gamma(t) &= \langle s(z, t) - 1 \rangle_z , \\ f(z, t) &= \frac{3\lambda + 2\mu}{\lambda + 2\mu} (s(z, t) - 1) - \frac{2\lambda}{2\lambda + \mu} \langle s(z, t) - 1 \rangle_z .\end{aligned}\quad (11)$$

These results can be further simplified in the case of PDMS because it is a nearly incompressible elastic solid, i.e. a material for which $\mu \ll \lambda$. Hence, the observed deformation is

$$\begin{aligned}\xi_x(x, y, z, t) &= \langle s(z, t) - 1 \rangle_z \cdot x , \\ \xi_y(x, y, z, t) &= \langle s(z, t) - 1 \rangle_z \cdot y , \\ \xi_z(x, y, z, t) &= 3 \int_0^z (s(z, t) - 1) dz - 2 \langle s(z, t) - 1 \rangle_z \cdot z .\end{aligned}\quad (12)$$

In practice, the measurable quantities in an experiment are the overall thickness $d(t)$ and length $L(t)$ of the sheet. They are

$$\begin{aligned}d(t) &= d_0 + 2\xi_z(d_0/2, t) = \langle s(z, t) \rangle_z \cdot d_0 , \\ L(t) &= L_0 + 2\xi_x(L_0/2, t) = \langle s(z, t) \rangle_z \cdot L_0 .\end{aligned}\quad (13)$$

In the end, we find that the inhomogeneous swelling strain $s(z, t) - 1$ induces a homothetic transformation on the overall geometry of the swollen sheet: the length and thickness evolve as if the sheet is homogeneously swollen by the solvent at a concentration $\langle c(z, t) \rangle_z$. Thereby, the overall length of a square swelling sheet is unambiguously defined by

$$\frac{L(t)}{L_0} = \langle s(z, t) \rangle_z . \quad (14)$$

C. Combining diffusion and deformations

The swelling ratio $s(z, t)$ is given by the diffusion of a swelling solvent into the immersed sheet. Therefore, the transient length of the swelling sheet $L(t)$ is found by combining the main results from the two previous subsection, in Eq. (4) and Eq. (14), to yield

$$\frac{L(t)}{L_0} - 1 = (S_\infty - 1) \cdot \left(1 - \frac{4}{\pi^2} \sum_{n=0}^{\infty} \frac{1}{(2n+1)^2} \exp\left(-\frac{D(2n+1)^2 \pi^2 t}{d^2}\right) \right) . \quad (15)$$

For initial times, this expression simplifies [1] to

$$\frac{L(t)}{L_0} - 1 = (S_\infty - 1) \frac{2}{d} \sqrt{\frac{Dt}{\pi}} . \quad (16)$$

A comparative plot between the full solution (15) and the initial time approximation (16) is shown on Fig. 2.b, revealing a good agreement until $t \approx d^2/D$.

II. HEIGHT PROFILES FOR CHANNELS OF VARIOUS WIDTH

- [1] J. Crank, *The Mathematics of Diffusion*, Oxford Science Publications, 1975.
- [2] R. B. Hetnarski and M. R. Eslami, *Thermal Stresses - Advanced Theory and Applications*, Springer, 2008.

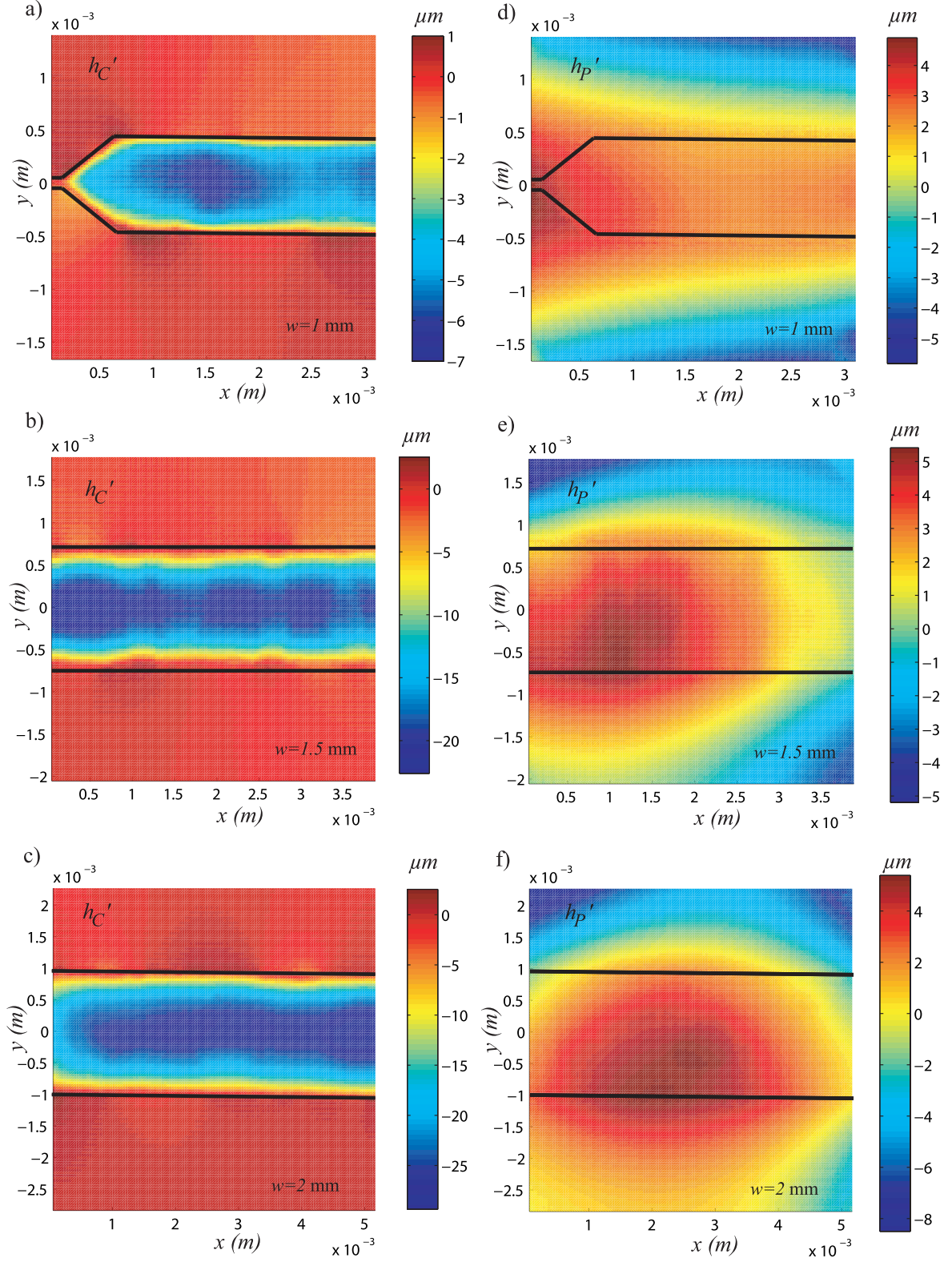


FIG. 3. Deformations of microchannels measured by the Synthetic Schlieren method. The position of the channel is outlined by solid lines. a-c) Height profiles h'_C of the roof of the test section swollen by hexadecane for channels of width 1 mm, 1.5 mm and 2 mm respectively. d-f) Height profiles h'_P of the top surface of the PDMS block swollen by hexadecane for the same channels of width 1 mm, 1.5 mm and 2 mm respectively.

Bibliography

- [1] R.A. Millikan. On the elementary electrical charge and the avogadro constant. *Physical Review*, 2(2):109–143, 1913.
- [2] The nobel prize in physics.
- [3] J. Lederberg. A simple method for isolating individual microbes. *Journal of bacteriology*, 68(2):258, 1954.
- [4] B. Rotman. Measurement of activity of single molecules of β -d-galactosidase. *Proceedings of the National Academy of Sciences*, 47(12):1981–1991, 1961.
- [5] A. Theberge, F. Courtois, Y. Schaerli, M. Fischlechner, C. Abell, F. Hollfelder, and W. Huck. Microdroplets in microfluidics: An evolving platform for discoveries in chemistry and biology. *Angewandte Chemie International Edition*, 49:5846–5868, 2010.
- [6] D.C. Duffy, J.C. McDonald, O.J.A. Schueller, and G.M. Whitesides. Rapid prototyping of microfluidic systems in poly(dimethylsiloxane). *Anal. Chem.*, 70:4974–4984, 1998.
- [7] J. C. McDonald, D. C. Duffy, J. R. Anderson, Chiu D. T., H. Wu, O. J. A. Schueller, and G. M. Whitesides. Fabrication of microfluidic systems in poly(dymethylsiloxane). *Electrophoresis*, 21:27–40, 2000.
- [8] T. Thorsen, R.W. Roberts, F.H. Arnold, and S.R. Quake. Dynamic pattern formation in a vesicle-generating microfluidic device. *Physical Review Letters*, 86(18):4163–4166, 2001.
- [9] S.L. Anna, N. Bontoux, and H.A. Stone. Formation of dispersions using “flow focusing” in microchannels. *Applied Physics Letters*, 82:364, 2003.
- [10] P. Calvert. Inkjet printing for materials and devices. *Chemistry of Materials*, 13(10):3299–3305, 2001.
- [11] S.M. Joscelyne and G. Trägårdh. Membrane emulsification - a literature review. *Journal of Membrane Science*, 169(1):107–117, 2000.

- [12] C.N. Baroud, F. Gallaire, and R. Dangla. Dynamics of microfluidic droplets. *Lab Chip*, 10(16):2032–2045, 2010.
- [13] H. Song, J.D. Tice, and R.F. Ismagilov. A microfluidic system for controlling reaction networks in time. *Angewandte Chemie*, 115(7):792–796, 2003.
- [14] H. Song, D.L. Chen, and R.F. Ismagilov. Reactions in droplets in microfluidic channels. *Angew. Chemie, int. ed.*, 45:7336–7356, 2006.
- [15] E. Brouzes, M. Medkova, N. Savenelli, D. Marran, M. Twardowski, J.B. Hutchison, J.M. Rothberg, D.R. Link, N. Perrimon, and M.L. Samuels. Droplet microfluidic technology for single-cell high-throughput screening. *Proc. Nat. Acad. Sci.*, 106(34):14195, 2009.
- [16] K. Churski, P. Korczyk, and P. Garstecki. High-throughput automated droplet microfluidic system for screening of reaction conditions. *Lab Chip*, 10(7):816–818, 2010.
- [17] H.C. Zec, T.D. Rane, and J.T.H. Wang. Microfluidic platform for on-demand generation of spatially indexed combinatorial droplets. *Lab on a Chip*, in press, 2012.
- [18] SY Teh, R. Lin, LH Hung, and AP Lee. Droplet microfluidics. *Lab Chip*, 8(2):198–220, 2008.
- [19] K.W. Oh, K. Lee, B. Ahn, and E.P. Furlani. Design of pressure-driven microfluidic networks using electric circuit analogy. *Lab Chip*, 12(3):515–545, 2012.
- [20] N. Champagne, R. Vasseur, A. Montourcy, and D. Bartolo. Traffic jams and intermittent flows in microfluidic networks. *Physical review letters*, 105(4):44502, 2010.
- [21] H.N. Joensson, M.L. Samuels, E.R. Brouzes, M. Medkova, M. Uhlén, D.R. Link, and H. Andersson-Svahn. Detection and analysis of low-abundance cell-surface biomarkers using enzymatic amplification in microfluidic droplets. *Angewandte Chemie*, 121(14):2556–2559, 2009.
- [22] E. Farkas. Microtitrations in serology and virology. *Current Contents Citation Classic*, (30), 1992.
- [23] BioPioneer Inc.
- [24] K. Piroird. *Dynamiques spéciales de gouttes non-mouillantes*. PhD thesis, Ecole Polytechnique, 2011.
- [25] M. A. Unger, H. P. Chou, T. Thorsen, A. Scherer, and S. R. Quake. Monolithic microfabricated valves and pumps by multilayer soft lithography. *Science*, 288:113–116, 2000.
- [26] T. Thorsen, S.J. Maerkl, and S.R. Quake. Microfluidic large-scale integration. *Science*, 298(5593):580–584, 2002.

- [27] Y. Bourquin, J. Reboud, R. Wilson, and J.M. Cooper. Tuneable surface acoustic waves for fluid and particle manipulations on disposable chips. *Lab on a Chip*, 10(15):1898–1901, 2010.
- [28] HS Hele-Shaw. Flow of water. *Nature*, 58(1509):520–520, 1898.
- [29] M.G. Pollack, R.B. Fair, and A.D. Shenderov. Electrowetting-based actuation of liquid droplets for microfluidic applications. *Applied Physics Letters*, 77:1725, 2000.
- [30] J. Lee, H. Moon, J. Fowler, T. Schoellhammer, and C.J. Kim. Electrowetting and electrowetting-on-dielectric for microscale liquid handling. *Sensors and Actuators A: Physical*, 95(2):259–268, 2002.
- [31] M.J. Jebrail, M.S. Bartsch, and K.D. Patel. Digital microfluidics: A versatile tool for applications in chemistry, biology and medicine. *Lab Chip*, 2012.
- [32] H. Morgan, B. Hadwen, G. Broder, D. Morganti, A. Jacobs, C. Brown, Y. Kubota, and J. Hector. Programmable large area digital microfluidic array with integrated droplet sensing for bioassays. *Lab on a Chip*, 2012.
- [33] A. Huebner, D. Bratton, G. Whyte, M. Yang, A.J. deMello, C. Abell, and F. Hollfelder. Static microdroplet arrays: a microfluidic device for droplet trapping, incubation and release for enzymatic and cell-based assays. *Lab Chip*, 9(5):692–698, 2009.
- [34] Y. Bai, X. He, D. Liu, S.N. Patil, D. Bratton, A. Huebner, F. Hollfelder, C. Abell, and W.T.S. Huck. A double droplet trap system for studying mass transport across a droplet-droplet interface. *Lab on a Chip*, 10(10):1281–1285, 2010.
- [35] M.L. Cordero, D.R. Burnham, C.N. Baroud, and D. McGloin. Thermocapillary manipulation of droplets using holographic beam shaping: Microfluidic pin ball. *Applied Physics Letters*, 93:034107, 2008.
- [36] E. Verneuil, M.L. Cordero, F. Gallaire, and C.N. Baroud. Laser-induced force on a microfluidic drop: Origin and magnitude. *Langmuir*, 25(9):5127–5134, 2009.
- [37] M.L. Cordero, H.O. Rolfsnes, D.R. Burnham, P.A. Campbell, D. McGloin, and C.N. Baroud. Mixing via thermocapillary generation of flow patterns inside a microfluidic drop. *New Journal of Physics*, 11:075033, 2009.
- [38] F. Hauksbee. An account of an experiment touching the direction of a drop of oil of oranges, between two glass planes, towards any side of them that is nearest press’d together. *Royal Society of London Philosophical Transactions Series I*, 27:395–396, 1710.

- [39] G. I. Taylor and T. G. Saffman. A note on the motion of bubbles in Hele-Shaw cell and porous medium. *Quarterly Journal of Mechanics and Applied Mathematics*, 12:265–279, 1959.
- [40] I. Newton. *Opticks: or a treatise of the reflections, refractions, inflections & colours of light*. Dover Pubns, 1979.
- [41] J.C. Maxwell. Capillary action. *Encyclopaedia Britannica*, 5:256–275, 1876.
- [42] G. Monge. *Mémoire sur quelques effets d’attraction ou de répulsion apparente entre les molécules de matière*. De l’Imprimerie Royale, 1787.
- [43] P.G. de Gennes, F. Brochard-Wyart, D. Quéré, M. Fermigier, and C. Clanet. *Gouttes, bulles, perles et ondes*. Belin Paris, 2002.
- [44] W. Wick. *A drop of water: A book of science and wonder*. Scholastic, 1997.
- [45] P.S. Laplace. *Traité de mécanique céleste; supplément au dixième livre, sur l’action capillaire*. 1806.
- [46] G.K. Batchelor. *An introduction to fluid dynamics*. Cambridge Univ Pr, 1967.
- [47] T. Young. An essay on the cohesion of fluids. *Philosophical Transactions of the Royal Society of London*, 95:65–87, 1805.
- [48] L. Feng, S. Li, Y. Li, H. Li, L. Zhang, J. Zhai, Y. Song, B. Liu, L. Jiang, and D. Zhu. Super-hydrophobic surfaces: From natural to artificial. *Advanced materials*, 14(24):1857–1860, 2002.
- [49] J. Jurin. An account of some experiments shown before the royal society; with an enquiry into the cause of the ascent and suspension of water in capillary tubes. by james jurin, md and r. soc. s. *Philosophical Transactions*, 30(351-363):739–747, 1717.
- [50] C. Gay, P. Rognon, D. Reinelt, and F. Molino. Rapid plateau border size variations expected in three simple experiments on 2d liquid foams? *The European Physical Journal E: Soft Matter and Biological Physics*, 34(1):1–11, 2011.
- [51] C.W. Park and GM Homsy. Two-phase displacement in Hele-Shaw cells: theory. *Journal of Fluid Mechanics*, 139:291–308, 1984.
- [52] C. Delaunay. Sur la surface de revolution dont la courbure moyenne est constante. *J. Math. Pures Appl*, 6(1841):309–315, 1841.
- [53] S.D. Poisson. Nouvelle théorie de l’action capillaire. *Annalen der Physik*, 101(6):270–287, 1832.
- [54] H. Bouasse. *Capillarité: phénomènes superficiels*. Delagrave, 1924.

- [55] P. Renvoisé, JWM Bush, M. Prakash, and D. Quéré. Drop propulsion in tapered tubes. *EPL (Europhysics Letters)*, 86:64003, 2009.
- [56] E. Lorenceau and D. Quere. Drops on a conical wire. *Journal of Fluid Mechanics*, 510:29–45, 2004.
- [57] M. Prakash, D. Quéré, and J.W.M. Bush. Surface tension transport of prey by feeding shorebirds: the capillary ratchet. *science*, 320(5878):931–934, 2008.
- [58] Y. Zheng, H. Bai, Z. Huang, X. Tian, F.Q. Nie, Y. Zhao, J. Zhai, and L. Jiang. Directional water collection on wetted spider silk. *Nature*, 463(7281):640–643, 2010.
- [59] M.A. Rubega and B.S. Obst. Surface-tension feeding in phalaropes: discovery of a novel feeding mechanism. *The Auk*, pages 169–178, 1993.
- [60] C.F. Gauss. *Principia generalia theoriae figurae fluidorum in statu aequilibrii*. Dieterich, 1830.
- [61] C.F. Gauss and H. Weber. *Allgemeine grundlagen einer theorie der gestalt von flüssigkeiten im zustand des gleichgewichts*. Number 135. W. Engelmann, 1903.
- [62] BV Derjaguin and NV Churaev. Structural component of disjoining pressure. *Journal of Colloid and Interface Science*, 49(2):249–255, 1974.
- [63] N.D. Denkov, V. Subramanian, D. Gurovich, and A. Lips. Wall slip and viscous dissipation in sheared foams: Effect of surface mobility. *Colloids and Surfaces A: Physicochemical and Engineering Aspects*, 263(1):129–145, 2005.
- [64] H. Wong, S. Morris, and CJ Radke. Three-dimensional menisci in polygonal capillaries. *Journal of Colloid and Interface Science*, 148(2):317–336, 1992.
- [65] J.L. Basdevant. *Le principe de moindre action et les principes variationnels en physique*. Vuibert, 2010.
- [66] R.P. Feynman, R.B. Leighton, and M. Sands. *The Feynman Lectures on Physics, Vol. I*, volume 26. 1961.
- [67] R. Feynmam, R. Leighton, and M. Sands. *The Feynman Lectures on Physics, vol. 2*, volume 19. 1977.
- [68] H. von Helmholtz. Zur theorie der stationären ströme in reibenden flüssigkeiten. *Verh. Naturh.-Med. Ver. Heidelb*, 11, 1868.
- [69] B.J.W.S. Rayleigh. *The theory of sound*, volume 2. Macmillan, 1896.
- [70] L. Onsager. Reciprocal relations in irreversible processes. i. *Physical Review*, 37(4):405, 1931.

- [71] L. Onsager and S. Machlup. Fluctuations and irreversible processes. *Physical Review*, 91(6):1505–1512, 1953.
- [72] KB Glasner. Variational models for moving contact lines and the quasi-static approximation. *European Journal of Applied Mathematics*, 16(6):713–740, 2005.
- [73] GI Taylor. The formation of emulsions in definable fields of flow. *Proceedings of the Royal Society of London. Series A, Containing Papers of a Mathematical and Physical Character*, 146(858):501–523, 1934.
- [74] S. Manservigi and R. Scardovelli. A variational approach to the contact angle dynamics of spreading droplets. *Computers & Fluids*, 38(2):406–424, 2009.
- [75] P.G. Saffman and G. Taylor. The penetration of a fluid into a porous medium or Hele-Shaw cell containing a more viscous liquid. *Proceedings of the Royal Society of London. Series A. Mathematical and Physical Sciences*, 245(1242):312–329, 1958.
- [76] PG Saffman. Viscous fingering in Hele-Shaw cells. *Journal of Fluid Mechanics*, 173:73–94, 1986.
- [77] S. Tanveer. Analytic theory for the determination of velocity and stability of bubbles in a Hele-Shaw cell. *Theoretical and Computational Fluid Dynamics*, 1(3):135–163, 1989.
- [78] E. Meiburg. Bubbles in a Hele-Shaw cell: Numerical simulation of three-dimensional effects. *Physics of Fluids A: Fluid Dynamics*, 1:938, 1989.
- [79] AP Aldushin and BJ Matkowsky. Extremum principles for selection in the saffman–taylor finger and taylor–saffman bubble problems. *Physics of Fluids*, 11:1287, 1999.
- [80] Eric Weisstein. Tree. From MathWorld—A Wolfram Web Resource.
- [81] L.M. Milne-Thomson. *Theoretical hydrodynamics*. Dover Pubns, 1996.
- [82] M. Porez. *Modèle dynamique analytique de la nage tridimensionnelle anguilliforme pour la robotique*. PhD thesis, Université de Nantes, 2007.
- [83] T. Maxworthy. Bubble formation, motion and interaction in a Hele-Shaw cell. *Journal of Fluid Mechanics*, 173:95–114, 1986.
- [84] A. R. Kopf-Sill and G.M. Homsy. Bubble motion in a Hele-Shaw cell. *Physics of Fluids*, 31:18–26, 1988.
- [85] D. Rabaud, P. Thibault, J.P. Raven, O. Hugon, E. Lacot, and P. Marmottant. Manipulation of confined bubbles in a thin microchannel: Drag and acoustic bjerknes forces. *Physics of Fluids*, 23:042003, 2011.

-
- [86] FP Bretherton. The motion of long bubbles in tubes. *Journal of Fluid Mechanics*, 10(02):166–188, 1961.
- [87] LH Tanner. The spreading of silicone oil drops on horizontal surfaces. *Journal of Physics D: Applied Physics*, 12:1473, 1979.
- [88] D. Burgess and MR Foster. Analysis of the boundary conditions for a Hele-Shaw bubble. *Physics of Fluids A: Fluid Dynamics*, 2:1105, 1990.
- [89] SRK Maruvada and C.W. Park. Retarded motion of bubbles in Hele-Shaw cells. *Physics of Fluids*, 8:3229, 1996.
- [90] V.G. Levich and D.B. Spalding. *Physicochemical hydrodynamics*, volume 689. Prentice-Hall Englewood Cliffs, NJ, 1962.
- [91] K.J. Stebe, S.Y. Lin, and C. Maldarelli. Remobilizing surfactant retarded fluid particle interfaces. i. stress-free conditions at the interfaces of micellar solutions of surfactants with fast sorption kinetics. *Physics of Fluids A: Fluid Dynamics*, 3:3, 1991.
- [92] JS Lee and YC Fung. Stokes flow around a circular cylindrical post confined between two parallel plates. *J. Fluid Mech*, 37(657-670):16, 1969.
- [93] J. Lee, M. J. Kim, and H. H. Lee. Surface modification of poly(dymethylsiloxane) for retarding swelling in organic solvents. *Langmuir*, 22:2090–2095, 2005.
- [94] F. Moisy, M. Rabaud, and K. Salsac. A synthetic schlieren method for the measurement of the topography of a liquid interface. *Experimental Fluids*, 46:1021–1036, 2009.
- [95] R. Dangla, F. Gallaire, and C.N. Baroud. Microchannel deformations due to solvent-induced pdms swelling. *Lab Chip*, 10(21):2972–2978, 2010.
- [96] François Gallaire, Patrice Laure, and Charles N. Baroud. Marangoni induced force on a drop in a microchannel. *To be published*, 3000+.
- [97] C.W. Park, SRK Maruvada, and D.Y. Yoon. The influence of surfactant on the bubble motion in Hele-Shaw cells. *Physics of Fluids*, 6:3267, 1994.
- [98] F. Fairbrother and A.E. Stubbs. 119. studies in electro-endosmosis. part vi. the bubble-tube method of measurement. *J. Chem. Soc.*, (0):527–529, 1935.
- [99] J.W.M. Bush. The anomalous wake accompanying bubbles rising in a thin gap: a mechanically forced marangoni flow. *Journal of Fluid Mechanics*, 352(1):283–303, 1997.

- [100] LW Schwartz and HM Princen. A theory of extensional viscosity for flowing foams and concentrated emulsions. *Journal of colloid and interface science*, 118(1):201–211, 1987.
- [101] D.M. Campana, S. Ubal, M.D. Giavedoni, and F.A. Saita. Numerical prediction of the film thickening due to surfactants in the landau–levich problem. *Physics of Fluids*, 22:032103, 2010.
- [102] B. Scheid, J. Delacotte, B. Dollet, E. Rio, F. Restagno, EA Van Nierop, I. Cantat, D. Langevin, and HA Stone. The role of surface rheology in liquid film formation. *EPL (Europhysics Letters)*, 90:24002, 2010.
- [103] Review article to be published.
- [104] W. Engl, M. Roche, A. Colin, P. Panizza, and A. Ajdari. Droplet traffic at a simple junction at low capillary numbers. *Physical review letters*, 95(20):208304, 2005.
- [105] T. Glawdel, C. Elbuken, and C. Ren. Passive droplet trafficking at microfluidic junctions under geometric and flow asymmetries. *Lab Chip*, 11(22):3774–3784, 2011.
- [106] K. Ahn, C. Kerbage, T.P. Hunt, RM Westervelt, D.R. Link, and DA Weitz. Dielectrophoretic manipulation of drops for high-speed microfluidic sorting devices. *Applied Physics Letters*, 88:024104, 2006.
- [107] N.O. Young, J.S. Goldstein, and M.J. Block. The motion of bubbles in a vertical temperature gradient. *Journal of Fluid Mechanics*, 6(03):350–356, 1959.
- [108] Y.K. Bratukhin and AL Zuev. Thermocapillary drift of an air bubble in a horizontal Hele-Shaw cell. *Fluid Dynamics*, 19(3):393–398, 1984.
- [109] B. Selva, V. Miralles, I. Cantat, and M.C. Jullien. Thermocapillary actuation by optimized resistor pattern: bubbles and droplets displacing, switching and trapping. *Lab Chip*, 10(14):1835–1840, 2010.
- [110] B. Selva, I. Cantat, and M.C. Jullien. Temperature-induced migration of a bubble in a soft microcavity. *Physics of Fluids*, 23:052002, 2011.
- [111] W.H. Tan and S. Takeuchi. A trap-and-release integrated microfluidic system for dynamic microarray applications. *Proceedings of the National Academy of Sciences*, 104(4):1146, 2007.
- [112] W. Shi, J. Qin, N. Ye, and B. Lin. Droplet-based microfluidic system for individual caenorhabditis elegans assay. *Lab on a Chip*, 8(9):1432–1435, 2008.
- [113] H. Boukellal, Š. Selimović, Y. Jia, G. Cristobal, and S. Fraden. Simple, robust storage of drops and fluids in a microfluidic device. *Lab Chip*, 9(2):331–338, 2009.

- [114] M. Sun, S.S. Bithi, and S.A. Vanapalli. Microfluidic static droplet arrays with tuneable gradients in material composition. *Lab on a Chip*, 2011.
- [115] J. Shim, G. Cristobal, D.R. Link, T. Thorsen, Y. Jia, K. Piattelli, and S. Fraden. Control and measurement of the phase behavior of aqueous solutions using microfluidics. *Journal of the American Chemical Society*, 129(28):8825–8835, 2007.
- [116] C.H.J. Schmitz, A.C. Rowat, S. Koster, and D.A. Weitz. Dropspots: a picoliter array in a microfluidic device. *Lab on a Chip*, 9(1):44, 2009.
- [117] K. Stephan, P. Pittet, L. Renaud, P. Kleimann, P. Morin, N. Ouaini, and R. Ferrigno. Fast prototyping using a dry film photoresist: microfabrication of soft-lithography masters for microfluidic structures. *Journal of Micromechanics and Microengineering*, 17:N69–N74, 2007.
- [118] P. Abbyad, R. Dangla, A. Alexandrou, and C.N. Baroud. Rails and anchors: Guiding and trapping droplet microreactors in two dimensions. *Lab Chip*, 11:813–821, 2011.
- [119] R. Dangla, S. Lee, and C.N. Baroud. Trapping microfluidic drops in wells of surface energy. *Physical Review Letters*, 107(12):124501, 2011.
- [120] K.A. Brakke. The surface evolver.
- [121] A. Ashkin. Optical trapping and manipulation of neutral particles using lasers. *Proceedings of the National Academy of Sciences*, 94(10):4853, 1997.
- [122] R.R. Pompano, W. Liu, W. Du, and R.F. Ismagilov. Microfluidics using spatially defined arrays of droplets in one, two, and three dimensions. *Annual Rev. Anal. Chem.*, 2011.
- [123] I. Barbulovic-Nad, S.H. Au, and A.R. Wheeler. A microfluidic platform for complete mammalian cell culture. *Lab on a Chip*, 10(12):1536–1542, 2010.
- [124] W. Du, L. Li, K.P. Nichols, and R.F. Ismagilov. Slipchip. *Lab Chip*, 9(16):2286–2292, 2009.
- [125] F. Shen, W. Du, J.E. Kreutz, A. Fok, and R.F. Ismagilov. Digital pcr on a slipchip. *Lab Chip*, 10(20):2666–2672, 2010.
- [126] Etienne Fradet, Craig McDougall, Paul Abbyad, Remi Dangla, David McGloin, and Charles N. Baroud. Combining rails and anchors with laser forcing for selective manipulation within 2d droplet arrays. *Lab Chip*, pages 4228–4234, 2011.
- [127] B. Ahn, K. Lee, H. Lee, R. Panchapakesan, L. Xu, J. Xu, and K.W. Oh. Guiding, distribution, and storage of trains of shape-dependent droplets. *Lab Chip*, 11(22):3915–3918, 2011.

- [128] J. Xu, B. Ahn, H. Lee, L. Xu, K. Lee, R. Panchapakesan, and K.W. Oh. Droplet-based microfluidic device for multiple-droplet clustering. *Lab Chip*, 12(4):725–730, 2012.
- [129] L. Xu, H. Lee, R. Panchapakesan, and K.W. Oh. Fusion and sorting of two parallel trains of droplets by using a railroad- like channel network and guiding tracks. *Lab Chip*, in press, 2012.
- [130] T. Gervais, J. El-Ali, A. Gunther, and K. F. Jensen. Flow-induced deformation of shallow microfluidic channels. *Lab On a Chip*, 6:500–507, 2006.
- [131] P. Garstecki, H. A. Stone, and G. M Whitesides. Mechanism for flow-rate controlled breakup in confined geometries : A route to monodisperse emulsions. *Physical Review Letters*, 94:164501, 2005.
- [132] V. van Steijn, C.R. Kleijn, and M.T. Kreutzer. Predictive model for the size of bubbles and droplets created in microfluidic t-junctions. *Lab Chip*, 10(19):2513–2518, 2010.
- [133] C. Holtze, AC Rowat, JJ Agresti, JB Hutchison, FE Angile, CHJ Schmitz, S. Köster, H. Duan, KJ Humphry, RA Scanga, et al. Biocompatible surfactants for water-in-fluorocarbon emulsions. *Lab Chip*, 8(10):1632–1639, 2008.
- [134] J. Clausell-Tormos, D. Lieber, J.C. Baret, A. El-Harrak, O.J. Miller, L. Frenz, J. Blouwolff, K.J. Humphry, S. Köster, H. Duan, et al. Droplet-based microfluidic platforms for the encapsulation and screening of mammalian cells and multicellular organisms. *Chemistry & biology*, 15(5):427–437, 2008.
- [135] J.C. Baret. Surfactants in droplet-based microfluidics. *Lab Chip*, 12(3):422–433, 2012.
- [136] SR Majumdar and DH Michael. The equilibrium and stability of two dimensional pendent drops. *Proceedings of the Royal Society of London. A. Mathematical and Physical Sciences*, 351(1664):89–115, 1976.
- [137] J. Plateau. Statique expérimentale et théorique des liquides soumis aux seules forces moléculaires. 1873. *Gauthier-Villars, Paris*, 1873.
- [138] L. Rayleigh. On the stability of liquid jets. *Proc. London Math. Soc*, 10(4), 1878.
- [139] C. Delaunay. Sur la surface de revolution dont la courbure moyenne est constante. *J. Math. Pures Appl*, 6(1841):309–315, 1841.
- [140] P. Guillot, A. Colin, A.S. Utada, and A. Ajdari. Stability of a jet in confined pressure-driven biphasic flows at low reynolds numbers. *Physical review letters*, 99(10):104502, 2007.

- [141] B. Dollet, W. van Hoeve, J.P. Raven, P. Marmottant, and M. Versluis. Role of the channel geometry on the bubble pinch-off in flow-focusing devices. *Physical review letters*, 100(3):34504, 2008.
- [142] P.M. Korczyk, O. Cybulski, S. Makulska, and P. Garstecki. Effects of unsteadiness of the rates of flow on the dynamics of formation of droplets in microfluidic systems. *Lab on a Chip*, 11(1):173–175, 2011.
- [143] L. Rayleigh. Investigations in capillarity. *Philosophical Magazine*, 48:321, 1899.
- [144] W.D. Harkins and FE Brown. The determination of surface tension (free surface energy), and the weight of falling drops: The surface tension of water and benzene by the capillary height method. *Journal of the American Chemical Society*, 41(4):499–524, 1919.
- [145] C. Clanet and J.C. Lasheras. Transition from dripping to jetting. *Journal of Fluid Mechanics*, 383(1):307–326, 1999.
- [146] N. Damean, L.F. Olguin, F. Hollfelder, C. Abell, and W.T.S. Huck. Simultaneous measurement of reactions in microdroplets filled by concentration gradients. *Lab Chip*, 9(12):1707–1713, 2009.
- [147] M.P.N. Bui, C.A. Li, K.N. Han, J. Choo, E.K. Lee, and G.H. Seong. Enzyme kinetic measurements using a droplet-based microfluidic system with a concentration gradient. *Analytical Chemistry*, 83(5):1603–1608, 2011.
- [148] T. Nisisako and T. Torii. Microfluidic large-scale integration on a chip for mass production of monodisperse droplets and particles. *Lab Chip*, 8(2):287–293, 2007.
- [149] M.K. Mulligan and J.P. Rothstein. Scale-up and control of droplet production in coupled microfluidic flow-focusing geometries. *Microfluidics and Nanofluidics*, pages 1–9, 2012.
- [150] M.B. Romanowsky, A.R. Abate, A. Rotem, C. Holtze, and D.A. Weitz. High throughput production of single core double emulsions in a parallelized microfluidic device. *Lab Chip*, 12(4):802–807, 2012.
- [151] T. Kawakatsu, Y. Kikuchi, and M. Nakajima. Regular-sized cell creation in microchannel emulsification by visual microprocessing method. *Journal of the American Oil Chemists' Society*, 74(3):317–321, 1997.
- [152] I. Kobayashi, K. Uemura, and M. Nakajima. Controlled generation of monodisperse discoid droplets using microchannel arrays. *Langmuir*, 22(26):10893–10897, 2006.
- [153] I. Kobayashi, M. Nakajima, K. Chun, Y. Kikuchi, and H. Fujita. Silicon array of elongated through-holes for monodisperse emulsion droplets. *AIChE journal*, 48(8):1639–1644, 2002.

- [154] C. Priest, S. Herminghaus, and R. Seemann. Generation of monodisperse gel emulsions in a microfluidic device. *Applied physics letters*, 88:024106, 2006.
- [155] F. Malloggi, N. Pannacci, R. Attia, F. Monti, P. Mary, H. Willaime, P. Tabeling, B. Cabane, and P. Poncet. Monodisperse Colloids Synthesized with Nanofluidic Technology. *Langmuir*, pages 10–1441, 2010.
- [156] R.M. Lorenz, G.S. Fiorini, G.D.M. Jeffries, D.S.W. Lim, M. He, and D.T. Chiu. Simultaneous generation of multiple aqueous droplets in a microfluidic device. *Analytica chimica acta*, 630(2):124–130, 2008.
- [157] S. Sugiura, M. Nakajima, S. Iwamoto, and M. Seki. Interfacial tension driven monodispersed droplet formation from microfabricated channel array. *Langmuir*, 17(18):5562–5566, 2001.
- [158] I. Kobayashi, T. Takano, R. Maeda, Y. Wada, K. Uemura, and M. Nakajima. Straight-through microchannel devices for generating monodisperse emulsion droplets several microns in size. *Microfluidics and nanofluidics*, 4(3):167–177, 2008.
- [159] N. Tarchichi, F. Chollet, and J.F. Manceau. New regime of droplet generation in a T-shape microfluidic junction. *Microfluidics and Nanofluidics*, page in press.
- [160] RW Atherton and GM Homsy. On the derivation of evolution equations for interfacial waves. *Chemical Engineering Communications*, 2(2):57–77, 1976.